

NASA Conference Publication 2314

Space Photovoltaic Research and Technology 1983

*High Efficiency, Radiation Damage,
and Blanket Technology*

(NASA-CP-2314) SPACE PHOTOVOLTAIC RESEARCH
AND TECHNOLOGY 1983. HIGH EFFICIENCY,
RADIATION DAMAGE, AND BLANKET TECHNOLOGY

(NASA) 266 p HC A12/MP A01

CSCL 10A

N84-29307
THRU

N84-29346

Unclas

G3/44 17806

*Proceedings of a conference
held at NASA Lewis Research Center
Cleveland, Ohio
October 19-20, 1983*

NASA

NASA Conference Publication 2314

Space Photovoltaic Research and Technology 1983

*High Efficiency, Radiation Damage,
and Blanket Technology*

*Proceedings of a conference
held at NASA Lewis Research Center
Cleveland, Ohio
October 18-20, 1983*



National Aeronautics
and Space Administration

Scientific and Technical
Information Branch

1984

FOREWORD

The solar cell has been an indispensable element of the U.S. space program. The development of the silicon solar cell into an efficient, reliable, and commercially available device has made our many accomplishments in space possible. Not only has the silicon cell been the workhorse power source for satellites, but it is now also a leading candidate for generating solar-electric power on the ground. Looking to the future, to the proposed space station, one sees that the job of photovoltaic power generation is far from over and that the need for high-efficiency, long-life, inexpensive photovoltaic devices is stronger than ever.

This meeting, the sixth of its kind, was intended to be a direction-setting forum. Each invited expert was expected to express his or her judgment (1) to help set suitable goals for space solar cell research and development, (2) to define the obstacles preventing the attainment of these goals, and (3) to bring to the surface the most viable approaches to overcome these obstacles.

At this conference, we added three related overview papers. These covered the topics energy storage, plasma interactions, and space station status. The intent was to present to the photovoltaic community status reports in related technologies.

This was a working meeting where strong emphasis was placed on the exchange and discussion of ideas and opinions against a background of technical presentations. The atmosphere was informal yet structured, and individual interaction was encouraged. The discussions were focused on four areas. These areas and the individuals who generally accepted the responsibility of managing them are

High efficiency cells, John Fan, MIT/Lincoln Laboratories
Radiation damage, Paul Stelia, Jet Propulsion Laboratory
Advanced devices, Michael Ludowise, Varian Associates
Array technology, Hans Rauschenbach, TRW

Oral reports from workshops in each of these areas were presented and discussed in a plenary session. Written summaries of the workshop conclusions prepared by the workshop chairs are included in this proceedings.

The coordinated efforts of Henry Curtis, Carolyn Clapper, George Mazaris, and Shirley Livingston were responsible for the successful organization and conduct of this meeting.

Henry Brandhorst
NASA Lewis Research Center

Conference Chair

PRECEDING PAGE BLANK NOT FILMED

CONTENTS

NASA-OAST PHOTOVOLTAIC ENERGY CONVERSION PROGRAM Jerome P. Mullin and John C. Loria, NASA Headquarters	1
STRUCTURALLY STABLE, THIN SILICON SOLAR CELLS R. A. Arndt and A. Meulenberg, COMSAT Laboratories	8
RECENT ADVANCES IN LPE GaAs-BASED SOLAR CELLS G. S. Kamath, R. Y. Loo, and R. C. Knechtli, Hughes Research Laboratories	12
PROCESS IN MANUFACTURING HIGH EFFICIENCY AlGaAs/GaAs SOLAR CELLS BY MO-CVD Y. C. M. Yeh, K. I. Chang, and J. Tandon, Applied Solar Energy Corporation	18
OPTIMAL DESIGN OF GaAs-BASED CONCENTRATOR SPACE SOLAR CELLS FOR 100 AMO, 80° C OPERATION Chandra Goradia and Manju Ghalla-Goradia, Cleveland State University, and Henry Curtis, NASA Lewis Research Center . .	25
TWO-DIMENSIONAL COMPUTER SIMULATION OF EMVJ AND GRATING SOLAR CELLS UNDER AMO ILLUMINATION J. L. Gray and R. J. Schwartz, Purdue University	34
RADIATION TESTING OF GaAs ON CRRES AND LIPS EXPERIMENTS Terry M. Trumble and Kenneth Masloski, Air Force Wright Aeronautical Laboratories	41
SOLAR CELL DEGRADATION IN PROTON RADIATION ORBITS H. S. Raushenbach and J. Y. Yaung, TRW Space & Technology Group	49
MODEL OF SOLAR CELL PROTON DAMAGE J. Y. Yaung, TRW Defense Systems Group	56
PIECEWISE SIMULATION PROTON TEST OF GALLIUM ARSENIDE AND THIN SILICON SOLAR CELLS D. G. Peterson and S. A. Billets, Lockheed Missiles & Space Company, Inc.	63
RADIATION TOLERANCE OF LOW RESISTIVITY, HIGH VOLTAGE SILICON SOLAR CELLS V. G. Weizer, I. Weinberg, and C. K. Swartz, Lewis Research Center	74
ON-ORBIT PERFORMANCE OF LIPS GALLIUM ARSENIDE SOLAR CELL EXPERIMENT T. Bavaro, R. Francis, and M. Pennell, The Aerospace Corporation .	81

INFLUENCE OF OXYGEN ON DEFECT PRODUCTION IN ELECTRON-IRRADIATED, BORON-DOPED SILICON Henry M. DeAngelis and Peter J. Drevinsky, Rome Air Development Center	90
DEFECT STUDIES IN ONE-MEV ELECTRON IRRADIATED GaAs AND IN $Al_xGa_{1-x}As$ P-N JUNCTION SOLAR CELLS Sheng S. Li and W. L. Wang, University of Florida, and R. Y. Loo, Hughes Research Laboratory	91
CELL AND DEFECT BEHAVIOR IN LITHIUM-COUNTERDOPED SOLAR CELLS I. Weinberg, NASA Lewis Research Center, S. Mehta, Cleveland State University, and C. K. Swartz, NASA Lewis Research Center	102
DEFECT INTERACTIONS IN GaAs SINGLE CRYSTALS H. C. Gatos and J. Lagowski, Massachusetts Institute of Technology	111
EQUIVALENT ELECTRON FLUENCE FOR SOLAR PROTON DAMAGE IN GaAs SHALLOW JUNCTION CELLS John W. Wilson, NASA Langley Research Center, and L. V. Stock, Old Dominion University	112
RESEARCH DIRECTIONS AND PROGRESS IN SERI ADVANCED HIGH EFFICIENCY CONCEPTS PROGRAM John P. Benner and Lee A. Cole, Solar Energy Research Institute	118
OPTIMAL DESIGN OF HIGH-EFFICIENCY SINGLE-JUNCTION AND TANDEM CONCENTRATOR SPACE CELLS AT 80° C AND 100 SUNS John C. C. Fan and B. J. Palm, Massachusetts Institute of Technology	120
DEVELOPMENT OF GaAs/Si AND GaAlAs/Si MONOLITHIC STRUCTURES FOR FUTURE SPACE SOLAR CELLS M. B. Spitzer, S. M. Vernon, R. G. Wolfson, and S. P. Tobin, Spire Corporation	128
DEVELOPMENT OF A 30 PERCENT EFFICIENT 3-JUNCTION MONOLITHIC CASCADE SOLAR CELL C. R. Lewis, W. T. Dietze, and M. J. Ludowise, Varian Associates, Inc.	140
HIGH-EFFICIENCY SOLAR CELLS FABRICATED BY VACUUM MO-CVD L. M. Fraas, J. A. Cape, L. D. Partain, and P. S. McLeod, Chevron Research Co.	148
PLASMON DEVICE DESIGN: CONVERSION FROM SURFACE TO JUNCTION PLASMONS WITH GRATING-COUPLEDERS Lynn M. Anderson, NASA Lewis Research Center	155
INTERACTIONS BETWEEN VOLUME AND SURFACE EM WAVES IN LAYERED STRUCTURES S. Ushioda, University of California	156

PRELIMINARY CONCEPT OF A 100-KILOWATT MINIATURIZED CASSEGRAINIAN CONCENTRATOR SOLAR ARRAY Robert E. Patterson, TRW Space & Technology Group	157
PERFORMANCE MEASUREMENT OF LOW CONCENTRATION RATIO SOLAR ARRAY FOR SPACE APPLICATION Michael W. Mills, Rockwell International Corporation	163
PREFLIGHT STUDY OF SAN MARCO D/L GaAs SOLAR CELL PANELS John H. Day, Jr., NASA Goddard Space Flight Center	176
PRELIMINARY SPACE STATION SOLAR ARRAY STRUCTURAL DESIGN STUDY John T. Dorsey, Harold G. Bush, and Martin M. Mikulas, Jr., NASA Langley Research Center	182
DEVELOPMENT AND SUPPORT STRUCTURES FOR HIGH-POWER SOLAR ARRAYS Karl Knapp, Astro Research Corporation	193
PANEL FABRICATION UTILIZING GaAs SOLAR CELLS N. Mardesich, Spectrolab, Inc.	205
TRANSPARENT ARRAYS - PROGRESS TOWARD HIGHER EFFICIENCY G. J. Pack, Lockheed Missiles & Space Company, Inc.	210
THE NASA WELDING ASSESSMENT PROGRAM John Scott-Monck, Jet Propulsion Laboratory, and John Bozek, NASA Lewis Research Center	220
HIGH SPEED, LOW COST, LEO-THERMAL-CYCLING FACILITY R. E. Hart, Jr., and L. G. Sidorak, NASA Lewis Research Center	223
IMPROVED TECHNIQUES OF PARALLEL GAP WELDING AND MONITORING N. Mardesich and M. S. Gillanders, Spectrolab, Inc.	228
ELECTROCHEMICAL STORAGE Lawrence H. Thaller, NASA Lewis Research Center	235
SOLAR ARRAY - PLASMA INTERACTIONS Carolyn K. Purvis, NASA Lewis Research Center	236
SPACE STATION A. F. Forestieri, NASA Space Station Task Force	237
HIGH-EFFICIENCY CONVENTIONAL CELL WORKSHOP John C. C. Fan, Massachusetts Institute of Technology	251
RADIATION DAMAGE WORKSHOP Paul M. Stella, Jet Propulsion Laboratory	253
ADVANCED DEVICES WORKSHOP M. Ludowise, Varian Associates, Inc.	255
SOLAR ARRAY TECHNOLOGY WORKSHOP H. S. Rauschenbach, TRW Space & Technology Group	257

N84
29308

UNCLAS

NASA-OAST PHOTOVOLTAIC ENERGY CONVERSION PROGRAM

Jerome P. Mullin and John C. Loria
National Aeronautics and Space Administration
Washington, D.C.

NASA's operational Space Shuttle capability is ushering in a new era of peaceful ventures in space. Future missions, such as space systems with manufacturing and advanced scientific laboratory capabilities, advanced direct broadcast satellites in GEO, and outer planet exploratory spacecraft will be characterized by energy demands extending to 10^5 kWhrs. Photovoltaic energy conversion systems face significant challenges in meeting these expanding energy demands. The ability to deliver large amounts of power in space for long periods of time at a reasonable cost is, therefore, a focus of NASA-OAST's Office of Energy Systems efforts. (Figure 1)

PHOTOVOLTAIC ENERGY CONVERSION PROGRAM

The NASA program in photovoltaic energy conversion includes research and technology development efforts on solar cells, blankets, and arrays. The overall objectives are to increase conversion efficiency, reduce mass and cost, and to increase the operating lifetimes of photovoltaic converters and arrays. (Figure 2)

Technology thrusts fall into three areas: (1) cell research and technology, (2) blankets and arrays, and (3) advanced devices. Cell research and technology includes fundamental studies in cell physics, radiation damage and annealing, and development of high specific power cells. Blanket and array technologies involve identification and demonstration of low-cost fabrication techniques, interconnect welding studies, and research on planar and concentrator arrays. Advanced devices include research in such areas as thermophotovoltaic energy converters, multiple bandgap cascade solar cells, and surface plasmon converters.

Understanding, and subsequently eliminating, the life limiting failure mechanisms in silicon solar cells and development of advanced GaAs cells hold promise of lifetimes up to 10 years in GEO with 15% EOL efficiencies. Improved welding techniques can reduce costs and increase reliability. A leading contender for near-term high power generation is the Cassegrainian concentrator array. Indications are that this concentrator, with flux levels of about 100 suns, can be produced at relatively low cost. A 4 mm^2 GaAs cell should soon be available to operate at 80°C with 20% efficiency. An array of such devices would

yield over 200 W/m^2 . Because of recent advances in thin, gridded-back cells and low-cost superstrate designs, planar arrays are still of very high interest.

TECHNOLOGY REQUIREMENTS

The 1983 Report of a Workshop held at Woods Hole last year by the Aeronautics and Space Engineering Board (ASEB) of the National Research Council on "NASA's Space Research and Technology Program" describes spacecraft power systems technology development as being "essential" in solar arrays and solar cells. Solar cell welding, high-performance thin cells, GaAs cells, low-cost cells, radiation-resistant and "hardened" solar cells and arrays are listed as significant technology issues that require attention. Large flexible solar arrays, because of their relatively high power-to-weight ratios, are predicted to play an important role in providing higher power for future spacecraft, and their continued development is predicted to be an important part of our overall power systems technology program. The desired advances enumerated in the ASEB report include solar arrays up to 250kW in size, cell efficiencies up to 22%, lifetimes greater than 10 years, and radiation resistance up to 5×10^{15} electrons/sq.cm. (Figure 3) The NASA Photovoltaic Energy Conversion Program is geared to achieve these goals by the 1990 time period.

SPACE STATION

The dominant feature of the Space Station will be the size of the power subsystem. (Figure 4) Bus power requirements at the 75kW level translate into multi-hundred kilowatt solar array power levels. Two major components of the total life cycle cost for photovoltaic power generation in low earth orbit are annual cost of reboost fuel for drag make-up, and initial cost of the solar array. Substantial reductions in drag make-up requirements and cell costs can be obtained using concentrator arrays with GaAs cells. With these potential performance benefits and others, such as reduced current leakage caused by interaction with the space plasma and resistance to hostile space environments, GaAs concentrator arrays become compelling candidates for advanced development for Space Station.

SPACECRAFT

Spacecraft needs differ considerably from those of Space Station. (Figure 5) Space Station is characterized by rugged use by many users calling for high power levels, ~5000 day-night cycles/year, and heavy emphasis on cost reduction. High orbit spacecraft are special purpose systems with more modest power demands; only ~100 day-night cycles/year, and emphasis on weight reduction. Whereas the low earth orbiting space station will experience dense plasmas which cause power

losses by drainage and chemical attack, spacecraft experience dilute plasmas where spacecraft charging and damaging arcing occur.

Current spacecraft payload mass fractions are only of the order of 25% of the total spacecraft mass. (Figure 6) Power and propulsion constitute about 50% of the total mass. The mass available for payload can be doubled if the bus mass fraction of current spacecraft can be reduced by 1/3. Indications are that large benefits are potentially available in the power and propulsion technology areas to accomplish this reduction in the bus mass. Four-fold reductions in the mass of the power systems and three-fold reductions in propulsion system mass are realizable through advanced technology which will yield 100 W-hr/kg storage systems, 250 W/kg solar arrays, 100 volt power distribution systems, and xenon ion propulsion systems. (Figure 7)

STATE OF THE ART

The U.S. state of the art in solar arrays is represented by the 66 W/kg SEP array design. (Figure 8) A full-scale, reduced-power version of this array will be flown on STS-14 in June, 1984. However, this array is based on technology of the early 1970's. Significant advances have since been achieved. Large area (5.9cm x 5.9cm) silicon cells with wrap-around contacts have been baselined for the Air Force MILSTAR program. This will be the first use of welded interconnects with lightweight Kapton blanket technology. Implementation will help to overcome the European lead in welded lightweight GEO blanket technology. The OAST 50 μ m Si cells represent a light-weight radiation-resistant standard for silicon cells. These thin cells have been incorporated into thin Kapton blankets. Deployment of this thin blanket has been proposed using the STACBEAM (Stacking Triangular Articulated Compact Beam), which is a low mass/volume alternative to the ASTROMAST. A transparent 6 μ m GaAs solar cell, with a specific power of 5.7 kW/kg has been tested in the laboratory. This transparent cell will result in lower cell temperatures and, consequently, higher efficiencies, thereby increasing the potential pay-off of the GaAs solar cell. Current plans are to work toward integrating these recent developments into advanced array designs. We invite your help in formalizing these plans. We look to you for new ideas and new ways to accelerate the technology advances which will result in solar arrays with specific powers 4 to 5 times that of the SEP array.

SUMMARY

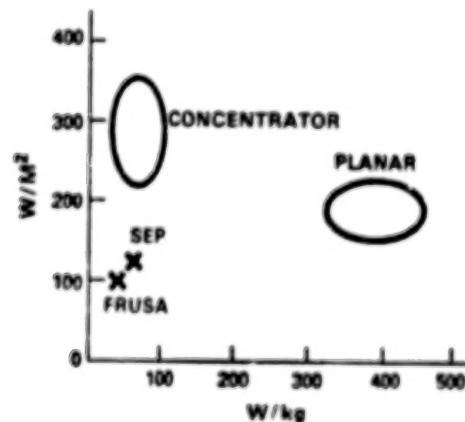
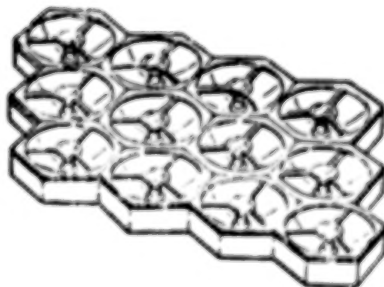
The NASA-OAST Photovoltaic Energy Conversion Program remains broadly based with the focus on integrating technological advances which will result in space energy systems to enhance and to enable current and future space activities. The trend toward high power requirements remains a major challenge which can be best met with an array of technological advances.

ORIGINAL PAGE IS
OF POOR QUALITY

- **POWER IS ENABLING TECHNOLOGY**
 - HIGH CAPACITY - LEO
 - HIGH PERFORMANCE - GEO
 - EXPLORATION
 - PROPULSION
- **SOLE NATIONAL CAPABILITY**
 - SPACE NUCLEAR POWER
 - ELECTRIC PROPULSION
- **DEVELOPING ADVANCED CONCEPTS**
 - GENERATION
 - STORAGE
 - THERMAL
 - PROPULSION
- **FOUNDATION FOR MAJOR AGENCY/COMMERCIAL/DEFENSE THRUSTS**
 - SPACE STATION
 - COMMUNICATIONS/RESOURCES
 - SPACE BASED RADAR

Figure 1. - Significance of space energy systems.

- TECHNOLOGY THRUSTS**
- CELL RESEARCH & TECHNOLOGY
 - ADVANCED DEVICES
 - BLANKETS & ARRAYS



OBJECTIVES

- DECREASED COST & MASS
- INCREASED EFFICIENCY & LIFETIME
- IMPROVED UNDERSTANDING
- LEO/HEO/GEO/PLANETARY CAPABILITY

Figure 2. - Photovoltaic energy conversion program.

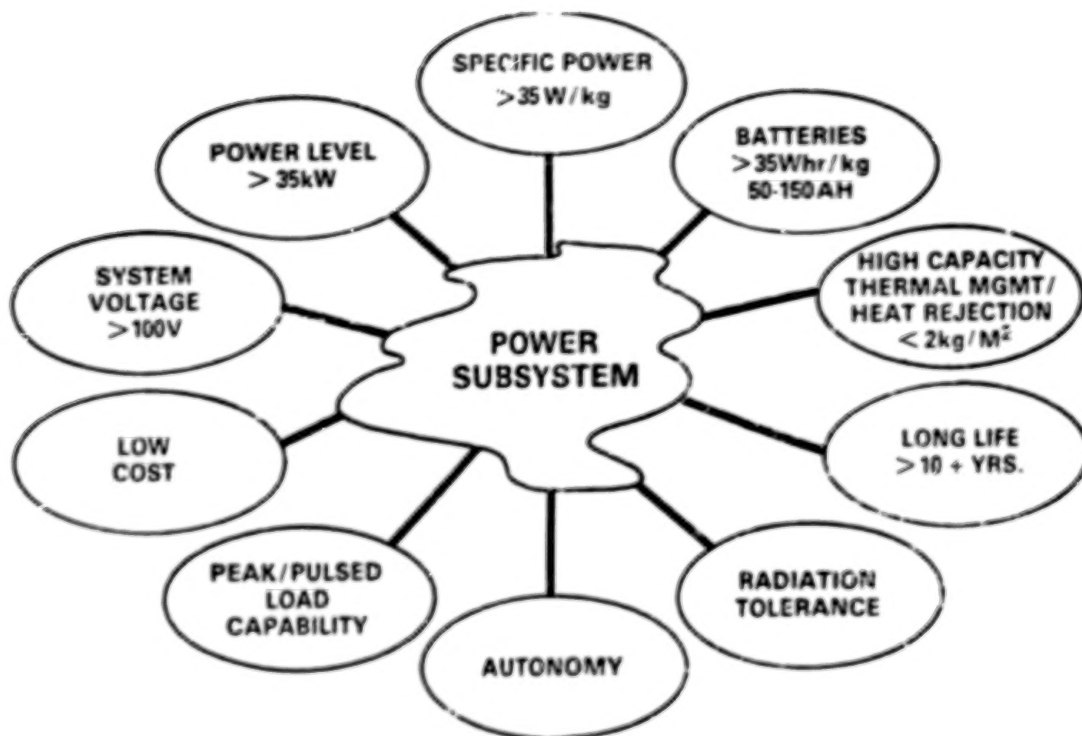


Figure 3. - Satellite power needs for the 1990's. (Woods Hole - August 1982.)

POWER SUBSYSTEM

- SIZE — DOMINANT FEATURE OF SPACE STATION
- MASS — LARGE MASS (5 W/kg — 10 W/kg)
- COST — (500-1,000 \$/kW-hr HISTORICALLY FOR SPACE STATION)

HISTORICAL FOCUS

- PAST 5 YRS MULTI-HUNDRED KILOWATT PROGRAM EMPHASIS
- RECENT TECHNICAL FACTORS IMPACTING PROGRAM
 - DRAG
 - OXIDATION
 - PLASMA INTERACTIONS
 - THERMAL CYCLING

Figure 4. - Space station technology.

ORIGINAL PAGE IS
OF POOR QUALITY

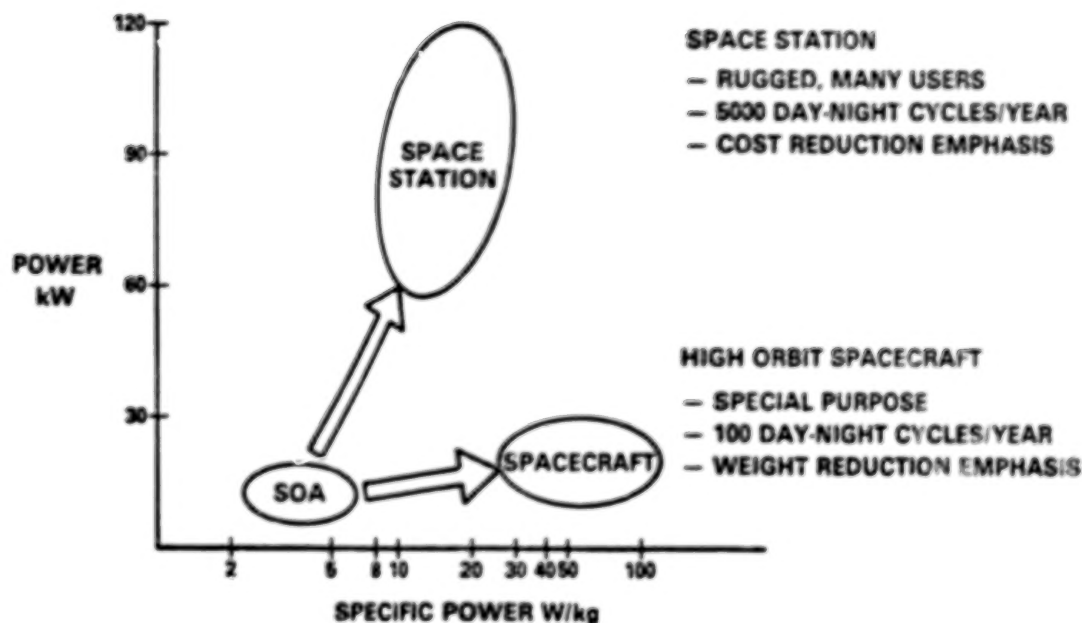


Figure 5. - Spacecraft bus technology. (Spacecraft needs differ from those of space station.)

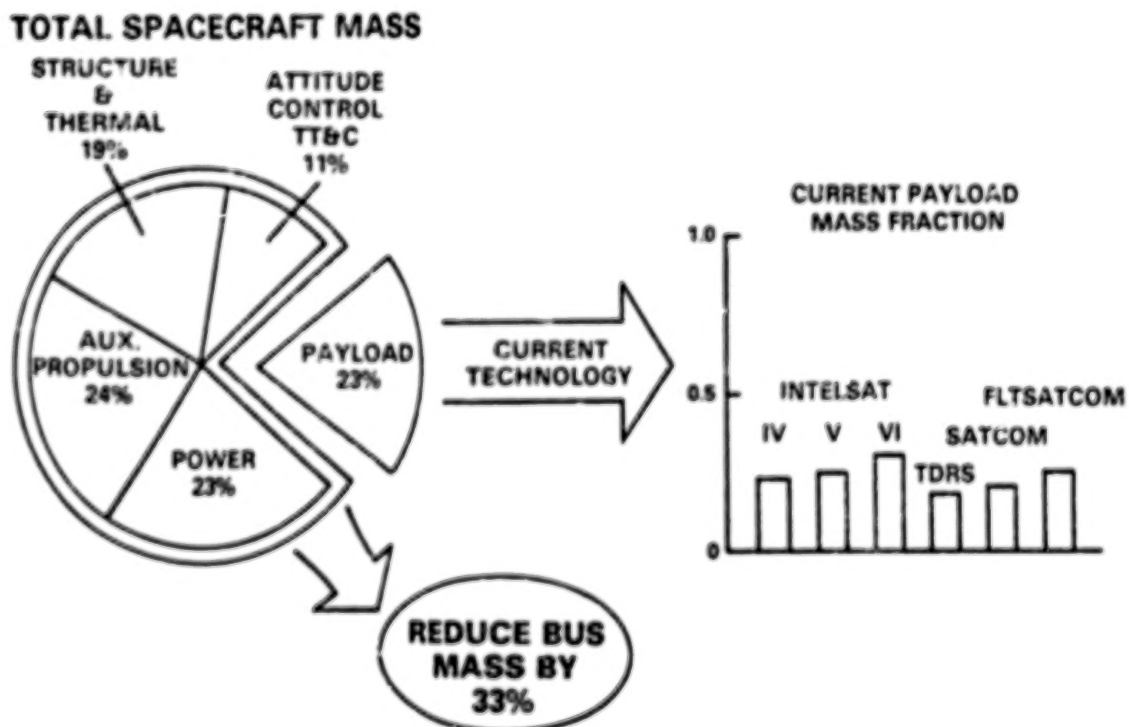
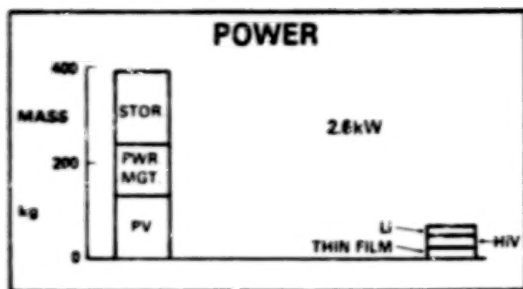


Figure 6. - Current spacecraft bus technology.

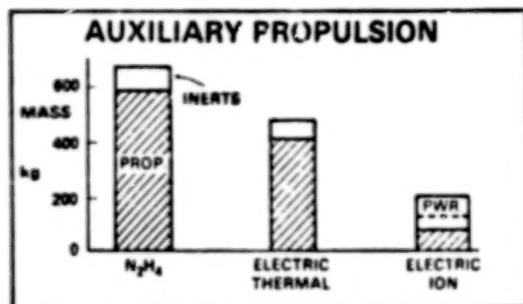
ORIGINAL PAGE 19
OF POOR QUALITY



TDRS

**ASEB REPORT
RECOMMENDATIONS
JUNE 1983**

- NASA REVITALIZATION OF ON-ORBIT PROPULSION—#1 SPECIFIC PRIORITY
- "DEVELOPMENT ESSENTIAL IN BATTERIES, SOLAR ARRAYS AND CELLS"



TDRS

SATCOM
INTELSAT V

ADVANCED
XENON
SYSTEM

Figure 7. - Spacecraft bus technology. (Specific achievable goals endorsed by ASEB.)

R&T ADVANCES

ADVANCED CELLS

GOAL:
250 W/kg
1988

STATE-OF-THE-ART



SEP ARRAY
66 W/kg
200 μ , 11% CELLS
COMPLETED 1976

**LARGE AREA
MILSTAR CELL**



**14% 6 μ TRANSPARENT
GALLIUM ARSENIDE**



**LOW MASS
BLANKET TECHNOLOGY**



50m CELL BLANKET

**14% 60 μ SILICON
DEPLOYMENT**



STACBEAM

Figure 8. - Lightweight arrays for spacecraft.

N84
29309

UNCLAS

N84 29309

STRUCTURALLY STABLE, THIN SILICON SOLAR CELLS*

R. A. Arndt and A. Meulenberg
COMSAT Laboratories
Clarksburg, Maryland

Thin ($\sim 50 \mu\text{m}$) silicon solar cells offer some advantages over thicker cells for space applications. One of these is that the mass of the cell is much less, and since the power output is only fractionally smaller, the power-to-weight ratio increases. Another advantage is that, after moderate ($\sim 10^{15} \text{cm}^{-2}$) levels of 1 MeV electron irradiation, the maximum power of thin cells is greater than that of thicker cells that are otherwise identical. Thus, not only is excess weight eliminated by use of thin cells but the actual power available at end-of-life is greater for satellite missions in most radiation environments.

One problem that seems to persist with thin cells is the low production-yield. Even though $50 \mu\text{m}$ thick cells are flexible, they are fragile and subject to breakage in almost all stages of fabrication. Reported fabrication yields are almost never greater than 50%. The fact that the thin wafers are often bowed increases the handling problems during fabrication and array assembly.

We have developed a structure that overcomes many of the handling (and, therefore, breakage) problems and which has exhibited yields on a limited number of cells (~ 100) of at least 75%. The cells resulting from this structure are quite flat and structurally reinforced to reduce the extreme care usually required with thin cells. A schematic cross section of this structure is shown in Figure 1.

The fabrication process as developed by COMSAT Labs is (briefly) as follows. A 6 mil, circular wafer is oxidized on both sides. One side is then patterned with a rectangular array of holes in the oxide that are nominally 75 mils square and separated by 2 mil spacings. Wells are then etched into the silicon with KOH to a depth of 4 mils, leaving a 2 mil, unetched thickness. Two areas on the surface are left unetched to provide pads for bonding or testing. All oxide is then removed and the rest of the processing is normal; the unetched face is used as the illuminated face. When all other processing is complete, a 2 X 2 cm cell is sawed from the starting wafer leaving a border that is approximately 10 mils wide. The effective thickness, determined by weighing an unmetallized sample, of such a cell is $\sim 2.4 \text{ mil}$ ($61 \mu\text{m}$).

The structure is not sensitive to variations in processing. Starting wafers that are square, instead of circular, can be used to avoid the final sawing step. However, the wide borders of the circular wafers do provide support during

*This paper is based upon work performed at COMSAT Laboratories under a corporate task.

processing and are convenient handles. Since most the strength of the final structure is in the ribs, variations in wafer thickness and in the thinning process are less critical than in the case of planar, thin cell processing. Non-reflective surfaces, different etch-mask oxides, and different etchants could be used without detracting from the structure. Observation of the breakage modes indicate that larger (e.g., 4 cm X 4 cm or 2 cm X 6 cm) rib-reinforced cells might be viable as well. Variations in the structure could also be introduced to optimize the cell mass and production yield.

Several cells were fabricated in each of two resistivity, p-type wafers; 0.1 Ω -cm and 1.0 Ω -cm. The cells had double antireflective (DAR) layers of Ta_2O_5 and Al_2O_3 . The cells were not optimized for beginning-of-life performance by the use of techniques such as p^+ back contacts, passivated surfaces, or dot contacts.¹ A typical I-V curve of a 1 Ω -cm cell with a fused silica coverslide (0.35 μ m filter) obtained under AMO illumination at 25°C is shown in Figure 2. The 0.1 Ω -cm cells exhibited much the same maximum power, but V_{OC} was ~615 mV and I_{SC} was ~142 mA. Most of the cells exhibited maximum power outputs of ~66 mW, but a few were as high as 68 mW.

Sample cells from each resistivity were irradiated at the Naval Research Laboratory with 1 MeV electrons to fluences of $4 \times 10^{14} \text{ cm}^{-2}$ and $9 \times 10^{14} \text{ cm}^{-2}$. The maximum power (AMO, 25°C) for the 1 Ω -cm cells, after these fluences, is shown on Figure 3 by the X's. For comparison, Figure 3 also shows the output power of a 2 Ω -cm, 10 mil thick Violet cell as a function of 1 MeV electron fluences. The V_{OC} of 0.1 Ω -cm cells did not degrade much (~5%) from the $9 \times 10^{14} \text{ cm}^{-2}$ fluence, but I_{SC} dropped a great deal and the output power dropped (to 44 mW) commensurately. The output of these rib-reinforced cells compares favorably with the Violet cells as well as with that of a 50 μ m, 10 Ω -cm, textured surface cell² (61 mW) for the same irradiation conditions.

The rib-reinforced cell described here should be a very good candidate for space use in that it is lightweight and produces good power output after irradiation. Further, the yield (~75%, or greater) is such that it should be more economical to fabricate than other structures of similar thickness.

REFERENCES

1. A. Meulenberg, Jr., "Development Toward an 18% Efficient Silicon Solar Cell," NASA Contract NAS-3-22217, Final Report, April 1983.
2. B.E. Auspaugh, et al., "Electrical Characteristics of Spectrolab BSF, BSR, Textured, 10 Ω -cm, 50 Micron Advanced OAST Solar Cells As a Function of Intensity Temperature, and Irradiation," JPL Publication 78-15, Vol. VI, June 15, 1979.

ORIGINAL PAGE 13
OF POOR QUALITY

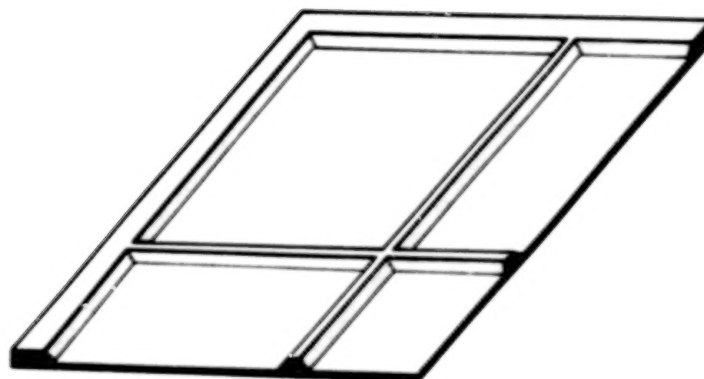


Figure 1. - Perspective view showing one corner of a rib-reinforced cell.

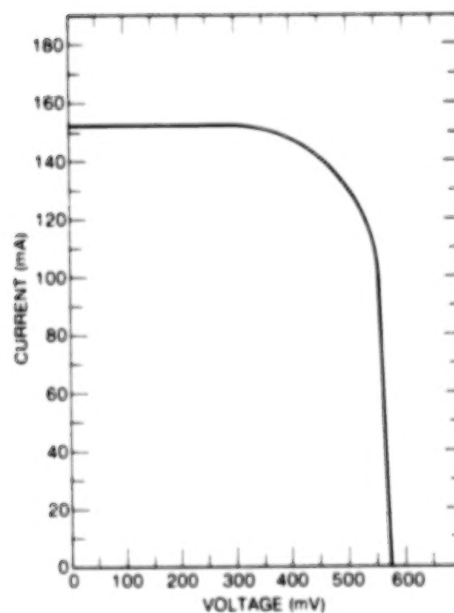


Figure 2. - Typical I-V curve for a 1 Ω -cm rib-reinforced cell under AMO illumination at 25° C.

ORIGINAL DESIGN IS
OF POOR QUALITY

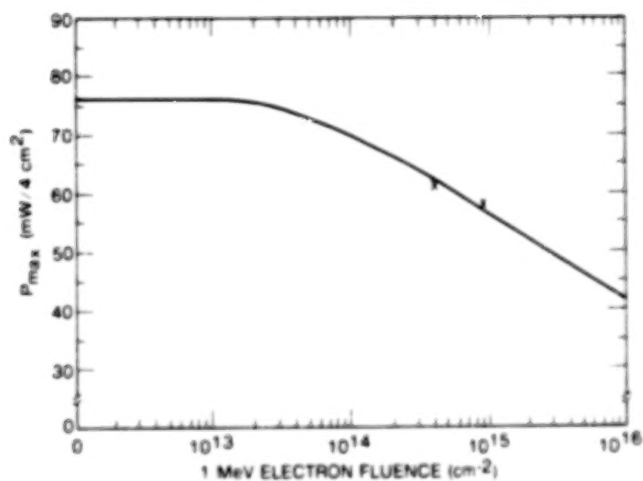


Figure 3. - Maximum power output of a Violet cell ($2 \Omega\text{-cm}$, 10 mil) as a function of 1 MeV electron fluence under AMO illumination at 25°C . The X's are data points for a rib-reinforced cell ($1 \Omega\text{-cm}$) under the same conditions.

N84
29310

UNCLAS

N84 29310

RECENT ADVANCES IN LPE GaAs-BASED SOLAR CELLS

G. S. Kamath, R. Y. Loo, and R. C. Knechtli
Hughes Research Laboratories
Malibu, California

Several modifications have been made to our infinite solution LPE system that help fabricate both GaAs-based cells with $\eta_{amo} > 25\%$ and thin cells that effectively reduce power-to-weight ratio for space applications. The most important development is the multiwell crucible for multilayer growth. Using a split crucible in one of our systems, we have grown as many as five layers in succession with varying Al levels and dopants. The structures grown have been used to produce thin GaAs cells only 10 to 20 μm thick and also to grow cascade cell components. Results of these studies will be presented and their applications to the future development of GaAs-based cells discussed.

INTRODUCTION

Developments during the last five years have led to increased acceptance of the GaAs cell as a viable candidate for space power applications. Hughes Research Laboratories (HRL) has built a few small space panels (see Fig. 1), and their performance has been in agreement with predictions based on ground-based experiments. It has been realized for some time that the significant advantages offered by GaAs solar cells for space applications could be considerably augmented by developing either a thin cell or a multijunction cell. The first would increase the power-to-weight advantage, and the second would result in higher efficiency per unit-area. These potential benefits have led HRL to direct our efforts to perfecting techniques for the fabrication of the novel device structures.

Since the infinite solution technique has been developed successfully at HRL to mass produce large-area GaAs cells, we decided to modify the technique for the fabrication of thin cells and multijunction cells. A major requirement was the ability to grow multilayer structures of (AlGa)As and GaAs interchangeably. We have developed techniques to meet the need and have demonstrated the suitability of our LPE technique to grow the complex epitaxial structures.

EXPERIMENTAL DETAILS

The LPE growth system developed at HRL has been described previously (ref. 1) and is shown in Figure 2. The solutions of GaAs or (AlGa)As used for growth have been as large as 6 kg, and we have grown layers out of one solution for periods of four years. One solution was used to fabricate over ten thousand cells during these years and gave cells with reproducible efficiencies of over 16% AMO. Large scale production of cells from these systems was made possible by growing layers that yield up to eighty 2 cm x 2 cm cells per epitaxial growth, and the performance characteristics of these cells have been reported previously (ref. 2).

To enable us to grow the novel structures needed for thin cells and cascade cells, we modified the system in two aspects. First, we substituted a multiwell

graphite crucible that could house several solutions in one LPE system. Second, we provided the system with a more powerful five-zone temperature controller that allowed us to obtain the precise temperature profile in the system, as well as a reproducible cooling cycle which continuously tailored the profile for uniform growth of a series of layers (Fig. 3).

The multiwell system houses up to five solutions with varying Al compositions and dopants. In choosing the dopants, care has to be taken to ensure a vapor pressure as low as possible to minimize cross contamination. We use Sn for n-type and Ge and/or Be for p-type whenever possible. Since the behavior of these dopants varies with the Al concentration in the solution, the choice has to be made specifically for each solution. For example, Ge is ideal for p-type doping of solutions with up to 45% Al. If an Al level higher than that is necessary, Be has to be used. In addition, the diffusion characteristics of the dopants at the growth temperature have to be considered. For example, if we need to create a p-n homojunction by diffusion of the p-type dopant from the window layer, Be is a good choice since its diffusion can be controlled at the growth temperature relatively easily. On the contrary, when we need to have a sharp interface between n and p layers and thus have minimum interdiffusion, the choice of dopants for n- and p-type would be Sn and Ge. Another factor which is important is to maintain the solution levels in the various wells uniform so that the substrate can be moved from one solution to another without causing appreciable temperature profile variations. Finally, the concentration levels of the solutions have to be adjusted to permit successive growth of layers with reproducible control.

The precise control of temperature profiles and cooling rates necessitated the modification of our temperature control system for the LPE furnace. We instituted a computer-operated five-zone temperature controller that maintains the required temperature profile in the solutions with great reproducibility. The controller has been able to adjust the entire growth cycle through a series of epitaxial growths to give us multilayer structures.

RESULTS AND DISCUSSION

The combination of the multiwell system and the five-zone control enabled us to fabricate an all-(AlGa)As cell, shown in Figure 2. We have varied the Al composition in the buffer layer from 0 to 50% Al. With this initial accomplishment as a base, we proceeded to grow multilayer structures for cascade cells.

The availability of the system also motivated us to explore the possibility of making thin GaAs cells for space. We had clearly demonstrated in prior experimentation that a 2-mil GaAs cell with only 50 μm of GaAs is equal in performance to our conventional 12-mil cell. Fan (ref. 3) and others have shown in their work that only a few microns of GaAs are needed to ensure the maximum efficiency of the cell as predicted by theory from the very short minority carrier diffusion length in the material. Our earlier cells were obtained by polishing off the extra GaAs after cell fabrication. Since it is known that (AlGa)As can be used as a stop etch layer (ref. 4), we decided to grow a GaAs cell structure on a GaAs substrate separated by a (AlGa)As layer and determine the feasibility of using the stop etch layer to control the removal of the GaAs reproducibly. These structures were grown using the new system, and they have provided us with reproducibly controllable structures. We are refining various parameters in the process to give us large-area cells and exploring the possibility of modifying the technique to permit the reuse of the

substrates. Various approaches being used to fabricate thin GaAs solar cells are shown in Figure 4.

SUMMARY AND CONCLUSION

The availability of the thin cells will greatly enhance the economic viability of the GaAs cell by making it competitive with silicon in power-to-weight ratio in space applications. In addition, it would greatly lower the cost of the cell itself, especially if the reusable substrate becomes a reality. Finally, the present extension of the infinite solution technique to multiwell systems enables us to fabricate cascade cell structures that can deliver efficiencies in excess of 20% AMO available from the GaAs cell.

REFERENCES

1. Kamath, G. S.: Proc. IEEE, Vol. 1, 1981, p 416.
2. Kamath, G. S.: Proc. IEEE, Vol. 3, 1983, p 1224
3. Fan, C. C., et al.: Proc. 14th IEEE Photovoltaic Specialists Conference, 1980, p. 1102; Proc 16th IEEE Photovoltaic Specialists Conference, 1982, p. 692.
4. LaRue, R. A., et al.: Proc. 16th IEEE Photovoltaic Specialists Conference, 1982 p. 228.

ORIGINAL PAGE 13
OF POOR QUALITY

12823-1

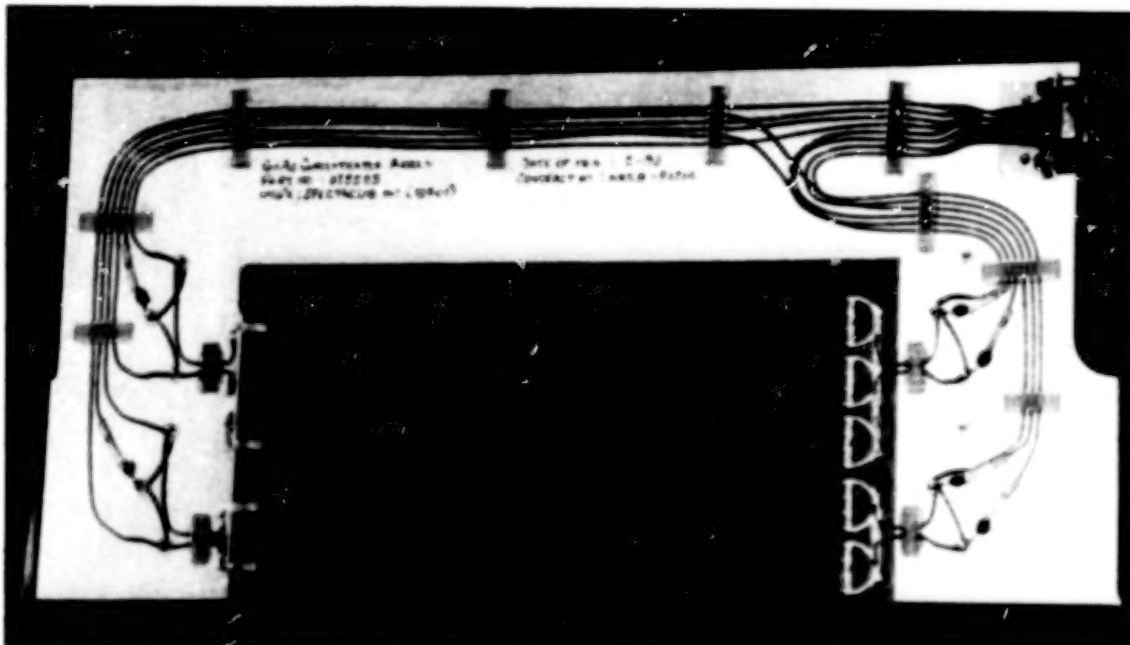


Figure 1. - GaAs solar cell panel using HRL 2 cm x 2 cm cells.

ORIGINAL PAGE 19
OF POOR QUALITY



Figure 2. - HRL multiwell epitaxial growth system.



Figure 3. - The five-zone temperature controller.

ORIGINAL PAGE IS
OF POOR QUALITY

13136-1R1

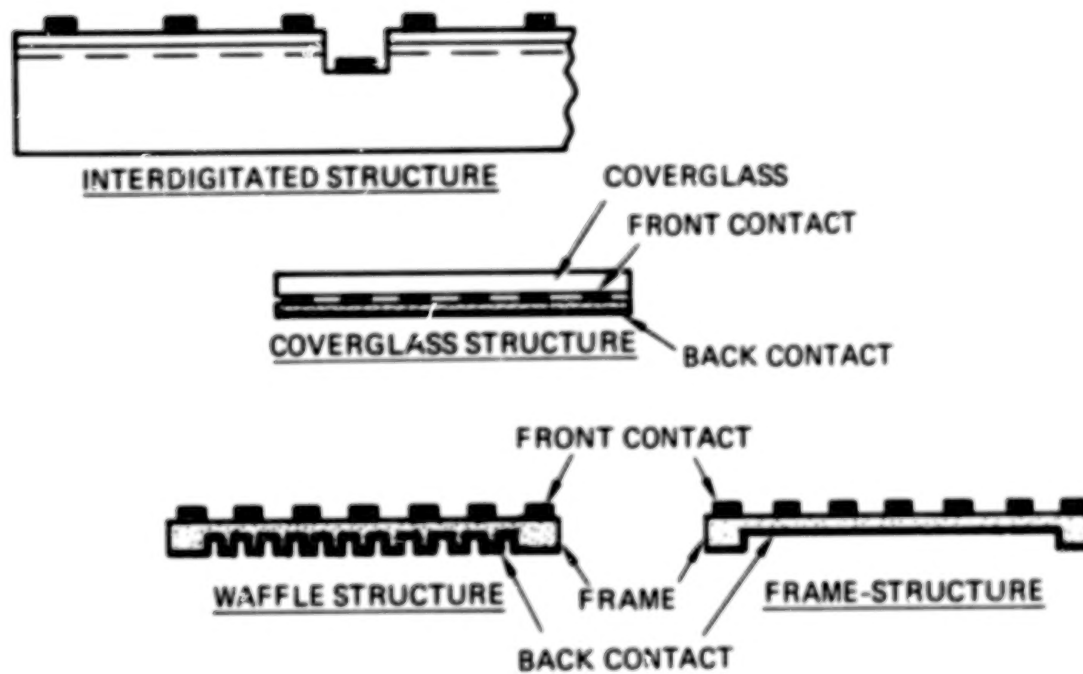


Figure 4. - Various thin cell structures of GaAs.

N84
29311

UNCLAS

N84 29311

PROCESS IN MANUFACTURING HIGH EFFICIENCY AlGaAs/GaAs
SOLAR CELLS BY MO-CVD

Y. C. M. Yeh, K. I. Chang, and J. Tandon
Applied Solar Energy Corporation

Applied Solar Energy Corporation (ASEC) is currently developing manufacturing technology for mass producing high efficiency GaAs solar cells. This paper reports our progress using a high throughput MO-CVD reactor to produce high efficiency GaAs solar cells. Thickness and doping concentration uniformity of MO-CVD GaAs and AlGaAs layer growth are discussed. In addition, new tooling designs are given which increase the throughput of solar cell processing. To date, we have produced 2cm x 2cm AlGaAs/GaAs solar cells with AMO efficiency up to 16.5%.

INTRODUCTION

Applied Solar Energy Corporation (ASEC) is currently developing manufacturing technology for mass producing high efficiency GaAs solar cells under a contract from the Materials Laboratory, Wright Patterson Air Force Base. After extensive reviewing of publications on solar cell structures and coupled with our past working experience on various solar cells, we have concluded that the most viable solar cell structure, capable of producing radiation-resistant solar cells of AMO efficiency greater than 16% with large area (2x2cm² or greater), is the AlGaAs/GaAs heteroface GaAs solar cell. The physical structure of such a solar cell is shown in Figure 1. In reaching such a conclusion, consideration was given not only to the theoretical aspects, but also to various manufacturing aspects.

In order to meet throughput goals for mass producing GaAs solar cells, we have purchased and installed a large MO-CVD system (Cambridge Instrument Model MR-200) with a susceptor which was initially capable of processing 20 wafers (up to 75mm diameter) during a single growth run. In the MR-200, the sequencing of the gases and the heating power are controlled by a microprocessor-based programmable control console. Hence, operator errors can be reduced, leading to a more reproducible production sequence.

THICKNESS UNIFORMITY OF EPI-FILMS PRODUCED BY THE ORIGINAL SUSCEPTOR

After installation of the MO-CVD system, tests were first conducted to determine the

thermal time-constant of the system. This information is needed to predict the instantaneous temperature of the susceptor. Then in turn, the heating power can be programmed. The heating time constant of the MO-CVD system has been determined to be about 6.3 minutes as shown in figure 2.

Next, growth runs of GaAs epi-layers were conducted. Initially, we observed large fluctuations in layer thicknesses as a function of positions. The thickness distribution of the initial GaAs growth run (run 1) is shown in figure 3. In figure 3, positions 0 through 9 represent the ten individual facets of the barrel susceptor. In the original susceptor, two 75mm diameter pockets were machined in each facet, the up-stream pockets are labeled as row A and the down-stream pockets are labeled as row B. Subsequently, modifications were made in the injection nozzle, which improved the thickness uniformity considerably during later growth runs (run 2) as shown in figure 3. The percentage thickness deviation versus yield of both runs is shown in table I. By injection nozzle modification, the thickness uniformity has been improved to $\pm 28\%$ from the original $\pm 48\%$ value.

Further modifications were made in reducing the turbulent flow of the gas mixture, resulting in a thickness uniformity of $\pm 12\%$. The thickness uniformity is also quite good for samples made within each pocket. The thickness variation of an $\text{Al}_x\text{Ga}_{1-x}\text{As}$ epi-layer grown on a single crystal wafer of 75mm diameter is shown in figure 4.

THICKNESS AND DOPING CONCENTRATION OF EPI-FILMS PRODUCED BY THE NEW HIGH PACKING DENSITY BARREL SUSCEPTOR

Since the original susceptor had circular pockets, the area utilization of the susceptor was poor. In order to improve the throughput of the MO-CVD system, a new high packing density barrel susceptor was designed and fabricated. The engineering drawing of such a susceptor is shown in figure 5. By using this susceptor, up to ninety rectangular wafers of 2.5cm x 4.5cm size can be loaded in one growth run, greatly improving the throughput of the MO-CVD system. The side view of the new susceptor is shown in the upper-left portion of figure 5. In this case, the narrow end (in the left side) is the top up-stream side when the barrel susceptor is being used in our vertical reactor. In the lower-left of figure 5, nine 2.5cm x 4.5cm rectangular wafers are shown to be loaded in one facet of the new susceptor. Letters A through I signify the relative position of wafers on each facet.

The layer thickness distribution of epi-layer growth using the new susceptor can best be characterized by the growth of AlGaAs on GaAs substrate, since AlGaAs can be selectively etched off providing accurate thickness information. The AlGaAs layer thickness distribution using the new susceptor is shown in table II. For this new susceptor, the layer thickness is fairly uniform ($\pm 17\%$), for pockets A,B,D,E,G and H i.e., in the pockets located in the top two up-stream rows. However, the layer thickness in the bottom-row pockets is considerably thinner. New modifications in the pocket location have been engineered to reduce this problem and a third generation susceptor has been ordered.

The doping-concentration distribution of the epi-layers grown using this new susceptor is shown in table III. The values of doping concentration were measured using a Polaron Semiconductor Profile Plotter, and cross referenced with Hall measurement data. In table III, G, H, and I represent the pockets located in the top, middle, and bottom rows, respectively. Hence, from table III, it is clear that the doping concentration decreases towards the down-stream rows. This is most likely due to the non-uniform temperature

distribution along the flow-axis of the susceptor. The new modified susceptor is designed to reduce this problem.

PHOTOVOLTAIC RESULTS OF AlGaAs/GaAs SOLAR CELLS

Using the high throughput susceptor, we have successfully fabricated 2cm x 2cm solar cells with AMO efficiencies at 28°C up to 16.6%. The light I-V characteristics of the best cell is shown in figure 6. The measurement was confirmed at JPL with a X-25 solar simulator (Calibrated with GaAs BF cell). The values of Voc (open circuit voltage), Isc (short-circuit current), FF (fill-factor) for the best cell are 0.998V, 112 mA and 0.80, respectively.

CONCLUSION

AlGaAs/GaAs solar cells with energy conversion efficiency higher than 16% AMO can be fabricated on a production scale MO-CVD system.

TABLE I. - THICKNESS UNIFORMITY OF GaAs EPI-LAYERS
GROWN IN ASEC'S MO-CVD SYSTEM

RUN NO.	THICKNESS DEVIATION	YIELD
1	± 20%	62%
	± 28%	81%
	± 48%	100%
2	± 20%	72%
	± 28%	100%

NOTE: RUN NO. 1 - BEFORE INJECTION NOZZLE
MODIFICATION
RUN NO. 2 - AFTER MODIFICATION

ORIGINAL PAGE IS
OF POOR QUALITY

TABLE II. - AlGaAs LAYER THICKNESS DISTRIBUTION OF NEW
HIGH-DENSITY BARREL SUSCEPTOR

AVERAGE THICKNESS (MICROMETER)		
A: 0.49 ± 0.03	D: 0.47 ± 0.04	G: 0.54 ± 0.05
B: 0.48 ± 0.04	E: 0.46 ± 0.04	H: 0.51 ± 0.05
C: 0.35 ± 0.06	F: 0.40 ± 0.03	I: 0.36 ± 0.05

AVERAGE THICKNESS FOR A,B,D,E,G, & H:
 0.49 ± 0.08 MICROMETER ($\pm 16\%$)

TABLE III. - N-GaAs DOPING CONCENTRATION DISTRIBUTION
OF NEW HIGH-DENSITY BARREL SUSCEPTOR

POSITION	AVE. DOPING CONCENTRATION (cm^{-3})
G	$9.3 \times 10^{17} \pm 50\%$
H	$3.2 \times 10^{17} \pm 40\%$
I	$1.2 \times 10^{17} \pm 40\%$

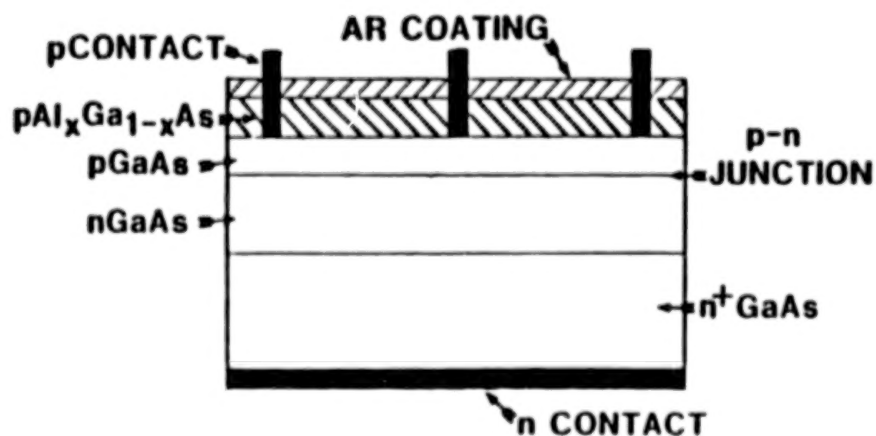


Figure 1. - Structure of AlGaAs/GaAs heteroface solar cell.

ORIGINAL PAGE 19
OF POOR QUALITY

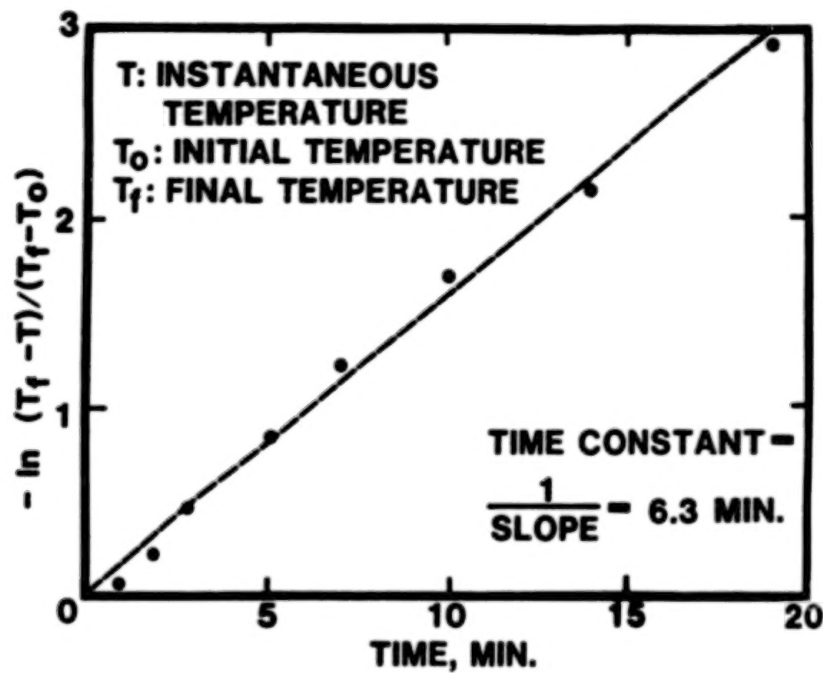


Figure 2. - Heating time constant determination of MO-CVD system.

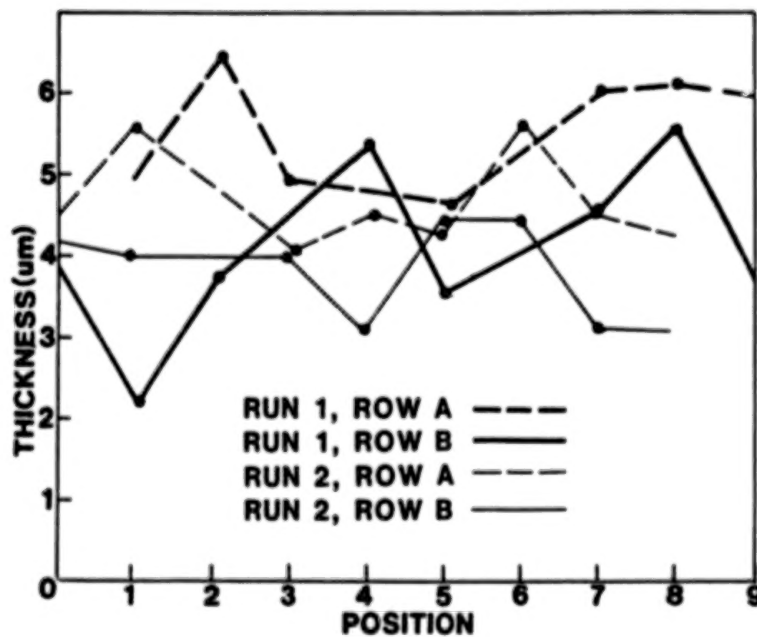


Figure 3. - Thickness of distribution of GaAs epi-layers.

DATE: MAY 3, 1983
SAMPLE # R-9 1B
AVE. THICKNESS (um)
0.454 +4.6%
-7.5%

POSITION	THICKNESS(um)
1	0.445
2	0.460
3	0.465
4	0.420
5	0.473
6	0.473
7	0.455
8	0.432
9	0.475

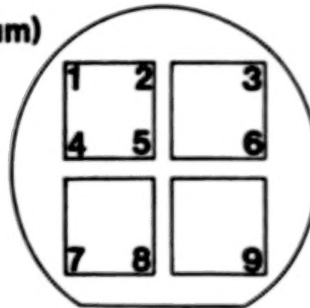


Figure 4. - $Al_xGa_{1-x}As$ epi-layer thickness determination.

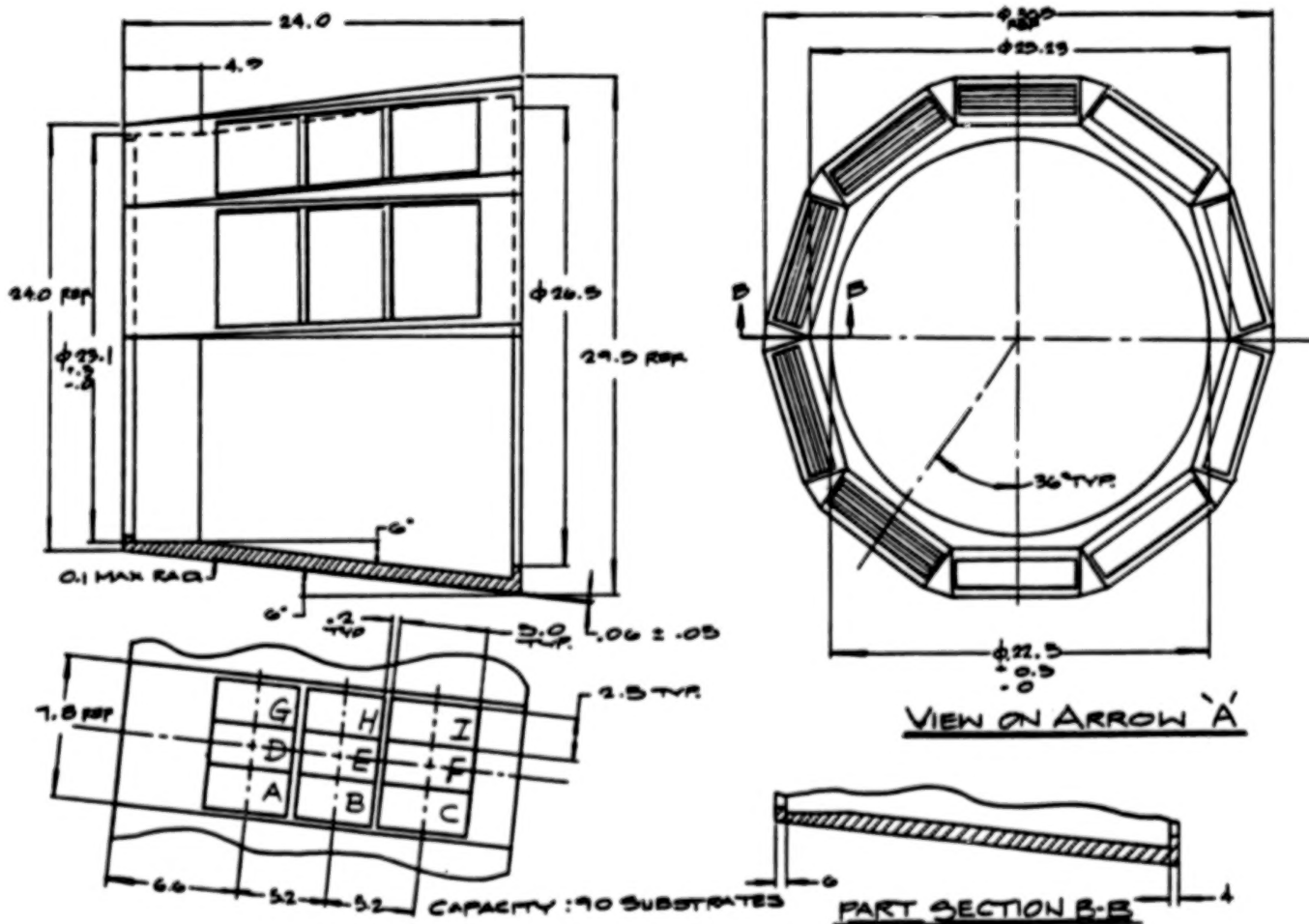


Figure 5. - Proposed tooling design for high-packing-density barrel susceptor.

FIGURE 6. - LIGHT CURRENT-VOLTAGE CHARACTERISTICS OF POOR QUALITY

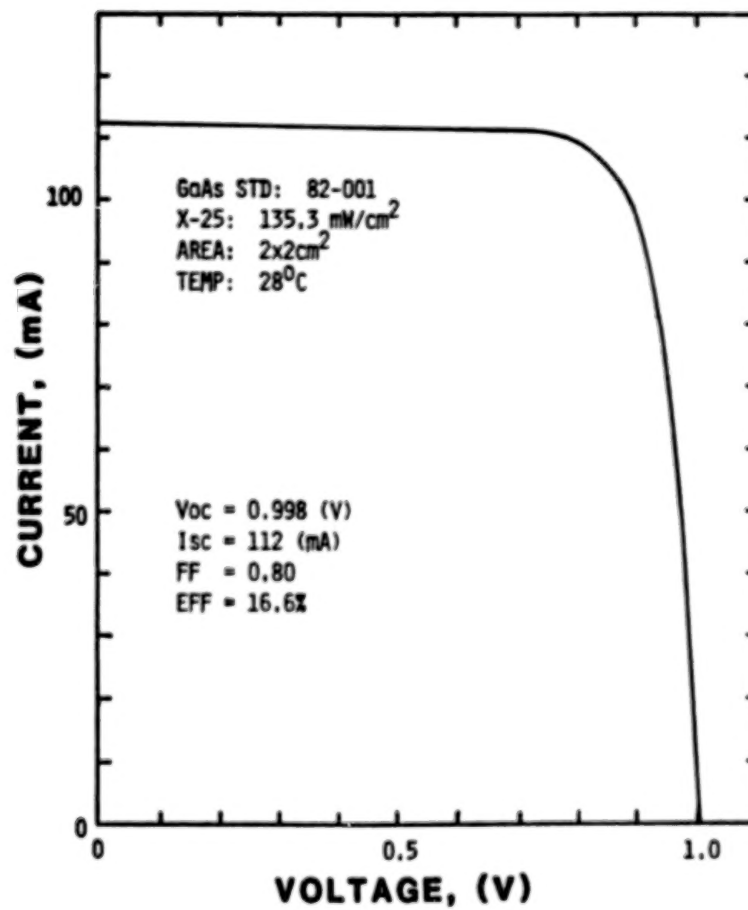


Figure 6. - Light current-voltage characteristics of AlGaAs/GaAs solar cell.

N84
29312

UNCLAS

OPTIMAL DESIGN OF GaAs-BASED CONCENTRATOR
SPACE SOLAR CELLS FOR 100 AMO, 80° C OPERATION

Chandra Goradia and Manju Ghalla-Goradia*
Cleveland State University
Cleveland, Ohio

Henry Curtis
NASA Lewis Research Center
Cleveland, Ohio

Using a detailed computer code and reasonable values of electrical and optical material parameters from current published literature, parameter optimization studies were performed on three configurations of GaAs-based concentrator solar cells for 100 AMO, 80°C operation. These studies show the possibility of designing GaAs-based solar cells with efficiencies exceeding 22% at 100 AMO 80°C and probable efficiency degradation of less than 15% after a 70% reduction in diffusion length in each cell region.

INTRODUCTION

In a continuing effort to increase the beginning-of-life (BOL) efficiency, radiation tolerance and the power/area and power/weight ratios of space solar cell panels, NASA has established a near-term goal of developing GaAs-based (with or without an AlGaAs window) space concentrator solar cells with a BOL efficiency of 22% or higher at 100 AMO, 80°C and with high radiation tolerance; a longer term goal is to develop multibandgap cascade solar cells with efficiencies exceeding 30%.

The use of sunlight concentration offers the advantages of 1) higher efficiency, 2) lower cost per watt, and 3) partial shielding of the solar cells against space radiation. The 80°C operation is a result of the current design of the Casagrainian concentrator for 100x concentration. While this higher temperature operation reduces the efficiency somewhat, it provides a partial continuous annealing of radiation damage in the solar cells. It may later turn out that a still higher operating temperature of say 150°C to 200°C may be more desirable to provide total continuous annealing of radiation damage at some sacrifice in efficiency.

In an attempt to design a GaAs-based solar cell with 22% or higher efficiency at 100 AMO and 80°C, we developed a detailed computer code that can simulate both $p^+Al_xGa_{1-x}As/pGaAs/nGaAs/nGaAs$ (p/n AlGaAs/GaAs) and $nAl_xGa_{1-x}As/nGaAs/pGaAs/p^+GaAs$ (n/p AlGaAs/GaAs) solar cells, as well as similar GaAs cells without the AlGaAs window. Details on our computer model will be published elsewhere.

*Work of first two authors supported under NASA Grant NAG3-249.

CALCULATED RESULTS AND DISCUSSION

Using our computer simulation model, we did a parameter optimization study on three cell configurations, namely, the p/n AlGaAs/GaAs, n/p AlGaAs/GaAs and the n/p GaAs shallow homojunction. The p/n GaAs homojunction is not considered to be a viable space solar cell because radiation tolerance requires a shallow emitter which would result in an unacceptably high series resistance. For each configuration, actually two parameter optimizations were done: one without any regard to radiation degradation and the other taking into account radiation degradation. Since neither space-equivalent 1 MeV electron fluence nor doping-dependent damage coefficients in n and p GaAs are reasonably well known, radiation damage calculations were done by decreasing the minority carrier diffusion length in each cell region by the same factor which took on values of 0.9, 0.7, 0.5, 0.3 and 0.1. This was along the lines of [7] and while it does not accurately predict cell performance degradation in a space radiation environment, we feel that the method is useful in both initial cell design and for a relative comparison among different cell configurations.

Table 1 gives the optimum values of the key geometrical and material parameters of the three GaAs-based cell configurations at 100 AMO, 80°C, taking radiation degradation into account. By using somewhat wider emitter and base regions and by using a uniform base region doping of $5 \times 10^{17} \text{ cm}^{-3}$, slightly higher efficiencies (by a factor of 1.01) than those of Table 1 can be obtained at the sacrifice of increased radiation degradation. By the same token, somewhat improved radiation tolerance can be obtained at some sacrifice in BOL efficiency by making the emitter and base regions narrower and less heavily doped. Thus, the optimum cell designs of Table 1 may be regarded as those obtained by a tradeoff between high BOL efficiency and a radiation degradation of 10 to 15% after a 70% reduction in diffusion length in each cell region.

Table 2 shows how the photogenerated and dark currents under the open-circuit condition are distributed amongst the window, emitter, base and space charge regions for each of the three optimized cell configurations at 100 AMO, 80°C. It is seen that for high efficiency and high radiation tolerance, the majority of the photogenerated current should come from the p-GaAs region, whether it is the emitter or the base, since it has long diffusion lengths. Unlike with silicon solar cells, a non-negligible contribution to the photogenerated current comes from the emitter region; over 60% for the p/n AlGaAs/GaAs cell and over 15% even in the n/p GaAs shallow homojunction cell. The majority of the dark current, on the other hand, always comes from the base region, with non-negligible contributions from the emitter and space charge regions.

The performance parameters of Table 1 were based on the assumption that the recombination velocity S_{12} at the window/emitter interface is 10^4 cm/s for the p/n and n/p cells with a window and is 10^6 cm/s at the front surface for the n/p shallow homojunction cell. Figure 1 shows the effect of variation of this recombination velocity S_{12} on the performance parameters J_{sc} , FF and η . Not shown is V_{oc} which degrades by less than 5% over the range of S_{12} . It is seen that for cells with an AlGaAs window the major degradation in cell efficiency occurs for $S_{12} > 10^5$

cm/s and is due almost wholly to a decrease in J_{sc} . The percentage degradation in efficiency as S_{12} varies from 10^4 to 10^7 cm/s is related to the fractional contribution to the photocurrent by the emitter region; the larger the fraction of the total photocurrent that comes from the emitter, the larger the degradation. The slight increase in FF with increasing S_{12} is due to the decrease in the ohmic (IR) voltage drop across the series resistance at the maximum power point due to reduced current. There are actually two conflicting factors affecting the variation of FF with S_{12} ; as S_{12} increases, the FF increases due to the above reason but decreases due to a reduction in V_{oc} . Since the first factor dominates, there is a net increase in FF with S_{12} .

Figures 2, 3 and 4 show the variation of J_{sc} , V_{oc} , FF and η with temperature for illumination intensities of 1, 10 and 100 for the three cell configurations. Also indicated along the appropriate curves are the values of dJ_{sc}/dT , dV_{oc}/dT and $d\eta/dT$. Note that as expected, the magnitude of dV_{oc}/dT decreases with increasing illumination intensity. Note also that dJ_{sc}/dT decreases and $|dV_{oc}/dT|$ increases as we go from the p/n AlGaAs/GaAs to the n/p AlGaAs/GaAs to the n/p GaAs shallow homojunction cell.

The degradation of FF is due to three factors, all tending to decrease FF with increasing T. These are: 1) decrease of V_{oc} , 2) increase of I_{sc} and 3) increase of the series resistance R_s itself. The last two factors together give a larger ohmic voltage drop across the series resistance with increasing temperature.

In spite of the performance degradation with increased temperature, Figures 2, 3, 4 show that GaAs-based cells can yield efficiencies in excess of 18% at 100 AMO at 200°C. If it turns out that operation at 200°C provides total or almost total continuous annealing of these cells against radiation damage, then these cells could be optimized differently for operation at 200°C, 200 AMO and without regard to radiation damage. It may then be possible to operate a GaAs-based cell with an efficiency of ~20% at 100 AMO, 200°C with a very long life in a space radiation environment.

Finally, Figure 5 shows the degradation of J_{sc} , V_{oc} , FF and η for the three cell configurations as a function of L/L_0 , the ratio of the diffusion length to its BOL value, in each of window, emitter, base and buffer/BSF regions. Also indicated are the fractional degradations $(\eta_{BOL} - \eta_{EOL})/\eta_{BOL}$, expressed in percent, for each cell configuration. Here η_{EOL} is defined as η at $L/L_0 = 0.3$. Assuming that there exists an effective diffusion-length damage coefficient K_L for each cell configuration under normally incident 1 MeV electrons and that this K_L value is independent of the electron fluence ϕ and that the standard degradation equation $1/L^2 = 1/L_0^2 + K_L \phi$ holds, it is easy to calculate that the fluence increases by three orders of magnitude, one order each, as L/L_0 goes from 0.995 to 0.953 to 0.7 to 0.3. A very crude calculation, using $K_L \sim 10^{-8}/e^-$ and $L_0 \sim 10 \mu m$, then shows that an $L/L_0 = 0.3$ corresponds

to an exposure to a fluence of roughly 10^{15} 1MeV electrons/cm². Of course, we do not know what that corresponds to in terms of number of years in geostationary earth orbit (GEO).

It should be made clear that the calculated results of Figure 5 should be regarded as being useful only for a relative comparison of the three cell configurations and not for the prediction of cell performance in a space radiation environment or, for that matter, even in the laboratory under 1MeV electrons. There are still too many unknowns to be able to do that with any degree of confidence. Amongst those unknowns, in addition to the uncertainties mentioned above, is the one about the effect of radiation on the interface or surface recombination velocity S_{12} . This was assumed constant in the calculations of Figure 5. However, it most likely increases with increasing exposure to radiation. In that case, the performance degradation would be more severe than that indicated in Figure 5.

Bearing in mind the above comments, it appears that the n/p GaAs shallow homojunction will most likely exhibit the least amount of radiation degradation while the n/p AlGaAs/GaAs will most likely have the highest end-of-life efficiency in spite of the somewhat higher radiation degradation.

CONCLUDING REMARKS

Using a computer code and realistic and reasonable values of geometrical and material parameters, we have presented optimal designs of the p/n AlGaAs/GaAs, n/p AlGaAs/GaAs and the n/p GaAs shallow homojunction solar cells. These optimally designed cells could possibly meet or closely approach the NASA goal of $\eta > 22\%$ at 100 AMO, 80°C.

Of the three cell configurations, the n/p AlGaAs/GaAs appears to have, at 100 AMO, 80°C, the highest beginning-of-life efficiency of about 24% and the highest end-of-life efficiency of about 21%, after 70% degradation of diffusion length in all cell regions. The n/p GaAs shallow homojunction cells appears to exhibit the highest radiation tolerance while having lower BOL and EOL efficiencies than the n/p AlGaAs/GaAs cell. The p/n AlGaAs/GaAs cell has a BOL efficiency of about 23%, intermediate between those of the other two, but appears to have the lowest radiation tolerance and lowest EOL efficiency.

These cells can be operated at 100 AMO, 200°C with efficiencies of 18%, 19% and 20.6% for the n/p GaAs, p/n AlGaAs/GaAs and n/p AlGaAs/GaAs cells respectively.

TABLE 1. - OPTIMUM PERFORMANCE AND DESIGN PARAMETERS FOR GaAs-BASED SOLAR CELLS FOR 100 AMO, 80° C OPERATION

Parameter	Optimum Value		
	p/n AlGaAs/GaAs	n/p AlGaAs/GaAs	n/p GaAs
<u>Performance:</u>			
Short Ckt. Current Density J_{sc} , A/cm ²	3.539	3.563	3.362
Open Ckt. Voltage V_{oc} , V	1.124	1.105	1.086
Fill Factor FF, %	79.25	83.87	81.99
Conversion Efficiency, %	22.97	24.05	21.81
<u>General:</u>			
Shape	Circular	Circular	Circular
Cell Area, cm ²	1	1	1
Grid Coverage, %	6.2	6.2	6.2
AR coating	3-layer	3-layer	2-layer
Specific Contact Resistance, ohm-cm ²	1E-4	1E-4	1E-4
Intrinsic Carrier Concentration in GaAs at 300K n_i , cm ⁻³	1.8E6	1.8E6	1.8E6
Calculated Series Resistance R_s , mΩ	21.9	9.03	15.3
<u>AlGaAs Window:</u>			
Aluminum Fraction x	0.85	0.85	---
Bandgap at 353K E_g (353K), eV	2.089	2.089	---
Width W_1 , μm	0.05	0.05	0
Diffusion Length L_1 , μm	0.33	0.13	---
Doping, Uniform, cm ⁻³	1.5E19	5E18	---
SRV at Top of Window S_p , cm/s	1E7	1E7	---
SRV at Window/Emitter Interface S_{12} , cm/s	1E4	1E4	1E6
<u>GaAs Emitter:</u>			
Width W_2 , μm	0.5	0.11	0.04
Diffusion Length L_2 , μm	3.2	0.69	0.57
Exponential Doping, cm ⁻³	1.5E19 to 3.1E18	5E18 to 2.5E18	5E18 to 3.8E18
Uniform Electric Field E_2 , V/cm	960	1920	2000
<u>GaAs Base:</u>			
Width W_3 , μm	2.0	2.5	2.5
Diffusion Length L_3 , μm	6.7	23.5	23.5
Doping, exponential, cm ⁻³	5E16 to 3.6E17	5E16 to 2.6E17	5E16 to 2.6E17
Uniform Electric Field E_3 , V/cm	300	200	200
<u>GaAs Buffer/BSF Layer:</u>			
Width W_4 , μm	2.0	2.0	2.0
Diffusion Length, μm	0.53	2.63	2.63
Uniform Doping, cm ⁻³	5E18	1E19	1E19
Effective SRV at Base/BSF Interface S_{34} , cm/s	2.8E3	3.4E3	3.4E3

ORIGINAL PAGE IS
OF POOR QUALITY

TABLE 2. - DISTRIBUTION OF PHOTOGENERATED / J_{ph} DARK CURRENTS AMONGST
WINDOW, EMITTER, BASE AND SPACE CHARGE REGIONS OF THE
CELL UNDER OPEN CIRCUIT AT 100 AND, 80° C

Region	p/n	AlGaAs/GaAs	n/p	AlGaAs/GaAs	n/p	GaAs
	J_{ph}	J_{dark}	J_{ph}	J_{dark}	J_{ph}	J_{dark}
	A/cm ²	A/cm ²	A/cm ²	A/cm ²	A/cm ²	A/cm ²
Window	0.071	---	0.069	---	---	---
Emitter	2.80	0.57	1.50	0.12	0.61	1.45
Base	0.64	2.11	1.60	3.10	2.00	1.64
<u>Space Charge</u>	<u>0.12</u>	<u>0.95</u>	<u>0.43</u>	<u>0.38</u>	<u>0.77</u>	<u>0.29</u>
TOTAL	3.63	3.63	3.60	3.60	3.38	3.38

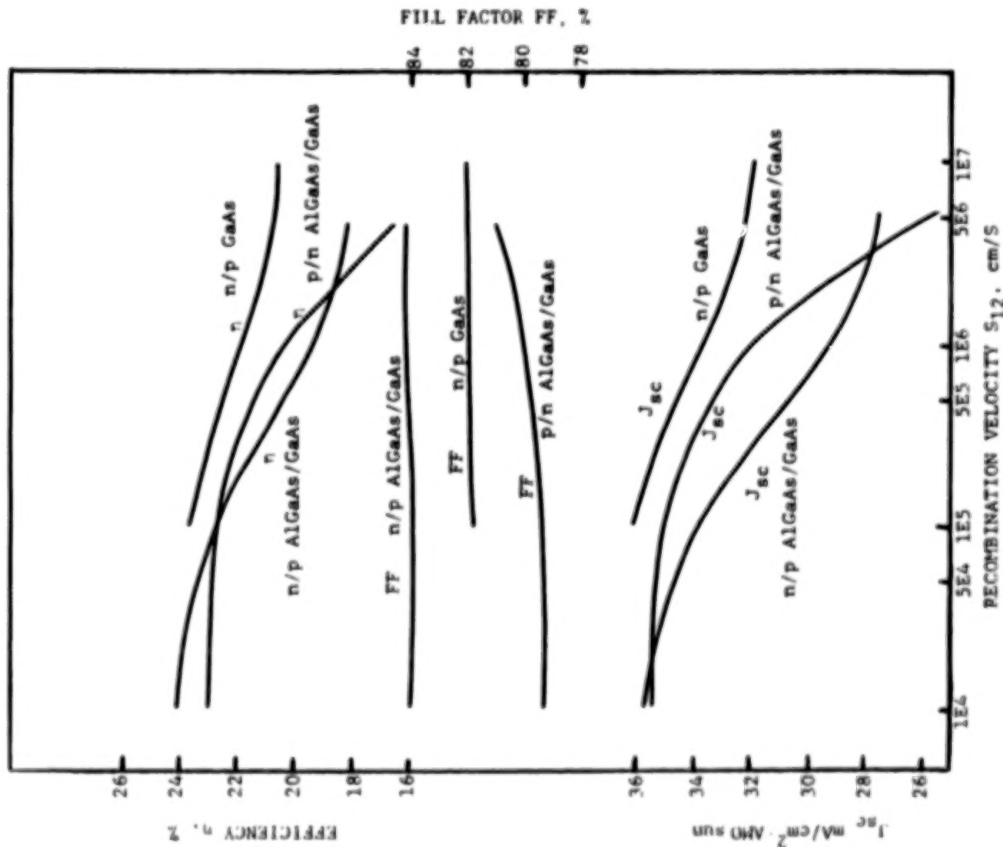


Figure 1. - Performance parameters of optimized cells as functions of interface or surface recombination velocity at 100 AMO, 80° C.

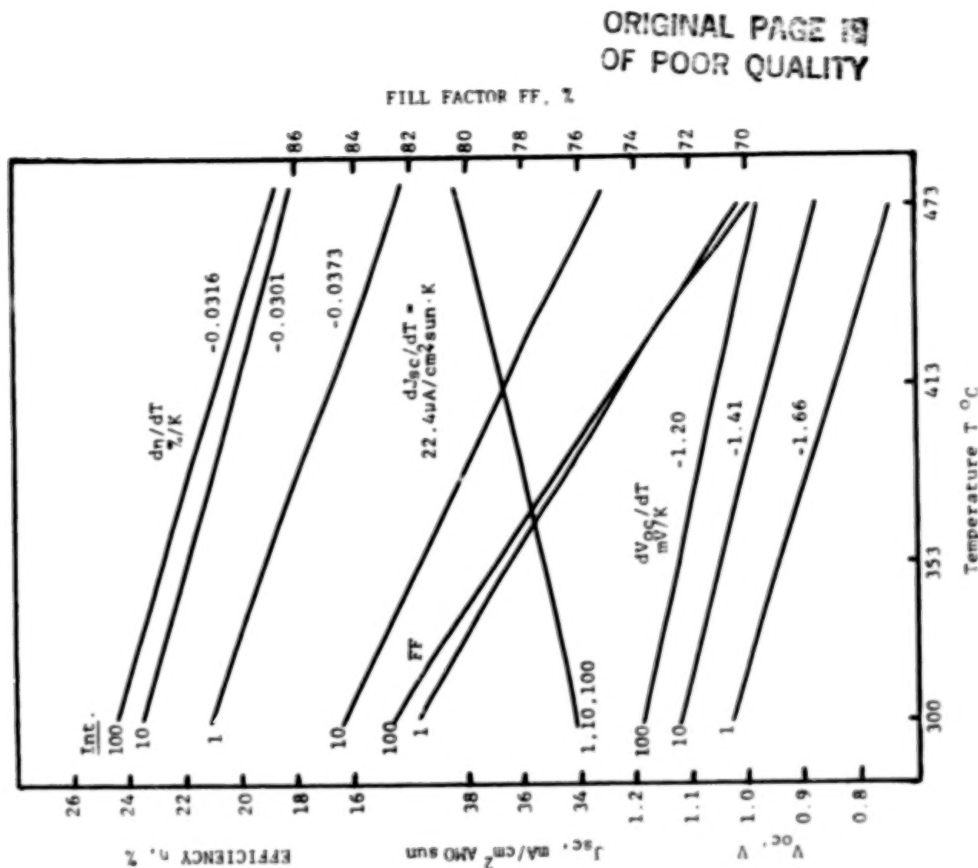


Figure 2. - Performance parameters as functions of temperature and intensity for p/n AlGaAs/GaAs cell.

ORIGINAL PAGE IS
OF POOR QUALITY

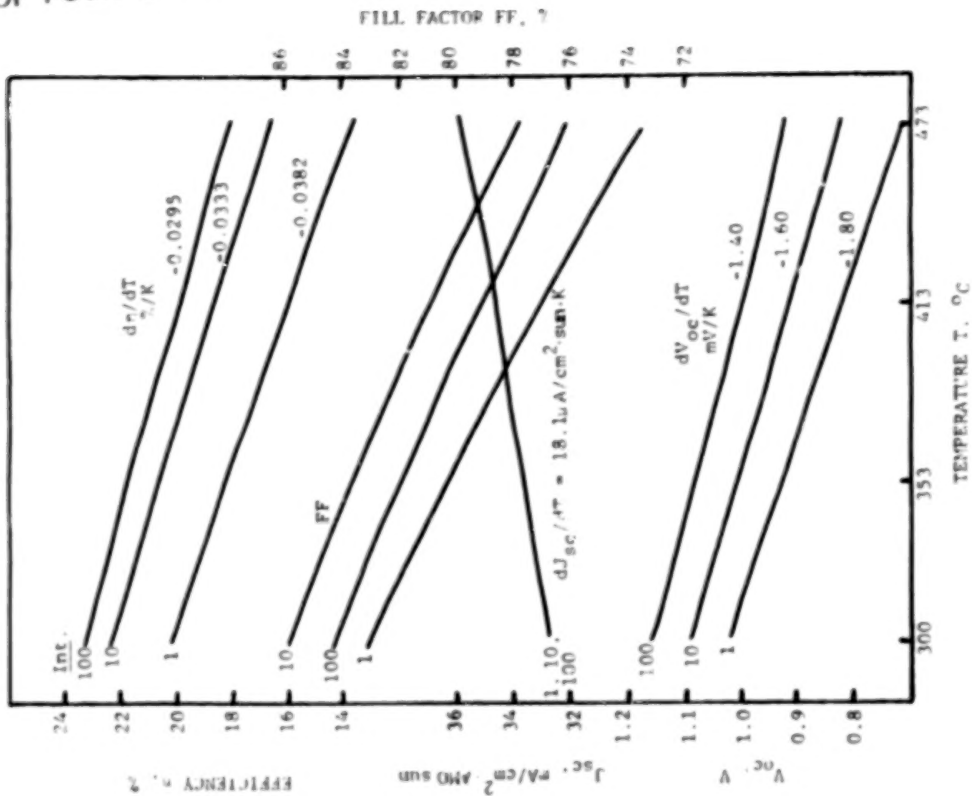


Figure 3. - Performance parameters as functions of temperature and intensity for n/p AlGaAs/GaAs cell.

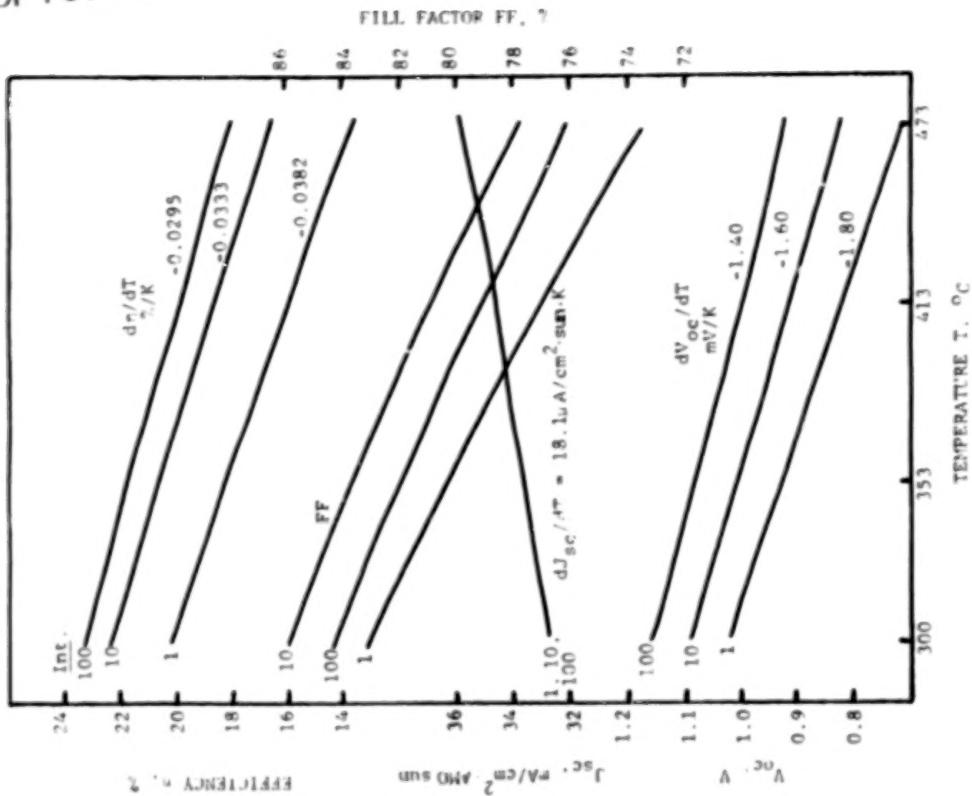


Figure 4. - Performance parameters as functions of temperature and intensity for n/p GaAs cell.

OPTICALLY
OF POOR QUALITY

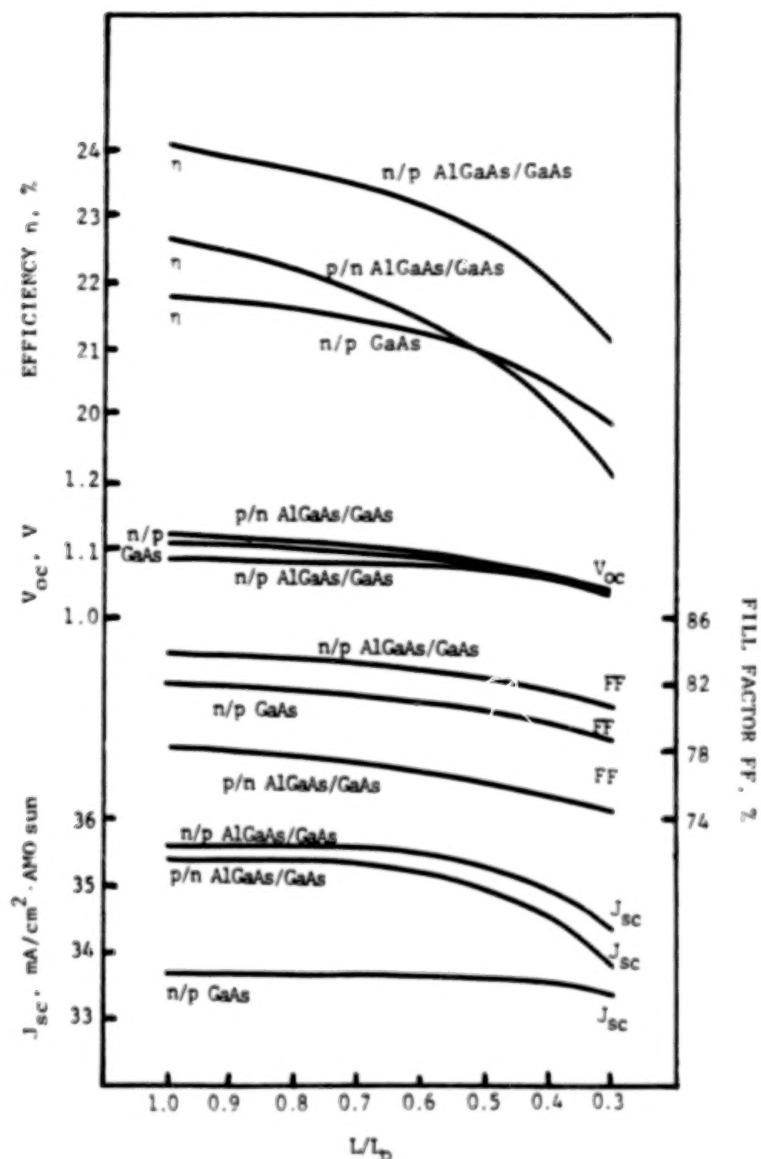


Figure 5. - Performance parameters as functions of normalized diffusion length in each cell region.

N84
29313

UNCLAS

TWO-DIMENSIONAL COMPUTER SIMULATION OF EMVJ AND GRATING SOLAR CELLS UNDER AMO ILLUMINATION

J. L. Gray and R. J. Schwartz
School of Electrical Engineering
Purdue University
West Lafayette, Indiana

The design of photovoltaic cells for space applications can be a difficult task since these devices must be designed for "end-of-life" operation. The degradation of minority carrier diffusion length due to radiation damage can make the end-of-life performance of a cell radically different from its as fabricated performance. In order to experimentally evaluate the end-of-life performance of a cell, it must be irradiated in the laboratory to simulate the effects of a space environment. However, this procedure of design, fabrication, evaluation, and redesign can be very time consuming. In addition, it is often difficult to determine which design parameter is responsible for a change in cell performance. Even variations in wafer characteristics and processing parameters can be difficult to trace and therefore introduce uncertainties in cell evaluation. Because so many uncertainties are involved, the determination of an optimum cell design is no easy matter.

Most of these difficulties can be eliminated by making use of detailed solar cell simulation programs. A particular design change can be studied with the absolute certainty that nothing else has changed. The effects of radiation damage can be studied merely by altering the carrier diffusion length and redoing the computer simulation. In addition, since the simulation will solve for the electrostatic potential and hole and electron concentrations throughout the interior of the device, one can peer inside the cell itself and "see" where recombination occurs, how the current flows, whether the back-surface-field is effective, etc. Since most cell structures are two-dimensional in nature, a code which solves the semiconductor equations in two-dimensions is necessary in order to best simulate the various devices. All this can be accomplished much more quickly than a device can be fabricated. Therefore, as an aid to designing cells, such a computer code can be invaluable.

In this paper, a computer program, SCAP2D (Solar Cell Analysis Program in 2-Dimensions), is used to evaluate the Etched Multiple Vertical Junction (EMVJ) and grating solar cells. It should be noted that it is only our aim to demonstrate how SCAP2D can be used to evaluate cell designs and that the cell designs studied are by no means optimal designs.

THE SCAP2D PROGRAM

The SCAP2D program solves the three coupled, nonlinear partial differential equations, Poisson's Equation and the hole and electron continuity equations, simultaneously in two-dimensions using finite differences to discretize the equations and Newton's Method to linearize them. The variables solved for are the electrostatic potential and the hole and electron concentrations. Each linear system of equations is solved directly by Gaussian Elimination. Convergence of the Newton Iteration is assumed when the largest correction to the electro-

static potential or hole or electron quasi-potential is less than some predetermined error, typically 10^{-6} kT. A typical problem involves 2000 nodes with a Jacobi matrix of order 6000 and a bandwidth of 243.

The metal-semiconductor contacts are assumed to be ideally ohmic; that is, charge neutrality prevails and both carriers retain their equilibrium values. Other interfaces are described by a Hall-Shockley-Read formulation of surface recombination and by a fixed surface charge density.

Bandgap narrowing is taken into account as described in Ref. 1 and a Caughey-Thomas formulation of carrier mobility is used. Auger and a single trap HSR bulk recombination mechanism are assumed.

SCAP2D SIMULATION RESULTS

The SCAP2D program has been used to examine the effects of radiation damage, simulated by reducing the carrier diffusion lengths, on the operation of the EMVJ and grating solar cells. Simple schematics of these devices are shown in Figures 1 and 2. It can be seen that the grating cell is just a special case of the EMVJ cell in which the depth of the etched groove is zero. In order to keep the comparisons simple, the only design parameters which were varied were cell thickness, etched groove depth, and grid spacing. In addition, so that the shadowing factor is constant, it is assumed that the etched groove width is such that shadowing is 5% for each device.

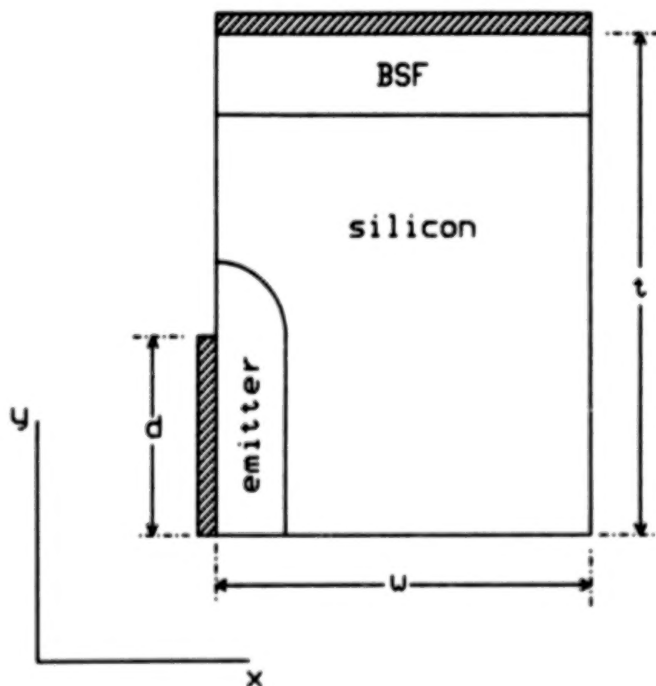


Figure 1. - Schematic of the EMVJ cell used for the SCAP2D simulations.

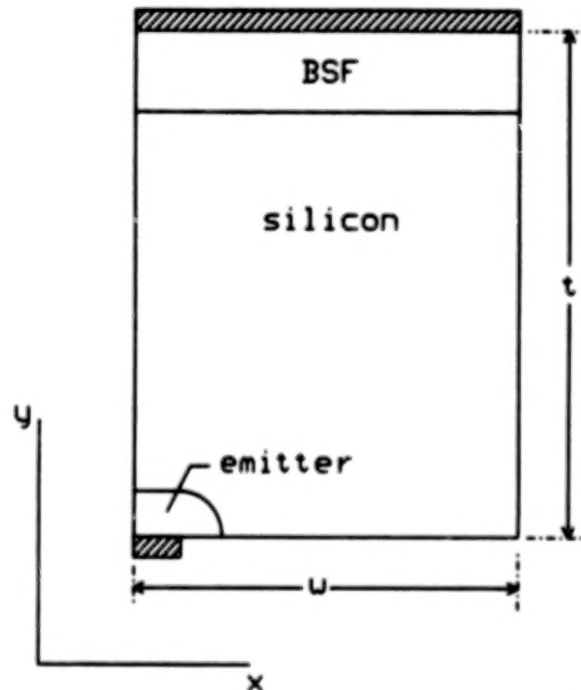


Figure 2. - Schematic of the grating cell used for the SCAP2D simulations.

TABLE 1. - DEVICE PARAMETERS

	Device	t	w	d
1	EMVJ	250 μ m	125 μ m	100 μ m
2	EMVJ	250 μ m	25 μ m	100 μ m
3	EMVJ	75 μ m	25 μ m	25 μ m
4	Grating	75 μ m	25 μ m	0
5	Grating	250 μ m	25 μ m	0

The remaining design parameters are held fixed as follows. All doping profiles are complimentary error functions with junction depths of 3 microns. The emitter profile has a surface concentration of $1.5 \times 10^{20} \text{ cm}^{-3}$ while the back-surface-field (BSF) has a surface concentration of $3 \times 10^{20} \text{ cm}^{-3}$. The base has a resistivity of about 10 ohm-cm. A fixed charge density of 10^{12} charges per cm^2 is assumed at the illuminated surface which has a flatband surface recombination velocity of 1000 cm/sec. Minority carrier diffusion lengths of from 35 to 800 microns were used in the simulations. The simulations were performed for an AM0 solar spectrum with an incident power of 135 mW/cm². A perfect anti-reflective coating is assumed.

In Table 1 the simulated devices are described in terms of the three variable parameters: t, the device thickness, w, the grid half spacing, and d, the etched groove depth. Tabulated results of the simulations, giving the open-circuit voltage, short-circuit current, fill factor, efficiency, and collection efficiency, are listed in Table 2 for different values of minority carrier diffusion length.

One fact that is immediately evident is that for long diffusion lengths, the EMVJ cell shows no advantage over the grating cell. Indeed, for a minority carrier diffusion length of 350 microns, cell design has almost no effect on cell efficiency. This is to be expected since all the critical device dimensions are less than a diffusion length. For example, comparing Devices 3 and 4, which have comparable overall dimensions, for a minority carrier diffusion length of 350 microns, we see that there is no advantage to having etched groove junctions. In fact, since the emitter volume is so much larger in the EMVJ cell as compared to the grating cell, there is more recombination and the open-circuit voltage is reduced. As the diffusion length is reduced, however, the advantages of an etched junction become apparent. The purpose of the etched groove is to provide a collecting junction close to any generated excess carrier. For carriers to be efficiently collected, they should be generated within about a diffusion length of the junction or they may recombine before they can be collected. The EMVJ cell allows carriers generated deep within the device to be collected. In the grating cell these carriers have a greater distance to diffuse in order to be collected, and therefore more of them recombine and are lost. For a minority carrier diffusion length of 35 microns, the EMVJ cell (Device 3) is superior to the grating cell (Device 4). This is due to the greater collection efficiency of the EMVJ cell. Thus, for high end-of-life efficiency, a deep etched groove junction is desirable.

ORIGINAL PAGE IS
OF POOR QUALITY

TABLE 2. - SCAP2D SIMULATION RESULTS

[L is minority carrier diffusion length.]

		V_{OC} (volts)	J_{SC} (mA/cm ²)	η (%)	FF	η_{coll} (%)
L = 800 μ m	1	.628	46.3	17.4	.808	98.4
	2	.598	45.8	16.3	.807	97.2
	3	.624	42.9	16.3	.823	97.3
L = 350 μ m	1	.608	44.7	15.7	.778	94.9
	2	.587	45.6	15.6	.785	97.0
	3	.619	42.8	15.8	.804	97.1
	4	.635	44.4	16.1	.789	98.3
	5	.616	45.4	15.8	.764	96.4
L = 110 μ m	1	.530	33.7	10.4	.783	71.6
	2	.528	44.7	13.6	.779	95.1
	3	.571	42.2	13.8	.773	95.6
	4	.571	40.7	13.2	.771	92.3
	5	.539	39.9	12.3	.773	84.7
L = 35 μ m	1	.471	14.7	4.0	.772	33.2
	2	.469	40.6	10.8	.767	86.3
	3	.492	37.4	10.6	.782	84.8
	4	.498	29.7	8.4	.766	67.3
	5	.495	20.6	8.2	.756	62.9

Another critical parameter for end-of-life performance is the grid spacing. As long as the spacing is shorter than a diffusion length, cell performance is not very dependent on this parameter. This can be seen by comparing Devices 1 and 2 for diffusion lengths of 350 and 800 microns. The improved performance of Device 1, though it has a larger grid spacing than Device 2, is again due to the different relative emitter volumes. For short diffusion lengths, however, the difference in performance is dramatic. For Device 1, with a grid half spacing of 125 microns, most of carriers generated between the grid lines are too far from the junction to be collected efficiently. Therefore, it is important to keep the grid half spacing less than the expected end-of-life diffusion length.

Cell performance is least sensitive to the device thickness. When a device has a back-surface-field, two competing effects determine the optimum thickness. The device needs to be thick enough so that nearly all the incident photons with sufficient energy generate electron-hole pairs, and the device needs to be thin enough so that the BSF barrier will be effective. In order for the BSF to be effective, the thickness of the device must be less than a diffusion length. If the end-of-life diffusion length is expected to be much less than 100 microns, devices thin enough to make the BSF work may not be practical.

In Figure 3, the minority carrier concentration in the base of Device 3 is shown for a diffusion length of 800 microns. The illuminated surface is along the x-axis at $y = 0$. The collecting contact is parallel to the y-axis. We can see that the BSF is very effective at containing the minority carriers in this case as the carrier concentration is nearly constant throughout the base region. Looking at the same device for a diffusion length of 35 microns in Figure 4, the back-surface-field is not effective since the minority carriers tend to recombine before they encounter the BSF. Both figures show the minority carrier concentration at the maximum power point.

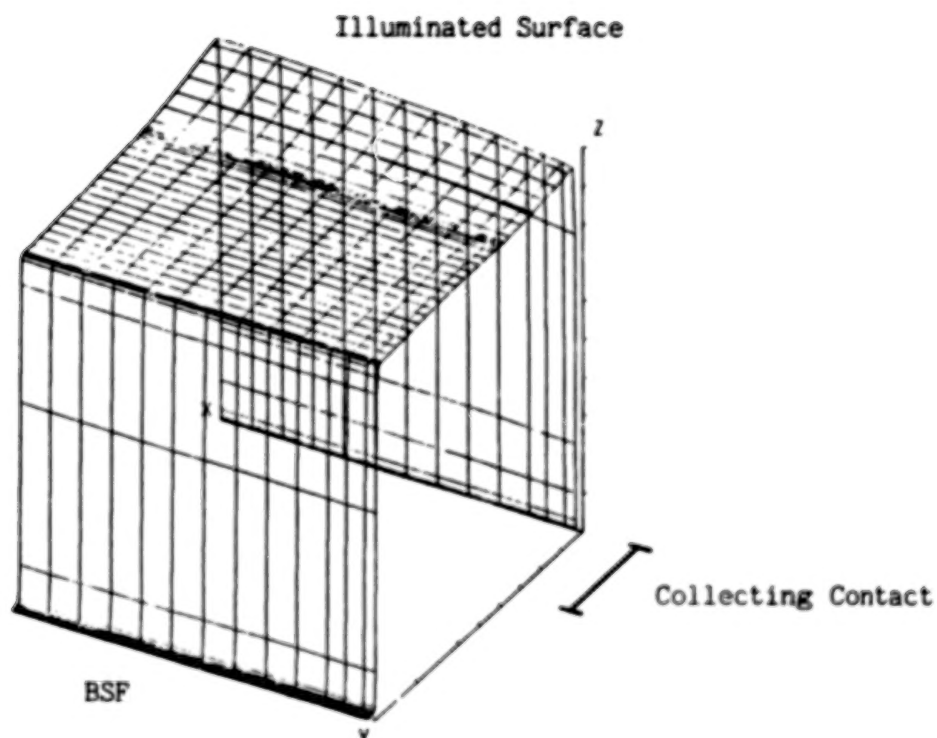
CONCLUSIONS

Using a detailed simulation program, SCAP2D, the effects of radiation damage, as simulated by changing the minority carrier diffusion length, on EMVJ cell design were studied. The design parameters examined were device thickness, grid half spacing, and etched groove junction depth. For long diffusion lengths, cell performance was relatively insensitive to these parameters. End-of-life (small minority carrier diffusion length), was found to be very sensitive to both the grid half spacing and to the etched groove depth. These parameters must be chosen so that most carriers are generated within a diffusion length of the collecting junction. Because end-of-life diffusion lengths are small, BSF's do not greatly improve cell performance, and therefore end-of-life design is not very sensitive to cell thickness.

REFERENCE

1. M. S. Lundstrom; R. J. Schwartz; and J. L. Gray: Transport Equations for the Analysis of Heavily Doped Semiconductor Devices. Solid-State Electronics, Vol. 24, 1981, pp. 195-202.

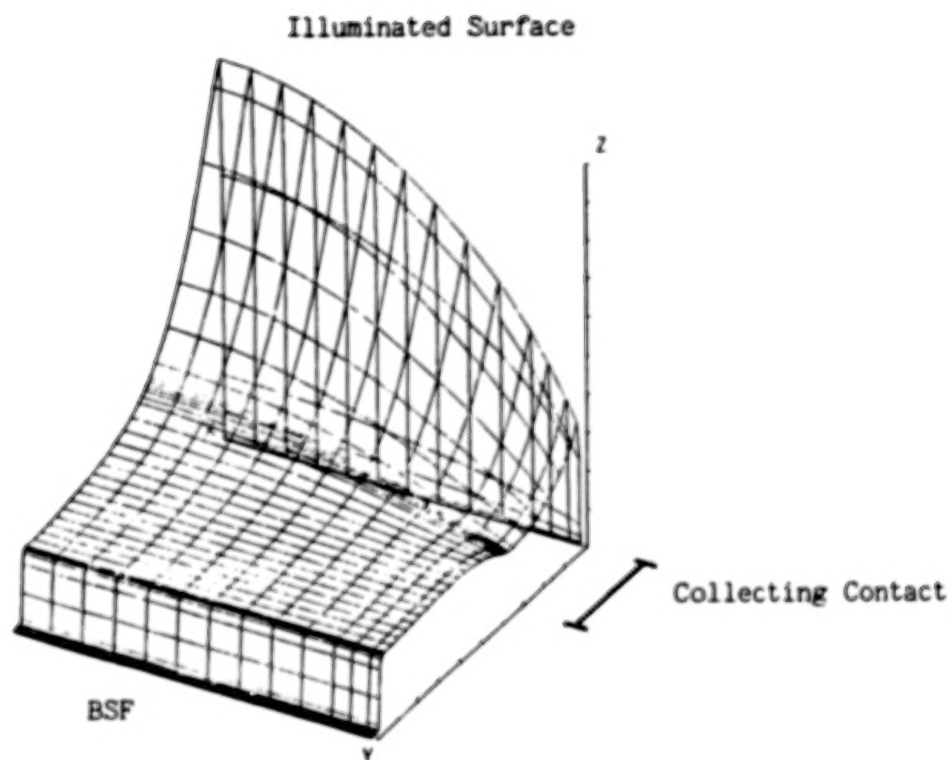
ORIGINAL PAGE 19
OF POOR QUALITY



x-axis: 5 to 25 microns
y-axis: 0 to 75 microns
z-axis: 0 to $3 \times 10^{15} \text{ cm}^{-3}$

Figure 3. - Minority carrier concentration within the base of Device 3 operating at the maximum power point with a minority carrier diffusion length of 800 μm . The x and y axes have the same meaning as in Fig. 1. The z-axis is the minority carrier concentration.

ORIGINAL PAGE 13
OF POOR QUALITY



x-axis: 5 to 25 microns
y-axis: 0 to 75 microns
z-axis: 0 to $3 \times 10^{14} \text{ cm}^{-3}$

Figure 4. - Minority carrier concentration within the base of Device 3 operating at the maximum power point with a minority carrier diffusion length of $35 \mu\text{m}$.

N84
29314

UNCLAS

RADIATION TESTING OF GaAs ON CRRES AND LIPS EXPERIMENTS

Terry M. Trumble and Kenneth Masloski
Air Force Wright Aeronautical Laboratories (AFWAL/PDOC)
Wright-Patterson Air Force Base, Ohio

In the past decade the radiation damage of solar cells has become a prime concern to the U.S. Air Force due to longer satellite lifetime requirements (i.e., 7½ years) with the accompanying increase in radiation fluence. To complement existing radiation testing accomplished in industry and through AFWAL in-house radiation testing, two major efforts were undertaken, flight experiments on the Navy Living Plume Shield (LPS) satellite and the NASA/Air Force Combined Release and Radiation Effects Satellite (CRRES). This paper describes each experiment, the rationale behind it, and its approach and status.

LIPS Background

The Living Plume Shield satellite is a Navy test satellite launched 9 February 1983. The satellite electrical power is provided by three double sided solar array panels that were erected after the satellite was in orbit. One side of one panel contains 300 2cm x 2cm GaAs solar cells having a beginning-of-life (BOL) efficiency of 15½%. The other sides contain silicon solar cells. The LIPS is a slowly rotating gravity gradient oriented satellite in a 600nm circular orbit inclined at 63°. The radiation environment predicted for a one year exposure is a fluence of 1.9×10^{13} e/cm².

The specially built GaAs panel is shown in figure 1. The panel consists of 300 2cm x 2cm cells electrically connected in 12 parallel banks of 25 cells in series. Open circuit voltage of the array approaches 25 volts, short circuit current at air mass zero is 1.2 amperes and maximum power at beginning-of-life is 23 watts. Table 1 provides the physical specifications on the GaAs cells, while table 2 provides the material specifications of the cells and figure 2 shows the baseline design. The experimental GaAs panel provides a portion of the satellite's power along with five conventional silicon panels. A resistor load bank was designed to obtain current and voltage of the GaAs panel under various load conditioning. This data can be telemetered back to earth on a daily basis.

APPROACH

Data has been available from the LIPS satellite on an intermittent basis. The first 30 days no data could be taken because the GaAs panel was not oriented toward the sun or the satellite was not over the tracking station. Initial data indicated a 5.5% power loss and about a 5% loss in current. The most recent data is combined with earlier data to cover the period from day 32 to day 170 (figure 3). Data up to day 230 has been received with the maximum power averaging around 21 watts and short circuit current around 1.12 amperes.

The initial power drop was unexpected based on laboratory tests of similar GaAs cells. The most recent data; however, does correlate quite nicely with predicted values. Reasons for the initial 5% power drop are not certain. This effort was also noticed in the NTS-II flight experiment where after eighty days the cells annealed and recovered a portion of the initial drop.

CRRES Background

The goal of the CRRES GaAs flight test is to measure the effect of space radiation (protons, electrons, ions) on gallium arsenide solar cells while simultaneously measuring the radiation flux levels and energy distributions. Also methods of space thermal annealing will be investigated. A matrix of effects involving coverglass thickness, coverglass material, adhesives, soldering versus welding and substrate materials will be studied using small sample segments. This information will be very beneficial towards determining optimal GaAs panel design.

APPROACH

Two GaAs solar cell panels will be made, a 10" x 14" ambient temperature panel with 12 cell strings and a 5" x 8.125" annealing panel with 8 cell strings. The ambient panel will be designed as a matrix experiment utilizing combinations of coverglass thickness, coverglass material, adhesives, soldering and welding, and cell efficiencies. The annealing panel will contain two ambient temperature reference cell strings and will test two cells strings each for continuous annealing at 150°C, forward current heating for 2 hours at 250°C and intermittent annealing using a heater for heating at 250°C for two hours. The CRRES will fly two orbits, a circular LEO orbit at 300km for 45 days maximum, and an elliptical orbit 330km to 35000km for the remaining three years.

Table 3, the Need for Space Flight Testing, illustrates the dramatic difference in the simulated space environment versus the real space environment. The survival and production of power by GaAs solar cells on the LIPS experiment is a step forward, however, not until we can identify and isolate GaAs solar cell degradation causes can an optimum panel be built. Only a controlled experiment in a space environment can accomplish part of this task. Correlation of cell degradation versus particle flux at specified times using on-board radiation monitoring experiments will help to accomplish part of this task. The CRRES satellite experiment is designed to provide newer, more accurate information for upgrading the radiation belt models.

Figure 4 is a graphic illustration of the complexity of the radiation modeling problem, excluding temporal effects.

SUMMARY

The capsule summary shown in this paper is provided primarily as an update on events in the area of GaAs solar cell radiation studies. Additional work is proceeding at JPL on protons, omnidirectional effects of radiation and backside radiation. In January 1984 the real time radiation testing and annealing studies in

ORIGINAL PAGE 19
OF POOR QUALITY

a vacuum will begin at the Naval Research Laboratory. As further data is received from the Navy on the LIPS satellite a more comprehensive analysis of the data will be completed. This data should substantiate the fact that GaAs solar cells are at least as good as laboratory testing shows, and possibly measurably better. Data scatter from the LIPS and periods of no data have raised all sorts of speculation as to the appropriate way to interpret the data. Based upon present data, a series of tests are being planned for the second LIPS panel at Wright Patterson AFB. Ground testing on this panel is expected to start within the next few months.

TABLE 1. - GaAs PHYSICAL SPECIFICATIONS

Cell size	
Length	0.79 in.
Width	0.79 in.
Height	0.030 in. (with cover glass)
	0.012 in. (without cover glass)
Cell area	
Total	0.620 in ²
Active	0.562 in ²
Cell weight	
Without cover	0.67 gm
With cover	0.91 gm
Upper contact	
Number of gridlines	24 lines
Gridline length	0.74 in.
Gridline width	0.0024 in.
Contact bar length	0.753 in.
Contact bar width	0.31 in.
Gridline total thickness	~6.0 μ m
Lower contact	
Length	0.79 in.
Width	0.79 in.
Area	0.620 in ²
Total thickness	~6.0 μ m
Cover glass	
Length	0.77 in.
Width	0.80 in.
Area	0.616 in ²
Thickness	0.012 in.

ORIGINAL PAGE IS
OF POOR QUALITY

TABLE 2. - GaAs HESP II SOLAR CELL MATERIAL SPECIFICATIONS

Cell material	GaAs
Substrate	
Orientation	100
Type	n ⁺
Dopant	Te
Concentration	$>7 \times 10^{17} \text{ cm}^{-3}$
Thickness	0.015 in.
First epilayer	
Type	n
Dopant	Sn
Concentration	$1 \times 10^{17} \text{ cm}^{-3}$
Thickness	10 μm
Resistivity	0.014 $\Omega\text{-cm}$
Diffused layer	
Type	p
Dopant	Be
Concentration	$1 \times 10^{18} \text{ cm}^{-3}$
Thickness	$<0.5 \mu\text{m}$
Second epilayer (window layer)	
Composition	(AlGa) As
Type	p ⁺
Dopant	Be
Concentration	$1 \times 10^{18} \text{ cm}^{-3}$
Thickness	$<0.5 \mu\text{m}$
Sheet resistivity	0.03 $\Omega\text{-cm}$
Junction depth	$<0.5 \mu\text{m}$
Upper surface	
First metallization	
Metal	AuZn
Thickness	2000 \AA
Second metallization	
Metal	Ag
Thickness	$>3.0 \mu\text{m}$
Antireflection coating	
Material	Ta ₂ O ₅
Length	0.77 in.
Width	0.79 in.
Thickness	750 \AA
Lower surface	
First metallization	
Metal	AuGeNi
Thickness	2000 \AA
Second metallization	
Metal	Ag
Thickness	$>3.0 \mu\text{m}$
Cover glass	
Adhesive	Dow Corning 93-500
Material	Corning 7940-fused silica
Length	0.77 in.
Width	0.80 in.
Thickness	0.012 in.
AR coating (on top of glass)	MgF ₂

ORIGINAL PAGE IS
OF POOR QUALITY

TABLE 3. - NEED FOR SPACEFLIGHT TESTING

SPACE ENVIRONMENT	LABORATORY ENVIRONMENT
SIMULTANEOUS EVENTS	SINGULAR EVENTS
• PROTONS, ALL ENERGIES	• PROTONS ONE ENERGY
• ELECTRONS, ALL ENERGIES	• ELECTRONS ONE ENERGY
• IONS, HIGH MEV ENERGIES	• NO ION TESTING
• SOLAR FLARE	• SHAKER TABLE
• THERMAL	• VACUUM OVEN
• REAL TIME	• ACCELERATED TESTING
• SHUTTLE ENVIRONMENT	
- ACOUSTICS	
- VIBRATION	
- G'S	

ORIGINAL PAGE 19
OF POOR QUALITY

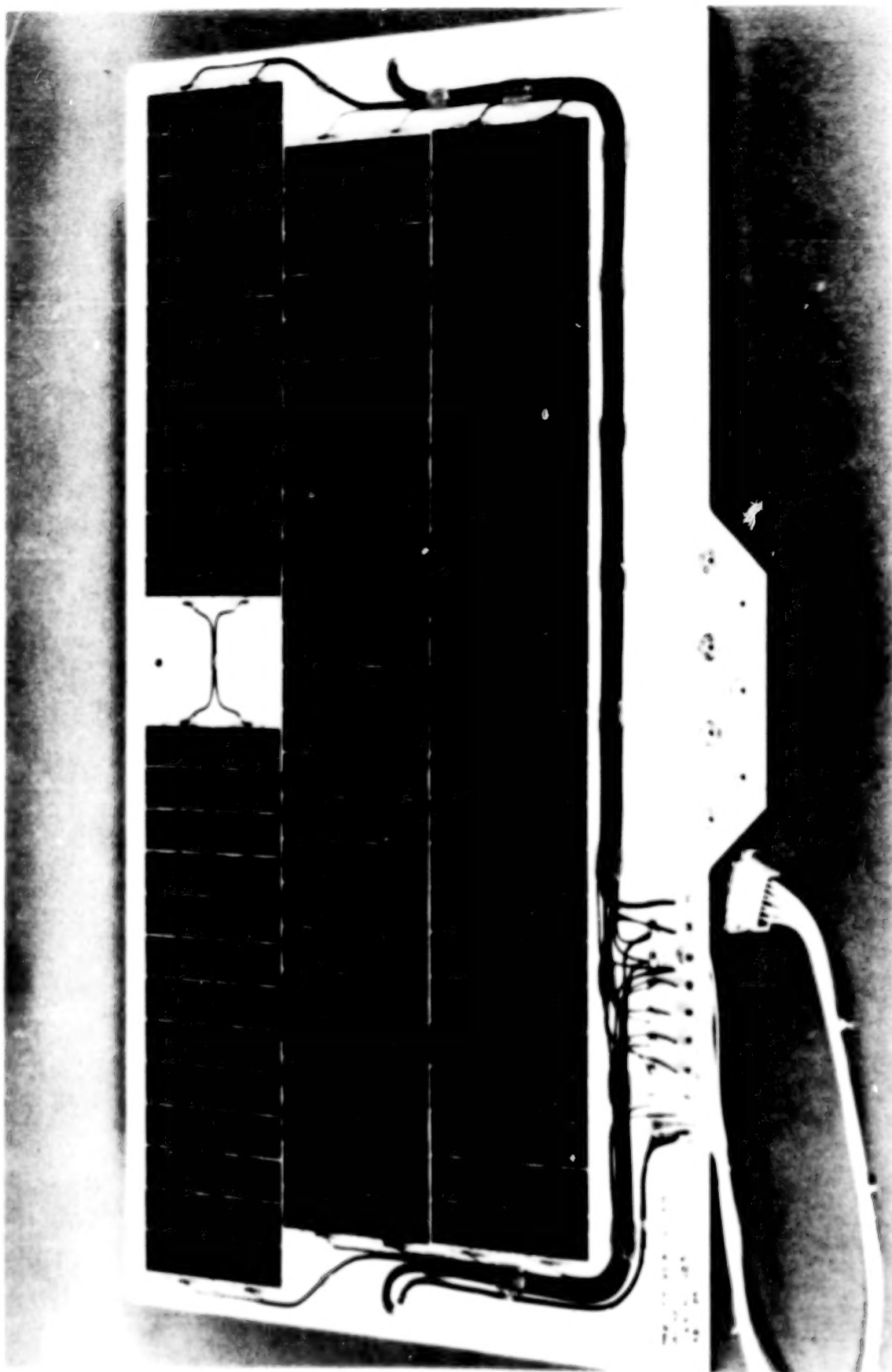
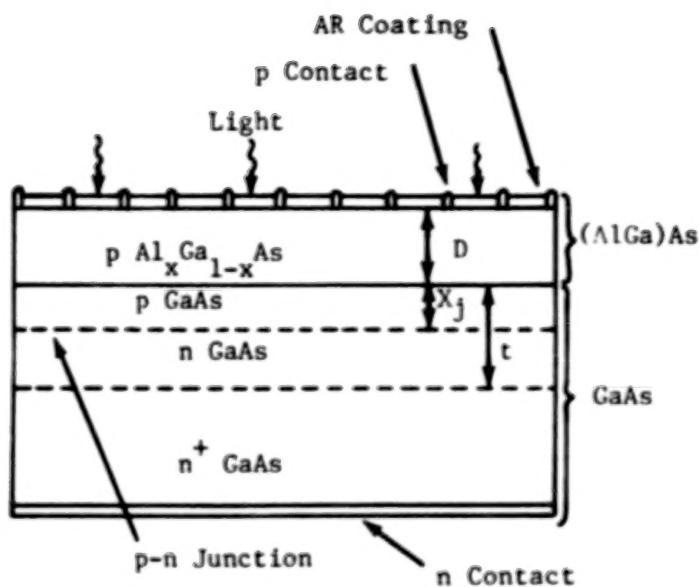


Figure 1. - LIPS GaAs panel.

ORIGINAL PAGE IS
OF POOR QUALITY



$$p = 10^{18} \text{ cm}^{-3} \text{ (Be)}$$

$$n = 10^{17} \text{ cm}^{-3} \text{ (Sn)}$$

$$n = 10^{18} \text{ cm}^{-3} \text{ (Te)}$$

$$D < 0.5 \mu\text{m}$$

$$X_j < 0.5 \mu\text{m}$$

$$t > 10 \mu\text{m}$$

NUMBER OF FINGERS = 24

p Contact: Au-Zn-Ag

n Contact: Au-Ge-Ni-Ag

AR COATING: Ta_2O_5

$p \text{ Al}_x \text{ Ga}_{1-x} \text{ As}$

$$x = 0.86 \pm 0.04$$

Figure 2. - GaAs solar cell baseline design.

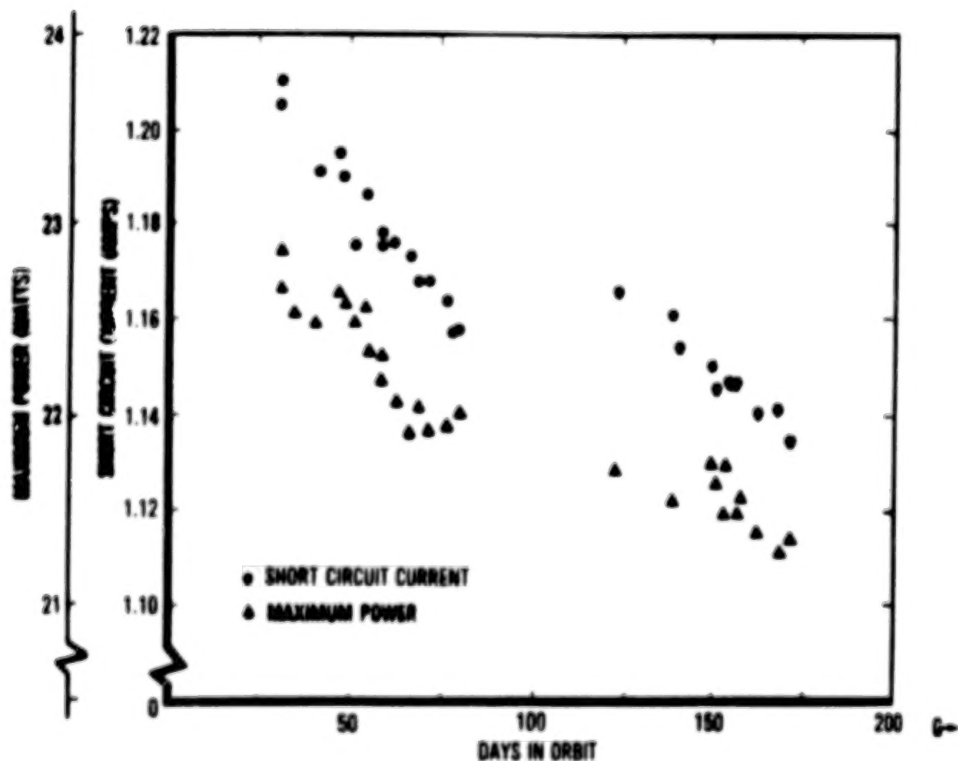


Figure 3. - LIPS data.

ORIGINAL PAGE IS
OF POOR QUALITY

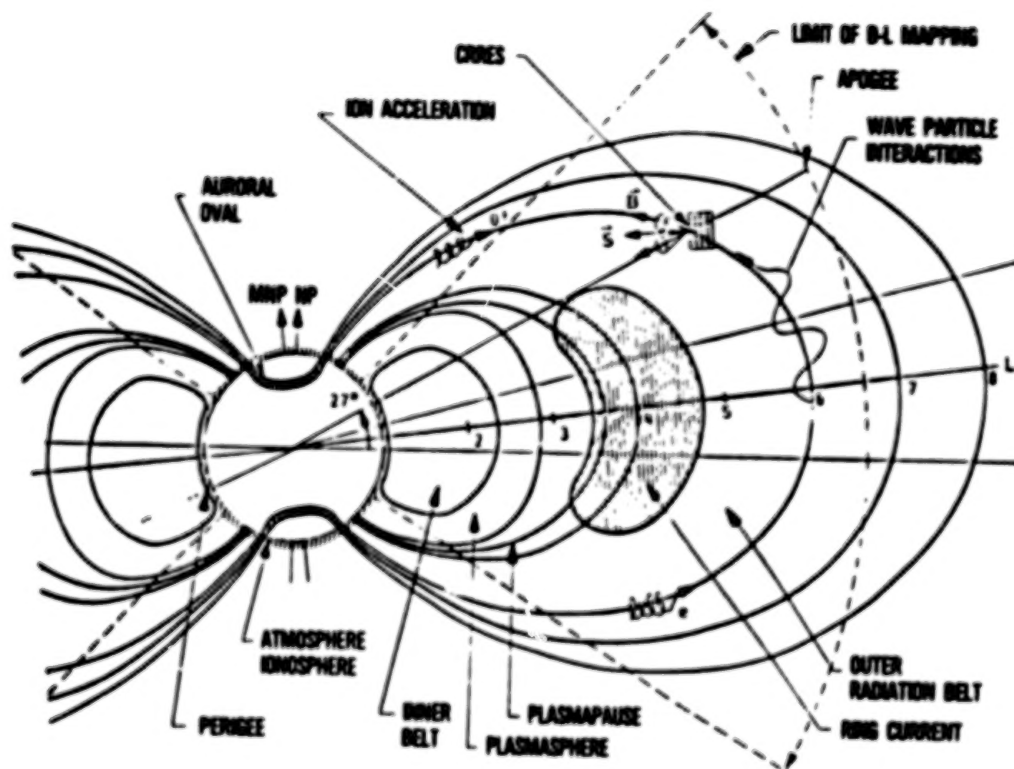


Figure 4. - Radiation environment.

N84
29315

UNCLAS

N84 29315

SOLAR CELL DEGRADATION IN PROTON RADIATION ORBITS

H. S. Rauschenbach and J. Y. Yaung
TRW Space & Technology Group
Redondo Beach, California

Discrepancies between predicted and observed solar cell degradation in orbits other than LEO and GEO have been ascribed to shortcomings in solar cell test data and analytical procedures used to relate cell test data to the orbital environment. Tentative relative proton damage coefficients for modern silicon (Si) and gallium arsenide type (GaAs) solar cells have been calculated and presented. The potential errors in predicting cell degradation in a 5600 nmi orbit that may arise from the use of the existing cell data base have been bounded and the need for further testing has been delineated.

INTRODUCTION

Significant discrepancies have been observed between predicted and actual in-orbit silicon solar cell array degradation in orbits other than in low earth orbits and in geosynchronous orbit (refs. 1 and 2, for example).

These discrepancies have been diagnosed to probably arise from a combination of a lack of appropriate solar cell test data and from inadequacies in the models that relate the unidirectional and mono-energetic proton test data to the omnidirectional flux-energy spectra actually found in orbit.

DISCUSSION

Recent proton radiation tests on late model silicon solar cells (refs. 3, 4, and 5) have indicated that the relative damage coefficients for protons used in the prediction of solar cell degradation utilizing the damage-equivalent 1-MeV electron fluence method, may be outdated. Figures 1 and 2 illustrate the range of the new test data (curves "A" and "B") together with the typically used damage coefficient curve (curve "C") from reference 6. The test data was obtained on different silicon solar cell types in different proton energy ranges as follows: p+ cells for 50 to 300 keV and 15 to 40 MeV, and non-p+ cells for 2 to 10 MeV. The relative damage coefficients shown here are defined as the ratios of the quantity of protons at a given energy and fluence to the quantity of 1-MeV electrons that produce the same degradation of the cell's initial maximum power output.

Significant in figures 1 and 2 is the shift in the silicon cell's peak sensitivity by nearly one order of magnitude toward lower proton energies. Such shift in sensitivity is not totally surprising because the old data (JPL curve) was obtained on relatively deep-diffused junctions tested in tungsten light, while the newer data was obtained on shallow-diffused junctions tested in simulated AMO (air mass zero) sunlight. The change in the cell's sensitivity to proton damage with fluence had also been predicted previously (ref. 7).

The effects of using the three different damage coefficient curves in figures 1 and 2 on the predicted silicon cell degradation are illustrated in figures 3 and 4 for non-p+ and p+ cells, respectively. The impact is especially severe in the lower coverglass thickness range that is of greatest practical interest.

At first sight it appears that for a given coverglass thickness in figures 3 or 4, there should be only one single curve to represent curves "A" and "B", matching curve "A" at lower values of coverglass thickness and matching curve "B" at higher values. However, the presently employed method of relating the orbital omnidirectional flux/energy spectrum to unidirectional, mono-energetic solar cell test data does not provide details that permit a ready correlation to the proton fluence as shown in figures 3 or 4. Therefore, the problem has been bounded by the curves shown.

The relative damage coefficient work we had done on GaAs solar cells and reported previously (ref. 8) was revisited because we encountered inconsistencies in the validation of a solar cell proton radiation degradation model we were also developing. Therefore, the original GaAs solar cell test data (refs. 2, 3, and 4) were reanalyzed and the relative proton damage coefficients as shown in figure 4 were calculated.

It is interesting to note that the peak sensitivities of the Si and GaAs cells (figs. 1, 2, and 5) are of about the same magnitude and occur in about the same proton energy range. Similarly to the Si cells, the relative degradation rate of GaAs cells is also strongly related to coverglass thickness as shown in figures 6 and 7.

CONCLUSIONS AND RECOMMENDATIONS

The data presented in the foregoing should be considered tentative, even though it is based on the best data available to us at this time. It is important to realize that these data come from different experiments that have not necessarily been correlated. The data is presented here for the purpose of not only identifying the shortcomings in the existing data base, but also to illustrate the likely peak proton radiation sensitivities of Si and GaAs cells and to identify the need for comparative Si and GaAs proton radiation testing, especially in the proton energy range between about 100 and 500 keV and in the fluence range between about 10^{10} and 10^{13} p/cm². This need exists also for comparative 1-MeV electron radiation testing of solar cells from the same batches on which the proton radiation testing was performed, because any inaccuracies in either the proton or the electron radiation test results reflect equally into an inaccuracy of the value of the relative damage coefficients.

Only after such comparative testing has been performed will it be meaningful to conduct trade studies such as represented by figures 6 and 7.

REFERENCES

1. Statler, R. L., Walker, D. H., and Lambert, R. J.: The NTS-1 Solar Cell Experiment after Two Years in Orbit. 12th IEEE Photovoltaic Specialist Conference, Baton Rouge, Louisiana, Proc., pp. 208-215, November 15-18, 1976.
2. Meulenberg, A.: Basis for Equivalent Fluence Concept in Space Solar Cells. Proceedings of Space Photovoltaic Research and Technology, NASA Lewis Research Center, NASA Conference Publication 2256, 1982.
3. Loo, R., Kamath, S., and Knechtli, R.: Low Energy Proton Radiation Damage to (AlGa)As-GaAs Solar Cells. HRL, January 1979.
4. Loo, R.: Medium Energy Proton Radiation Damage to (AlGa)As-GaAs Solar Cells. HRL, March 1981.
5. Loo, R., Goldhammer, L., Kamath, S., Knechtli, R. C.: High Energy Proton Radiation Damage to (AlGa)As-GaAs Solar Cells. HRL, NASA-3148, June 1979.
6. Solar Cell Radiation Handbook. NASA-JPL, Third Edition, JPL Publications 82-69, November 1, 1982.
7. Tada, H. Y.: A New Dimension in Solar Cell Degradation Estimate in Space RDC Matrix Method. Records of the 10th IEEE Photovoltaic Specialists Conference, 1973.
8. 1982 Space Photovoltaic Research and Technology Conference, NASA Lewis Research Center, Cleveland, Ohio.

ORIGINAL PAGE IS
OF POOR QUALITY

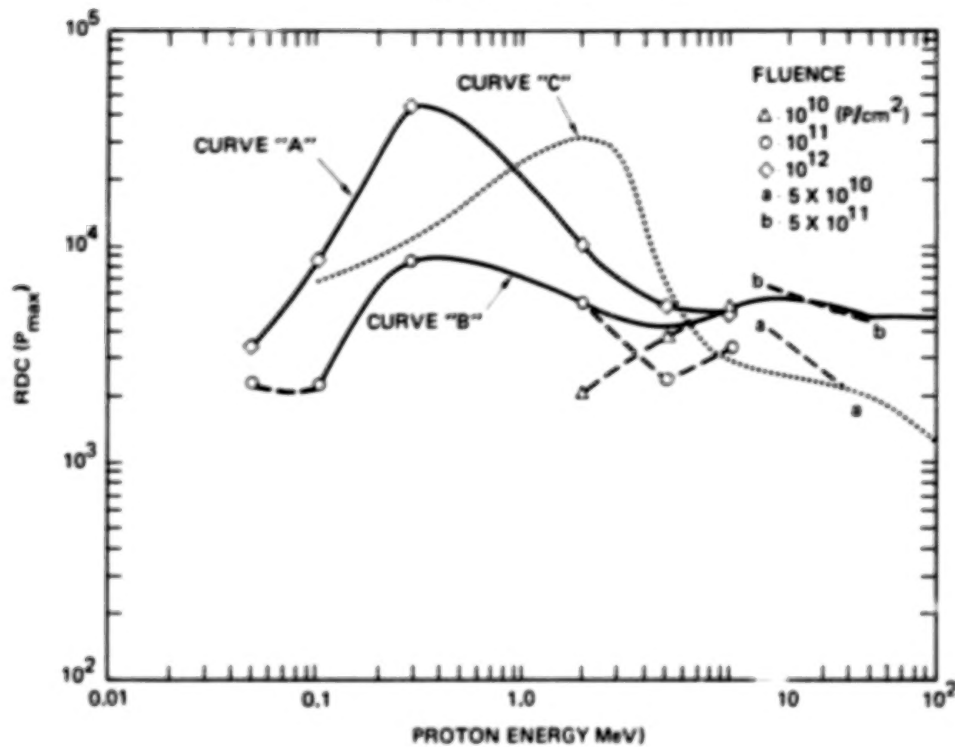


Figure 1. - Proton relative damage coefficient (RDC) curves of non-BSF Si cell (P_{max}).

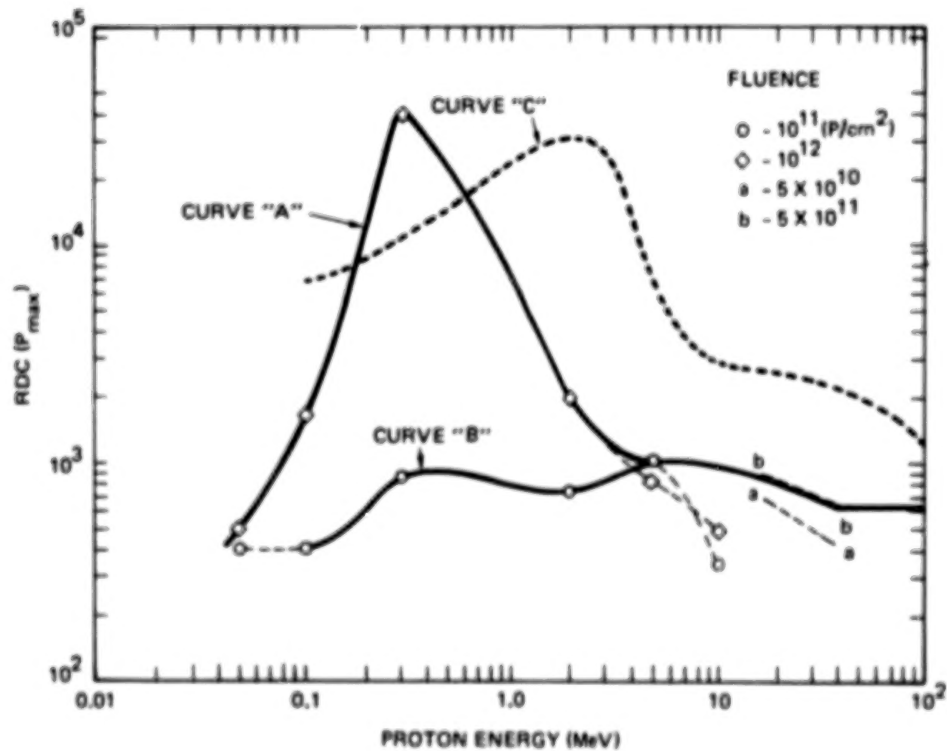


Figure 2. - Proton relative damage coefficient (RDC) curves of BSF Si cell (P_{max}).

ORIGINAL PAGE IS
OF POOR QUALITY

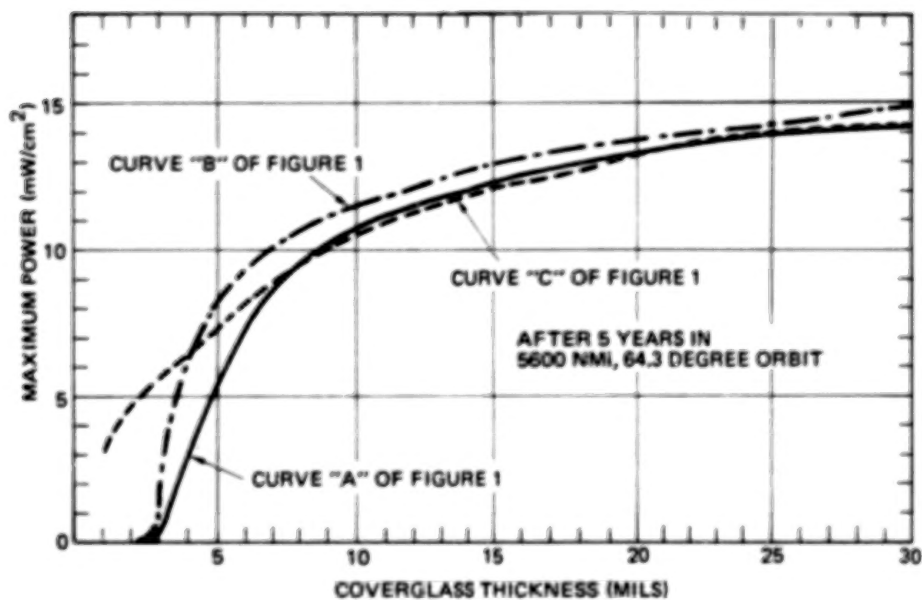


Figure 3. - Predicted power output of Si non-p+ solar cells using three different RDC curves.

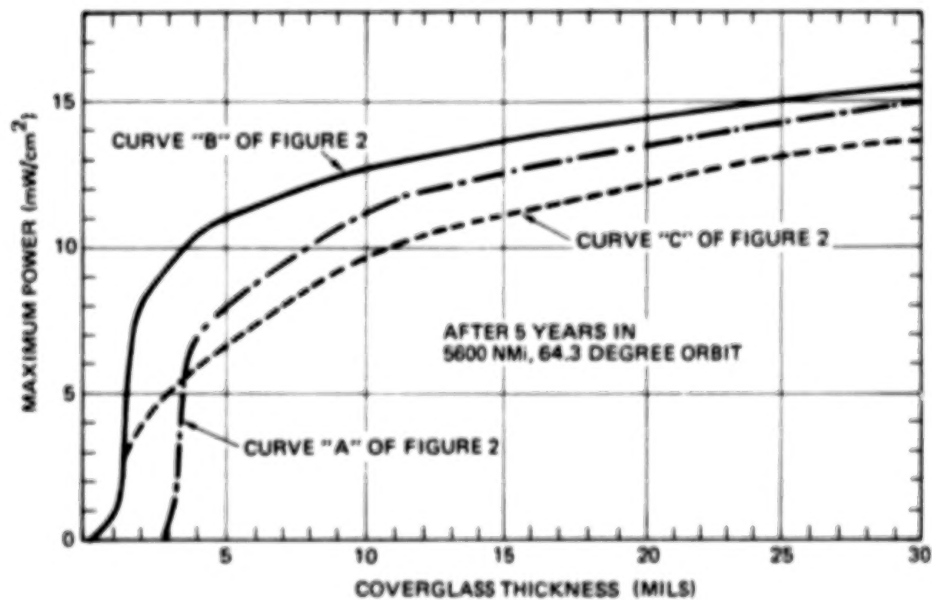


Figure 4. - Predicted power output of Si p+ solar cells using three different RDC curves.

ORIGINAL PAGE IS
OF POOR QUALITY

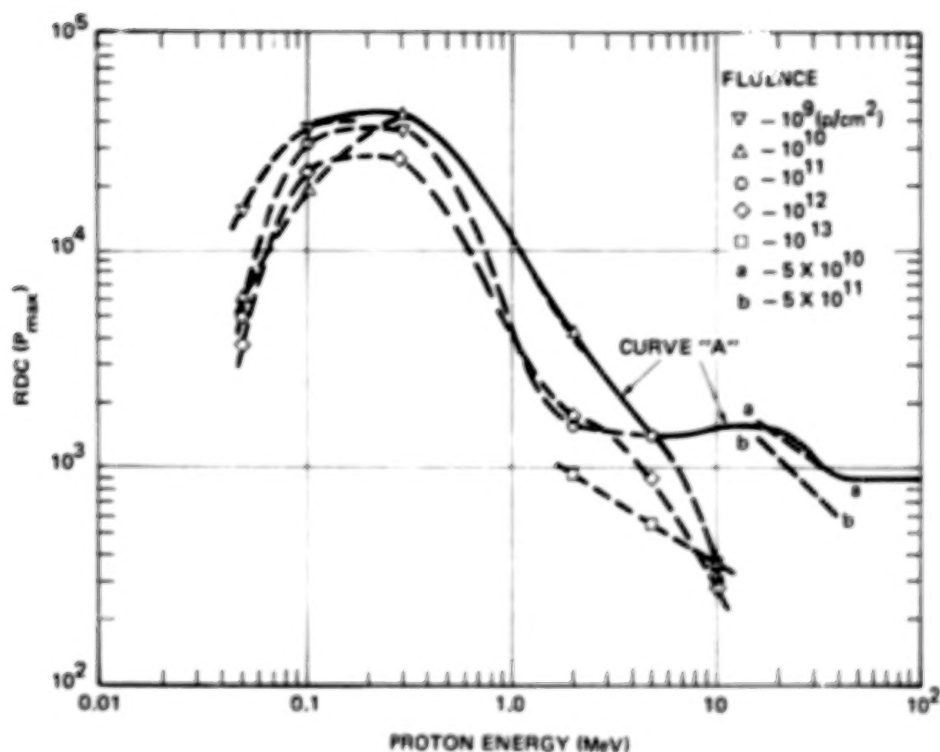


Figure 5. - Proton relative damage coefficient (RDC) of (AlGa) As-GaAs cell having junction depth of $0.5 \mu m$.

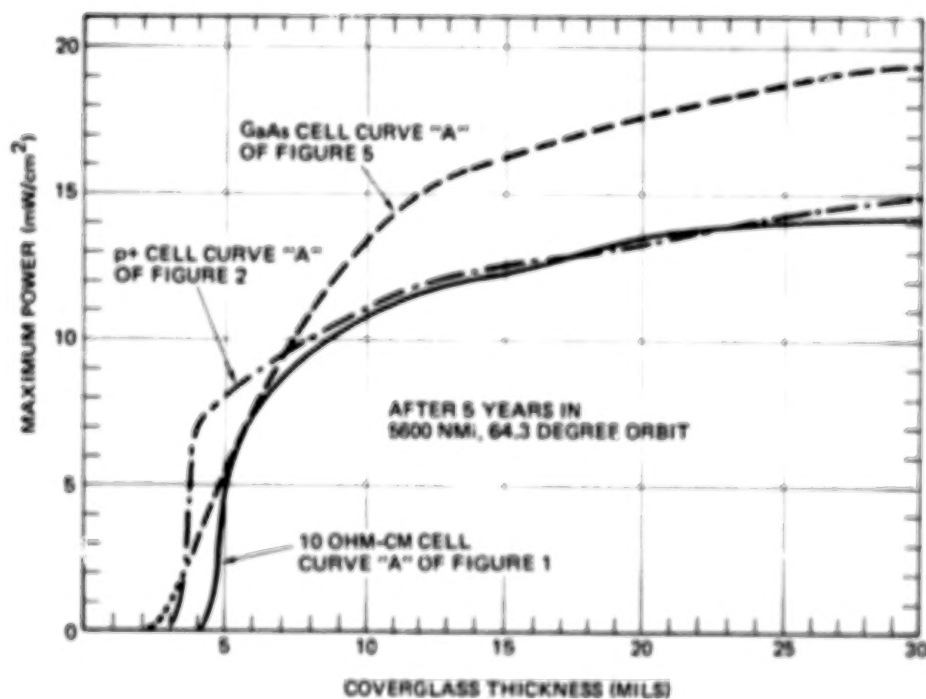


Figure 6. - Predicted power output of Si and GaAs solar cells using high-valued RDC's for Si cells.

ORIGINAL PAGE IS
OF POOR QUALITY

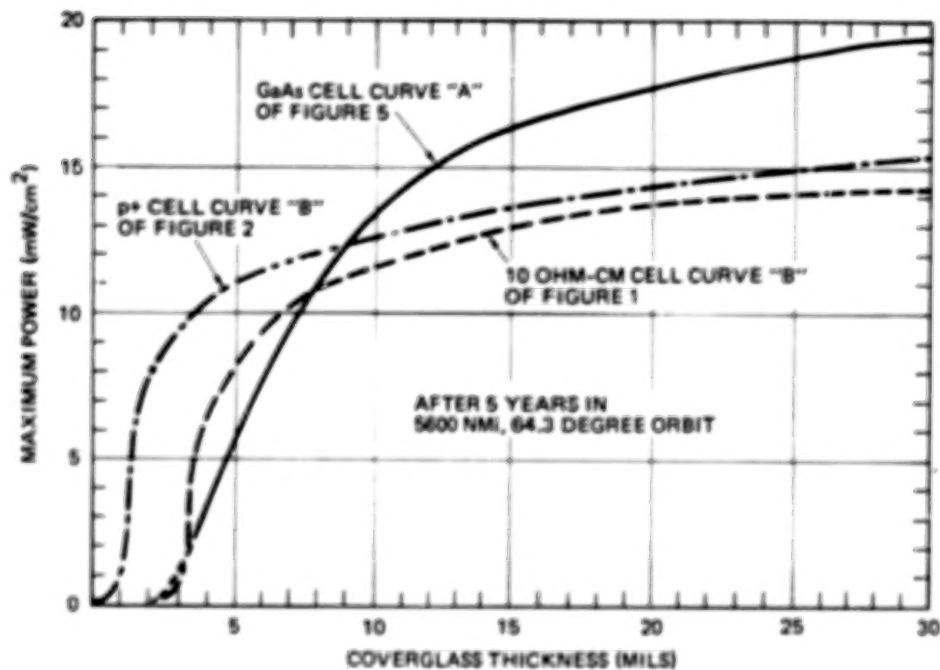


Figure 7. - Predicted power output of Si and GaAs solar cells using low-valued RDC's for Si cells.

N84
29316

UNCLAS

N84 29316

MODEL OF SOLAR CELL PROTON DAMAGE

J. Y. Yaung
TRW Defense Systems Group
Redondo Beach, California

Experiments (refs. 1, 2 and 3) have demonstrated that both GaAs cells and shallow-diffusion Si cells are more susceptible to low energy (<1 MeV) proton damage than older type Si cells. Mathematical models to predict the low energy proton damage for both types of solar cells have not been found in the literature.

R. A. Arnlt, et al., (ref. 4) used a three-layer approximation to model the nonpenetrating proton damage to a Si cell. Arnlt's model is limited to predicting Si cell proton damage at energies above 0.5 MeV. John Wilson et al., (ref. 5) developed a short circuit current (I_{sc}) degradation model for GaAs cells irradiated by protons from low energy to 100 MeV.^{SC} Wilson's model was found to be satisfactory in predicting the I_{sc} degradation of GaAs cells only, but not that of Si cells.

This paper describes a modification of Wilson's model that has been developed by preserving the optical wavelength dependency in the photogeneration of minority carrier pairs. By so doing, a generic model of solar cell proton damage was developed that predicts the experimental I_{sc} degradations for both GaAs solar cells and Si solar cells closely and predicts the experimental spectral responses of proton-irradiated cells reasonably well. The expansion of this model for V_{oc} and P_{max} is currently in progress.

INTRODUCTION

Experiments (refs. 1, 2, and 3) covering the proton energy range of 50 keV to 40 MeV have been performed on both modern silicon (Si) and gallium arsenide (GaAs) type solar cells. Tentative proton relative damage coefficients derived from this data base have shown a significant shift in the silicon cell's peak sensitivity toward lower proton energies (ref. 6). Such a shift in the peak sensitivity requires understanding of the solar cell proton damage. Mathematical models to predict the low energy proton damage for both types of solar cells have not been found in the literature. Thus, a modeling effort was initiated by the author.

MODELING

In the space environment, protons create displacement damage in solar cells. These displacements are normally considered as recombination centers for the electron-hole pairs formed by photon absorption. The increased recombination in the solar cell will degrade its electrical performance. The displacement distribution will be spatially nonuniform when the incident proton energy is insufficient to penetrate through the active region of the cell. Diffusion lengths of solar cells with a spatially nonuniform minority carrier lifetime in the active region cannot be accurately measured by conventional experimental methods. Thus, the conventional

radiation damage approach utilizing the diffusion length (ref. 7) has not been successful in predicting the low energy proton degradation of solar cells.

R. A. Arnlit, et al., (ref. 4) used a three-layer approximation to model the nonpenetrating proton damage to a Si cell. Arnlit's model is limited to predicting Si cell proton damage above 0.5 MeV. Recently John Wilson, et al., (ref. 5) developed a short circuit current (I_{sc}) degradation model for GaAs cells irradiated by protons from low energy to high energy. Wilson's model treats the effect of proton-generated displacements as an additional recombination probability, added to that of the minority carrier pairs before reaching the junction. The final form of I_{sc} degradation was shown to be

$$I_{sc}/I_{sc_0} = 1 - \int_0^t \eta_c(x) F(x) \rho(x) dx / \int_0^t \eta_c(x) \rho(x) dx \quad (1)$$

where

$\eta_c(x)$ = current collection probability

$\rho(x) = K \alpha e^{-\alpha x}$

$F(x) = 1 - E_2 \left[\sqrt{6} \sigma_r \phi |D(E_x) - D(E_{xj})| \right]$

K = integrated solar photon flux in the absorption band

α = photoabsorption coefficient averaged over the solar spectrum

$E_2(z)$ = exponential integral of order 2

σ_r = electron-hole recombination cross section

ϕ = proton fluence

and

$D(E)$ = a function of displacement number (ref. 5) calculated by transport theories.

In the preliminary analysis for silicon solar cells, the average photoabsorption coefficient (α) was found to simulate the solar cell I_{sc} degradation not very well (figure 1). To improve the simulation accuracy, the photoabsorption coefficient was expressed as function of wavelength, $\alpha(\lambda)$. For the same reason the integrated solar photon flux was also expressed as function of wavelength $K(\lambda)$. Thus, the expression for the photoabsorption rate density at depth x becomes

$$\rho(x, \lambda) = K(\lambda) \alpha(\lambda) e^{-\alpha(\lambda)x} \quad (2)$$

where $K(\lambda)$ is the differential photon flux incident upon the solar cell. The undamaged short circuit current can be solved analytically if a Green's function solution is employed,

$$I_{sc_0}(\lambda) = \int_{\lambda_1}^{\lambda_2} \int_0^t G(x, |\lambda - \lambda'|) \rho(x, \lambda') dx d\lambda' \quad (3)$$

where $\rho(x, \lambda')$ is the photo-generated electron-hole pair distribution, and the Green's function represents a solution of the differential continuity equation at a fixed wavelength (λ'). Since the solutions of the continuity equation are normally determined at a fixed wavelength, $G(x, |\lambda - \lambda'|)$ can be simplified to $\eta_c(x) \delta(\lambda - \lambda')$, where $\eta_c(x)$ is the collection efficiency. The collection efficiency is known in terms of diffusion constants, lifetimes, and surface recombination rates of the minority carriers, electric fields, and cell dimension (ref. 8). Thus, the expression in Equation (3) can be integrated over λ' and reduced to

$$I_{sc_0}(\lambda) = \int_0^t \eta_c(x) \rho(x, \lambda) dx \quad (4)$$

Similarly the short circuit current of a proton-irradiated cell can be derived based on the assumptions in the Wilson model.

$$I_{sc}(\lambda) = \int_0^t \eta_c(x) [1 - F(x)] \rho(x, \lambda) dx \quad (5)$$

Equations (4) and (5) represent a method for spectral response calculation for unirradiated and proton-irradiated solar cells.

The normalized output current of an irradiated cell can thus be calculated as follows:

$$\frac{I_{sc}}{I_{sc_0}} = \frac{\int_{\lambda_1}^{\lambda_2} I_{sc}(\lambda) d\lambda}{\int_{\lambda_1}^{\lambda_2} I_{sc_0}(\lambda) d\lambda} \quad (6)$$

where $I_{sc_0}(\lambda)$ and $I_{sc}(\lambda)$ are expressed in Equations (4) and (5).

DISCUSSION OF RESULTS

Figure 1 illustrates the preliminary analysis for silicon solar cell I_{SC} degradation based on the unmodified Wilson's model, i.e., Equation (1). The apparent mismatch of the peak response toward a lower proton energy initiated the modeling effort mentioned above. Shown in figures 2 and 3 are the successful modeling results of the I_{SC} degradations on silicon and GaAs solar cells, respectively, utilizing spectral modifications.

Since the expression in Equations (4) and (5) can be used to calculate the spectral responses of a solar cell when divided by $K(\lambda)$, spectral response simulations were performed for both types of cells before and after proton irradiation at the energy of 290 keV. Figures 4 and 5 show the comparisons of experimental and simulated spectral response for GaAs and Si solar cells, respectively.

The overall predictive capability of this model appears satisfactory. However, a sharp dip in the $0.8 \sim 0.9 \mu m$ range in figure 5 can be attributed to the irregular spikes occurring in the corresponding range of wavelengths in the experimental solar simulator (refer to figure 6).

REFERENCES

1. Loo, R., Kamath, S., and Knechtli, R.: Low Energy Proton Radiation Damage to (AlGa)As-GaAs Solar Cells. Hughes Research Laboratory, Malibu, California, January 1979.
2. Loo, R.: Medium Energy Proton Radiation Damage to (AlGa)As-GaAs Solar Cells. Hughes Research Laboratory, Malibu, California, March 1981.
3. Loo, R., Goldhammer, L., Kamath, S., Knechtli, R. C.: High Energy Proton Radiation Damage to (AlGa)As-GaAs Solar Cells. Hughes Research Laboratory, Malibu, California, NASA-3148, June 1979.
4. Arnlit, R. A., and Westerlund, L. H.: A Model for Nonpenetrating Proton Damage to Silicon Solar Cells. COMSAT Technical Review, Volume 1, No. 1, Fall 1971.
5. Wilson, J. W., et al.: A Model for Proton-Irradiated GaAs Solar Cells. NASA Langley Research Center, April 1982.
6. Rauschenbach, H. S., Yaung, J. Y.: Solar Cell Degradation in Proton Radiation Orbits. To be given at the 1983 Space Photovoltaic Research and Technology Conference, NASA Lewis Research Center, Cleveland, Ohio.
7. Solar Cell Radiation Handbook. NASA-JPL, Third Edition, JPL Publication 82-69, November 1, 1982.
8. Hovel, H. J.: Semiconductors and Semimetals. Volume IV, Solar Cell, Academic press, 1975, pp 18-22.
9. Loo, R., Kamath, S., and Knechtli, R.: Electron Radiation Damage of (AlGa)As-GaAs Solar Cells. Hughes Research Laboratory, Malibu, California, October 1979.

ORIGINAL PAGE IS
OF POOR QUALITY

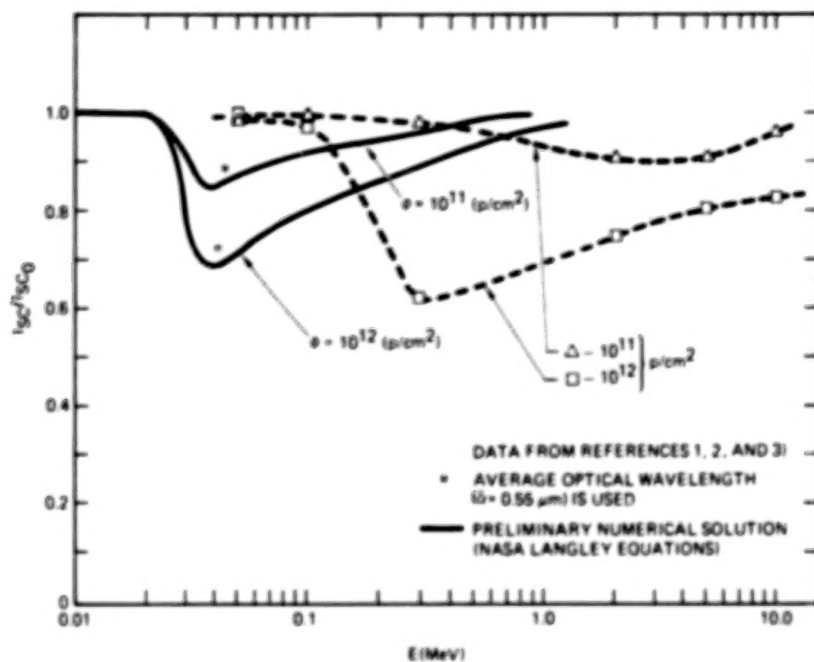


Figure 1. - Preliminary results of predicting I_{sc} damage on silicon solar cell.

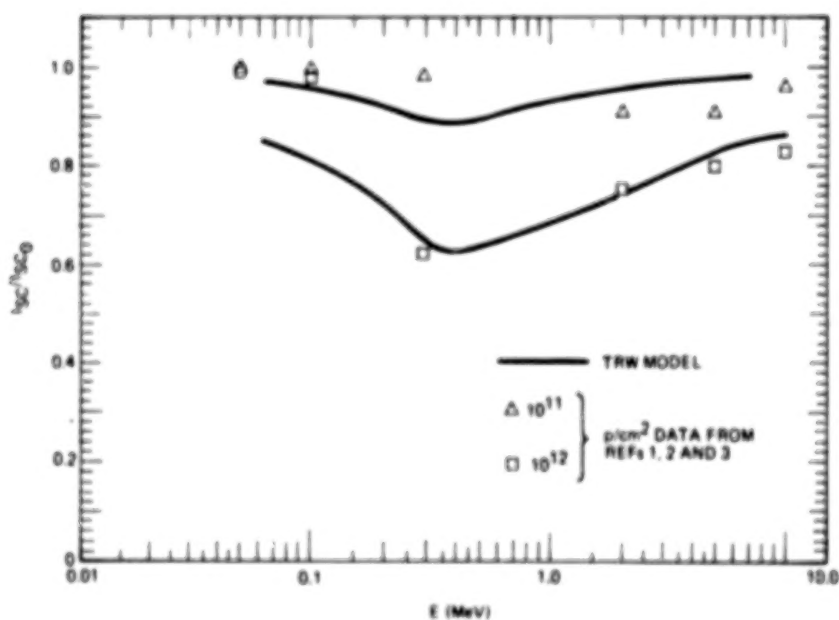


Figure 2. - Final results of predicting I_{sc} damage on silicon solar cell.

ORIGINAL PAGE IS
OF POOR QUALITY

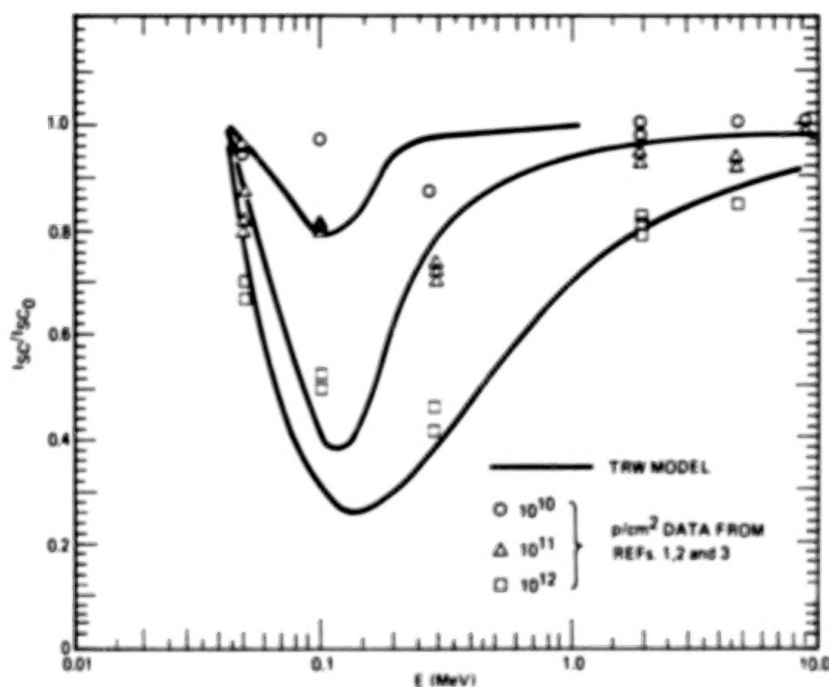


Figure 3. - Final results of predicting I_{sc} damage on GaAs solar cell.

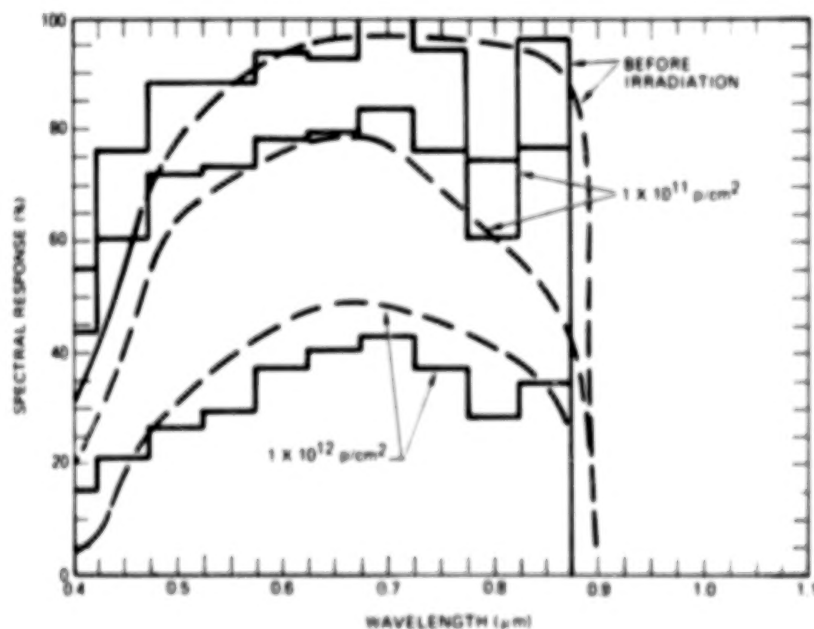


Figure 4. - Experimental and simulated spectral responses for (AlGa)As-GaAs solar cell before and after proton irradiation (proton energy = 290 keV).

ORIGINAL PAGE 19
OF POOR QUALITY

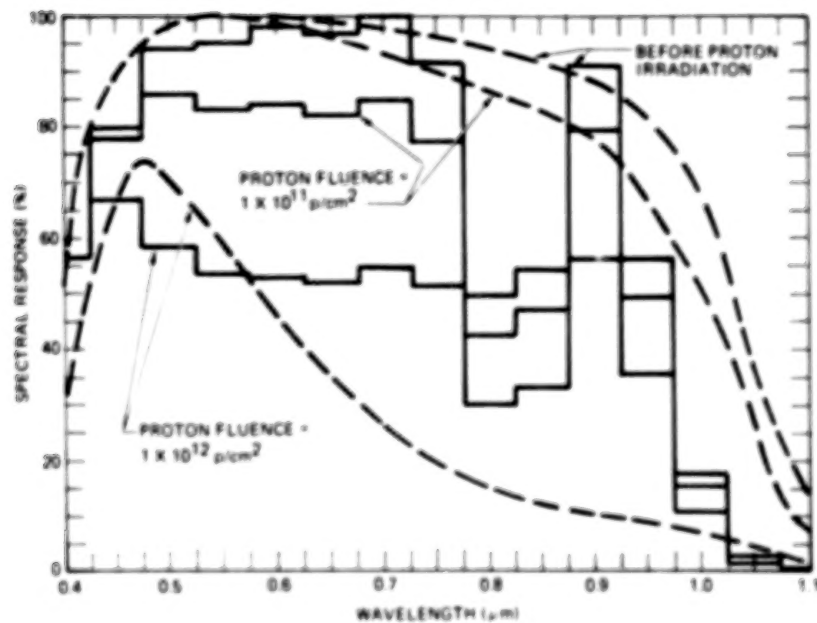


Figure 5. - Experimental and TRM-simulated spectral responses for silicon solar cell before and after proton irradiation (proton energy = 290 keV).

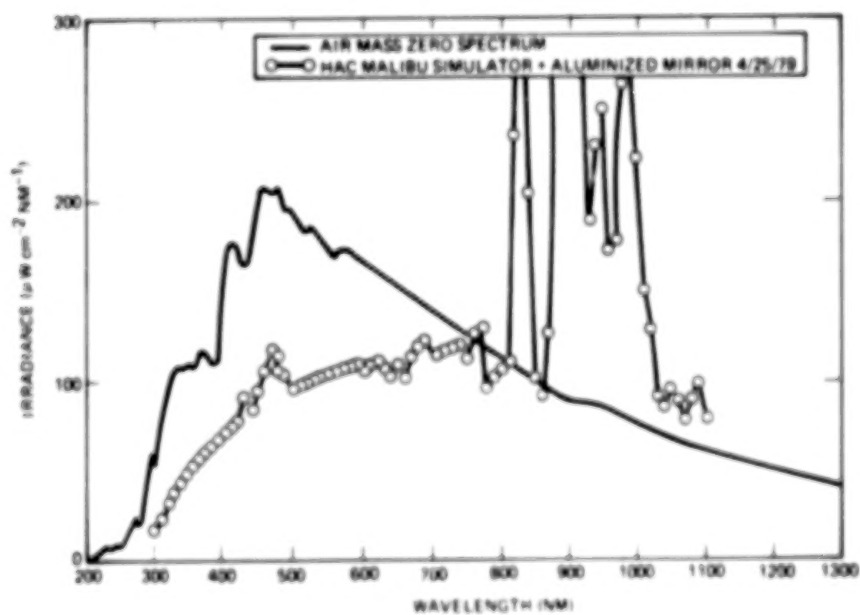


Figure 6. - Solar simulator spectrum in relation to AMO spectrum (ref. 9).

N84
29317

UNCLAS

N84 29317

PIECEWISE SIMULATION PROTON TEST OF GALLIUM ARSENIDE
AND THIN SILICON SOLAR CELLS

D. G. Peterson and S. A. Billets
Lockheed Missiles & Space Company, Inc.
Sunnyvale, California

There is general interest within the industry in the emerging Gallium Arsenide solar cell technology for use as primary power on certain future earth orbiting satellites. The assessment of the relative merits of Gallium Arsenide over silicon in a space radiation environment is hampered by the fact that a general degradation model for Gallium Arsenide does not exist. The primary purpose of this test was to provide direct comparison of the degradation of Gallium Arsenide cells to a control silicon solar cell in a specific orbit environment of interest to Lockheed. In addition, the test methodology provided an ideal vehicle to evaluate the front and back degradation characteristics of thin (2 mil) silicon solar cells.

The test consisted of a step proton irradiation, simulating the proton radiation environment existing in a 1110 km (600 n.m.) polar orbit. Two different types of Gallium Arsenide solar cells and two different types of thin silicon cells were irradiated, using current technology 200 μm (.008 in.) thick silicon cells as controls. The test specimens were sequentially exposed to seven fluence/energy intervals between 1.5 to 58 MeV, simulating the given energy spectra for 5 years, calculated to exist under a 150 μm (.006 in.) thick coverslide. Front and back, and low and high energy effects were separately evaluated. The results of the test are presented.

INTRODUCTION

This report covers the work performed on a proton irradiation test of two types of Gallium Arsenide and thin 50 μm (.002 in.) silicon solar cells during the period between Feb 82 to Oct 82.

Because of their high conversion efficiency and superior temperature performance, Gallium Arsenide solar cells offer a large potential payoff for space power applications. Although their electrical performance has been well characterized (ref. 1), radiation degradation characteristics are still not well understood. (ref. 2.).

Lockheed has a strong interest in and commitment to Gallium Arsenide solar cell technology, currently being engaged in a major cell development program with Applied Solar Energy Corp., that is expected to result in a procurement of 50,000 cells for end item production in 1986. The lack of a radiation model is one of the major concerns confronting us in attempting to assess the place of Gallium Arsenide cells in future programs. A parallel technology of interest to Lockheed is the development of thin silicon cells in conjunction with lightweight flexible arrays to increase the (watts per pound) of the solar array (ref. 3). Little work has been done to characterize the degradation characteristics through the back of the thin cell.

This test was undertaken to gain some empirical insight into the degradation characteristics of Gallium Arsenide and thin silicon solar cells with limited cells and in reasonable time.

OBJECTIVES

The general objective of this test was to investigate the degradation characteristics of these cell types by proton irradiation, to a typical orbit environment (1110 km (600 n. m.) circular polar) by simulating piecewise the radiation particle spectrum for that orbit. The specific objectives of the test for all cell types was as follows:

- a. Comparison of front proton degradation response (infinite backshield) to silicon control cell.
- b. Comparison of back and front proton degradation response (flexible blanket) to silicon control cell.
- c. Separate effects of low and high energies.
- d. Separate effects of front and back irradiations.
- e. Show feasibility of performing a piecewise (integral) simulation test for a typical orbit.

TEST METHODOLOGY

The normal proton test fluences must be derived from the omnidirectional fluences existing at the given altitude. The proton particle spectrum existing at the 1110 km (600 n.m.) circular polar orbit was generated from the NASA AP7 environment tables. This spectrum was integrated for 5 years and added to an estimated solar flare spectrum. A correction was then made to correct the omnidirectional fluence to the planer cell. The spectrum was then corrected for attenuation through a 150 μm (.006 in.) coverslide, including a factor to account for conversion of omnidirectional paths through the coverslide to an equivalent normal radiation. Bare cells were used in the test so that low energy effects at the cell might be investigated. Testing with a discrete energy spectra would make it nearly impossible to generate a low energy component under a coverslide.

This composite energy scale is shown in Figure 1. The energy scale is broken up into seven intervals for the purpose of calculating test values. The energy intervals are closer together at the low energy end because sensitivities are known to be greater and fluence levels higher at the low end. Since the spectrum is integral, the number of particles/cm² within each interval is simply the difference between fluence values at each end of the interval. The back energy spectrum was similarly evaluated, but without computations for the coverslide. Each interval was evaluated for total particles about the center energy and tabulated in Tables 1 and 2.

TEST SAMPLE

Some of the characteristics for each of the five types of solar cells in the experiment are shown in Table 3. The Hughes cells were LPE Gallium Arsenide solar cells with a 50 μm junction, provided to us by Wright-Patterson. The UTL Gallium Arsenide cells were terrestrial concentrator types. The 50 μm (.002 in.) thick silicon cells were of two types: 1) full back contact from Applied Solar Energy Corp., and 2) gridded back contact from Solorex. The Spectrolab silicon cell was an 200 μm (.008 in.) thick cell without a P+ back layer. This cell was used as a

control because its characteristics are well known and have been extensively evaluated.

The cell holder was configured to allow irradiation either from the front or through a 50 μ m Kapton sheet from the back. This scheme permits evaluation of degradation to a flexible solar cell blanket configuration. The Hughes cells came with a woven silver mesh interconnect attached to both front and back contacts. On all of the other cells, solder tabs were attached with conductive epoxy. The cells were then bonded to the holder as shown in Figures 2 and 3. A set of each of the five cell types were bonded to each of four windows in the holder. Three holders were built in all; one for front only irradiation, one for both front and back irradiation, and one to be used as a control.

The completed cell holder assembly is shown in Figure 4. The cell holder was mounted to a thermal control unit consisting of thermo-electric cells sandwiched between two aluminum plates and mounted to a heat sink. Thermocouples were bonded to the interconnects near the cell contacts and terminated into individual connectors. The cells were hardwired to a connector on the holder assembly. The entire assembly was configured for rapid exchange between the proton beam room and the electrical test area at the U.C. Davis facility with no handling of the fragile cells.

TEST SET-UP

The test was performed at the Cyclotron facility at the University of California in Davis, California. The Spectrolab X-25 Illuminator and associated test equipment were transported to Davis and set up in a room adjacent to the proton beam room so that electrical measurements could be made between irradiations. The cell temperature was controlled to 60°C for all electrical measurements, simulating a typical on-orbit operating temperature. A mechanical stepper permitted rapid measurement of each cell on a wheel.

The irradiation set-up is shown in Figure 5. A narrow proton beam was dispersed with a gold foil to provide a relatively uniform beam in air over the sample area. The beam energy spread, and fluence accuracy and uniformity are given in Table 4. The energy spread is fairly tight, from 5.5 to 58 MeV. The energy spreads more at the lower energies (1.5, 3 MeV) as shown in Figure 6. Although it is impossible to ascertain the exact energy content of these low energies, the spread probably more nearly simulates a continuous spectrum. The test sequence was conducted to minimize total time at the facility. The test sequence was as follows:

- a. Front irradiation of panel 1 and back irradiation of panel 2 at 5.5 to 58 MeV.
- b. Electrical test
- c. Front irradiation of panel 1 and back irradiation of panel 2 at 1.5 and 3.0 MeV.
- d. Electrical test
- e. Front irradiation of panel 2 at 1.5 to 58 MeV.
- f. Electrical test.

The energy range of 1.5 to 58 MeV are the limits of the U.C. Davis facility. This range adequately covers the range of interest for this particular orbit environment.

RESULTS

The degradation to maximum power is the principal figure of merit in evaluation of the cell for operation in a space environment. Normalized degradation for each of the five cell types and for each phase of the test are shown in Figures 7 and 8. The "front only" curve is a representation of degradation of cells mounted to a rigid panel with "infinite backshielding". The front and back curve represents degradation of cells mounted to a flexible blanket array.

For each curve, the first column shows the variation in measurement accuracy between data taken at Lockheed and repeated at Davis several days later. The last column shows the difference between final data taken at Davis and data taken 30 days later at Lockheed.

From an observation of the data, the following conclusions are presented:

- a. The Hughes Gallium Arsenide cell degraded 5% less than the silicon control cell for the "rigid panel" case and 10% less for the "flexible panel" case.
- b. The UTL Gallium Arsenide cell degraded 6% more than the silicon control cell for the "rigid panel" case and 2% less for the "flexible panel" case.
- c. All of the Silicon cells, including the control cells were within 2% of each other for the "rigid panel" case.
- d. Both of the thin silicon cell types suffered severe degradation for back irradiation, mostly from low energies.
- e. Silicon control cell degradation was within 1% of prediction for both low and high energies, based on JPL Radiation Handbook (ref. 4).
- f. For front irradiations, Silicon cells show annealing after 30 days (~5%), but Gallium Arsenide cells do not.
- g. For front and back irradiations, all cells show annealing.

In Figures 9 through 13 the electrical characteristics (IV curves) for typical cells in the test are given. Curves are shown for both preirradiation and post final irradiation for each cell type.

DISCUSSION OF METHOD AND RESULTS

This test demonstrates that a piecewise simulated proton test is feasible for rapidly demonstrating gross trends in proton degradation of new devices, given limited samples and time available.

The author recognizes the limitations in both the test methods and results obtained. The test did not address the effects of omnidirectionality; cells were irradiated at normal incidence only. The effects of omnidirectionality in the cover have been included in calculation of the normal fluence. As pointed out by Meulenberg (ref. 2), and others, the damage through the cell for protons is dependent on the path angle and that the damage mechanisms for Gallium Arsenide cells are different than for silicon cells. Since, in this test, a side by side comparison was made with silicon, some cancelling of the effect can be expected. Once the effect is well understood, it should be possible to integrate it into a general model. Until that is done, the best that can be accomplished is to rotate the sample in the proton beam to simulate omnidirectionality. This was, however, beyond the scope of this test, although it is planned for future tests.

No test of this type can address flux rate dependence of degradation, since years of slow irradiation in space are compressed into minutes of test irradiation. The assumption must be made that a strong relationship does not exist. Only long term flight data or possibly isotope irradiation will provide an answer.

The results of this test apply only to the conditions stated, i.e., 1110 km polar orbit, 5-year fluence and 150 μ m (.006 in.) thick coverslide. Although this is a limited case, it is typical for a large number of military missions of interest to Lockheed. These results do not contribute to generation of a general degradation model, since degradation at individual energy points are not available. A general model requires a large number of cells tested at discrete energy and fluence points.

This test included a limited number of energies. The closer that the number of test irradiations approach a continuous spectrum, the more significant would be the results. There will, however, always be a practical limit on the number of irradiations possible. In this case, seven was considered minimal to achieve the desired results. No irradiations were made at 0.2 MeV, although this appears to be a very degrading energy to Gallium Arsenide (ref. 5). We felt justified in this because our analysis of the residual energy spectra for a 1110 km orbit indicated that the fluence was highly attenuated under the coverslide at this energy. Future tests will include more low energy content.

The severe degradation to the thin cells from back irradiation cannot be explained from the simple model of degradation. This was an unexpected result. It may be that the selection of only two low energy points may have biased the test results towards the peak degradation response of the cells from the back. These results should not rule out thin cells for flexible panel consideration, but do point out the need for further analysis and testing.

CONCLUSIONS

This test has demonstrated the validity of performing a piecewise irradiating test on solar cells. The test has given added confidence that Gallium Arsenide cells are viable in low earth orbits. All of the specific objectives of the test have been met. The unexpected degradation of thin silicon cells irradiated from the back point to the need for further test analysis of these cells.

REFERENCES

1. High Efficiency Solar Panel GaAs Solar Cells. Contract review, Contract F33615-77-C-3150, 15 Jan 80
2. Meulenberg, A: Basis for Equivalent Fluence Concept in Space Solar Cells. Space Photovoltaic Research and Technology 1982, pp 185-194
3. Ho, F.; Iles, P: Recent Developments in Thin Silicon Solar Cells. Space Photovoltaic Research and Technology 1982, pp 17-24
4. Tada, H. Y.; Carter, J. R.: Solar Cell Radiation Handbook. JPL Publication 77-56, pp 4-12
5. Kamath, S.; Knechtli, R. C. and Loo, R.: Fabrication of High Efficiency & Radiation Resistant GaAs Solar Cells. Space Photovoltaic Research and Technology, 1980, pp 209-216

TABLE 1. - FRONT AND BACK IRRADIATION DATA

ENERGY (MeV)		TIME (MIN.)	FLUENCE (p/cm ²)	
			PLANNED	ACTUAL
	TEST			
↑ BACK	58.0	11.0	5.3E10	5.3E10
	42.0	11.0	2.3E10	2.3E10
	21.0	13.7	2.4E10	2.4E10
	10.8	23.3	4.6E10	2.7E10*
	5.5	15.7	2.6E10	4.9E10*
	TEST			
↓	3.0	8.7	7.1E10	7.1E10
	1.5	30.8	5.0E11	5.0E11
	TEST			
↑ FRONT	1.5	7.3	6.0E9	6.0E9
	3.0	10.4	8.4E9	8.4E9
	5.5	1.4	6.6E9	6.6E9
	10.8	14.0	1.6E10	1.6E10
	21.0	10.7	1.8E10	1.8E10
	42.0	11.0	2.3E10	2.3E10
	58.0	11.0	5.3E10	5.3E10
		TEST		

ORIGINAL PAGE IS
OF POOR QUALITY

TABLE 2. - FRONT IRRADIATION DATA

ENERGY (MeV)	TIME (MIN.)	FLUENCE (p/cm ²)	
		PLANNED	ACTUAL
TEST			
58.0	11.0	5.30E10	5.30E10
42.0	11.0	2.30E10	2.30E10
21.0	10.7	1.85E10	1.85E10
10.8	8.3	1.65E10	1.00E10*
5.5	4.0	6.60E9	1.85E10*
TEST			
3.0	10.4	8.40E9	8.40E9
1.5	7.3	6.00E9	6.00E9
TEST			

*ERROR IN SETUP

TABLE 3. - TEST SAMPLE DATA

CELL TYPE	MANUF.	THICKNESS	SIZE (cm)	POLARITY CONFIG.	JUNCT. DEPTH	BULK RESIST.	BACK CONFIG.	CONTACTS	AR COATING
GaAs	HUGHES	300 μ m (~12 mil)	2X2	P/N/N+	0.50 μ m	.015 Ω -cm	N+	Frt) Ag/Au/Zn Bk) Au/Ce/Ni	Ta ₂ O ₅
GaAs	UTL	250 μ m (~10 mil)	1.25 X 1.25	P/N	0.50 μ m	.01 Ω -cm	N+	Frt) Ag/Au/Zn (5 μ m) BK) Au/SN (2000 Å)	SiN
Si	ASEC	60-75 μ m	2X2	N/P	.35-.20 μ m	10 Ω -cm	BSF(B) BSR	Ag/Ti/Pd	MLAR (TiO ₂ -Al ₂ O ₃)
Si	SOLAREX	62-72 μ m	2X2	N/P	.15-.20 μ m	10 Ω -cm	BSF (Al pst)	Ag/Ti/Pd	Ta ₂ O ₅
Si	SPL	200 μ m	2X2	N/P	.10-.15 μ m	10 Ω -cm	BSR	Ag/Ti/Pd	Ta ₂ O ₅

ORIGINAL PAGE IS
OF POOR QUALITY

TABLE 1 - TEST ACCURACY

ENERGY MeV	FLUENCE UNCERTAINTY	ENERGY SPREAD
1.5	$\pm 10\%$	+30% -60%
3.0	$\pm 5\%$	+25% -40%
5.5	$\pm 8\%$	$\pm 10\%$
10.8	$\pm 7\%$	$\pm 3\%$
21.0	$\pm 6\%$	$\pm 3\%$
42.0	$\pm 6\%$	$\pm 3.5\%$
58.0	$\pm 10\%$	$\pm 2\%$

FLUENCE UNIFORMITY OVERSAMPLE ± 3 to $\pm 10\%$
PRIMARY BEAM ENERGY ACCURACY ± 30 KeV

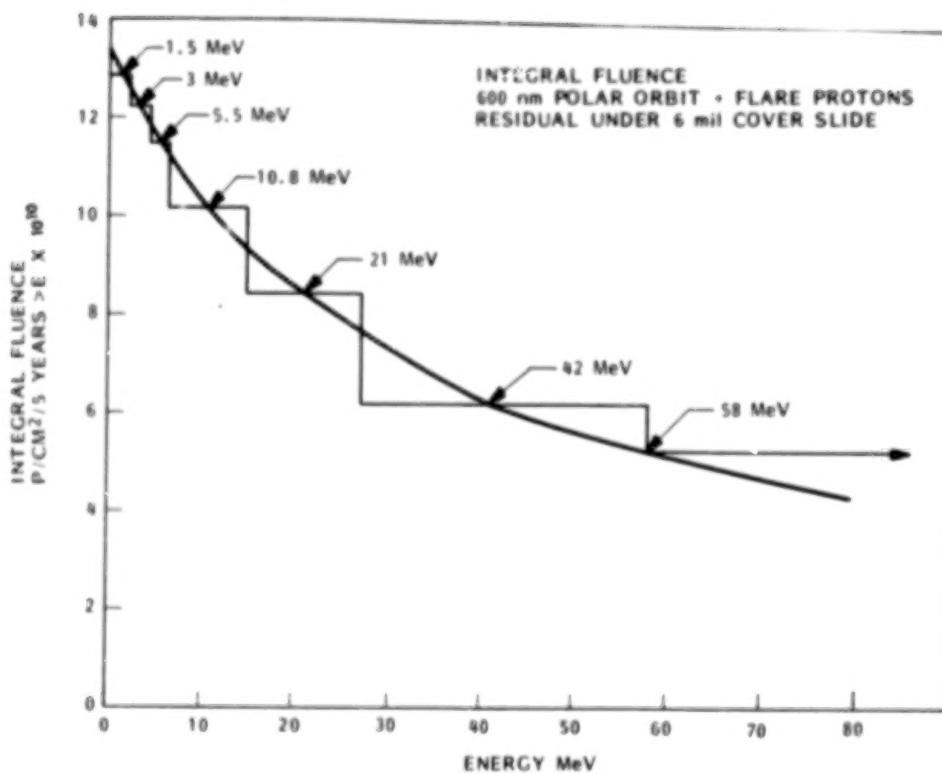


Figure 1. - Test fluence computation.

ORIGINAL PAGE IS
OF POOR QUALITY



Figure 2. - Cell holder (front).



Figure 3. - Cell holder (back).

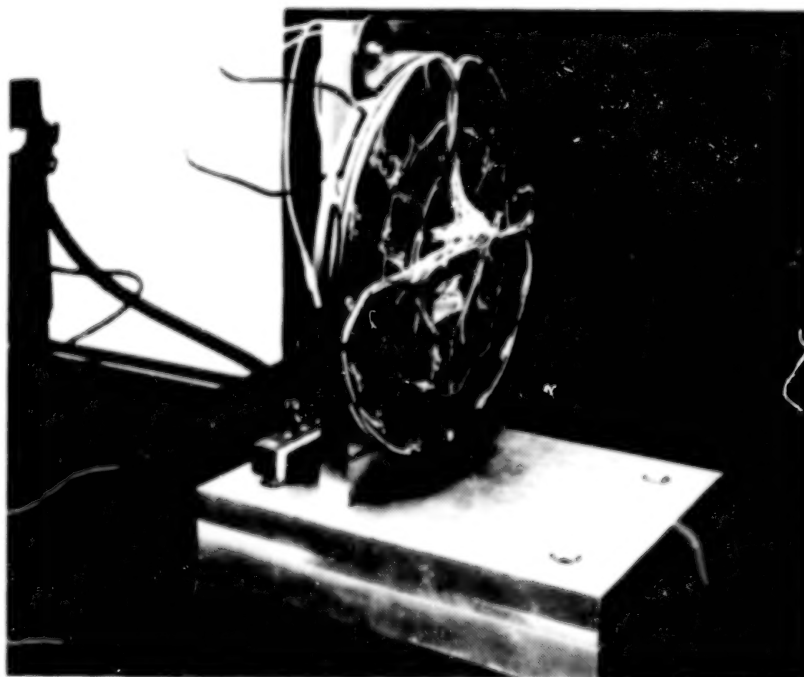


Figure 4. - Wired assembly.

ORIGINAL FACTOR
OF POOR QUALITY

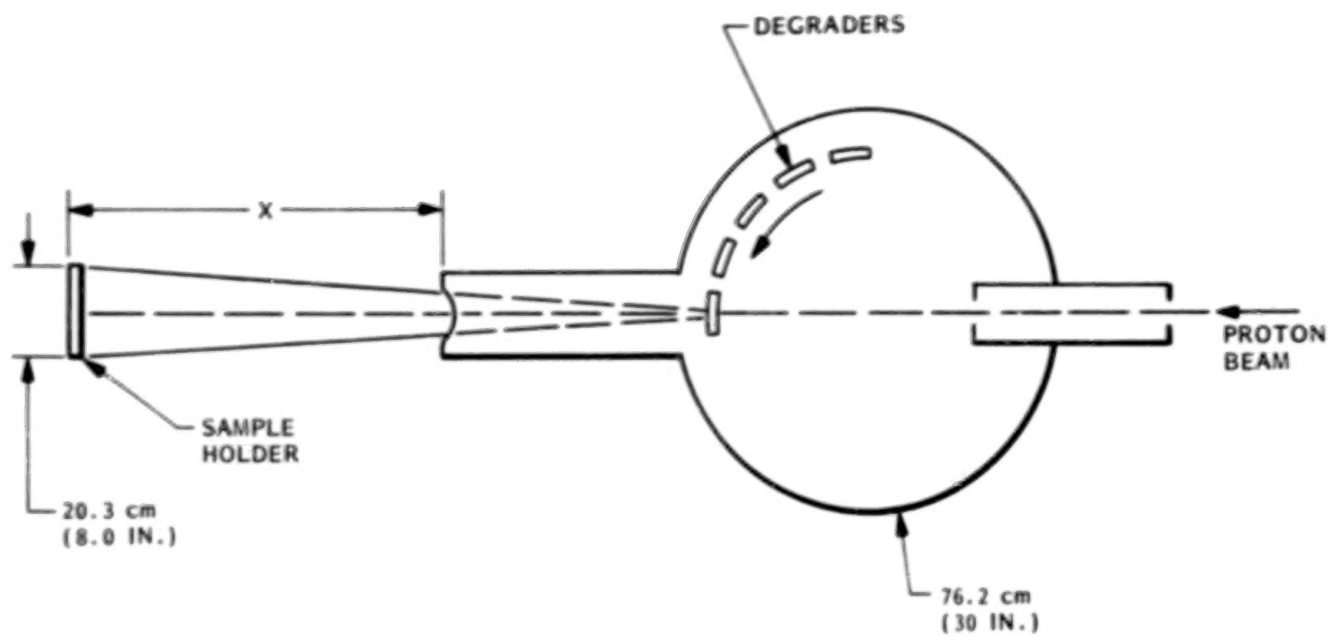


Figure 5. - Irradiation test setup.

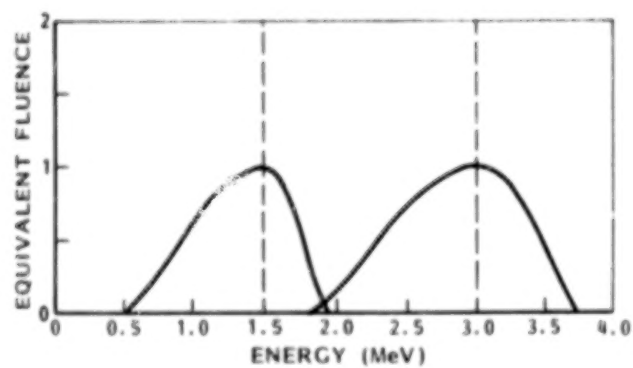


Figure 6. - Energy spread of low energies.

ORIGINAL PAGE 13
OF POOR QUALITY

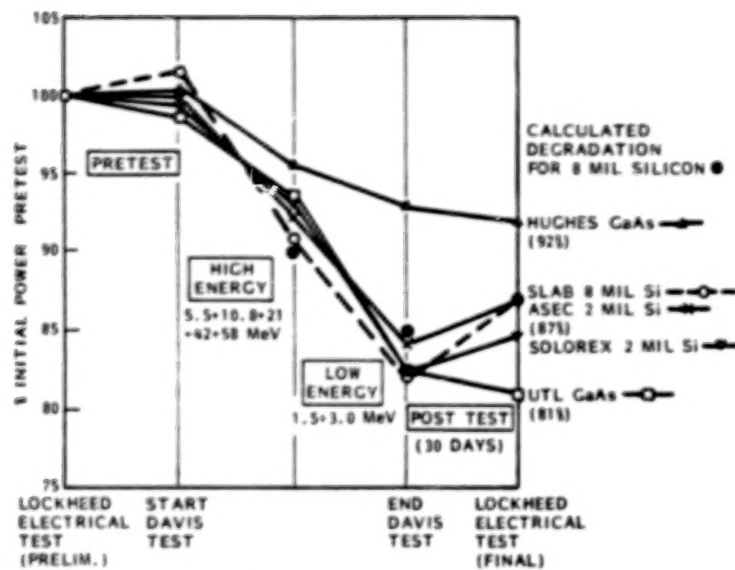


Figure 7. - Degradation to P_{max} (front only irradiation).

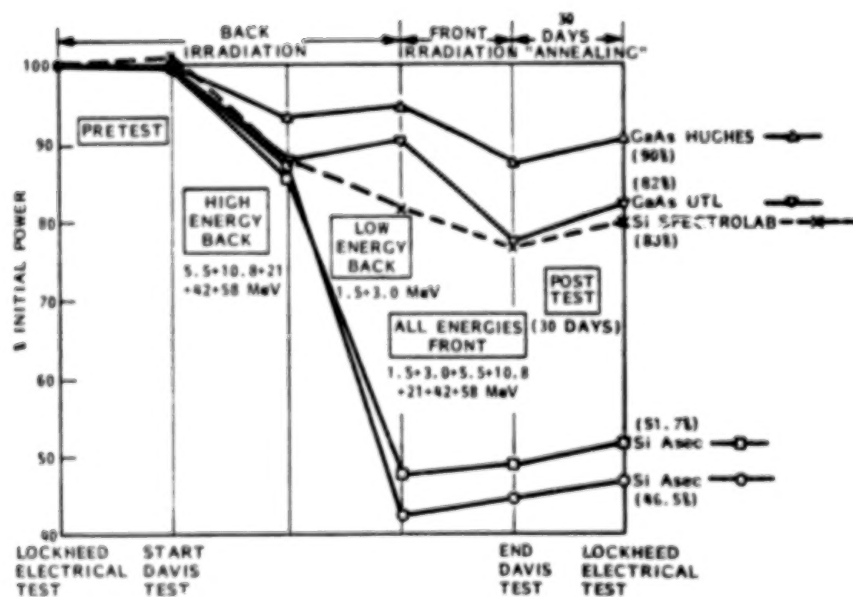


Figure 8. - Degradation to P_{max} (front and back irradiation).

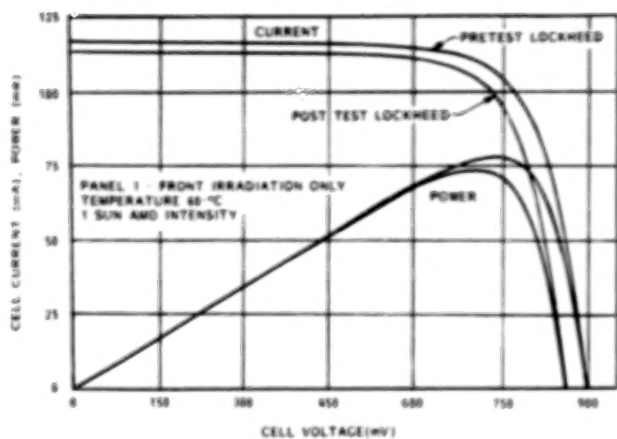


Figure 9. - Hughes gallium arsenide cell electrical characteristics.

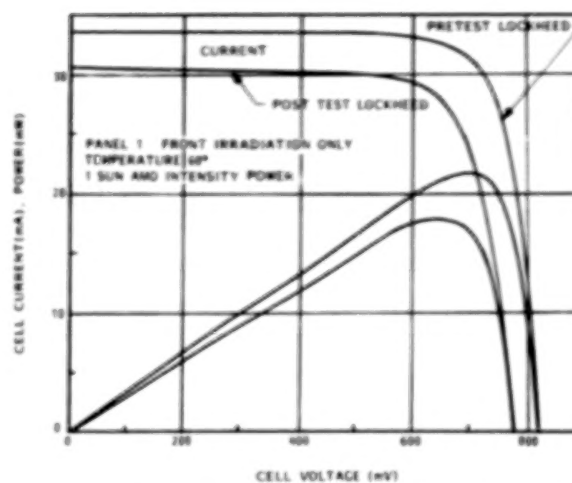


Figure 10. - UTL gallium arsenide solar cell electrical characteristics.

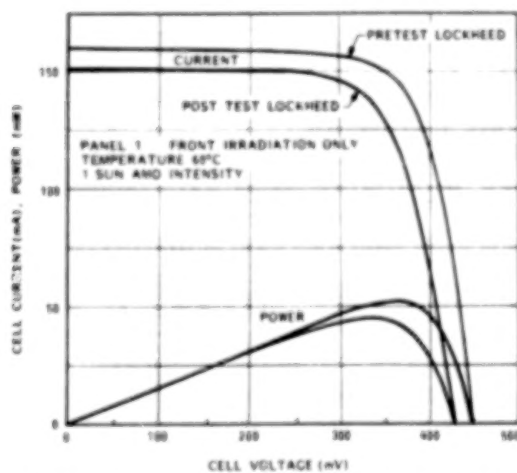


Figure 11. - Spectrolab silicon cell electrical characteristics.

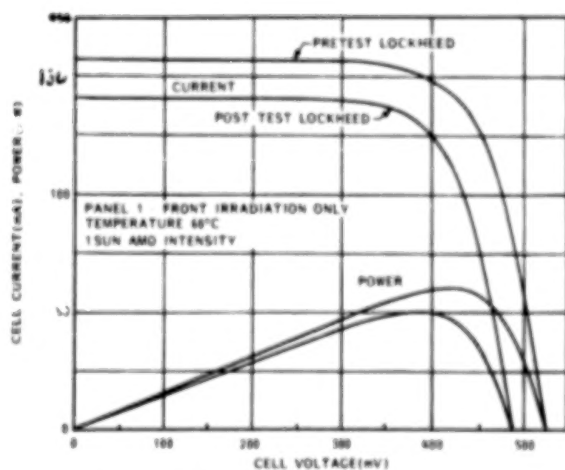


Figure 12. - Solorex cell electrical characteristics.

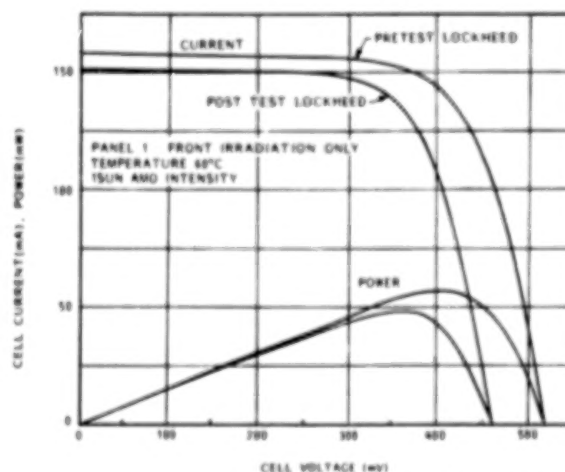


Figure 13. - ASEC cell electrical characteristics.

N84
29318

UNCLAS

RADIATION TOLERANCE OF LOW RESISTIVITY, HIGH VOLTAGE
SILICON SOLAR CELLS

V. G. Welzer, I. Weinberg, and C. K. Swartz
National Aeronautics and Space Administration
Lewis Research Center
Cleveland, Ohio

According to theoretical estimates, a 0.1 ohm-cm silicon solar cell should be able to produce an AMO open circuit voltage (V_{OC}) of about 700 mv (Ref. 1). Original attempts of a decade ago were only able to generate voltages in the neighborhood of 600 mv. Since then, a concerted effort by a number of laboratories has resulted in a series of incremental voltage improvements, the latest of which has yielded voltages in the mid-680 mV range (Ref. 2). While these cells have been successful, to varying degrees, in pushing beginning-of-life voltages to higher and higher levels, it was not at all certain that they could maintain their advantage in a radiation environment. To answer this question, an investigation was undertaken several years ago to determine the radiation sensitivity of the then-existing high voltage cells (Ref. 3). Included in this study were the Spire Corporation's ion-implanted emitter cell (Ref. 4), the University of Florida's hi-low emitter cell (Ref. 5), and the NASA multi-step diffused (MSD) cell (Ref. 6). Since that time, there have been several advances in the output of the low resistivity device, i.e., the Comsat MSD cell (Ref. 7), the MinMIS Cell (Ref. 8), and the MINP cell (Ref. 2). The purpose of this paper is to report the results of a study of the radiation tolerance of these latter three cell types.

EXPERIMENTAL PROCEDURE

The following is a brief description of the low resistivity (0.1 ohm-cm) silicon cells included in this investigation. Cell configurations for all three cells are shown in Figure 1. For a more detailed discussion the reader is referred to the cited references.

The COMSAT MSD Cell: This cell was fabricated using the MSD schedule developed at NASA Lewis and exploited further by the COMSAT Corporation. The MSD schedule consists of a deep initial diffusion followed by a chemical removal of the emitter surface. The emitter etching step is in turn followed by a shallow second diffusion. The COMSAT MSD cell, being more heavily etched than the previously studied NASA MSD cells, have considerably shallower junctions which result in significant efficiency gains, 14.5 percent being the highest efficiency achieved.

The MinMIS Cell: Developed by the University of New South Wales (UNSW) (Ref. 8). These cells were prepared by growing a thin ($<20\text{\AA}$) oxide layer on the base p-type silicon substrate which was followed by the deposition of low work function metallization, either a thin uniform metal layer or a fine, closely spaced grid structure. The MinMIS cell studied here was fabricated by the COMSAT Corporation with a uniform metallization deposited over the oxide consisting of a 100 \AA Erbium layer followed by a 50 \AA Chromium layer. It should

be noted that limited transmission through this metal layer is responsible for the rather low short circuit current (I_{SC}) in this cell (Table I).

The MINP Cell: This cell, also developed by the UNSW, is a result of incorporating MinMIS technology into the diffused cell. After a shallow phosphorus diffusion, the MINP structure is completed by depositing the MinMIS oxide and low work function metal grid on the emitter surface.

The pre-irradiation characteristics for all three cell types are shown in Table I. The AMO I-V characteristics were taken at 25°C on a xenon-arc simulator. Diffusion length data were obtained by an X-Ray excitation technique using 250 keV X-Rays. Irradiations were performed in a Dynamitron linear accelerator with 1 MeV electrons and fluences up to 1×10^{15} electrons/cm².

RESULTS AND DISCUSSION

The diffusion length damage coefficients, K_L were calculated from the relation

$$\frac{1}{L^2} - \frac{1}{L_0^2} = K_L \phi$$

where L_0 and L are the diffusion lengths before and after irradiation respectively, and ϕ is the 1 MeV electron fluence in electrons/cm². The results are given in Table II for the three cells tested. As can be seen in the table, considering the experimental uncertainties, the present K_L values are close to those previously found for 0.1 ohm-cm silicon cells (Ref. 9).

Plots of normalized I_{SC} as a function of fluences are shown in Figure 2, where behavior of a 10 ohm-cm n/p cell is shown for comparison. As can be seen, the MINP cell degraded somewhat more than did the MSD cell. The degradation characteristics of both these cells are similar to those found previously for the Spire ion-implanted cell and the NASA MSD cell (Ref. 3). However, the MinMIS cell, which degrades at lower fluences at about the same rate as do the other two cells, exhibits a severe drop in current at fluences greater than $\phi \sim 10^{14}$ e/cm². At 1×10^{15} e/cm² the cell is almost photovoltaically nonresponsive.

Figure 3 shows the effect of fluence on the normalized V_{OC} . Again, the behavior of the MSD and the MINP cells is close to that found for other 0.1 ohm-cm cells (Ref. 3). The MinMIS cell, on the other hand, shows a very drastic drop-off in voltage.

The red (0.9 micron) and blue (0.5 micron) normalized spectral responses are shown in Figures 4 and 5 respectively. As can be seen from the Figure, the most drastic difference between cell behavior occurs at the short wavelength end, where the MinMIS cell's spectral response drops off drastically compared to the other two cell types. To further consider this behavior, recall that of the three cell types, the MinMIS cell is the only one with an induced inversion layer, the remaining two cell types having built in emitters. In

this respect, it has been established that ionizing radiation affects the charge state of SiO_2 in MOS devices (Refs. 10 and 11). In the present case it is hypothesized that charge in the oxide plays a role in forming the n type inversion layer and that the change in the oxide charge state due to radiation diminishes the role of the oxide in creating the inversion layer. The net result is decreased effectiveness of the induced emitter and consequent degradation of cell performance. This behavior is similar to that observed in the Florida High-Low Emitter Cell, a cell which depends on oxide charge to create a junction in the silicon. At any rate, whatever the mechanism of cell degradation, the present data indicates that MinMIS cells are unsuitable for use in the space radiation environment.

CONCLUSIONS

It is concluded from the present work that:

1. The MinMIS cell degrades more rapidly than either the MSD or MINP cells under 1 MeV electron irradiation.
2. The blue response of the cell under irradiation indicates that emitter degradation is the principal cause of decreased cell performance in the MinMIS cell.
3. Changes in the MinMIS oxide charge state due to ionizing radiation contribute to the degradation in cell performance.
4. Cells of the MinMIS type are unsuitable for use in the space radiation environment.

REFERENCES

1. Godlewski, M. P., Brandhorst, H. W. Jr., and Baraona, C. R., Proceedings of the 11th IEEE Photovoltaic Specialists Conference, pp. 32-35, 1975.
2. Blakus, A. W., Green, M. A.: Appl. Phys. Lett. 39, 483 (1981).
3. Weinberg, I., Brandhorst, H. W. Jr., Swartz, C. K., Wiezer, V. G.: Conference Proceedings 2nd European Symposium on Photovoltaic generators in Space, Heidelberg, Germany, 1980, p. 93.
4. Minnucci, J. A., Matthei, K. W., Kirkpatrick, A. R., McCrosky, A.: Conference Proceedings 14th IEEE Photovoltaic Specialists Conference, 1980, p. 93.
5. Lindholm, F. A., Neugroschel, A., Sah, C. T., Godlewski, M. P., Brandhorst, H. W. Jr.: IEEE Transactions, ED 24, 402 (1977).
6. Godlewski, M. P., Mazaris, G. A., Klucher, T. M., Weizer, V. G.: Conference Proceedings 14th IEEE Photovoltaic Specialists Conference, 1980, p. 166.
7. Arndt, R. A., Muelenberg, A., Allison, J. F., Weizer, V. G.: Conference Proceedings 15th IEEE Photovoltaic Specialists Conference, 1981, p. 92.
8. Godfrey, R. B., Green, M. A.: IEEE Trans., ED 27, 737 (1980).
9. Srour, J. R., Othmer, S., Chin, K. Y., Curtis, O. L.: NASA CR-134768, 1975.
10. Collins, D. R., and Sah, C. T.: Appl. Phys. Lett. 8, 124-126, 1966.
11. Zaininger, K. H.: Appl. Phys. Lett. 8, 140-142, 1966.

TABLE I. - PREIRRADIATION CELL PARAMETERS

CELL TYPE	OPEN CIRCUIT VOLTAGE (V)	SHORT CKT. CURRENT (mA)	MAX. PWR. (mW)	FILL FACTOR (%)	DIFFUSION LENGTH (μ m)
MSD	646	141	72.5	80	218
MINMIS	633	75	25.4	55	326
MINP	678	175	63.9	67	219

ORIGINAL PAGE IS
OF POOR QUALITY

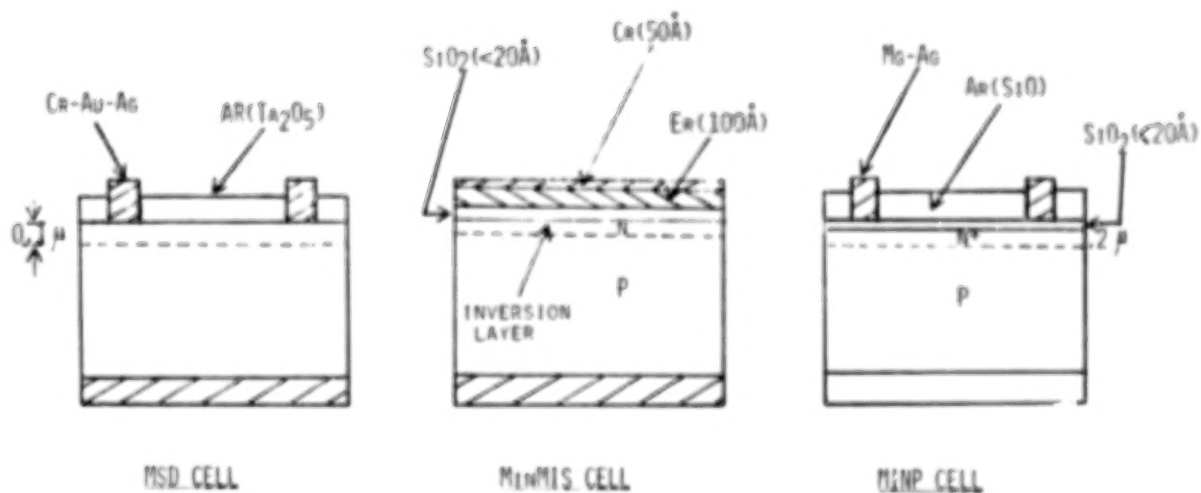
TABLE .I. - DIFFUSION LENGTH DAMAGE COEFFICIENTS

PRESENT DATA

CELL	K_L
MINP	$(2.2 \pm 0.7) \times 10^{-10}$
MSD	$(2.2 \pm 0.1) \times 10^{-10}$
MinMIS	$(2.5 \pm 0.9) \times 10^{-10}$

PREVIOUS DATA

0.1 OHM-CM CELLS 4×10^{-10} J.R. SROUR ET. AL.
NASA CR-134768, 1975



BASE RESISTIVITY ALL CELLS: 0.1 OHM-CM.

Figure 1. - High voltage cell configurations. Base resistivity of all cells, 0.1 ohm-cm.

ORIGINAL PAGE 13
OF POOR QUALITY

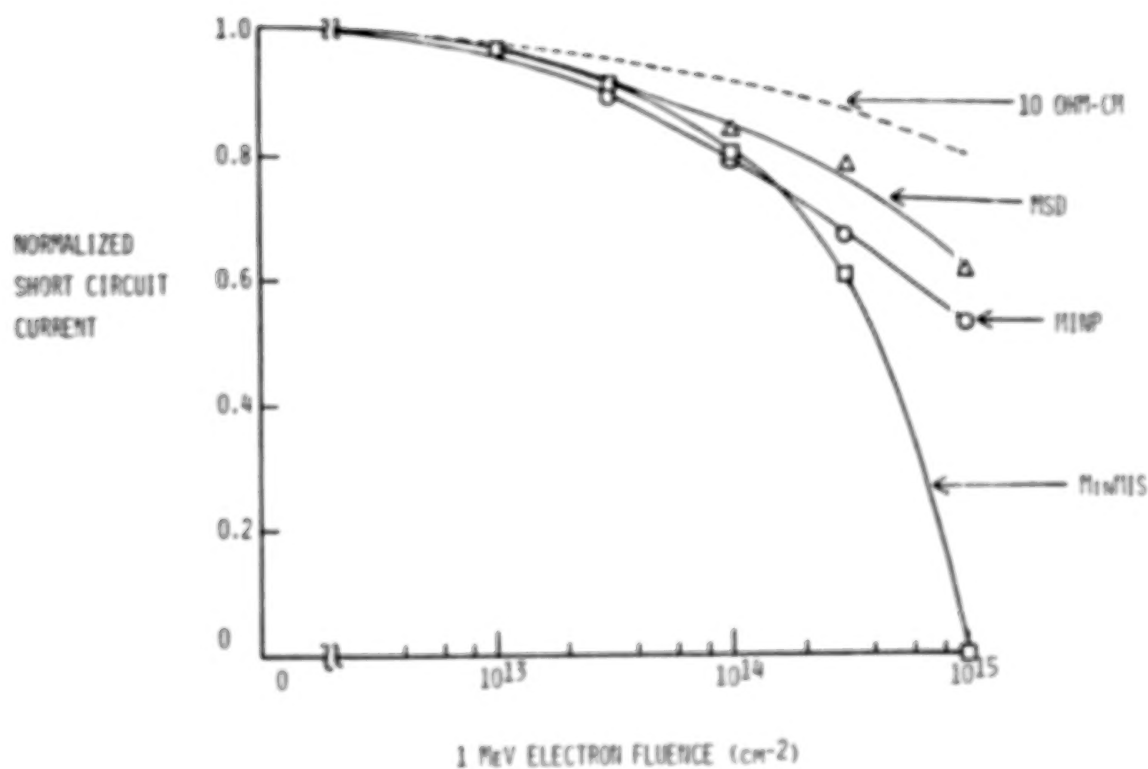


Figure 2. - Normalized short circuit current versus electron fluence.

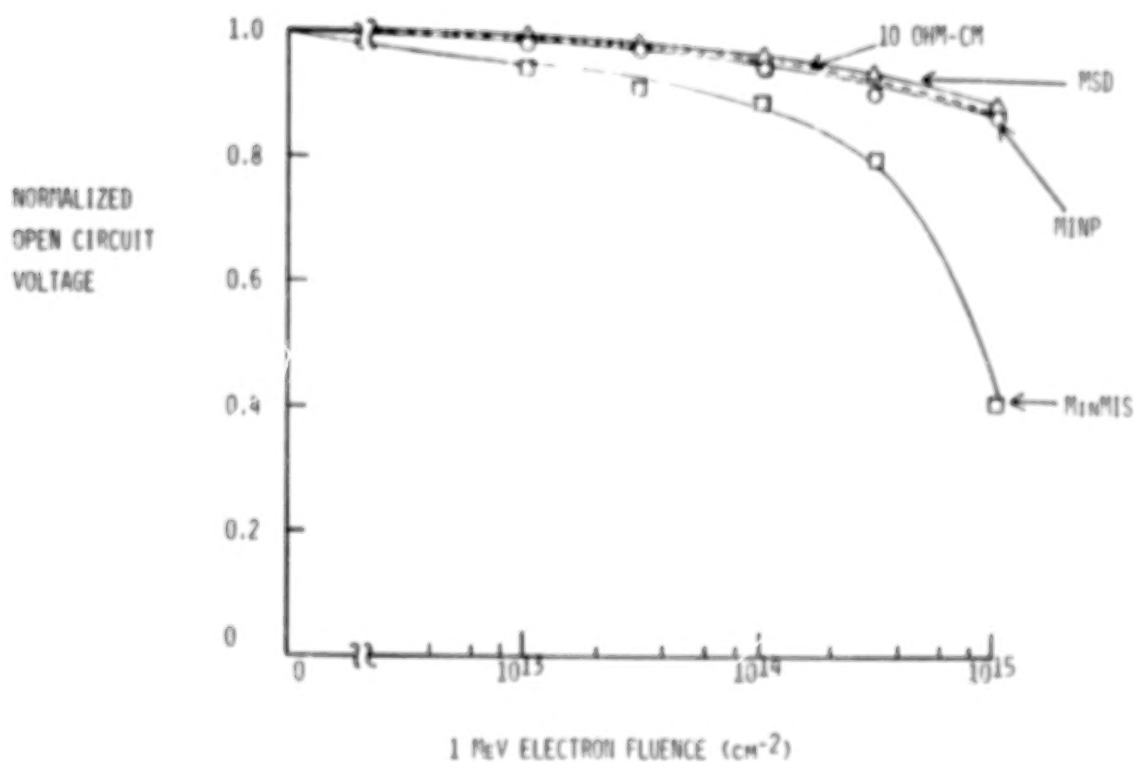


Figure 3. - Normalized open circuit voltage versus electron fluence.

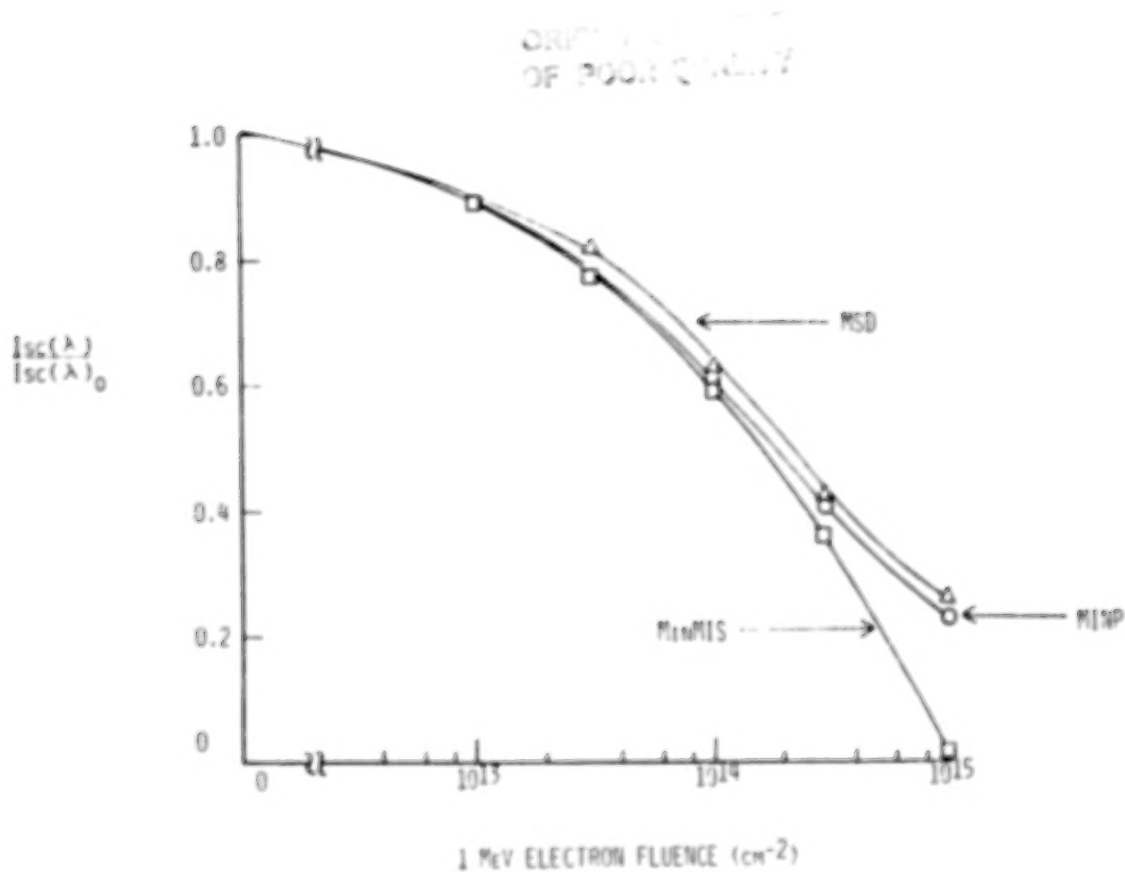


Figure 4. - Normalized spectral response at long wavelengths ($\lambda = 0.9 \mu\text{m}$).

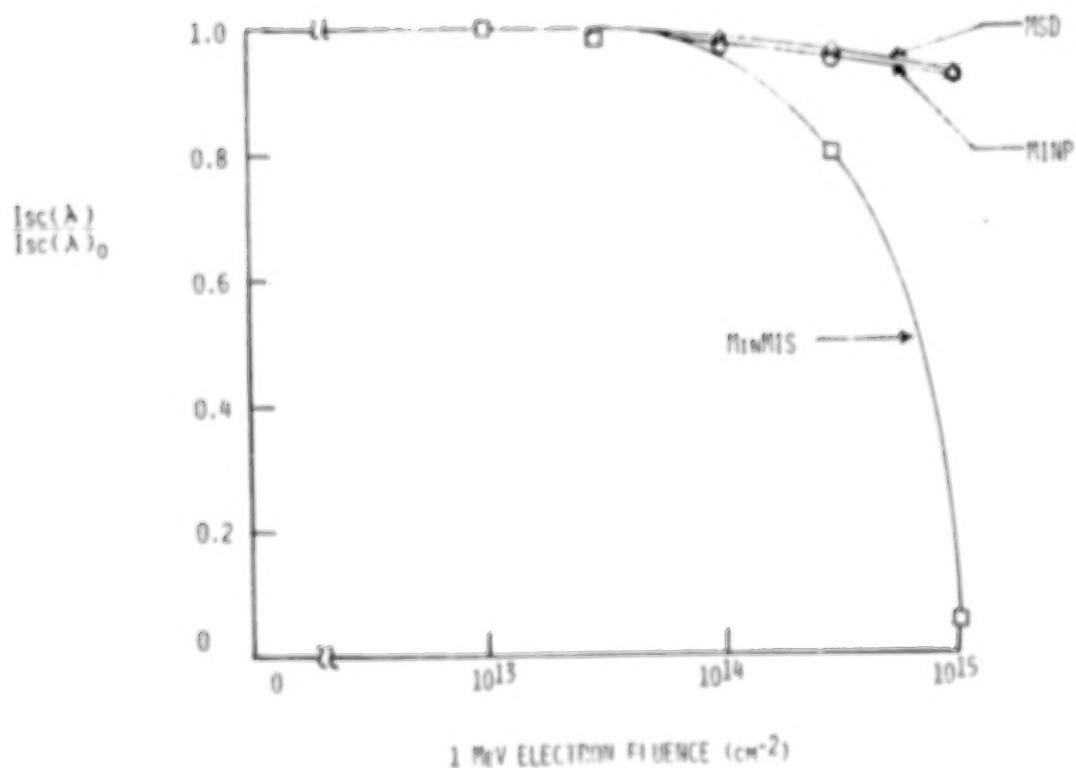


Figure 5. - Normalized spectral response at short wavelengths ($\lambda = 0.5 \mu\text{m}$).

N84
29319

UNCLAS

N84 29319

ON-ORBIT PERFORMANCE OF LIPS GALLIUM ARSENIDE SOLAR CELL EXPERIMENT

T. Bavaro, R. Francis, and M. Pennell
The Aerospace Corporation
El Segundo, California

Telemetry from the Living Plume Shield's (LIPS) gallium arsenide solar panel experiment was evaluated to determine degradation. The data were culled to preclude spurious results from possible shadowing or inaccurate measurements on a cold array. Two independent methods were then used to obtain the maximum power points and the various characteristics of the solar array. Fill factor, open circuit voltage, short circuit current, and series and shunt resistances were examined. The data analysis concluded that, to date, nearly all of the solar array degradation is due to the reduction in the short circuit current.

INTRODUCTION

The first increment of spaceflight data (32 to 123 days after launch) from the LIPS GaAs solar panel experiment has been reduced, analyzed, and evaluated. Algorithms were developed and computerized to calculate the daily maximum power by two independent techniques (ref. 1): (1) a least mean square polynomial fit to the power curve obtained with the intensity and temperature corrected currents and voltages (LMS method), and (2) an empirical expression for fill factor (ref. 2) based on open circuit voltage V_{oc} and the calculated series resistance R_s (FF method).

Telemetry Selection and Adjustment

The computer program discriminates against telemetry sets whose corrected values of maximum power are subject to large error due to excessive solar cell shadowing or extreme temperature shifts. Acceptable data have these defined limits:

Temperature	$0 < T < 70^{\circ} \text{ C}$
Incident angle	$0 < \theta < 30^{\circ} \text{ C}$
Power deviation	<15 percent

(related to preceding 10 data points)

In each method raw telemetry data were normalized to 28° C and a solar insolation of AMO normal to the panel surface. Changes in cell resistance as a function of temperature can be compensated for by an additional term in the voltage correction equation known as the curve factor temperature coefficient K (ref. 3). This value is not available for GaAs but would probably be less than a 1 percent correction based on silicon solar cells and the temperature limits on acceptable data. Therefore, K was set equal to zero for this analysis. The temperature coefficients, α and β , used for current and voltage correction are $3.01 \times 10^{-5} \text{ A/^{\circ} C} \cdot \text{cell}$ and $-2.04 \times 10^{-3} \text{ V/^{\circ} C} \cdot \text{cell}$, respectively. Sensitivity analysis indicates that for a 35 percent

error in either α or β the maximum error in the current and voltage correction for the stated temperature limits is only 5×10^{-3} A and 0.75 V out of 1.2 A and 20 V, respectively, for the beginning-of-life panel output. This is well within the experimental error and is insignificant in the calculation of maximum power.

Techniques of Determining Maximum Power Points

Once the telemetry voltages and currents are normalized, two algorithms are used to obtain maximum power output for each revolution and statistically averaged on a daily basis. The LMS method incorporates a fifth order polynomial to approximate the power curve, which is then maximized as a function of voltage. The order of the polynomial is excessive but was used to maintain a small selected deviation.

The FF method is based on parametric equations developed from solar cell empirical characteristics (ref. 2). The pertinent input parameters for this method are open circuit voltage, short circuit current, and series and shunt resistances. The general equation is

$$FF_1 = \left(\frac{V_{OC} - \ln(V_{OC} + 0.72)}{V_{OC} + 1} \right) \left(1 - r_s \right) - \left(\frac{V_{OC} + 0.7}{V_{OC} r_{SH}} \right) \\ \times \left(\frac{V_{OC} - \ln(V_{OC} + 0.72)}{V_{OC} + 1} \right)^2 \left(1 - r_s \right)^2$$

V_{OC} open circuit voltage normalized to thermal voltage
 r_{SH} shunt resistance normalized to cell characteristic resistance
 r_s series resistance normalized to cell characteristic resistance

For LIPS, calculated panel shunt resistances range between 600 and 1200 ohms and preclude any effect on fill factor. The fill factor is more affected by series resistance, however, whose panel values are between 2 and 3 ohms. The equation which applies is

$$FF_2 = \left(\frac{V_{OC} - \ln(V_{OC} + 0.72)}{V_{OC} + 1} \right) \left(1 - r_s \right)$$

OBSERVATIONS

Maximum Power of GaAs Array

The daily maximum power versus day is plotted in Figure 1 for the LMS method and in Figure 2 for the FF method. Data were unavailable for some days either because the input parameters were beyond acceptable limits or telemetry was unavailable. The effect is most apparent on graphed data between day 80 and day 117; a straight, dashed line connects these two days. A least-mean-squared smoothing curve was drawn through the calculated maximum power data in these figures to demonstrate the performance trend. The curves in Figures 1 and 2 were replotted in Figures 3 and 4 for comparison. The maximum power

points calculated by the two methods follow a similar trend. The smoothing curves compared in Figure 4 illustrate the correlation in power degradation more clearly. It should be noted that the dip in output power indicated by the FF method is questionable. This anomaly will be discussed later. The 1.2-W power decrease is equivalent to a 5 percent degradation from day 32, and the single LMS trend is shown in Figure 5.

Short Circuit Current (I_{SC})

There was a nearly monotonic decrease in I_{SC} from 1.21 to 1.16 A (table 1). This translates to a 4.1 percent loss in short circuit current. The decrease in current is a real trend, since a 1.5 percent error can only be associated with other effects (i.e., intensity and temperature corrections, ref. 3).

Open Circuit Voltage (V_{OC})

No trend in V_{OC} degradation was observed (table 1). The average deviation in V_{OC} was within the empirical precision of 1.0 percent for intensity and temperature correction (ref. 3).

Fill Factor (FF)

The FF remains essentially constant at 0.77 (table 1). Excellent correlation in fill factor was obtained between the LMS and FF methods. Fill factor was obtained explicitly from the FF method; whereas, it was obtained implicitly from the maximum power point (MPP) in the LMS method, that is,

$$FF_{LMS} = \frac{MPP}{I_{SC} \cdot V_{OC}} \quad (1)$$

The fill factor empirical expression has a 2 percent accuracy, which is equivalent to a one digit change in its second significant place.

Array Series Resistance (R_S)

The R_S , calculated from the current/voltage curve near V_{OC} , had an average value of 2.5 ohms with an experimental accuracy of ± 0.5 ohm (table 1). To date, no change in series resistance versus time was apparent within the accuracy of available telemetry. We concluded that R_S was relatively constant, not increasing, from day 32 to day 123 after launch.

Shunt Resistance (R_{SH})

An attempt was made to calculate R_{SH} from the current/voltage curve near I_{SC} . The shunt resistance is susceptible to more calculation error than R_S by nature of the input parameter values, that is,

$$R_{SH} = \frac{\Delta V}{\Delta I} \rightarrow \begin{matrix} \text{large} \\ \text{very small} \end{matrix} \quad \text{near } I_{SC} \quad (2)$$

and the overall telemetry accuracy. Values of R_{SH} ranged from 600 to 1100 ohms and indicated no performance degradation due to shunt resistance changes.

Error and Sensitivity of the Maximum Power Point (MPP) Calculations

As discussed, the MMP degraded 5 percent from day 32 to day 123 (figs. 1 to 5). Since the power points obtained by the two independent methods correlated extremely well with each other, confidence in the performance trend is high. The maximum standard deviation was 0.357 W for the LMS method and 0.531 W for the FF method for obtaining the daily maximum power from the telemetry.

Analysis showed that the FF method calculation was sensitive to the value of series resistance (ref. 2). A 0.5-ohm change or error in R_S will shift the fill factor two digits in its second significant place. The telemetry from each revolution exhibited this degree of inaccuracy in the determination of R_S . A 0.5-ohm increase occurred from day 69 to day 80 (table 1). This short term increase in R_S caused the fill factor to decrease by two digits during this time frame, which in turn caused the power dip in Figures 2 and 4. Since either no data existed or none were within acceptable limits between day 80 and day 117, the smoothed plotting curve just continues the curve in this region. In spite of the telemetry accuracy, however, the agreement and correlation in the fill factors in Table 1 were considered quite good.

CONCLUSIONS

The results of the first data set which included day 32 to day 123 after launch showed a gradual monotonic 4 percent decrease in short circuit current, which correlated extremely well with a 5 percent degradation in maximum output power, obtained by two independent techniques. In addition, the fill factor, open circuit voltage, and series resistance exhibited no apparent degradation and were constant within the experimental error and the accuracy of the telemetry. During this first time frame in which the solar panel performance has been monitored and telemetry data received, the results and analysis strongly suggested that power degradation was essentially the result of short circuit current degradation.

The original maximum power output of the LIPS solar panel generated at Spectrolab with an uncollimated xenon lamp solar simulator was 24.5 W with an I_{SC} of 1.29 A, a V_{OC} of 25 V, and a fill factor of 0.76. This was obtained from a composite of three current/voltage curves taken on separate sections of the panel. The maximum power was equivalent to a beginning-of-life (BOL) panel efficiency of 15 percent at AM0 (ref. 4). Since BOL data were not available on the panel after deployment in orbit and assuming no degradation of laboratory measured power output before and during launch, the BOL power degraded about 7 percent before day 32 after launch. Comparison of the BOL short circuit current with the day 32 value showed a 6.5 percent degradation. Again, there was good correlation of the power degradation with the short circuit current degradation. A total 12 percent power and short

circuit current degradation occurred up to day 123 after launch. A power plateau or degradation stabilization (fig. 5) may have been reached at 12 percent loss, although additional data are required. By comparison to published laboratory data on GaAs solar cells (ref. 5), a 12 percent degradation in BOL output power occurred after radiation damage imposed by a 1.0-MeV electron fluence of 2×10^{14} electrons cm^{-2} in JPL's dynamitron particle accelerator. Silicon cells having BOL 14 percent efficiency, BSF, and BSR would degrade 12 to 20 percent depending on cell thickness (ref. 6) under these fluence conditions. Stated differently, silicon solar cells with 6-mil cover glass in a LIPS type of low Earth orbit (600 n mi) will degrade 12 to 20 percent in the same time frame that GaAs degrades 12 percent. If GaAs power degradation indeed stabilizes, the power loss would be approximately half that of silicon after 1 year.

More experimental and orbital data are required to determine and understand the degradation mechanisms in the solar cell panel and the parameters contributing to a loss in short circuit current in this severe radiation orbit.

REFERENCES

1. "LIPS Gallium Arsenide Solar Array," by M. P. Pennell, Aerospace ATM 83 (3524-03)-1, August 10, 1983.
2. Solid State Electronics, Vol. 24, No. 8, pp. 788-789, 1981.
3. "A Method for Predicting Solar Cell Current-Voltage Curve Characteristics as a Function of Incident Solar Intensity and Cell Temperature," by J. D. Sandstrom, JPL Technical Report 32-1142 (1967).
4. Private Communication with Dr. R. Y. Loo, Hughes Research Laboratories, Malibu, CA., August 11, 1983.
5. Radiation Damage in GaAs Solar Cells, by R. Loo, G. S. Kamath, and R. C. Knechtli, 14th IEEE Photovoltaic Specialists Conference, pp. 1090, 1980.
6. "Solar Cell Radiation Handbook," by H. Y. Tada and J. R. Carter, Jr., JPL Publication 82-69, November 1, 1982.

ORIGINAL PAGE IS
OF POOR QUALITY.

TABLE - 1.

Day	I _{SC} (AMP)	V _{OC} (VOLT)	FF (MPP-LMS)	FF (MPP-FF)	R _S (OHM)
32	1.21	24.66	76	78	2.29
33	1.20	24.62	77	78	2.23
34	1.20	24.64	76	78	2.12
38	1.19	24.57	76	78	2.35
39	1.19	24.53	77	78	2.33
41	1.19	24.56	76	78	2.26
42	1.19	24.59	77	78	2.43
43	1.19	24.51	77	78	2.43
44	1.18	24.51	76	79	2.08
46	1.18	24.49	77	78	2.29
47	1.19	24.49	76	78	2.19
48	1.20	24.44	77	76	2.74
49	1.18	24.50	77	78	2.35
51	1.18	24.42	78	76	2.84
52	1.18	24.46	77	78	2.44
53	1.19	24.40	77	77	2.60
54	1.19	24.50	77	78	2.22
55	1.18	24.45	77	77	2.56
56	1.19	24.41	77	76	2.88
57	1.18	24.46	76	79	2.28
58	1.18	24.42	77	76	2.89
59	1.18	24.42	76	78	2.14
60	1.19	24.45	76	76	2.83
62	1.18	24.41	76	76	2.93
63	1.17	24.46	77	78	2.37
64	1.17	24.44	77	78	2.24
66	1.17	24.38	76	78	2.43
69	1.17	24.38	77	78	2.37
72	1.17	24.34	76	76	3.00
76	1.17	24.29	77	76	2.88
77	1.17	24.24	77	76	2.79
78	1.16	24.26	78	76	2.89
80	1.16	24.37	78	76	2.78
117	1.16	24.40	76	79	2.08
118	1.15	24.46	77	78	2.50
123	1.16	24.44	76	78	2.22

ORIGINAL PAGE IS
OF POOR QUALITY

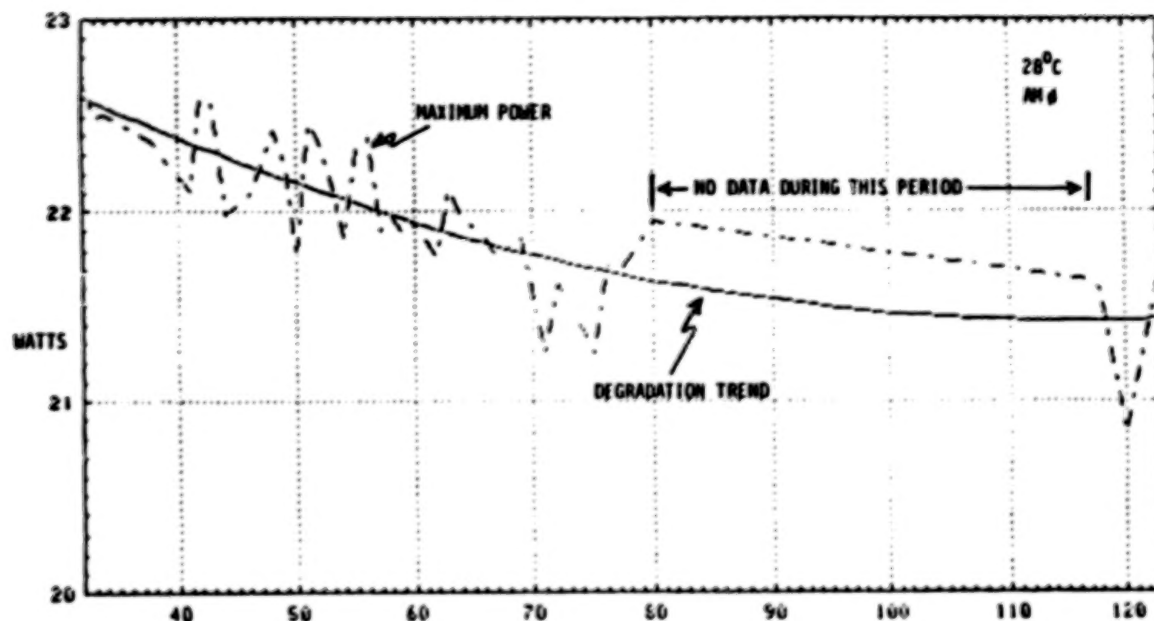


Figure 1. - Least-mean-square-method determination of maximum power points versus days after launch.

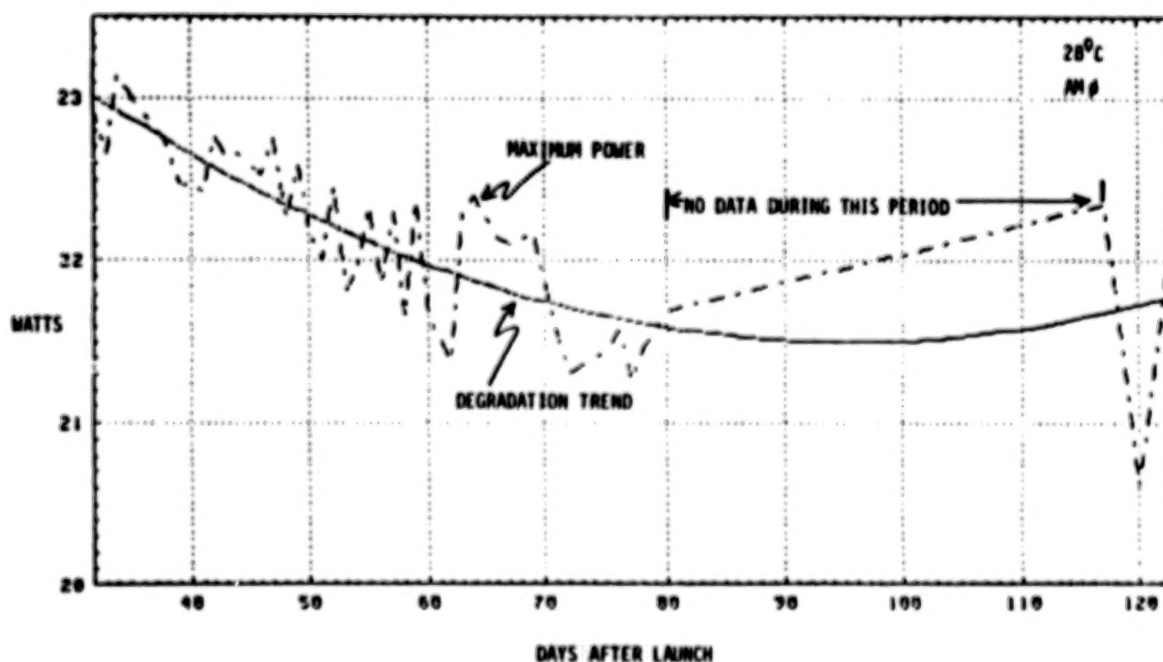


Figure 2. - Fill-factor-method determination of maximum power points versus days after launch.

ORIGINAL PAGE 12
OF POOR QUALITY

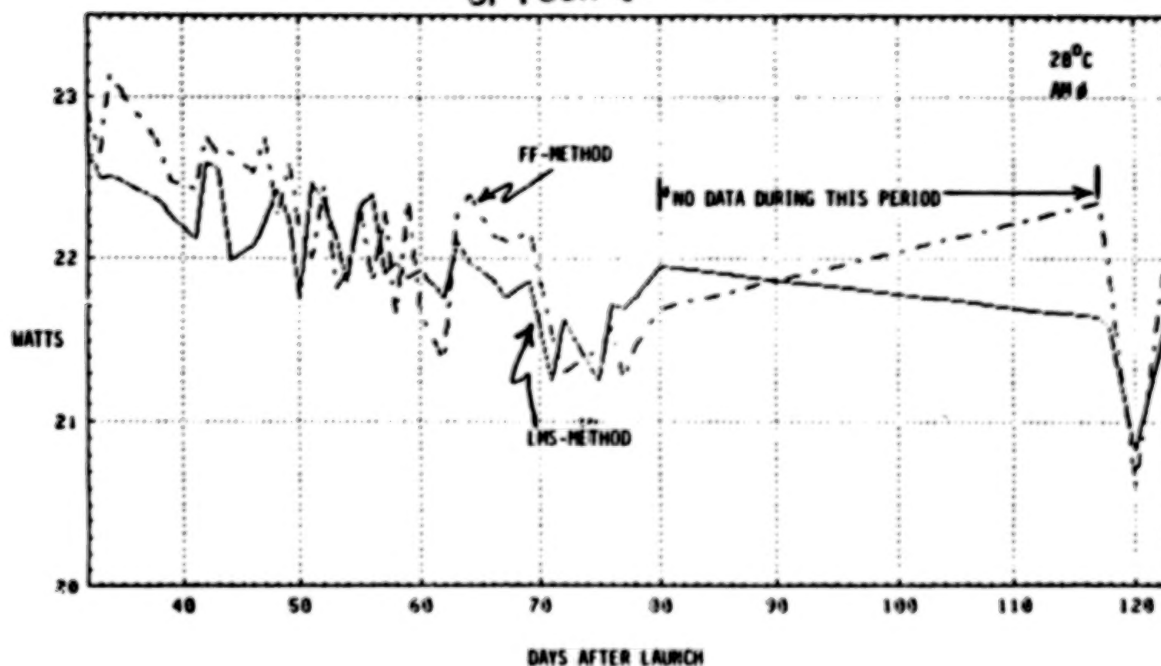


Figure 3. - Comparison of LMS method and FF method for determination of maximum power points versus days after launch.

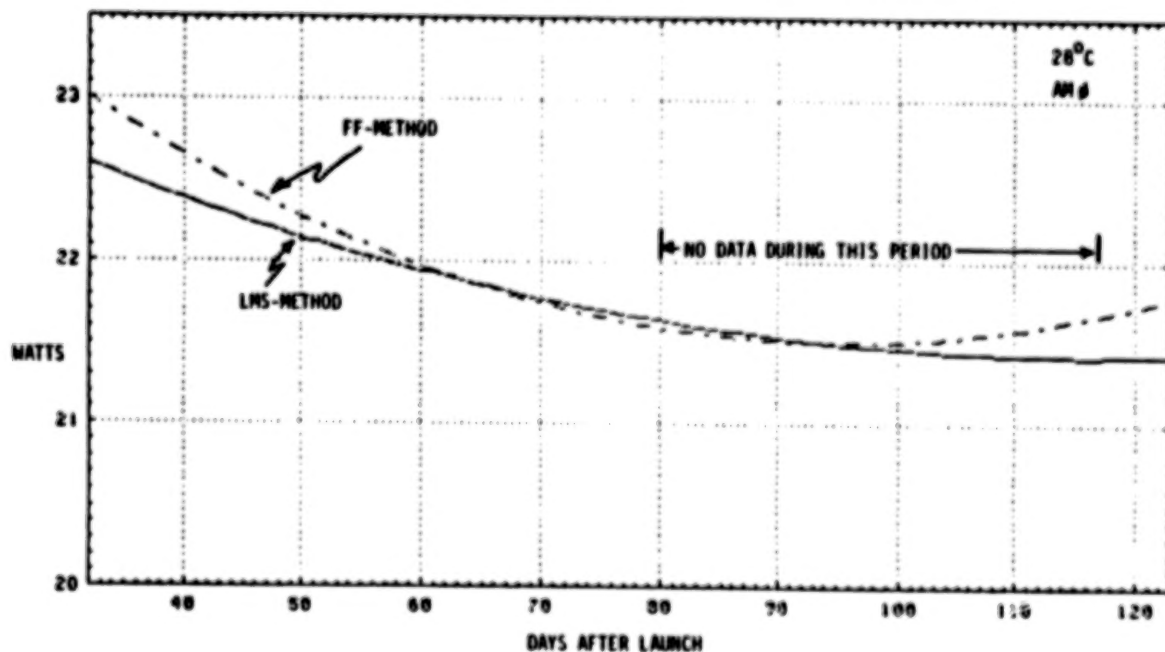


Figure 4. - Degradation trend of LIPS solar array from LMS and FF method.

ORIGINAL PAGE 12
OF POOR QUALITY

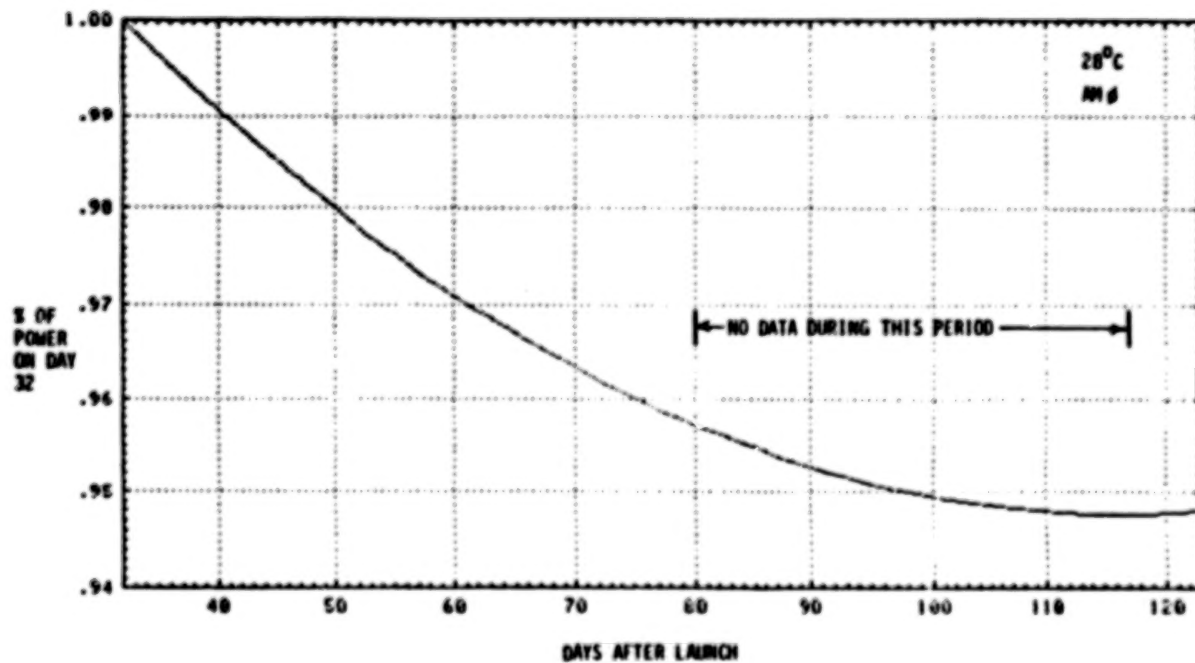


Figure 5. - Degradation of LIPS solar array normalized to day 32 versus days after launch.

N84
29320

UNCLAS

N84 29320

INFLUENCE OF OXYGEN ON DEFECT PRODUCTION
IN ELECTRON-IRRADIATED, BORON-DOPED SILICON

Henry M. DeAngelis and Peter J. Drevinsky
Rome Air Development Center
Hanscom Air Force Base, Massachusetts

Deep level transient spectroscopy (DLTS) measurements were made on float-zone and crucible-grown, boron-doped silicon irradiated with 1-MeV electrons. The minority carrier trap, which has been attributed to a boron-related state, was not seen in low-resistivity, float-zone silicon. However, a new majority carrier trap was observed in these samples. In the case of more lightly doped material the minority carrier trap was present, and its introduction rate was lower in float-zone than in crucible-grown silicon. For 1- and 10-ohm-cm float-zone material that had been oxidized during processing, the introduction rates for this trap were comparable to those for crucible-grown silicon. This behavior is a strong indication that the minority carrier trap involves oxygen and that it may be due to a boron-oxygen complex. On the other hand, the majority carrier trap seen in heavily doped, float-zone silicon may also involve boron but not oxygen. Observed trap concentrations suggest that oxygen content in the regions examined by DLTS is affected by processing techniques. Other differences were observed in defect production and annealing behavior of electron-irradiated, float-zone and crucible-grown silicon.

N84
29321

UNCLAS

DEFECT STUDIES IN ONE-MEV ELECTRON IRRADIATED GaAs
AND IN $\text{Al}_x\text{Ga}_{1-x}\text{As}$ P-N JUNCTION SOLAR CELLS*

Sheng S. Li and W. L. Wang
University of Florida
Gainesville, Florida

R. Y. Loo
Hughes Research Laboratory
Malibu, California

W. P. Rahilly
Aeropropulsion Laboratory

Studies of the radiation induced deep-level defects in one-MeV electron irradiated GaAs solar cells as a function of the electron fluence (i.e., 1×10^{14} to 10^{16} cm^{-2}) and of the grown-in defects in $\text{Al}_x\text{Ga}_{1-x}\text{As}$ p-n junction solar cells for $x = 0.05$ and $x = 0.17$ have been carried out in this work by using the Deep-Level Transient Spectroscopy (DLTS) technique. Defect parameters such as defect energy levels and density were determined. Carrier removal rate was deduced from the C-V measurement, and the results were compared with the published data for GaAs. The main electron traps observed for the one-MeV electron irradiated GaAs cells are $E_c - 0.31$, $E_c - 0.71$, and $E_c - 0.90$ eV, and the main hole trap is due to the $E_v + 0.71$ eV level. Electron trap density was found to vary from 5×10^{13} cm^{-3} for 1×10^{14} cm^{-2} electron fluence to 3.7×10^{14} cm^{-3} for 1×10^{16} cm^{-2} electron fluence; a similar result was also obtained for the hole trap density. As for the grown-in defects in the $\text{Al}_x\text{Ga}_{1-x}\text{As}$ p-n junction cells, only two electron traps with energies of $E_c - 0.20$ and $E_c - 0.34$ eV were observed in samples with $x = 0.17$, and none was found for $x < 0.05$. Auger analysis on the $\text{Al}_x\text{Ga}_{1-x}\text{As}$ window layer of the GaAs solar cell showed a large amount of oxygen and carbon contaminants near the surface of the AlGaAs epilayer. Thermal annealing experiment performed at 250 °C for up to 100 min. showed a reduction in the density of both electron traps.

* Research supported by AFWAL/APL through Universal Energy Systems, Inc., and in part by AFOSR.

I. Introduction

The objective of this work is to identify the radiation-induced deep-level defects in the one-MeV electron irradiated GaAs solar cells fabricated by the infinite solution melt liquid phase epitaxial (LPE) technique and the grown-in defects in the $\text{Al}_x\text{Ga}_{1-x}\text{As}$ p-n junction solar cells with different alloy compositions by using the Deep-Level Transient Spectroscopy (DLTS) technique. The I-V and C-V measurements are employed to determine the background concentration and the carrier removal rate vs electron fluence in GaAs cells irradiated by one-MeV electron for fluences of 1×10^{14} , 1×10^{15} , 5×10^{15} , and $1 \times 10^{16} \text{ cm}^{-2}$. The C-V and DLTS measurements were used to determine the defect parameters such as energy levels and defect density as well as capture cross section of electron and hole traps in both one-MeV electron irradiated GaAs solar cells and in $\text{Al}_{0.17}\text{Ga}_{0.83}\text{As}$ p-n junction cells. Thermal annealing study was performed on the $\text{Al}_{0.17}\text{Ga}_{0.83}\text{As}$ p-n junction cell to study its effects on the deep-level traps. Section II presents the results of I-V, C-V, and DLTS measurements on the one-MeV electron irradiated GaAs cells. Section III discusses the results of our I-V, C-V, and DLTS measurements on the $\text{Al}_{0.17}\text{Ga}_{0.83}\text{As}$ p-n junction cells; the results of our thermal annealing study on these cells will also be discussed. Conclusions are given in section IV. Section V lists the references.

II. One-MeV electron irradiated GaAs solar cells

In this section, the results of our study on the deep-level defects induced by the one-MeV electron irradiation in GaAs solar cells are discussed. The electron irradiation on the GaAs cells was performed for four different electron fluences (i.e., 1×10^{14} , 1×10^{15} , 5×10^{15} , and $1 \times 10^{16} \text{ cm}^{-2}$). The GaAs solar cells used in this study were fabricated at Hughes Research Laboratory, using the infinite solution melt LPE technique; an $\text{Al}_{0.9}\text{Ga}_{0.1}\text{As}$ window layer of 0.5 μm thick and a Sn-doped GaAs active layer of 10 μm thick were deposited on the GaAs substrate. The I-V and C-V measurements were performed to determine the carrier density and carrier removal rate in the GaAs active layer as well as the recombination mechanisms in these cells. The results of the I-V, C-V, and DLTS analysis are discussed next.

2.1 Results and discussion of the I-V measurements

In this section the results of the I-V measurements on the one-MeV electron irradiated GaAs cells for four different electron fluences are presented. Fig. 1 shows the forward I-V characteristics curves of the GaAs cells with electron fluences of 0, 1×10^{14} , 1×10^{15} , and $1 \times 10^{16} \text{ cm}^{-2}$. The results show that diode ideality factor "n" is 2.2 for the unirradiated, the electron fluences of 1×10^{14} and $1 \times 10^{15} \text{ cm}^{-2}$ irradiated cells, and

equals to 1.3 for the 1×10^{16} e/cm² irradiated cell. The reason for the diode ideality factor to be greater than 2 is probably due to the high series resistance in these cells. If the recombination current is the dominant current component, then values of "n" for the cell should be varied between one and two. The equation which governs the recombination-generation current under forward bias conditions depends on the depletion layer width and the carrier lifetime in the depletion region of the diode, and can be written as: [1]

$$I_{rg} = [2kTW_d A n_i / 2(V_{bi} - V) \tau_o] \exp(qV/nkT) \quad (1)$$

where $1 < n < 2$. From equation (1), it is noted that the recombination current in the diode is inversely proportional to the effective carrier lifetime in the depletion region. Increasing defect density due to electron irradiation in the depletion region of the cell will reduce the carrier lifetime in that region, and thus will result in the increase of the dark current and the decrease in the open-circuit voltage or conversion efficiency. From Fig.1, it is clearly shown that the recombination current under forward bias condition is indeed increased with increasing electron fluence. This result is consistent with our DLTS observation in that the defect density in the irradiated cells is also found to increase with increasing electron fluence. This will be discussed further in section 2.3.

2.2 Results of the C-V Measurement

The results of C-V measurements on one-MeV electron irradiated GaAs cells for different fluences are presented in this section. To deduce the background dopant density from the C-V measurements, the data were converted into a C^{-2} vs V plot, and the results are displayed in Fig.2. From the slope of C^{-2} vs V plot the background dopant densities were determined for these cells, and the results are listed in table 1. Note that the carrier removal rate vs electron fluence can be determined from this background dopant density change with electron fluence.

The carrier removal in GaAs cells by one-MeV electron bombardment is caused by the isolated defects and the multiple charge clusters, but it is usually dominated by the isolated defect formation.[2] Thus, the total defect density determined from the DLTS measurement should be less than the carriers which were removed by the one-MeV electron irradiation. The carrier removal rate in n-GaAs irradiated at room temperature is independent of the initial carrier density and the chemical nature of the donor species.[3,4], nor it depends strongly on the conductivity type of the materials.[3] Relatively few workers who have studied both n- and p-type GaAs reported roughly the same carrier removal rate for both types. [5-7] Fig. 3 shows the carrier removal rate vs electron fluence for the undoped and Sn-

doped GaAs, as well as the results published recently by several authors. [5-9] The carrier removal rate shows a wide range of variation from 0.5 to 5 cm⁻¹. The reason for the large variation in the value of carrier removal rate observed by different researchers is not due to the impurity effects [3] rather than in the electron beam flux. It is important to point out that the large carrier removal rate is produced by large beam flux while small beam flux produces small carrier removal rate. [7,8,9] The possibility of a higher damage rate with a higher flux is suggested by Moore et al. [8] They measured the lattice disorder per implanted As atom for both monoatomic and diatomic implantation beams and found that in the diatomic case the two correlated As ions which dissociated at the surface create two to three times more damage per atom than do the isolated As ion tracks when the low electron beam was used. The simple defects are more important to the carrier removal than the cluster defects. The production of cluster defects will increase with electron energy and its effect on the carrier removal may become comparable with simple defects at about 50 MeV electron energy. [3]

2.4 Results of the DLTS Measurement

The DLTS thermal scans of electron traps for the one-MeV electron irradiated Sn-doped GaAs solar cells for different electron fluences are displayed in Fig.4. It is noted that no electron trap was observed in the unirradiated GaAs samples which is consistent with the results reported by several researchers [10-14] for the LPE GaAs. As for the one-MeV electron irradiated GaAs cells three electron traps with energies of Ec-0.31, 0.71 and 0.90 eV were observed in these samples, with Ec-0.71 eV electron trap being the dominant trap level. This electron trap has always been observed in the one-MeV electron GaAs and other particle bombardment. [3,7,13] From Fig.4 and table .1 it is noted that the general trend in defect production is toward deeper spectrum and higher defect density when the electron fluence increases from 1×10^{14} to 1×10^{16} e/cm². Lang et al [14] have investigated defects produced in GaAs by different particles such as 185 KeV O⁺, 1.8 MeV (alpha)⁺, 450 KeV p⁺ and the one-MeV electrons. He observed that the general trend is toward a broader and deeper level defect spectrum as the mass of the high-energy particle is increased. In general, one finds that the heavier the bombardment particles or the higher energy particles, the more complex deep-level defects would be produced.

For the 1×10^{15} e/cm² electron irradiated GaAs sample studied here, there are two electron traps observed with energies of Ec-0.71 and Ec-0.90 eV and densities of 1.1×10^{14} and 8.2×10^{13} cm⁻³, respectively. The Ec-0.90 eV electron trap was not observed in samples irradiated with other fluences, and the annealing of this trap was not dependent on the donor density according to Aukermen and Graft's data. [11]. Thus, it appears that this level does

not form defect complexes with the donor impurities during the annealing process. As for 5×10^{15} and 1×10^{16} e/cm^2 electron irradiated samples, the main electron traps are due to the $E_c - 0.31$ and $E_c - 0.71$ eV levels. The density of both traps was found to increase with increasing electron fluence. Lang et al [14] has observed the $E_c - 0.31$ eV electron trap and found that its energy remained constant with respect to the valence band edge by changing the x fraction of the $\text{Al}_x\text{Ga}_{1-x}\text{As}$ samples irradiated by one-MeV electrons. In an attempt to identify the physical origin of this electron trap, Lang et al [14] prepared GaAs samples with different crystal orientations. They found a higher value of defect concentration from the easy Ga atom sites and lower defect density from the hard Ga atom sites. Jaros and Brand [15] have also shown that for GaAs one should expect vacancy states to be strongly tied to the valence band edge. Based on the above results, it is reasonable to assign the $E_c - 0.31$ eV electron trap level to a Ga-vacancy defect.

The dominant hole trap observed in the one-MeV electron irradiated GaAs samples is due to the $E_v + 0.71$ eV level. This is shown in Fig.5. Density of this hole trap is also found to increase with increasing electron fluence. The defect parameters such as defect energy level and density as well as capture cross section are listed in table.1 for GaAs cells irradiated with one-MeV electrons. It is noted from table. 1 that the total defect density is lower than the total carriers removed by the one-MeV electrons. This implies that the one-MeV electron irradiation in GaAs cells would produce defect clusters in addition to the point defects such as vacancies or interstitials.

III. The $\text{Al}_x\text{Ga}_{1-x}\text{As}$ p-n junction solar cells

In this section, the results of our C-V and DLTS study on the grown-in defects in the $\text{Al}_x\text{Ga}_{1-x}\text{As}$ p-n junction cells are presented. Two alloy compositions with $x = 0.05$ and $x = 0.17$ were studied. The results showed that for x equal or less than five atomic percentage no measurable electron or hole traps were detected in these samples. In addition, the Auger analysis was performed on the $\text{Al}_{0.9}\text{Ga}_{0.1}\text{As}$ window layer of the GaAs solar cells to assess the compositions and surface contaminants in the $\text{Al}_x\text{Ga}_{1-x}\text{As}$ epilayer.

3.1 Auger Analysis of the $\text{Al}_x\text{Ga}_{1-x}\text{As}$ LPE layer

In this section, a brief description of the Auger Spectroscopy analysis on one $\text{Al}_x\text{Ga}_{1-x}\text{As}$ -GaAs solar cell is given. The intention is to estimate the atomic compositions in the $\text{Al}_x\text{Ga}_{1-x}\text{As}$ epilayer and to analyze the chemical contaminants at the surface of this window layer. A semi-quantitative Auger analysis was performed on the AlGaAs epilayer at the surface, $1/4$, $1/3$, $1/2$, $3/4$ depth of this layer and at the interface of

the metallurgical junction of AlGaAs/GaAs solar cell. Each layer was removed by the sputtering etch technique, and the atomic percentage of each chemical species was calculated from the Auger data. The results of this analysis are summarized in table.2. From the results, it is shown that at the surface of the AlGaAs window layer there is significant contaminants due to carbon and oxygen and a small fraction of nitrogen. These contaminants disappear after the second sputtering etch or at 1/4 depth into the epilayer. The Auger analysis also reveals that an abrupt junction exists between the AlGaAs window layer and the GaAs active layer. Finally, we notice that the atomic percentages for the $\text{Al}_x\text{Ga}_{1-x}\text{As}$ layer appear to be nonstoichiometry with 53 % for As and 47 % atomic percentage for Al plus Ga at the interface of the AlGaAs/GaAs junction. Thus, it is possible that grown-in defects in the $\text{Al}_x\text{Ga}_{1-x}\text{As}$ epilayer could be due to Ga- or Al-vacancy related defects, as is evidenced by the Auger analysis.

3.2 Results of the C-V and DLTS Measurements

The background dopant (Sn-doped) density was determined by the C-V measurements as described in section 2.2. The DLTS measurement was performed on $\text{Al}_x\text{Ga}_{1-x}\text{As}$ p-n junction cells with $x = 0.05$ and $x = 0.17$. The results showed that no measurable deep-level defects were detected in samples with x equal or less than 0.05, and two electron traps with energies of $E_c - 0.20$ and $E_c - 0.34$ eV were observed in cell with $x = 0.17$. It is noted that both of these two electron traps were not detected in the LPE GaAs or $\text{Al}_x\text{Ga}_{1-x}\text{As}$ layer with x less than 0.05. Thus, the two new electron traps that observed in the $\text{Al}_{0.17}\text{Ga}_{0.83}\text{As}$ p-n junction cell are primarily associated with the nonstoichiometric related native defects such as Al- or Ga- vacancy defects as pointed out in section 3.1. In order to verify our point of views we performed low temperature thermal annealing study on this sample at 250 °C for up to 100 minutes, and measured the defect density vs annealing times. Fig.6 shows the DLTS scans of the electron traps vs annealing times (250 °C annealing). The density of each electron trap vs annealing time is also shown in the same graph for comparison. It is noted that the annealing rate is faster for the shallower trap than the deeper trap. Since the density of each electron trap can indeed be reduced by the thermal annealing process and does decrease with increasing annealing time, it is obvious that both electron traps are not impurity related defects but rather than caused by the nonstoichiometric effects. It should be interested to see how the density of these electron traps will vary with the values of x toward higher Al contents. Further studies should be conducted to find out the functional dependence of the electron or hole traps vs the alloy composition, x , in the $\text{Al}_x\text{Ga}_{1-x}\text{As}$ epilayer. Table 3 lists the defect parameters for the two electron traps observed in the $\text{Al}_{0.17}\text{Ga}_{0.83}\text{As}$ p-n junction solar cell as determined by the DLTS measurements.

VI. Conclusions

Studies of deep-level defects induced by the one-MeV electron irradiation in GaAs solar cells irradiated at room temperature for four different electron fluences (i.e., 1×10^{14} , 1×10^{15} , 5×10^{15} , and 1×10^{16} e/cm²) and of grown-in defects in Al_xGa_{1-x}As p-n junction cells for different values of "x" have been carried out in this work. For the one-MeV electron irradiated GaAs solar cells, there are three main electron traps with energies of $E_c - 0.31$, $E_c - 0.71$, and $E_c - 0.90$ eV and densities in the 1×10^{13} to 4×10^{14} cm⁻³ range and one hole trap with energy of $E_v + 0.71$ eV observed in these samples. The density of each trap was found to increase with increasing electron fluence. Since all these traps are believed to be Ga-vacancy related defects (except the $E_c - 0.90$ eV electron trap), the low temperature thermal annealing or periodic thermal annealing process have shown to be highly effective for reducing the density of these traps, as being shown by our previous studies. [7,12]

Our Auger analysis of the Al_xGa_{1-x}As window layer of the GaAs solar cells reveals that there is a significant amount of the carbon and oxygen contamination near the surface of the AlGaAs layer, and the nonstoichiometric nature of the Al_xGa_{1-x}As (i.e., As > 50 % and (Al+Ga) < 50 %) was observed in this layer.

The DLTS analysis of the grown-in defects in the Al_xGa_{1-x}As p-n junction solar cells for two values of "x" shows that for samples with "x" less than 0.05 no measurable deep-level defects were detected, and for cell with "x" equal to 0.17 two electron traps with energies of $E_c - 0.20$ and $E_c - 0.34$ eV were observed. Thermal annealing performed at 250 °C for up to 100 minutes on the x = 0.17 cell shows that the density of both electron traps decreases with increasing annealing time; with the shallower electron trap annealed at a faster rate than the deeper trap. Both electron traps observed in this sample is believed to be Al-vacancy related defects but not impurity related defects as confirmed by the 250 °C thermal annealing experiment.

From our DLTS study of defects in GaAs and Al_xGa_{1-x}As p-n junction solar cells, it is clearly shown that all the defects observed are not impurity related defects rather than they are due to native defects such as vacancy or vacancy related defects. Thus, it is obvious that low temperature thermal annealing or periodic thermal annealing process is a viable technique to reduce the native defects as well as the radiation induced defects in both the GaAs and Al_xGa_{1-x}As p-n junction solar cells fabricated by the LPE growth method.

VI. References

1. S.S.Li, C.Y.Lin, S.M.Bedair and J.A.Hutchby, J. of Electronic Materials, V.11, p.273 (1982).
2. A.H. Kalma, R.A. Berger, C.J.Fisher and B.A. Green, IEEE Trans. on Nuclear Sciences NS-22, p.2277 (1975).
3. D.V.Lang, "Review of radiation-induced defects in III-V compounds", Inst. Phys. Conf. Serv. V.31, p.70 (1977).
4. A.H.Kalma and R.A.Berger, IEEE Trans. Nuclear Science NS-19, p.209 (1972).
5. P.L.Pegler, J.A.Grimshaw and P.C.Banbury, Rad. Effects., 15, p.183 (1972).
6. D.V.Lang and L. Kimerling, "Lattice defects in semiconductor" Inst. Phys. Conf. Serv. 23, p.581 (1975).
7. S.S.Li, W.L.Wang, R.Y. Loo and W.P.Rahilly, Solid State Electronics V.26, p.835 (1983).
8. J.A.Moore, G.Carter and A.W.Tinsley, Rad. Effects, 25, p.49 (1975).
9. L.C.Kimerling, P.Petroff and, H.J.Leamy, Appl.Phys. Lett. 28, p.297 (1976).
10. S.S.Li, W. L. Wang, P.W.Lai, R.Y.Loo, G.S.Kamath and R.C.Knechtli, IEEE Trans. Elect. Devices, ED-27, p.857 (1980).
11. L.W.Aukerman and R.D.Graft, Phys. Rev. 127, p.1576 (1962).
12. L.W. Aukerman, P.W.Davis, R.D.Graft and T.S.Shiliday J. Appl. Phys. 34, p.3590 (1963).
13. S.S. Li, W.L. Wang, R.Y. Loo and W.P. Rahilly, 16th IEEE Photovoltaic Specialists Conference, p.211 (1982).
14. D.V.Lang, R.A.Rogan and L.C.Kimerling, Phys. Rev. B, V10, p.1187 (1977).
15. M. Jeros and S. Brand, Phys. Rev. B.14, p.4494 (1976).
16. K. Thommen, Rad. Effect., vol.2, p. 201 (1971).
17. A. Kahan, L. Bouthillette, and H. M. DeAngelis, Radiation Effects in Semiconductors, (N. Y. Gordon and Breach) p.281 (1971).

ORIGINAL PAGE IS
OF POOR QUALITY

TABLE 1. - DEFECT PARAMETERS MEASURED IN ONE-
MeV ELECTRON IRRADIATED GaAs SOLAR CELLS*

Electron Fluence (e/cm ²)	Ed Se-doped (cm ⁻³)	Electron Traps Et-Et (eV)	Et (cm ⁻³)	Hole Traps Et-Et (eV)	Et (cm ⁻³)	dp (cm ²)
1x10 ¹⁴	4.4x10 ¹⁶	0.71	5.2x10 ¹³			
1x10 ¹⁵	4.2x10 ¹⁶	0.71 0.90	1.1x10 ¹⁴ 8.2x10 ¹³	0.71	5.7x10 ¹³	4x10 ⁻¹³
5x10 ¹⁵	4x10 ¹⁶	0.31 0.71	7.6x10 ¹³ 2.2x10 ¹⁴	0.71	7.8x10 ¹³	4x10 ⁻¹³
1x10 ¹⁶	3.1x10 ¹⁶	0.31 0.71	3.2x10 ¹⁴ 3.7x10 ¹⁴	0.71	2.2x10 ¹⁴	4x10 ⁻¹³

* One-MeV electron irradiation was performed at room temperature on these cells at AFMIL/APL.

TABLE 2. - AUGER SPECTROSCOPY ANALYSIS OF
Al_xGa_{1-x}As LPE WINDOW LAYER ON
ON GaAs SOLAR CELL

Location	Elements Found (Atomic %)					
	C	N	O	Ga	Al	As
Outer surface	21	0.2	19	11	34	17
First Auger scan after sputtering	4	-	10	7	35	45
2nd Auger scan after start sputt.	0.6	-	1	6	38	55
Ave. at 1/4 layer depth	-	-	-	11	36	53
Ave. at 1/3 layer depth	-	-	-	11	37	53
Average just before GaAs interface	-	-	-	11	37	53

* The above data are all in atomic percentage with accuracy within a factor of 2.

TABLE 3. - DEFECT PARAMETERS OF ELECTRON
TRAPS IN Al_xGa_{1-x}As P-N
JUNCTION SOLAR CELLS

SAMPLES COMPOSITION	DOPANT DENSITY (Se-doped)	ENERGY LEVEL	TRAP DENSITY
x (%)	(cm ⁻³)	Et-Et (eV)	(cm ⁻³)
5	4.6x10 ¹⁶	-	-
17	5.3x10 ¹⁷	0.20	5.9x10 ¹⁶
	"	0.34	5.1x10 ¹⁶

ORIGINAL PAGE IS
OF POOR QUALITY

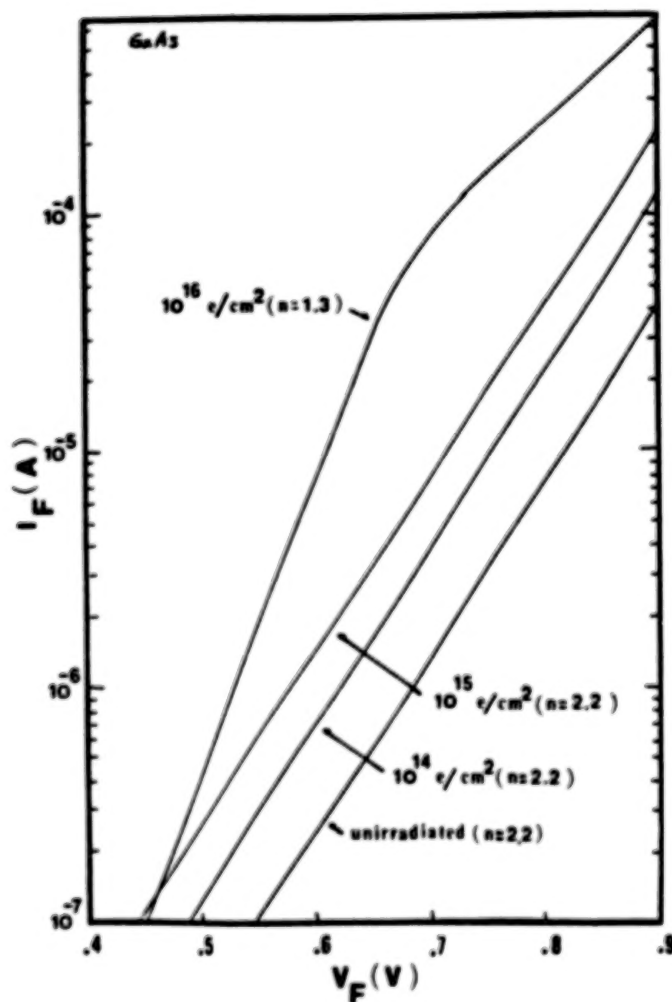


Figure 1. - Forward I-V curves of one-MeV electron irradiated GaAs solar cells with 0, 1×10^{14} , 1×10^{15} , and 1×10^{16} e/cm^2 fluence.

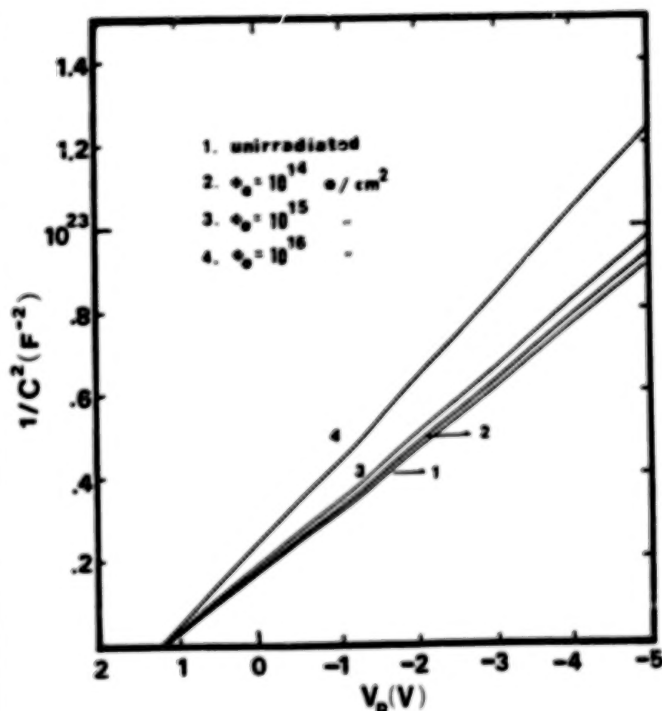


Figure 2. - $1/C^2$ versus V_R for GaAs solar cells irradiated by one-MeV electrons of different fluences.

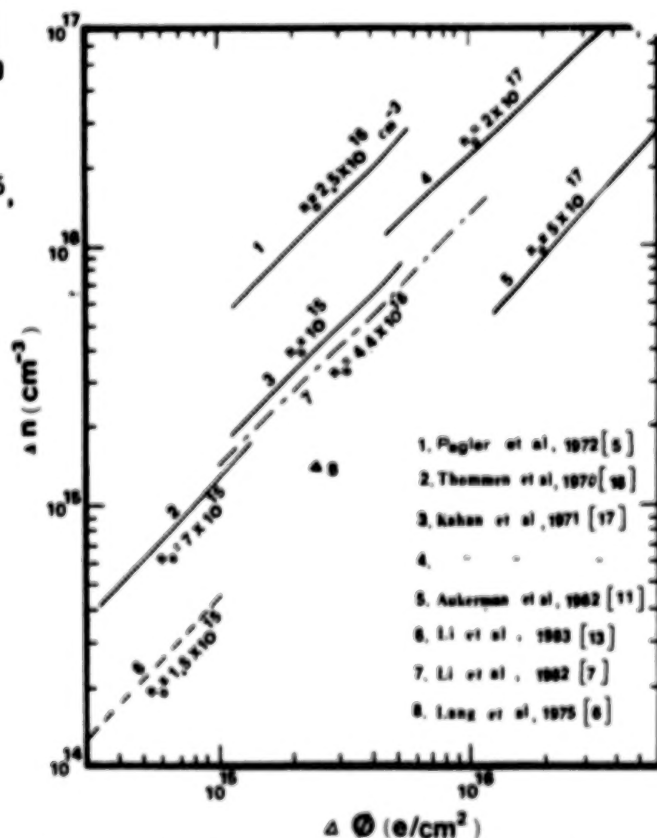


Figure 3. - Carrier removal rate versus electron fluence for one-MeV electron irradiated GaAs solar cells and published data for GaAs.

ORIGINAL PAGE IS
OF POOR QUALITY

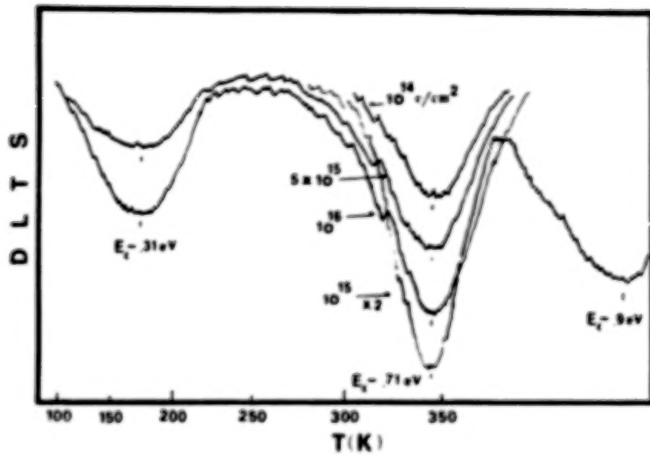


Figure 4. - DLTS scans of electron traps for one-MeV electron irradiated GaAs cells with different fluences.

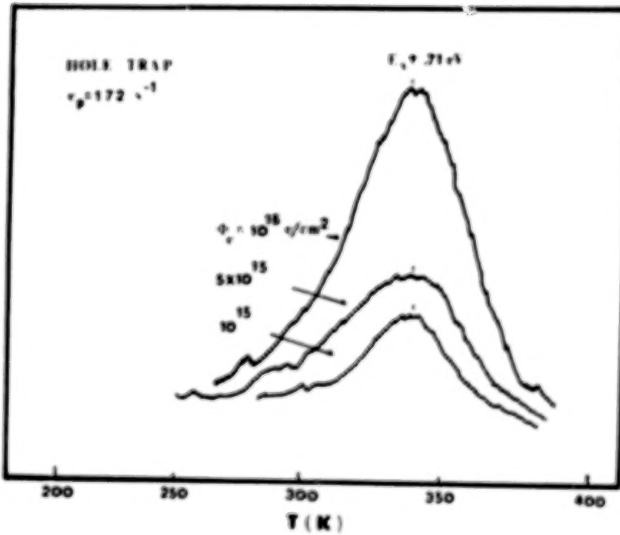


Figure 5. - DLTS scans of hole traps for one-MeV electron irradiated GaAs cells with different fluences.

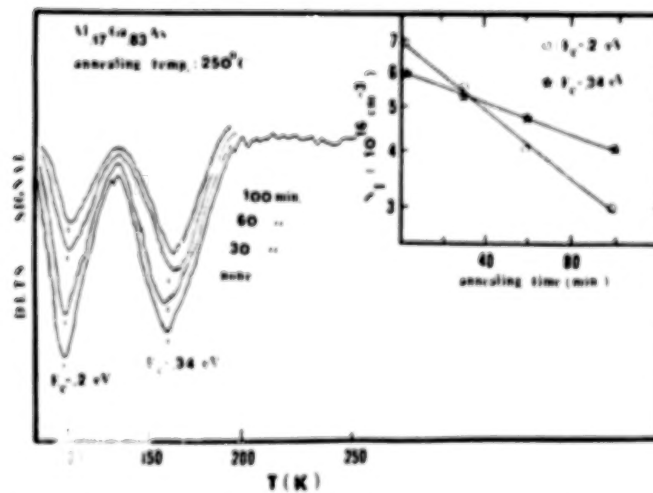


Figure 6. - DLTS scans of electron traps for $\text{Al}_{0.17}\text{Ga}_{0.83}\text{As}$ p-n junction solar cells annealed at 250°C for 30, 60, and 100 min. (Also shown is density of electron traps versus annealing time.)

N84
29322

UNCLAS

N84 29322

CELL AND DEFECT BEHAVIOR IN LITHIUM-COUNTERDOPED SOLAR CELLS

I. Weinberg, S. Mehta*, and C. K. Swartz
National Aeronautics and Space Administration
Lewis Research Center
Cleveland, Ohio

Previous extensive work on lithium-doped silicon solar cells was concerned with p^+/n cells in which lithium was used as the n -dopant (Ref. 1). On the present case, we concern ourselves with n^+/p cells in which lithium is introduced as a counterdopant, by ion-implantation, into the cells boron-doped p -region. Our objectives were to determine if the cells radiation resistance could be significantly improved by lithium counterdoping and to relate defect behavior to cell performance using deep level transient spectroscopy (DLTS).

EXPERIMENTAL DETAILS

The cells were fabricated from 1 ohm-cm boron-doped silicon. All cells were 2x2 cm, 250 micrometer thick with no anti-reflection coating. Introduction of lithium and cell junction formation were achieved by ion implantation. Electron beam annealing was used to selectively anneal the cells phosphorus doped n^+ region after ion implantation. Cell characteristics are shown in Table I. The lithium gradients listed in the Table were determined by four-point probe resistivity measurements at the cell back surface and C-V measurements at the cell junction to determine lithium concentrations. In all cases, the lithium concentrations were greatest at the cells back surface. After fabrication, the cells were progressively irradiated by 1 MeV electrons to a fluence of $10^{15}/\text{cm}^2$. Cell parameters were determined with a Xenon arc solar simulator while diffusion lengths were obtained using an X-ray excitation technique (Ref. 2). Using DLTS, defect concentrations, energy levels and capture cross sections were determined and the defects isochronally annealed. In order to minimize extraneous annealing, the cells were stored in liquid nitrogen before and after irradiation and measurement.

RESULTS

From Table I it is seen that the unirradiated lithium counterdoped cells yielded reduced maximum power (P_{max}) when compared to the 1 ohm-cm control cells. Since no attempt was made to optimize the counterdoped cells, it is not clear that lithium-counterdoping always reduces power output. However after irradiation, the effects of lithium on radiation induced defect formation increases the cells power output over that of the control cell. This is illustrated in Figure 1 where the lithium counterdoped cell clearly yields greater output at fluences greater than $7 \times 10^{12}/\text{cm}^2$. The superior radiation resistance of the counterdoped cells to 1 MeV electrons is further illustrated in Figure 2, where normalized P_{max} is plotted against fluence.

*NASA - Cleveland State University intern.

The tendency shown in Figures 1 and 2 was exhibited by all counterdoped cells fabricated from the 1 ohm starting material (Figure 3). Isochronal anneals of short circuit current are shown in Figure 4 where partial cell recovery is observed at 100°C. The DLTS spectrum of a lithium counterdoped cell is shown in Figure 5. Similar spectra were obtained for the 1 ohm-cm control cells. Energy levels and capture cross sections for the control and lithium counterdoped cells are shown in Table II while Figure 6 shows the isochronal annealing behavior of the defects in the lithium counterdoped cell.

DISCUSSION

Cell Behavior

The present results indicate a significantly increased radiation resistance for the lithium counterdoped cells when compared to the boron doped 1 ohm-cm control cell. This should be compared to the slight superiority found for lithium doped p⁺/n cells under beta irradiation (Ref. 3). It is also noted that the present cells show a much greater improvement in radiation resistance than the almost trivial increase we observed previously in 0.35 ohm-cm counterdoped cells prepared by diffusion technique (Ref. 4). The question of superior radiation resistance to 1 MeV electron irradiation being clearly established, we now turn our attention to defect behavior in these cells.

Defect Behavior

Examination of Table II clearly demonstrates that the lithium counterdoping results in an almost completely new set of defects, i.e., the defects at $E_v+0.23$, $E_v+0.33$, and $E_c-0.27$ eV present in the control cell are no longer detectable in the counterdoped cell. However, within experimental error (± 0.01 eV) the defect at $E_v+0.26$ eV can be considered as overlapping in energy the defect at $E_v+0.28$ eV in the counterdoped cell. The difference in capture cross section argues, however, for some change in this defect on counterdoping. From the preceeding, it is observed that counterdoping of silicon with lithium results in a different set of defects. However, very little is known concerning their structures. On the other hand, since more is known concerning the defects in boron-doped silicon, we can use this knowledge to obtain information regarding the behavior of lithium in altering the control cell defect structures.

Defect at $E_v+0.23$ eV

This defect has been unambiguously identified as the divacancy (Ref. 5 and Ref. 6). It has also been firmly established that lithium forms complexes with divacancies (Ref. 7). Hence, it is concluded that the defect at $E_v+0.23$ eV is altered on counterdoping by the complexing of lithium with divacancies.

Defect at $E_c-0.27\text{eV}$

The atomic constituency of this defect is unclear at present. However, there is general agreement that it contains boron (Refs. 6 and 8). It has also been well-established that lithium combines with boron (Ref. 9). We therefore conclude that the defect at $E_c-0.27\text{eV}$ is altered on counterdoping by the combination of lithium with boron.

Defect at $E_v+0.33\text{eV}$

This defect is sometimes called a carbon related defect (Ref. 8). It has been identified, alternately, as the vacancy-oxygen-carbon (V-O-C) complex (Ref. 6) or as a carbon interstitial-carbon substitutional (C_i-C_s) complex (Ref. 10). With respect to this latter identification, there is no evidence that lithium combines with carbon in silicon. However, the present data appears to indicate complexing with the $E_v+0.33$ defect, or its constituents. This rules out identification of this defect as $[C_i-C_s]$.

We now consider possible interactions with constituents of the assumed [V-O-C] complex. It has been established that lithium combines with oxygen in p-type silicon (Ref. 11) and single vacancies (Ref. 12). It is therefore possible that the lithium combined with either one or both of these defects to impede formation of the [V-O-C] complex. Interaction with [V-O-C] as a whole is ruled out because this defect is positively charged (Ref. 13). We thus speculate that counterdoping inhibits formation of the [V-O-C] defect by the interaction of lithium with oxygen and/or single vacancies.

Defect at $E_v+0.26\text{eV}$

A defect with energy level at $E_v+0.28\text{eV}$ has been identified as the carbon interstitial (Refs. 8 and 14). The present defect has an energy level which almost coincides with this value. However, the isochronal annealing data of Figure 6 rules out identification as the carbon interstitial in the counterdoped cells. This follows from the fact that the $E_v+0.28$ defect anneals out at 250°C in the counterdoped cell, while the carbon interstitial is known to disappear at $T < 100^\circ\text{C}$ (Refs. 8 and 14).

Summary of Defect Interactions

The available evidence indicates that lithium counterdoping alters the defects at $E_v+0.23$ and $E_c-0.27\text{eV}$ by combining with divacancies and boron. With respect to the defect at $E_v+0.33\text{eV}$, it is speculated that this defect is prevented from forming by the interaction of lithium with oxygen and/or single vacancies. The fact that lithium does not complex with carbon rules out the identification of this defect as the carbon interstitial-carbon substitutional pair in the boron doped control cell. From the preceding, we conclude that the increased radiation resistance of the lithium counterdoped cells is due to the complexing of lithium with divacancies and boron. It is also speculated that complexing with oxygen and single vacancies also contributes to the increased radiation resistance.

Isochronal Annealing

The annealing behavior of the defect at $E_v+0.43\text{eV}$ (Fig. 6) correlates with the isochronal annealing of I_{sc} . The most striking feature is the minimum in defect concentration corresponding to a rise in I_{sc} at 100°C . In general, an increase in the concentration of this defect accompanies decreased cell output while decreased concentration corresponds to increased cell output. It is noted that this is the only observed defect which influences cell output in this manner. We therefore conclude that the defect at $E_v+0.43\text{eV}$ is dominant in decreasing cell output as a result of the 1 MeV electron irradiation.

CONCLUSIONS

As a result of this research, it is concluded that

- Lithium counterdoping significantly increases the radiation resistance of 1 ohm-cm boron doped n^+/p silicon solar cells.
- Performance of the counterdoped cells can be improved by annealing at 100°C .
- In the counterdoped cells, isochronal annealing behavior of the deep level defects indicate that the defect at $E_v+0.43\text{eV}$ is the major defect which decreases cell output under 1 MeV electron irradiation.
- Lithium counterdoping alters defect structures originally present in the boron-doped control cells by combining with boron and vacancies and possibly with oxygen and single vacancies.

REFERENCES

1. F. A. Berman, "Effects of Lithium Doping on the Behavior of Silicon Solar Cells," JPL Technical Report No. 32-1514, 1971 (NASA CR-116793).
2. W. Rosenzweig, "Diffusion Length Measurements by Means of Ionizing Radiation." Bell System Tech. J, Vol. 41, pp. 1573-1588 (1962).
3. H. Y. Tada, J. R. Carter, Jr., B. E. Anspaugh, and R. G. Downing, "Solar Cell Radiation Handbook," Third Edition, JPL Publication 82-69, pp. 341-342 (1982).
4. A. M. Hermann, C. K. Swartz, H. W. Brandhorst, Jr., and I. Weinberg, 14th IEEE Photovoltaic Specialists Conference, pp. 840-846 (1980).
5. C. D. Watkins and J. W. Corbett, "Defects in Irradiated Silicon: Electron Paramagnetic Resonance of the Divacancy," Phys. Rev. 138A, pp. 543-555 (1966).
6. P. M. Mooney Et. Al., "Defect Energy Levels in Boron-Doped Silicon Irradiated with 1-MeV Electrons," Phys. Rev. B, 15, pp. 3836-3843 (1977).
7. R. C. Young, J. W. Westhead, and J. C. Corelli, "Interaction of Li and O with Radiation-Produced Defects in Si," J. Appl. Phys. Vol. 40, pp. 271-278 (1969).
8. H. M. DeAngelis and P. J. Drevinsky, "Defects in Electron-Irradiated, Gallium-Doped Silicon," Appl. Phys. Lett. 42, pp. 613-615 (1983).
9. R. C. Newman, "Infra-Red Studies of Crystal Defects," pp. 108-113, Taylor and Francis, London (1973).
10. L. C. Kimerling, "Defect States in Electron Bombarded Silicon: Capacitance Transient Analysis," Radiation Effects in Semiconductors, Conference Series No. 31, pp. 221-230, Institute of Physics, London (1977).
11. E. M. Pell, "Study of Li-O Interaction in Si by Ion Drift," J. Appl. Phys. 32, pp. 1048-1051 (1961).
12. J. A. Naber, H. Horiye, and B. C. Passenheim, "Lithium - An Impurity of Interest in Radiation Effects of Silicon," Radiation Effects, Vol. 8, p. 239-244 (1971).
13. Y. H. Lee, J. W. Corbett, and K. L. Brower, "EPR of a Carbon-Oxygen-Vacancy Complex in Irradiated Silicon," Phys. Stat. Solids (a), Vol. 41, pp. 637-647 (1977).
14. G. D. Watkins and K. L. Brower, "EPR Observation of the Isolated Interstitial Carbon Atoms in Silicon," Phys. Rev. Lett. 36, pp. 1324-1332 (1976).

TABLE I. - CELL CHARACTERISTICS

CELL	RESISTIVITY*	Li GRADIENT (cm^{-4})	I _{sc} (mA)	V _{oc} (mV)	P _{MAX} (mW)	FF %
CONTROL	1	-	97.1	595	44	76.1
Z-10	1.8	1.6×10^{17}	98.3	540	39.5	74.4
Y-11	1.7	5.2×10^{16}	100.4	494	33	66.5
Z-3	1.7	2.2×10^{17}	100.8	508	36.2	70.7
Y-6	1.5	2.6×10^{16}	96.2	541	39.8	76.4
Z-12	1.7	2.1×10^{17}	101.3	505	36.5	71.3
Y-7	1.4	1.2×10^{17}	100.1	555	41.6	74.9

* EXCEPT FOR CONTROL: MEASURED AT BACK CONTACT AFTER INTRODUCTION OF LITHIUM.

ALL CELLS 2x2 CM, 250 μM THICK: NO AR COATING

TABLE II. - ENERGY LEVELS AND CAPTURE CROSS SECTIONS

		1 OHM-CM BORON DOPED				1.8 OHM-CM Li COUNTERDOPED			
ENERGY LEVEL (eV)		$E_V + .23$	$E_V + .26$	$E_V + .33$	$E_C - .27$	$E_V + .28$	$E_V + .43$	$E_V + .52$	$E_C - .46$
CAPTURE CROSS SECTION (cm^2)	σ_P	3×10^{-16}	4×10^{-17}	2×10^{-16}		8.5×10^{-16}	2×10^{-13}	1×10^{-14}	
	σ_N				3×10^{-13}				9.3×10^{-18}

ORIGINAL PAGE IS
OF POOR QUALITY

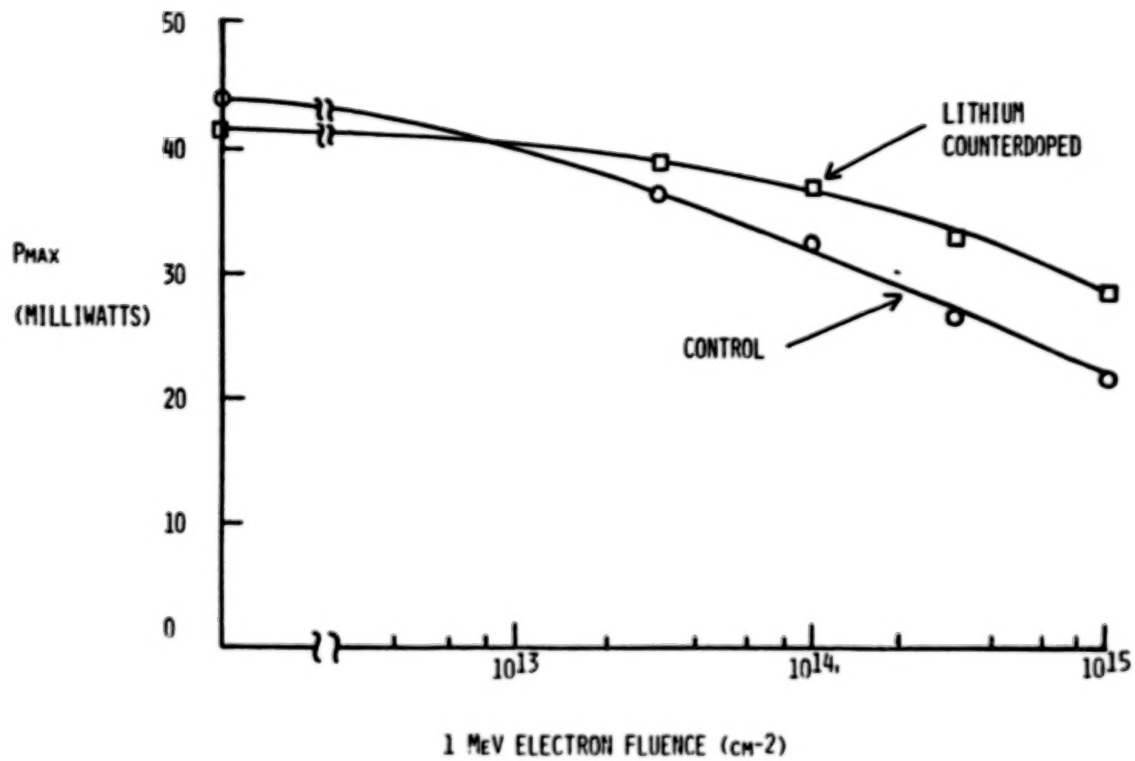


Figure 1. - P_{max} versus 1-MeV electron fluence.

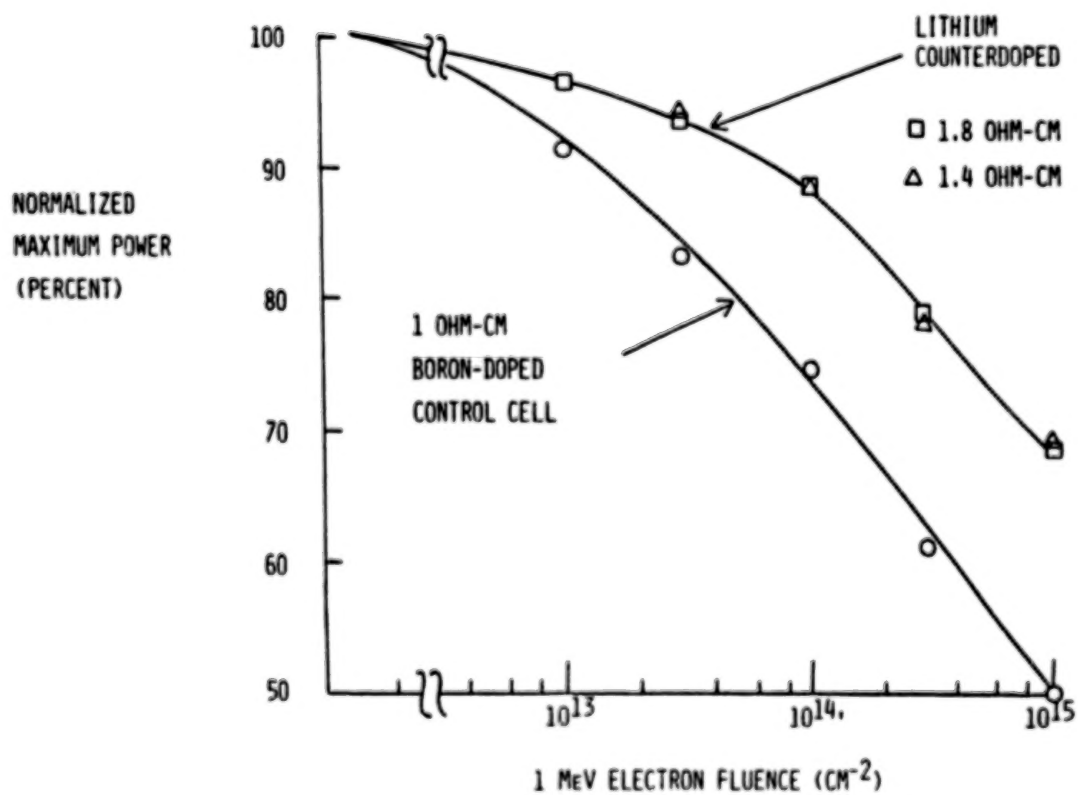


Figure 2. - Normalized maximum power versus 1-MeV electron fluence.

ORIGINAL PAGE IS
OF POOR QUALITY

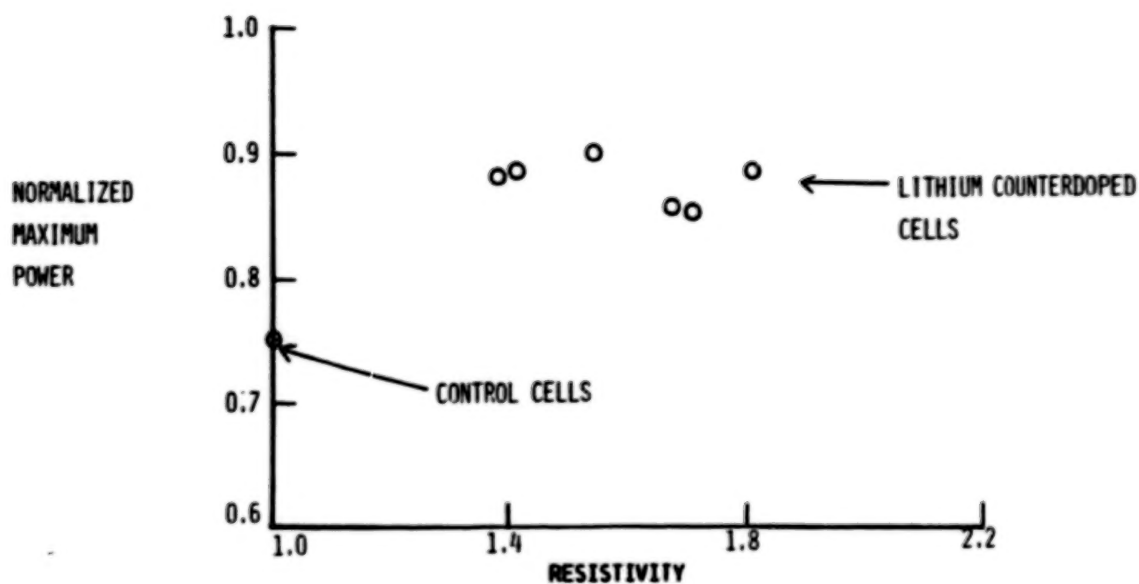


Figure 3. - Normalized maximum power versus resistivity.

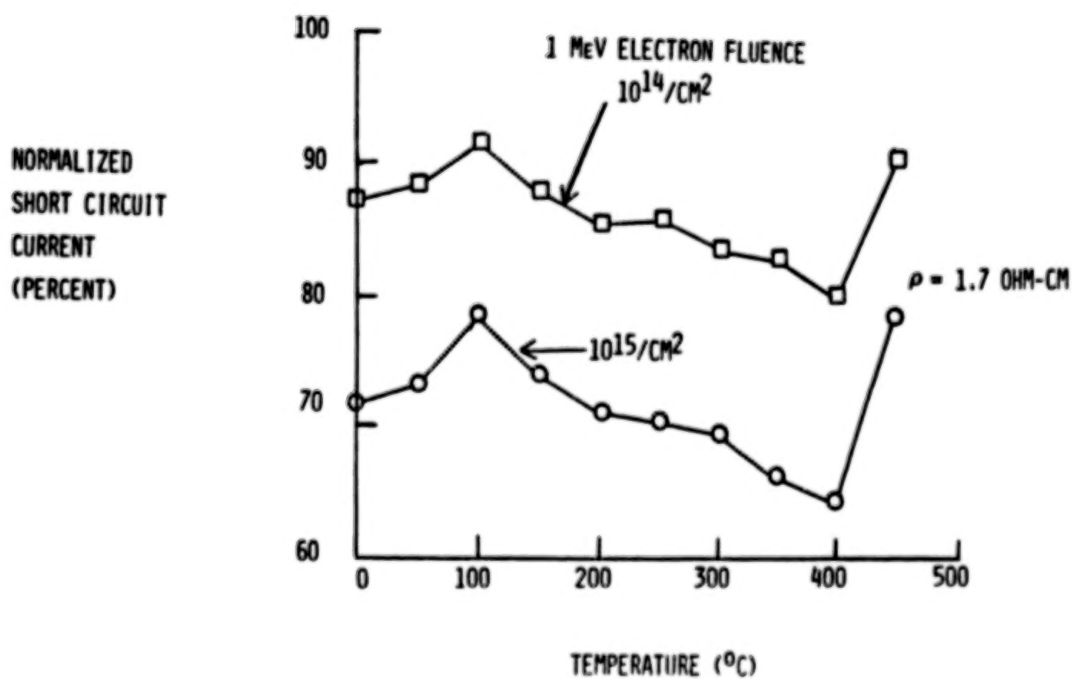


Figure 4. - Isochronal anneal of lithium-counterdoped silicon cells.

ORIGINAL PAGE IS
OF POOR QUALITY

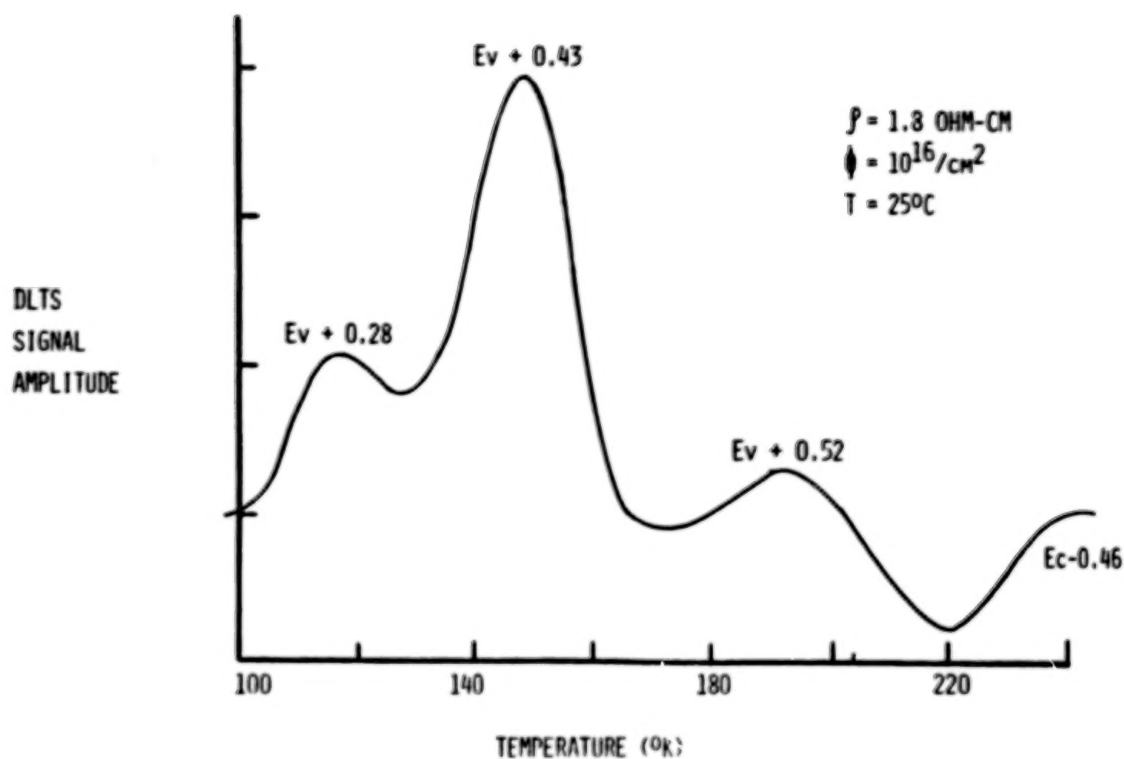


Figure 5. - DLTS spectrum of lithium-counter-doped silicon cells after 1-MeV electron irradiation.

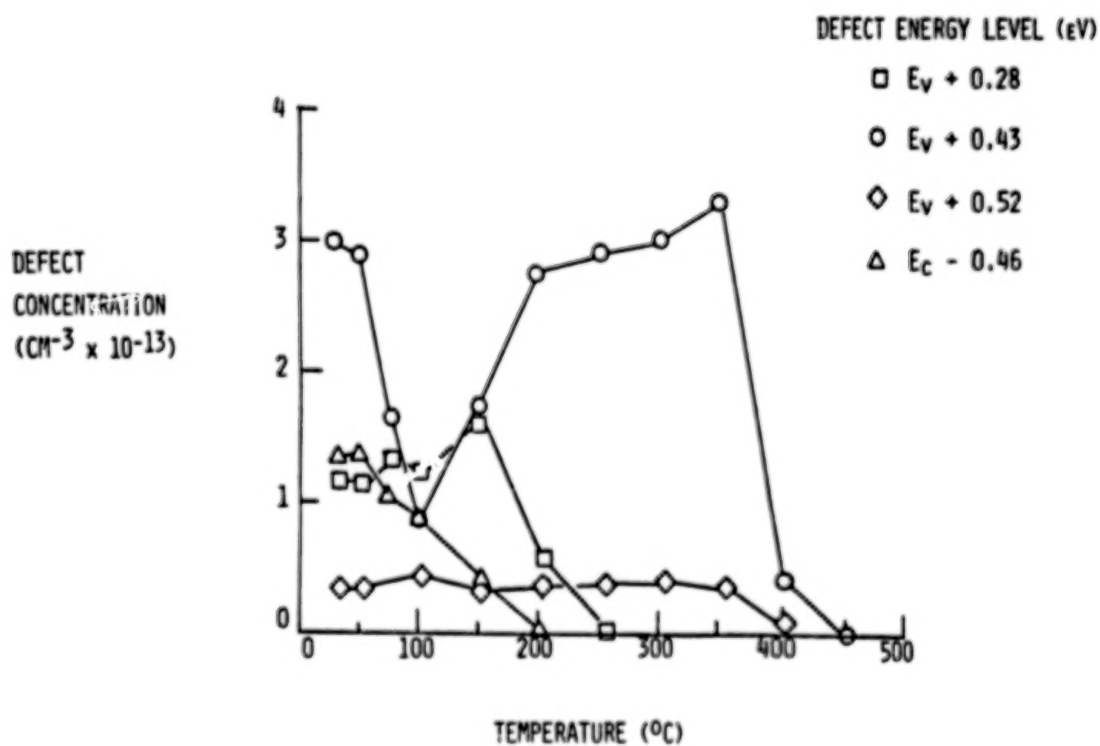


Figure 6. - Isochronal anneal of defects in lithium-counter-doped silicon solar cells using DLTS.

N84
29323

UNCLAS

DEFECT INTERACTIONS IN GaAs SINGLE CRYSTALS

H. C. Gatos and J. Lagowski
Massachusetts Institute of Technology
Cambridge, Massachusetts

The two-sublattice structural configuration of GaAs and deviations from stoichiometry render the generation and interaction of electrically active point defects (and point defect complexes) critically important for device applications and very complex. Of the defect-induced energy levels, those lying deep into the energy band are very effective lifetime "killers." The level 0.82 eV below the conduction band, commonly referred to as EL2, is a major deep level, particularly in melt-grown GaAs. We have shown that this level is associated with an antisite defect complex ($\text{As}_{\text{Ga}} - \text{V}_{\text{As}}$). We have further determined possible mechanisms of its formation and its annihilation.

N84
29324

UNCLAS

N84 29324

EQUIVALENT ELECTRON FLUENCE FOR SOLAR PROTON DAMAGE IN
GaAs SHALLOW JUNCTION CELLS

John W. Wilson
NASA Langley Research Center
Hampton, Virginia

L. V. Stock
Old Dominion University
Norfolk, Virginia

The short-circuit current reduction in GaAs shallow junction heteroface solar cells has been calculated according to a simplified solar cell damage model in which the nonuniformity of the damage as a function of penetration depth is treated explicitly. Although the equivalent electron fluence was not uniquely defined for low-energy monoenergetic proton exposure, it is found that an equivalent electron fluence can be found for proton spectra characteristic of the space environment. The equivalent electron fluence ratio has been calculated for a typical large solar flare event for which the proton spectrum is

$$\phi_p(E) = A/E \text{ (p/cm}^2\text{)}$$

where E is in MeV. The equivalent fluence ratio is a function of the cover glass shield thickness or the corresponding cutoff energy E_c . In terms of the cutoff energy, the equivalent 1 MeV electron fluence ratio is given as

$$r_p(E_c) = 10^9/E_c^{1.8}$$

where E_c is in units of KeV.

INTRODUCTION

It is customary in protection from a mixed radiation environment to develop concepts under which effects of radiations of different quality may be combined to ascertain the total environmental effect on device

performance.¹ From an electronic device point of view, the equivalent electron fluence is usually employed to determine the combinational rule. The equivalent electron fluence is defined as that fluence of electrons of fixed energy (usually 1 MeV) which produces the same effect on the device performance as a particle fluence of a particular type, energy and fluence level. Therefore, the fluence of electrons ϕ_e equivalent to a fluence of protons $\phi_p(E_p)$ of energy E_p is given by

$$R_e[\phi_e] = R_p[\phi_p(E_p)] \quad (1)$$

where R_e and R_p are the corresponding device response functions for electrons and protons. If relation (1) is satisfied, then the equivalent fluence ratio may be defined as

$$r_p(E_p) = \phi_e / \phi_p(E_p) \quad (2)$$

where the usefulness of the concept requires that $r_p(E_p)$ not depend on the magnitude of $\phi_p(E_p)$. The combined effects of electron and proton exposure are then taken as

$$R_{tot}[\phi_p(E_p), \phi_e] = R_e[\phi_e + r_p(E_p)\phi_p(E_p)] \quad (3)$$

where ϕ_e and $\phi_p(E_p)$ are the mixed environmental components.

The traditional understanding of equation (3) comes from the recognition of the role of the minority carrier diffusion length. The diffusion length is related to defects within the cell by

$$L^{-2} = L_0^{-2} + K_e \phi_e + K_p(E_p)\phi_p(E_p) \quad (4)$$

from which the equivalent fluence ratio is found from the damage coefficients as

$$r_p(E_p) = K_p(E_p)/K_e \quad (5)$$

Implicit in equation (4) is the assumption that the cell averaged diffusion length L is sufficient to define cell response. It was found experimentally in Si solar cells that the cell averaged diffusion length was not sufficient to define cell response for low energy proton damage for which

there is appreciable spatial nonuniformity in defect production within the active region.² Further studies in hetero-face shallow junction GaAs solar cells found an explicit dependence of the equivalent fluence ratio on the proton fluence level at low proton energies where spatial variations in defect production are present in the active region of the cell.³ In general, this implies that damage estimates and experimental testing must adequately simulate the mixed components within the environment. These results were derived on the basis of monoenergetic normal incident proton beams. The angular isotropy and continuous energy spectrum may yet make an equivalent electron fluence test meaningful for the space environment. This will now be considered within the context of a previously derived model^{3,4} as applied to solar flare produced particles.

SOLAR COSMIC RAYS

According to Webber⁵, the solar cosmic ray omnidirectional proton fluence (p/cm^2) per year is approximately

$$\Phi_p(>E_p) = 10^{9+0.02S} E_p^{-2} \quad (6)$$

where S is the yearly average sunspot number. A detailed study by Foelsche⁶ yields

$$\Phi_p(>E_p) = 5 \times 10^{11} E_p^{-1} \quad (7)$$

for low energy protons during the year 1960. The spectrum of Foelsche is used in the present study.

The defect areal density produced at a depth x within the solar cell is given by

$$D_c(x) = 2\pi \int_0^\infty dE_0 \int_0^1 d(\cos \theta) \{D(E_0) - D[E_0(x/\cos \theta)]\} \Phi_p(E_0) \quad (8)$$

where $D(E_0)$ is the total number of defects formed if the proton stops in the material, E_0 is the initial proton energy, $E_0(x/\cos \theta)$ is the residual proton energy after traveling a distance $x/\cos \theta$, θ is the colatitude and $4\pi\Phi_p(E_0)$ is the differential omnidirectional proton fluence spectrum incident on the cell face.

SHORT CIRCUIT CURRENT REDUCTION

The short circuit current may be approximated by

$$i_{sc} = \int_0^a \eta_c(x) [1 - F(x)] \rho(x) dx \quad (9)$$

where a is the depth of the active region, $\eta_c(x)$ is the unirradiated charge collection efficiency, $F(x)$ the fractional current loss due to irradiation and $\rho(x)$ is the photoabsorption density for forming electron-hole pairs in the cell. It has been shown that

$$F(x) = 1 - E_2[6 \sigma_r |D_c(x_j) - \eta_c(x)|] \quad (10)$$

where $E_2(Z)$ is the exponential integral of order 2, σ_r is the average recombination cross section at a defect site⁴, and x_j is the junction depth in the cell. The remaining short circuit current ratio is approximately

$$i_{sc}/i_{sc0} = 1 - \left[\int_0^a F(x) \rho(x) dx / \int_0^a \rho(x) dx \right] \quad (11)$$

where it is assumed $\eta_c(x)$ is nearly constant over the cell active volume. The remaining short circuit current was evaluated using equations (8), (10), and (11) with modification of the proton spectrum by first passing it through the equivalent of a thickness of cover glass. The form of the spectrum was taken as

$$\Phi_p(>E_p) = A/E_p \quad (12)$$

where A is numerically the fluence with energy greater than 1 MeV. Results are shown in figure 1 as a function of cover glass thickness for a 0.5 μm junction depth and 0.4 μm $Al_xGa_{1-x}As$ window.

The remaining short circuit current has been evaluated for normal incident 1 MeV electrons³ with results shown in figure 2. The equivalent electron fluence has been calculated for each cover glass thickness as given in Table I and is found to be independent of the damage level. Results are expressed as the equivalent fluence ratio

ORIGINAL PAGE IS
OF POOR QUALITY

$$r_p(E_c) = \phi_e / \phi_p(>1 \text{ MeV}) \quad (13)$$

where ϕ_e is the equivalent electron fluence level. Results are shown in the table along with the corresponding cutoff energies for each cover glass thickness.

TABLE I. EQUIVALENT FLUENCE RATIO $r_p(E_c)$ AS A FUNCTION OF COVER GLASS THICKNESS t AND THE CORRESPONDING CUTOFF ENERGY E_c

$t, \mu\text{m}$	E_c, KeV	$r_p(E_c)$
2.5	310	34,000
5.0	550	13,000
7.5	750	7,400
10.0	950	4,600
15.0	1250	2,800
20.0	1550	1,900

It is evident from table I that the equivalent fluence ratio can be written as a function of cutoff energy as

$$r_p(E_c) = 10^9 / E_c^{1.8} \quad (14)$$

where E_c has units of KeV. This result is clearly applicable to all omnidirectional proton spectra of the form in equation (12) and it remains to be seen if equation (14) has a more general validity.

REFERENCES

1. H. J. Tada; and J. R. Carter: Solar Cell Handbook. NASA, JPL Publ. 77-56, 1977.
2. W. C. Cooley; and M. J. Barrett: Space Environmental Effects on Solar Cell Power Systems. NASA Cr-92675, 1968.
3. J. W. Wilson; J. J. Stith; and G. H. Walker: On the Validity of Equivalent Electron Fluence for GaAs Solar Cells. Proceedings of the 1982 IEEE Photovoltaics Specialist Conference, San Diego, California, September 1982.

ORIGINAL PAGE IS
OF POOR QUALITY

4. J. W. Wilson; G. H. Walker, R. A. Outlaw; and L. V. Stock: A Model for Proton Irradiated GaAs Solar Cells. Proceedings of the IEEE Photovoltaics Specialist Conference, San Diego, California, September 1982.
5. W. R. Webber: An Evaluation of Solar Cosmic Ray Events During Solar Minimum. Boeing Report D2-84274-1, June 1966.
6. T. Foelsche: Specific Solar Flare Events and Associated Radiation Doses. ASTM Special Publication No. 363, 1964.
7. J. W. Wilson; J. J. Stith; and L. V. Stock: A Simple Model of Space Radiation Damage in GaAs Solar Cells. NASA TP- , 1983.

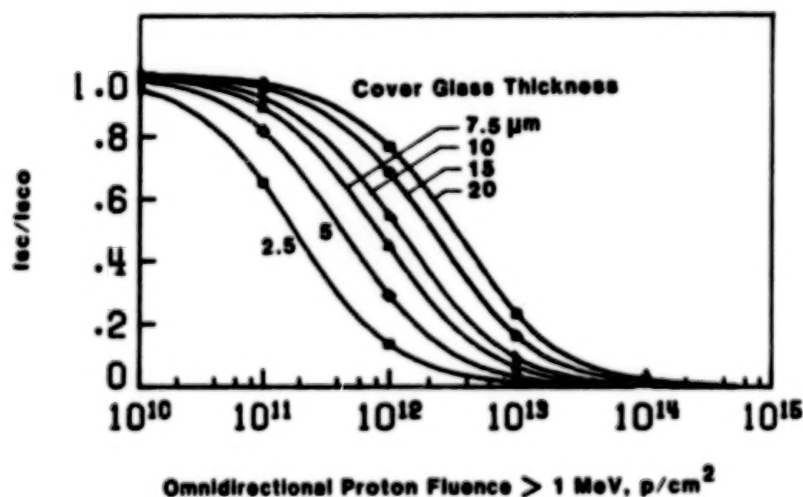


Figure 1. - Short circuit current remaining after solar cosmic ray damage for various cover glass shield thicknesses.

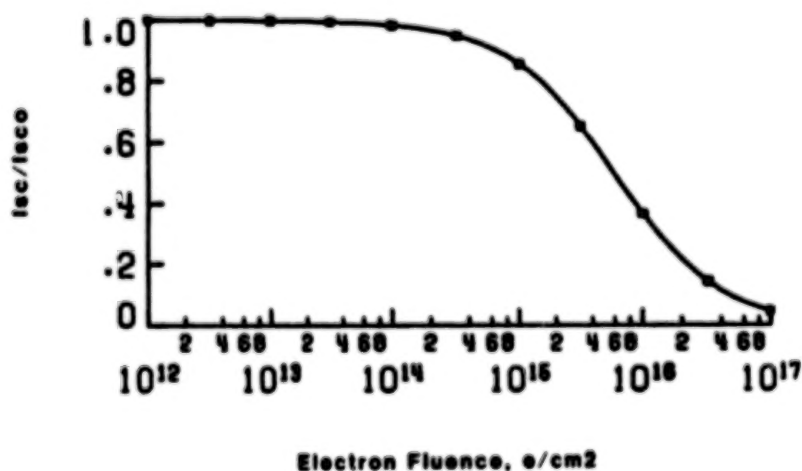


Figure 2. - Short circuit current remaining after 1-MeV electron exposure.

N84
29325

UNCLAS

N84 29325

RESEARCH DIRECTIONS AND PROGRESS IN SERI
ADVANCED HIGH EFFICIENCY CONCEPTS PROGRAM

John P. Benner and Lee A. Cole
Solar Energy Research Institute
Golden, Colorado

This program supports research on novel solar cell designs and materials with the objective of achieving the maximum attainable photovoltaic conversion efficiencies. This research is directed toward laboratory demonstrations of solar cells of greater than 30% efficiency under concentrated sunlight and thin film solar cells with one sun efficiencies of 17 to 20%. These demonstrations are necessary intermediate steps towards the realization of very high efficiency, multi-bandgap, thin-film solar cells.

Conversion efficiencies above 30% could be achieved by a cascade multijunction cell consisting of a high bandgap (1.7 eV) cell coupled optically and electrically on top of a lower bandgap (1.1 eV) cell. Use of a tunnel junction, fabricated in the high bandgap material, for the coupling layer has received the most study. Recent improvements in peak currents of this interconnect are quite promising. However, this cell structure poses difficult problems for materials fabrication as a result of the combined requirements of choice of bandgaps, low defect density material, and high doping densities. Recent improvements in the quality of materials and newly proposed cell structures which may simplify fabrication are significant steps in the development of the multijunction concentrator solar cell.

Several techniques are under study for preparation of thin films of III-V semiconductors for use in large area solar cells. Single crystal films have been prepared by heteroepitaxy on silicon and by separation from reusable substrates. Continued work with polycrystalline GaAs has yielded films with millimeter size grains. Further progress with thin film GaAs may lead to 17-20% efficient modules. If multijunction technology can be adapted to large area cells, module efficiencies may be improved beyond 20%.

Active Cells in Lattice Mismatched Ternary Compounds

- Quaternaries only in transparent grading layers and windows

Control Location of Defects

- Grading, Controlled Strain or Superlattices
- Separated films

Bottom Cells GaInAs, GaAsSb or Silicon

Top Cells GaAlAs or GaAsP

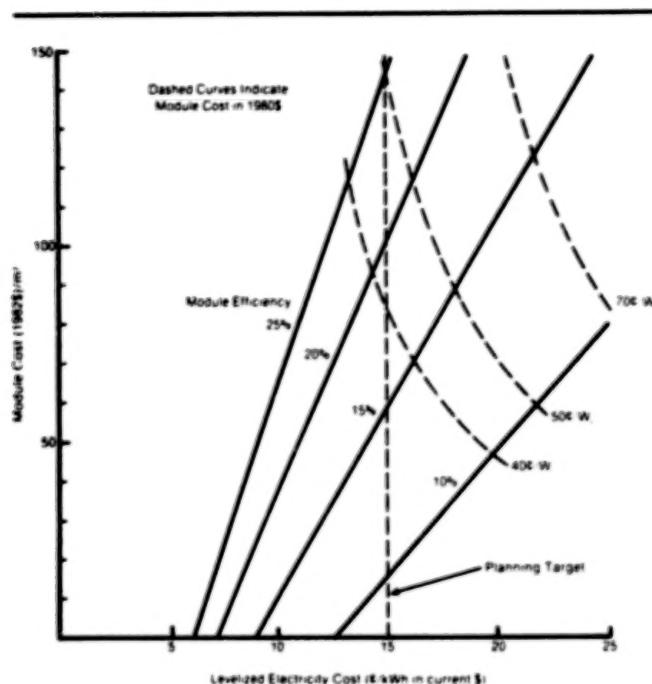
- GaInP eliminated due to susceptibility to even low defect densities

Novel Cell Structures

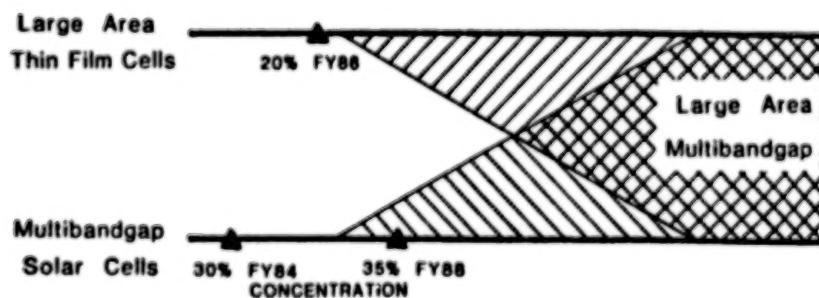
- Graded bandgaps - 3 terminal
- Metal interconnects - 4 terminal

Advanced high efficiency program goals.

ORIGINAL PAGE 19
OF POOR QUALITY



Module costs and efficiencies versus 30-year levelized electricity costs for flat plate photovoltaic systems. (\$50/m² area-related BOS.)



Advanced high efficiency program direction.

N84
29326

UNCLAS

N84 29326

OPTIMAL DESIGN OF HIGH-EFFICIENCY SINGLE-JUNCTION AND TANDEM CONCENTRATOR
SPACE CELLS AT 80° C AND 100 SUNS*

John C. C. Fan and B. J. Palm
Massachusetts Institute of Technology
Lexington, Massachusetts

Computer analysis has been used to determine the AMO conversion efficiency of single-junction crystalline cells, two-cell and three-cell crystalline tandem structures operating under 100 suns and at 80°C. For optimally designed devices, the calculated efficiencies are 24% for single-junction cells, 33-35% for two-cell tandem structures, and 37-39% for three-cell tandem structures. Practical efficiencies are expected to be about 15 relative percentage points lower in each case.

INTRODUCTION

Recently, there is much interest in using concentrator cells in space, partly for economic reasons but mostly because of the potential higher resistance of concentrator modules to radiation. One particularly attractive scheme is to use miniaturized Cassegrainian concentrating optics (ref. 1,2). Under such optics, it has been estimated that the optimal operating conditions for such cells in space are under 100 suns and at 80°C.

In the present study, we have calculated the performance of single-junction crystalline cells, two-cell and three-cell crystalline tandem structures operating under 100 suns and at 80°C. In making the calculations we have made the basic assumption that the material quality of the crystalline materials of all energy gaps is equal to that of the best GaAs and Si so far prepared. Using the procedure outlined in the Appendix, we have determined the optimal energy gaps for the component cells in each type of structure. For optimally designed devices, the calculated AMO, 100-sun efficiencies for operation at 80°C are 24% for single-junction cells, 33-35% for two cell tandem structures, and 37-39% for three-cell tandem structures. Practical efficiencies are expected to be about 15 relative percentage points lower in each case. As in the case of ~~see sun~~ calculations of crystalline/crystalline (ref. 3), amorphous/amorphous (ref. 4), amorphous/crystalline (ref. 5) tandem structures, there are advantages in using a four-terminal structure rather than a two-terminal structure, because the former yields slightly higher conversion efficiencies, and efficiencies are less sensitive to variations in energy gaps, radiation damage coefficients and operating temperatures.

*This work was sponsored by the National Aeronautics and Space Administration and the Department of the Air Force.

SINGLE-JUNCTION CONCENTRATOR CELLS

Figure 1 shows the calculated AMO conversion efficiencies at 100 suns as a function of energy gap (E_g) for single-junction cells operating at 80°C. (For

SINGLE JUNCTION CRYSTALLINE CELLS

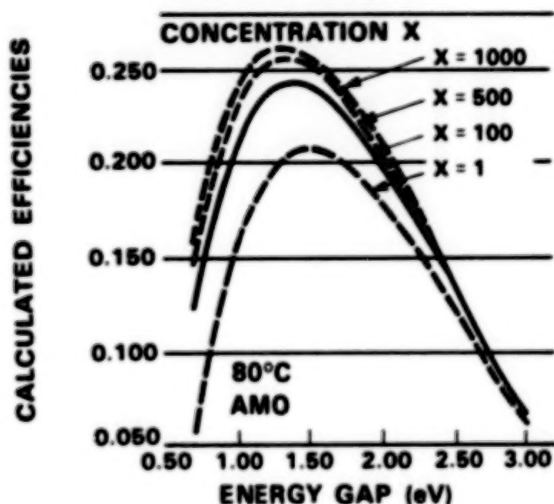


Fig. 1. Calculated AMO conversion efficiencies at 1 sun, 100-sun, 500-sun, and 1000-sun concentrations of single-junction solar cells made of materials having various bandgap energies. The cells are at an operating temperature of 80°C.

comparison, the calculated efficiencies for 1 sun, 500 suns and 1000 suns are also included.) For single-junction cells, the highest calculated efficiencies are obtained for energy gaps of about 1.40 eV, for which the calculated values are 24.3%. (Note, the optimal energy gaps shift to lower energies with increasing concentration, and substantial gains in conversion efficiencies can be obtained with modest concentration.) Gallium Arsenide (GaAs), which has an energy gap of about 1.40 eV (ref. 6) at 80°C, is the ideal material for single-junction cells, with practical AMO efficiencies of about 20-21%. The reduction in efficiency from the calculated value occurs mainly because our model does not include contact shading losses and because actual quantum efficiency and fill factor values of the cells are often lower than the calculated ones. Therefore, to achieve conversion efficiencies much above 20%, a different strategy — the utilization of tandem structures rather than single-junction cells — should be used.

TANDEM CONCENTRATOR CELLS

In the tandem configuration, solar cells with different energy gaps are stacked in tandem so that the cell facing the sun has the largest energy gap. This top cell absorbs the incident photons with energies equal to or greater than its energy gap and transmits the less energetic photons to the cells below. The next cell in the stack absorbs the transmitted photons with energies equal to or greater than its energy gap and transmits the rest downward in the stack, etc. In principle, any number of cells can be used in tandem. In practice, system considerations and economic reasons greatly affect the number of component cells used.

The design of tandem cells is considerably more complex than that of single-junction cells. For example, since the upper cells must transmit the photons with less energy than their respective bandgaps, their back contacts cannot

be continuous metal layers, which are used for this purpose in single-junction cells. If the cells in a stack are connected separately, different external load circuits must be provided for each cell. If instead the cells are connected in series, only one external load is used, but for maximum efficiency the thickness and bandgaps of the individual cells must be adjusted so that the photocurrents in all the cells are equal.

Two-Cell Tandem Structures

The simplest type of tandem structure consists of two cells, which can be connected to form either two-, three- or four-terminal devices. Owing to the serious restrictions (ref. 3) on connecting a number of three-terminal cells together for high-voltage operation, they will not be discussed further.

For the two-terminal (series-connected) structure, because of the requirement for photocurrent matching, the allowable range of optimal energy gap combinations is very narrow, as shown in Fig. 2, which shows AMO, 100-sun iso-efficiency plots

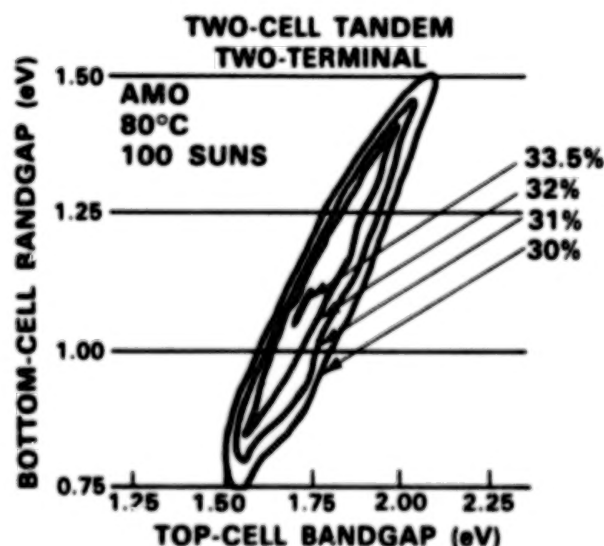


Fig. 2. Calculated AMO, 100 suns iso-efficiency plots for the two-cell, two terminal tandem structure at 80°C.

calculated for two-terminal structures at 80°C. In this figure the values of E_g for the top cell (E_{g1}) and bottom cell (E_{g2}) are given by the abscissa and ordinate, respectively. Thus the points on each plot show what energy gap combinations for the two cells yield the specified efficiency. The maximum calculated efficiency for the two-terminal structure is 33.5%. The highest practical efficiency would be about 28%, since practical efficiencies are expected to be at least 15 relative percentage points lower than the calculated values. Note this is much larger than the 20-21% for single-junction cells. Interestingly, as in the case of two-cell two-terminal tandem structure for one-sun operation at AMO and AMI at 27°C (ref. 3), the optimal combination is for the top cell at 1.70-1.75 eV, and the bottom cell is around 1.05 - 1.10 eV. This combination is very fortunate, since it allows the use of Si ($E_g = 1.10$ eV at 80°C) for the bottom cell. Other choices of materials for the bottom cell could be GaInAs or GaAsSb ternary compounds. The top cell could be fabricated from $Ga_{1-x}Al_xAs$ or $GaAs_{1-x}P_x$ with x about 0.3. The optimal two-terminal structure will require accurate control of the material properties of both cells so as to allow photocurrent matching.

ORIGINAL PAGE IS
OF POOR QUALITY.

Because photocurrent matching is not necessary for separately connected cells, four-terminal devices have several important advantages over two-terminal devices. First, the allowable range of optimal energy gap combinations for two cells is much wider. This feature is illustrated by Fig. 3, which shows AMO, 100-sun

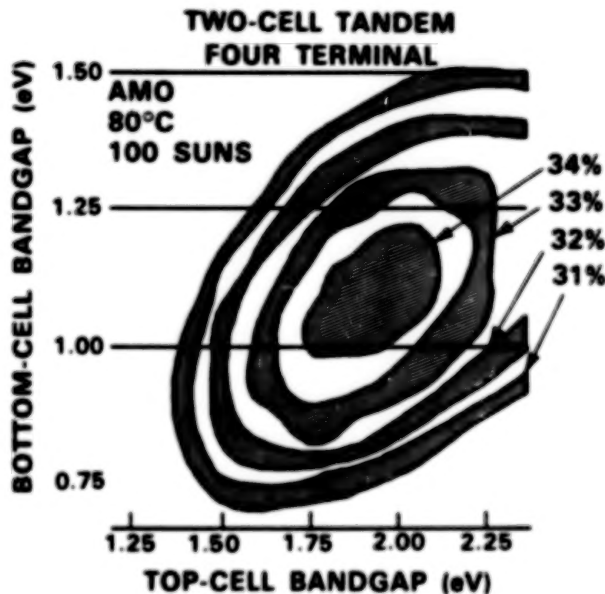


Fig. 3. Calculated AMO, 100 suns iso-efficiency plots for the two-cell, four-terminal tandem structure at 80°C.

iso-efficiency plots calculated for four-terminal structures at 80°C. Since the energy gap ranges are wider, the control of material preparation parameters can be much less stringent than that required for two-terminal structures. The maximum calculated efficiency for the four-terminal structure is 34.0%, slightly higher than the maximum value for the two-terminal structure. The highest practical efficiencies for the four-terminal structure are expected to be about 28-29%. In contrast with terrestrial applications, in space, however, the top and bottom cells are subjected to electron and proton bombardments. The degradation of each cell may be different. Although in Cassegrainian concentrating optics, the solar cells may be subjected to much less radiation damages than cells in flat-plate configurations, the optical elements such as Ag reflectors may degrade spectrally different in space environment. The degradations would cause the photocurrents of the component cells to be different. In a two-terminal case, this is a severe limitation. In the four-terminal case, this is not a problem. The top cell should be at 1.75 - 2.10 eV, and the bottom cell at 1.00-1.20 eV.

Three-Cell Tandem Structures

We have shown that there is a very significant gain in efficiency in going from a single-junction to a two-cell tandem structure. The gain in conversion efficiency from a two-cell to a three-cell tandem structure is much smaller. Figures 4 and 5 show the AMO 100-sun, iso-efficiency plots at 80°C for the three-cell tandem structures with the cells connected in series and separately respectively. The curves are plotted for middle-cell energy gaps at 1.40 eV, 1.45 eV, and 1.50 eV for the series-connected structure, and 1.45, 1.50 and 1.55 eV for the separately connected structure. (Separate calculations show that the maximum efficiencies are obtained with the middle-cell energy gaps in these ranges.) As shown in these two figures, in the three-cell structure, when the

ORIGINAL PAGE IS
OF POOR QUALITY

Fig. 4. Calculated AMO, 100 suns iso-efficiency plots for the three-cell tandem structures where the cells are series-connected. The middle cell has an energy gap of 1.40, 1.45 or 1.50 eV. The structure is at 80°C.

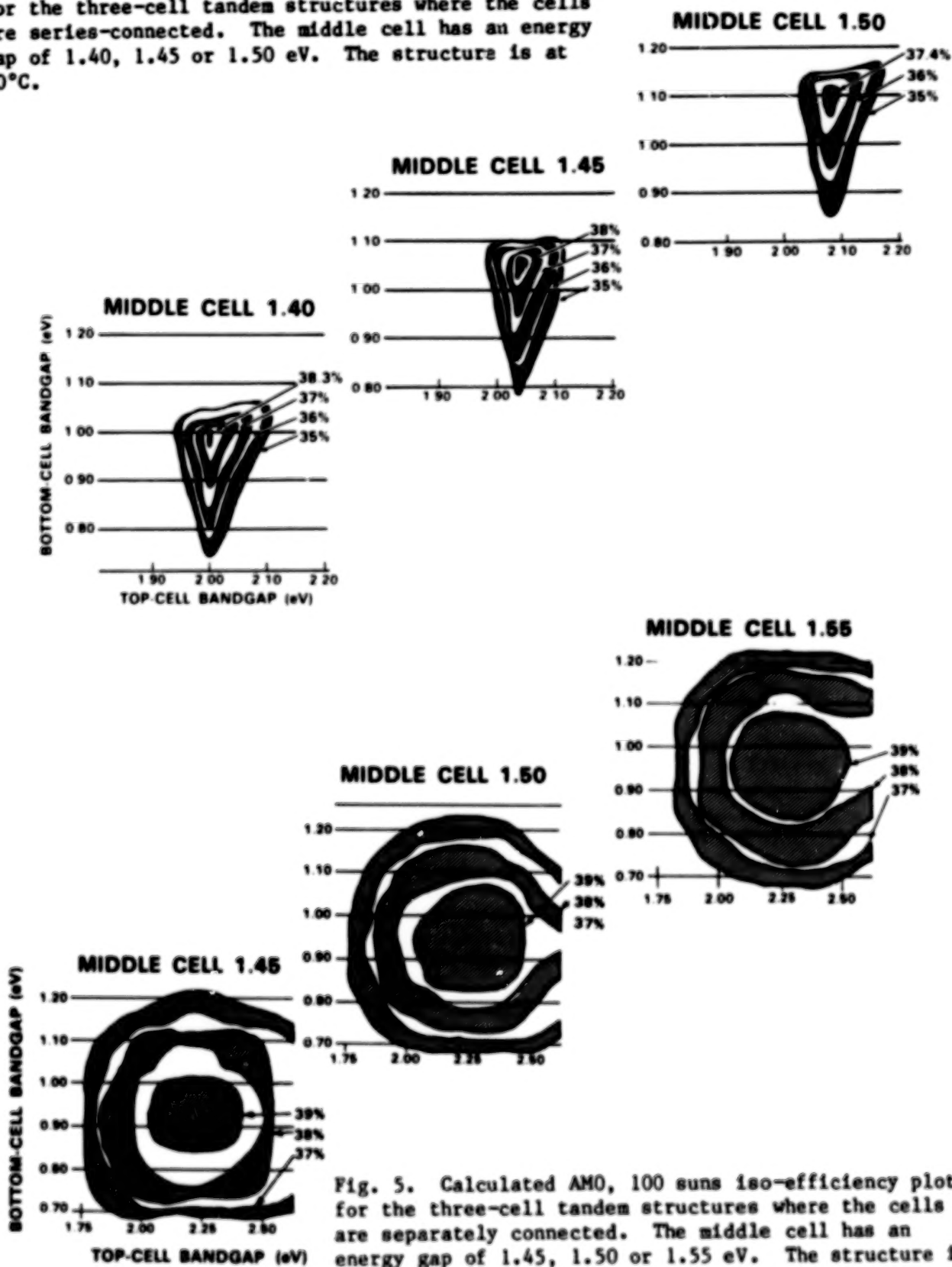


Fig. 5. Calculated AMO, 100 suns iso-efficiency plots for the three-cell tandem structures where the cells are separately connected. The middle cell has an energy gap of 1.45, 1.50 or 1.55 eV. The structure is at 80°C.

middle-cell bandgap increases, the optimal combination of the top cell and the bottom cell also favor higher bandgaps (i.e., the plots move toward upper-right-hand corner). The maximum calculated efficiencies at AMO are 38.0% for the series-connected structure and 39.0% for the separately connected structure. Practical efficiencies are about 5-6 absolute percent lower.

In the series-connected three-cell structure, the optimal combinations of energy gaps are extremely narrow, even more so than in the two-cell structure, and it is expected that degradation of the component cells and the concentrating optics in space could pose a severe limitation to the adoption of three-cell series-connected structures. In the separately connected case, this is not a problem. However, in three-cell structures, three independent power conditioning circuits are necessary, and the substantial increase in complexity in the tandem structure may be too high a price to pay for the increase in efficiencies.

In addition, for three-cell tandem structures, the optimal combination of energy gaps require the E_g of the top cell 2.0 - 2.4 eV, the middle cell 1.4 - 1.5 eV and the bottom cell 0.8 - 1.1 eV. Possible choices for the bottom cell can be Si, GaInAs or GaAsSb, and for the middle cell GaAs, CdTe, GaInP. The top cell material is harder to select. GaP, AlP and AlAs all have energy gaps in the range of 2.2 - 2.4 eV. However, they have indirect energy gaps, and thus not very suitable as top-cell materials. The energy gaps in $\text{GaAs}_{1-x}\text{P}_x$ ternary compounds remain direct up to 2.0-2.1 eV at 80°C, and could be marginally useful. For higher energy gaps, there is no good material available yet.

CONCLUSION

In conclusion, substantial efficiency increases are expected for two-cell crystalline tandem structures in comparison with single-junction cells. Our computer analysis indicated that practical AMO efficiencies of 28-29% at 100 suns and at 80°C can be expected. The further increases in efficiency for a three-cell tandem structure are smaller, and may not justify the added complexity (see Table 1). For two-cell tandem modules, the bottom cell should be around 1.0 - 1.1 eV,

TABLE 1. CALCULATED AND PRACTICAL AMO EFFICIENCIES OF SINGLE-JUNCTION, TWO-CELL AND THREE-CELL TANDEM STRUCTURES AT 100 SUNS AND 80° C

Number of cells	Calculated Maximum Efficiency	Practical Maximum Efficiency
1a	24%	20 - 21%
2b	33-35%	28 - 30%
3c	37-39%	31 - 33%
<hr/>		
$a_{E_g} = 1.4 \text{ eV}$		
$b_{E_{g1}} = 1.7 - 1.8 \text{ eV}$		
$E_{g2} = 1.0 - 1.1 \text{ eV}$		
$c_{E_{g1}} = 2.0 - 2.4 \text{ eV}$		
$E_{g2} = 1.4 - 1.5 \text{ eV}$		
$E_{g3} = 0.9 - 1.1 \text{ eV}$		

and Si, GaInAs, and GaAsSb could be excellent choices. For such cells, at AM0 and at 80°C a top-cell energy gap of 1.70 to 1.80 eV is optimal for both two- and four-terminal structures. The GaAs-AlAs and GaAs-GaP systems are very attractive candidates for the top cell. There is a distinct advantage in using a four-terminal structure rather than a two-terminal structure, because the former yields efficiencies less sensitive to variations in energy gap and is not as sensitive to the cell degradation in space-radiation environment.

APPENDIX

Calculations were carried out for one-cell, two-cell and three-cell structures. Here, we will illustrate a two-cell calculation. The other cases are similar. Let the top cell have a bandgap energy E_{g1} (in eV), and the bottom cell E_{g2} , with corresponding short-circuit current densities J_{sc1} and J_{sc2} . Since high-quality solar cells have already attained quantum efficiency values over 90%, we assume 100% quantum efficiency. Then the short-circuit current densities can be written as

$$J_{sc1} = \int_{0.2 \mu m}^{\lambda_{g1} (\mu m)} q F(\lambda) d\lambda \quad (1)$$

$$J_{sc2} = \int_{\lambda_{g1}}^{\lambda_{g2}} q F(\lambda) d\lambda \quad (2)$$

where $\lambda_g = 1.239/E_g$ (μm), q is the electronic charge, and $F(\lambda)$ is the solar photon flux density at λ , which varies with air mass (ref. 7).

The open-circuit voltage V_{oc} for each of the cells is given by

$$V_{oc} = \frac{kT}{q} \ln \left(\frac{XJ_{sc}}{J_{oo}} + 1 \right) \quad (3)$$

where X is the concentration ratio, k is Boltzmann's constant, and T is absolute temperature. The diode factor is assumed to be 1.0. J_{oo} is the dark saturation current, and if we assume a simple diffusion current, then

$$J_{oo} = KT^3 \exp \left(-\frac{qE_g}{kT} \right) \quad (4)$$

The value of K may be different for different materials. For our calculations of J_{oo} in A/cm^2 , we assume a fixed constant with a value of 0.05. This value was selected so that for AM1 conditions the calculated V_{oc} was 0.97 V for GaAs and 0.66 V for Si, values very close to the respective experimental values of 0.98 and 0.65 V.

ORIGINAL PAGE IS
OF POOR QUALITY

The fill factor ff for each of the cells is evaluated as follows:

$$ff = \frac{V_m}{V_{oc}} \left[1 - \frac{\exp\left(\frac{qV_m}{kT}\right) - 1}{\exp\left(\frac{qV_{oc}}{kT}\right) - 1} \right] \quad (5)$$

where V_m is given by the relationship

$$\left(\exp \frac{qV_m}{kT} \right) \left(1 + \frac{qV_m}{kT} \right) = \frac{XJ_{sc}}{J_{oo}} + 1 \quad (6)$$

For the two-terminal case, the J_{sc} value used in Eqs. 3 and 6 is the same for both cells, namely, the smaller value of J_{sc1} and J_{sc2} . The combined efficiency is then

$$\eta_{tot} = J_{sc} [V_{oc1} ff_1 + V_{oc2} ff_2] / P_{in} \quad (7)$$

For the four-terminal case, both J_{sc1} and J_{sc2} values are used in Eqs. 3 and 6 and

$$\eta_{tot} = [J_{sc1} V_{oc1} ff_1 + J_{sc2} V_{oc2} ff_2] / P_{in} \quad (8)$$

P_{in} is the incident solar power density. With the above equations, η_{tot} can be calculated as a function of E_{g1} and E_{g2} .

To obtain the iso-efficiency curves, values of η_{tot} were first calculated for different combinations of E_{g1} and E_{g2} at $T = 353$ K, $X = 100$ at AM0. The curves were then plotted for all combinations of E_{g1} and E_{g2} that produce values of η_{tot} within $\pm 1\%$ of the η_{tot} values stated on the curves.

REFERENCES

1. R. E. Patterson and H. S. Rauschenback, NASA Conference Publication No. 2256, Space Photovoltaic Research and Technology, Cleveland, OH 1982, p. 211 (1982).
2. R. E. Patterson, H. S. Rauschenback and M. D. Canady in Conference Record of the 16th IEEE Photovoltaic Specialists Conference, San Diego, California (IEEE, 1982), p. 39.
3. J. C. C. Fan, B-Y. Tsaur and B. J. Palm in Conference Record of the 16th IEEE Photovoltaic Specialists Conference, San Diego, California (IEEE, 1982), p. 692.
4. J. C. C. Fan and B. J. Palm, to be published in Solar Cells.
5. J. C. C. Fan and B. J. Palm, to be published in Solar Cells.
6. M. B. Panish and H. C. Casey, Jr., J. Appl. Phys. 40, 163 (1969).
7. M. P. Thekaekara, Conference of COMPLES, Dahrhan, Saudi Arabia, November 1975.

N84
29327

UNCLAS

N84 29327

DEVELOPMENT OF GaAs/Si AND GaAlAs/Si MONOLITHIC
STRUCTURES FOR FUTURE SPACE SOLAR CELLS*

M. B. Spitzer, S. M. Vernon, R. G. Wolfson and S. P. Tobin
Spire Corporation
Bedford, Massachusetts

The results of heteroepitaxial growth of GaAs and GaAlAs directly on Si are presented, and applications to new cell structures are suggested. The novel feature of this work is the elimination of a Ge lattice transition region. This feature not only reduces the cost of substrate preparation, but also makes possible the fabrication of high efficiency monolithic cascade structures. All films to be discussed were grown by organometallic chemical vapor deposition at atmospheric pressure. This process yielded reproducible, large-area films of GaAs, grown directly on Si, that are tightly adherent and smooth, and are characterized by a defect density of $5 \times 10^6 \text{ cm}^{-2}$. Preliminary studies indicate that GaAlAs can also be grown in this way.

A number of promising applications are suggested. Certainly these substrates are ideal for low-weight GaAs space solar cells. For very high efficiency, the absence of Ge makes the technology attractive for GaAlAs/Si monolithic cascades, in which the Si substrates would first be provided with a suitable p/n junction. The paper concludes with an evaluation of a three bandgap cascade consisting of appropriately designed GaAlAs/GaAs/Si layers.

INTRODUCTION

The reduction of the cost of GaAs space solar cells is an important aspect of research on light-weight high-efficiency cell technology (ref. 1). One approach to cost reduction comprises the heteroepitaxy of thin films of GaAs on low-cost Si substrates. Such an approach may also offer improved power-to-weight ratio, since Si substrates are less dense than GaAs. In the long term, heteroepitaxial structures of this type may be well suited to application to the fabrication of high efficiency cascade cells.

In order to achieve good heteroepitaxy, it is necessary to interpose between the crystals a lattice transition region, owing to the difference between the Si and GaAs lattice constants. Good results have been achieved in several laboratories (refs. 2,3,4) through the use of a Ge transition layer

*This work is supported by the Solar Energy Research Institute under contract No. XE-3-03033-01.

which is thought to grade the interface between the GaAs and Si crystals. With this technique, cell efficiency of 14% (AM1) has been achieved (ref. 2). The presence of the Ge, however, is not desirable in a cascade cell, owing to absorption which can occur if the transition layer thickness is not well-controlled.

In this paper, the results of ongoing research into a new type of GaAs-Si heteroepitaxy is reported. In this work, both GaAs and AlGaAs have been grown directly on Si, without a Ge transition layer. The film growth technology is applicable both to fabrication of GaAs cells on low-cost substrates, and to the development of advanced cascade structures. A review of crystal growth studies is presented, followed by a discussion of possible advanced cell designs.

CRYSTAL GROWTH STUDIES

The films to be discussed were grown by organometallic chemical vapor deposition at atmospheric pressure upon ordinary industry-standard Czochralski wafers that had a surface normal tilted 3° from $\langle 100 \rangle$ toward the $\langle 110 \rangle$ direction. The depositions were conducted in a vertical reactor, with the substrates mounted on a silicon-carbide-coated susceptor that was rotated during the deposition to improve uniformity. The entire deposition process was computer-controlled and the results to be discussed were therefore easily replicated. The growth conditions are summarized in table I.

Both GaAs and GaAlAs films have been grown as described above. In the case of GaAs, the resultant films were smooth, completely single crystal, and uniform across the entire 2-inch substrate surface. Figures 1a and 1b show Nomarski micrographs of GaAs and $\text{Ga}_{0.9}\text{Al}_{0.1}\text{As}$ films. Although both films were tightly adherent and exhibited no cracking, it can be seen that the smoothness of the GaAs film is superior. For this reason, growth studies and film characterization have largely been limited to GaAs. GaAlAs is also under investigation, but only preliminary data are available at this time. The remainder of the discussion will therefore be limited to results obtained on GaAs films.

The crystallinity of the GaAs films was analyzed using x-ray diffraction; Cu-K α radiation revealed a well-resolved (400) peak as shown in figure 2. The absence of polycrystalline regions was confirmed by transmission electron microscopy (TEM) analysis. Figure 3 illustrates TEM depth sections in a 3-micron-thick GaAs film grown on Si. Figure 3a shows the near interface region, characterized by a high dislocation density (approximately 10^{12} cm^{-2}). Figure 3b shows a TEM section at a depth of 0.5 microns that indicates that the dislocation density is reduced to about $5 \times 10^6 \text{ cm}^{-2}$. Figure 4 illustrates the dislocation density as a function of depth, measured on various TEM depth sections. It can be seen that the dislocation density decreases within the first 0.3 microns of the GaAs film. It is believed that this decrease is caused by the interaction and entanglement of dislocations in the near-interface region.

The dislocation density reported here is of the same order of magnitude as reported in reference 2, in which 14% (AM1) efficient cells were fabricated. Reduction of the dislocation density is evidently necessary for fabrication of cells of higher efficiency. It is believed that this reduction can be achieved in

a number of ways. Blakeslee and Mitchell (ref. 5) have described the alternation of thin layers of differing compounds; it may be possible to achieve a similar result with alternation of AlAs and GaAs layers. Tsaur et al. (ref. 2) have used interrupted growth to address reduction of dislocation density. Both techniques seek to bend the dislocation lines so as to prevent their extension into the active layer of the device, and it appears that both techniques can be applied to the films discussed above.

Our research into GaAs/Si and GaAlAs/Si heteroepitaxy has therefore identified two important areas for further research. First, as in the GaAs/Ge/Si approach, the dislocation density must be reduced. Second, the growth of GaAlAs on Si must be studied in greater depth. Both investigations are now underway and will lead to establishment of film growth technologies applicable to both low-cost GaAs cells and also multi-junction cascade cells.

APPLICATION TO SOLAR CELLS

In the previous section, we indicated the feasibility of the growth of GaAs and GaAlAs directly on Si. Although further research into the growth of these films is required, the results to date warrant a discussion of novel cell structures made possible by this new growth technology.

A GaAlAs/GaAs heteroface solar cell, grown on a low-cost Si substrate, would be of great interest for space applications, and we are pursuing its development at the present time. Figure 5 illustrates a profile plot of the cell structure that we are presently growing. Note that this structure has rather sharp transitions in doping and composition. The actual profiles are believed to be more sharp than the profile data indicate. We have fabricated solar cells from such crystals, grown on GaAs substrates, and have achieved cell efficiency of over 20% (AM1), as shown in figure 6. The transfer of this structure to a GaAs-coated Si substrate should be straightforward, provided that the defect density can be reduced to acceptable levels; however we have not fabricated cells on such substrates at the time of this writing.

Figure 7 illustrates the two-junction cascade discussed by a number of authors (refs. 6,7). Recently Fan et al., (ref. 7) calculated the efficiency for various bandgap combinations intended for space applications and found that 1.1 eV and 1.75 eV would yield efficiency of up to about 32% (AM0). This type of structure could in principle be fabricated with the heteroepitaxy described in the previous section. Growth of GaAlAs is as yet uncharacterized; thus whether such films can be grown within the required defect level limits remains to be established. Nevertheless, this is an important cascade solar cell that has rather high potential for satisfying high efficiency space solar cell requirements.

A more complicated three-junction structure with a higher theoretical efficiency is shown in figure 8. This structure consists of a GaAlAs cell grown epitaxially on a GaAs cell which itself is grown heteroepitaxially, as described above, upon a Si cell. There are good reasons for devoting serious consideration to this cell in addition to the higher theoretical efficiency. First, the development of GaAs/Si heteroepitaxy is more advanced and simpler than GaAlAs/Si heteroepitaxy. This militates for the use of GaAs for the lattice transition

region, at least at the present stage of development. In a three-cell cascade it is thus desirable to form the middle cell in GaAs, since the GaAs lattice transition region would otherwise introduce parasitic absorption.

The general complexity of the three-cell cascade that has a GaAs transition layer must be compared to the less complex two-bandgap GaAlAs/Si structure having a transition layer formed in high bandgap GaAlAs. A definitive selection of the best approach would be premature at this time.

A number of methods of current-matching may be applied to the GaAlAs/GaAs/Si cascade. Table 2 illustrates one selection of bandgaps that could be used. There is a large mismatch between the short circuit current (J_{sc}) of the GaAlAs/GaAs cells and that of the Si cell, but this can be remedied by using the technique developed by Tsaur et al. (ref. 2) in which selected areas of the GaAlAs/GaAs cells are removed to permit a fraction of the incident light to strike the Si cell directly. For example, a simple calculation shows that the matched current density of 17.6 mA/cm^2 is obtained by reducing the top and middle cell area by only 8%.

To fully address current-matching, one must consider the actual quantum efficiency of each cell, the spectral variation of reflectance resulting from the particular antireflection coating envisioned, and the transmission spectra of the desired encapsulation system. These factors can significantly affect the bandgap combinations that will yield the best current-matching. Secondary factors such as these can make possible the use of "non-ideal" bandgap combinations such as those in the GaAlAs/GaAs/Si cascade. Non-ideal combinations that utilize more developed semiconductors like GaAs and Si may be the best route to practical cascade cell fabrication in the near term.

CONCLUDING REMARKS

A summary of recent studies of GaAs and GaAlAs heteroepitaxy on Si has been presented. The intriguing applications of this technology include the high efficiency cascade cell as well as the low-cost GaAs cell on a Si substrate. The direction for future studies is clear and will involve: (1) an investigation of reduction of dislocations in the GaAs films, (2) heteroepitaxy of AlGaAs on Si, and (3) investigation of both design and fabrication technology for multi-bandgap cascade cells. Possible cell structures have been suggested and the rationale for consideration of non-ideal bandgap combinations has been reviewed.

REFERENCES

1. Rahilly, W. P., and Anspaugh, B.: Status of AlGaAs/GaAs Heteroface Solar Cell Technology. Rec. of the 16th IEEE Photovoltaic Specialists Conference, San Diego, 1982, pp. 21-24.
2. Tsaur, B-Y.; Fan, J. C. C.; Turner, G. W.; Davis, F. M.; and Gale, R.P.: Efficient GaAs/Ge/Si Solar Cells. Rec. of the 16th IEEE Photovoltaic Specialists Conference, San Diego, 1982, pp. 1143-1148.
3. Zwerdling, S., Wang, K. L.; and Yeh, Y. C. M.: High Efficiency, Thin-Film GaAs Solar Cells. J. Solar Energy Eng. 105, 237 (1983).
4. Vernon, S. M. and Wolfson, R. G.: Preparation of Silicon Substrates For Gallium Arsenide Solar Cells. Photovoltaics Advanced Research and Development 5th Annual Meeting, SERI/CP-311-2011, May 1983, pp. 23.
5. Blakeslee, A. E.; and Mitchell, K.: Device for Conversion of Electromagnetic Radiation into Electrical Current. United States Patent 4,278,474, July 14, 1981.
6. Bedair, S. M.; Phatak, S. B.; and Hauser, J. R.: Material and Device Considerations for Cascade Solar Cells. IEEE Trans. Electron Devices ED-27, 822 (1980).
7. Fan, J. C. C.; Tsaur, B-Y.; and Palm, B. J.: Optimal Design of High-Efficiency Tandem Cells. Rec. of 16th IEEE Photovoltaic Specialists Conference, San Diego, 1982, pp. 692-701.

TABLE 1 - RANGE OF OM-CVD GROWTH PARAMETERS
USED FOR HETEROEPITAXY

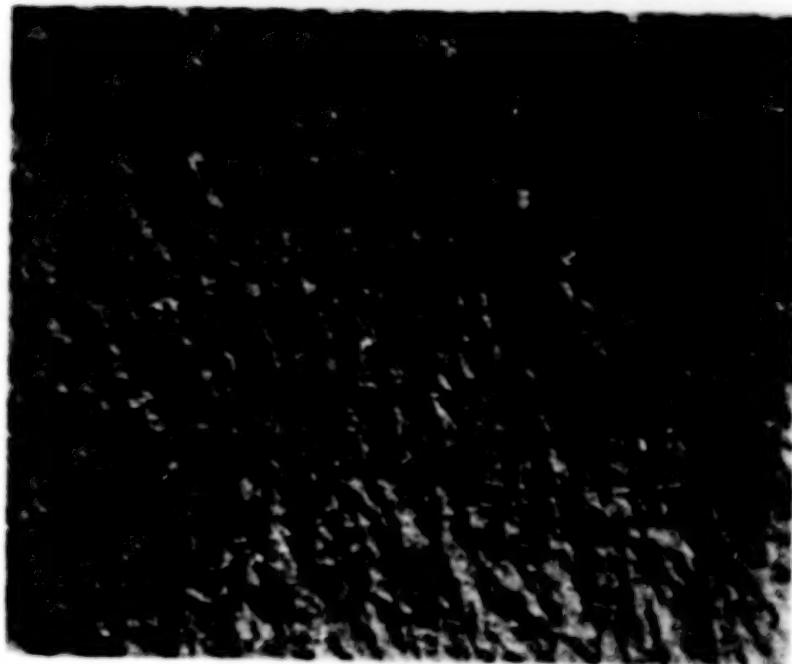
Temperature	550°C to 750°C
As:Ga ratio	5:1 or 10:1
H ₂ flow rate	5 slpm
Growth rate	3-5 μm/hr

TABLE 2.- AMO CURRENT-MATCHING IN THE THREE-CELL CASCADE

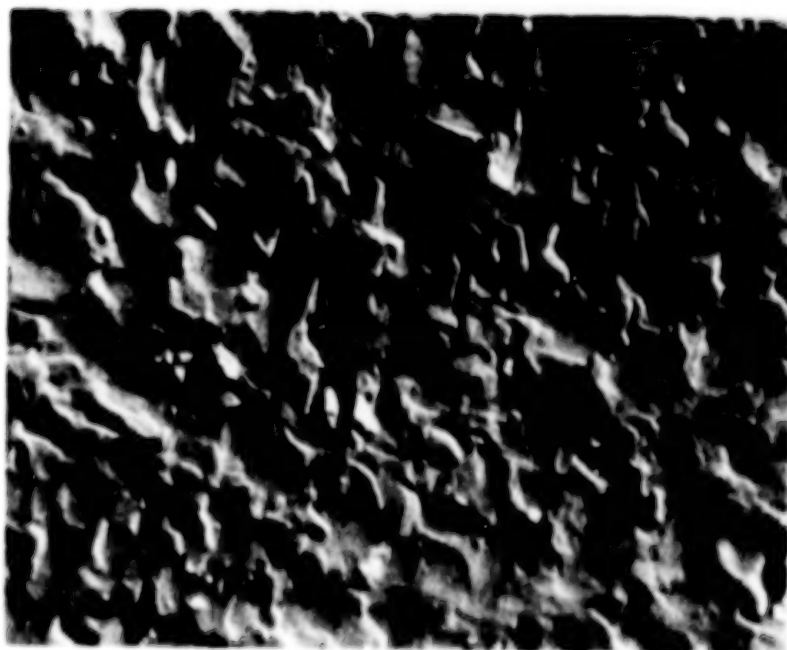
<u>Cell</u>	<u>Bandgap (eV)</u>	<u>Theoretical J_{sc} (mA/cm²)</u>	<u>J_{sc} fraction (mA/cm²)</u>
Top-GaAlAs	2.0	19.1	19.1
Middle-GaAs	1.43	38.2	19.1
Bottom-Si	1.12	52.8	14.6

Notes: The theoretical J_{sc} is the maximum current available from a single junction cell. The J_{sc} fraction is the maximum available current after absorption in the antecedant cells in the cascade. A reduction in top and middle cell area by 8% is required for current matching.

ORIGINAL PAGE IS
OF POOR QUALITY



(a) GaAs film.



(b) $\text{Ga}_{0.9}\text{Al}_{0.1}\text{As}$ film.

Figure 1. - Nomarski micrographs of films grown directly on Si. Magnification, 1000.

ORIGINAL PAGE 19
OF POOR QUALITY

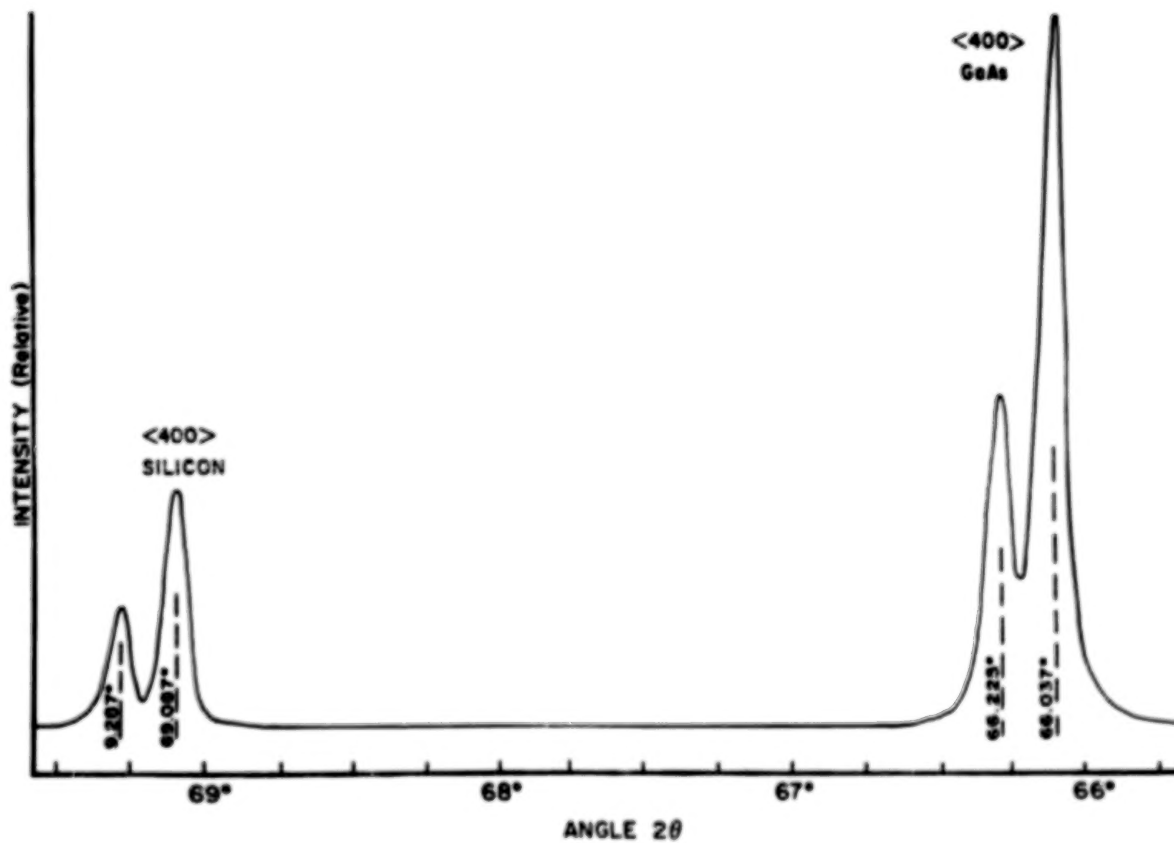


Figure 2. - X-ray diffraction pattern from GaAs film grown directly on Si.

ORIGINAL PAGE IS
OF POOR QUALITY

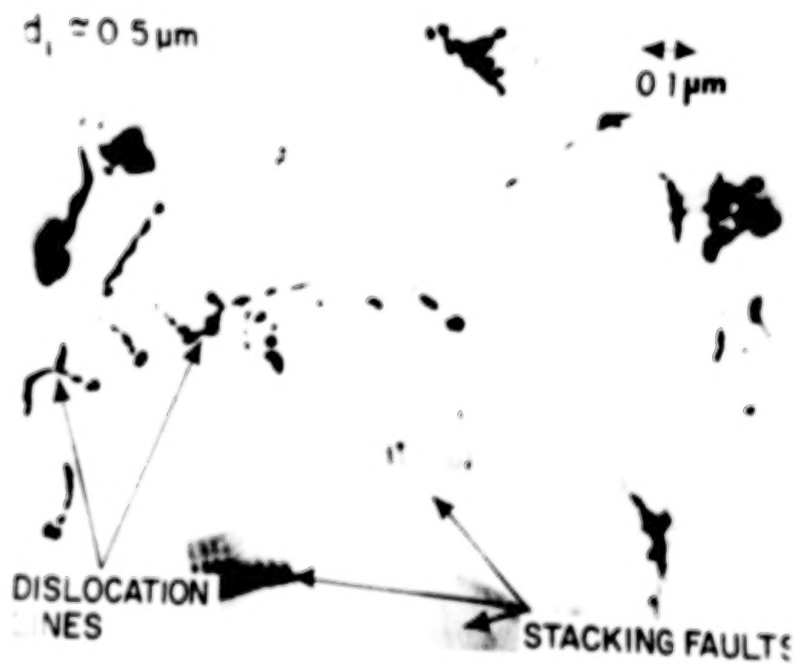
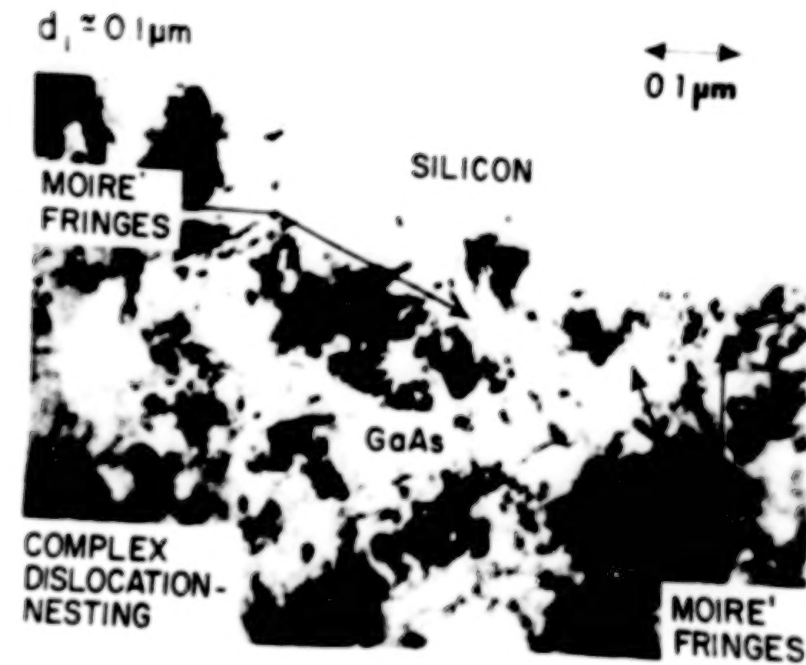


Figure 3. - TEM depth section of a 3-micron thick film of GaAs grown directly on Si at approximately 0.1 and 0.5 μm from interface.

ORIGINAL PAGE IS
OF POOR QUALITY

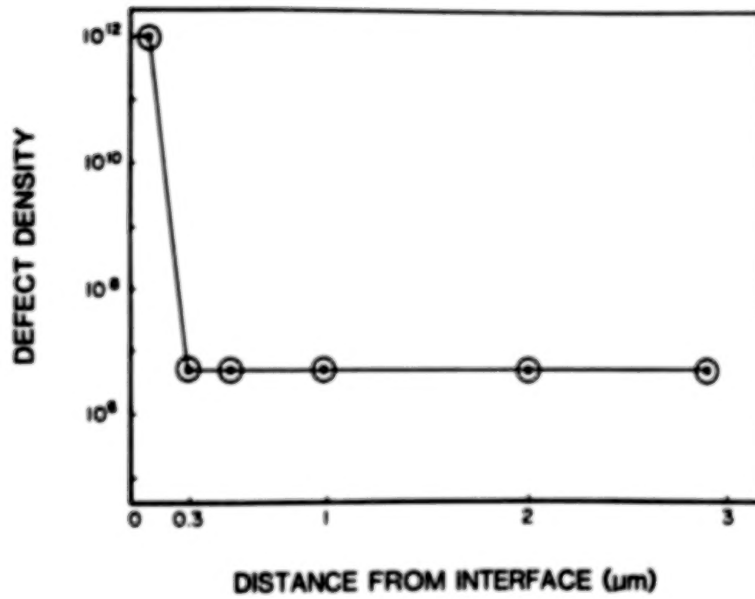


Figure 4. - Dislocation density as a function of depth measured by TEM sectioning.

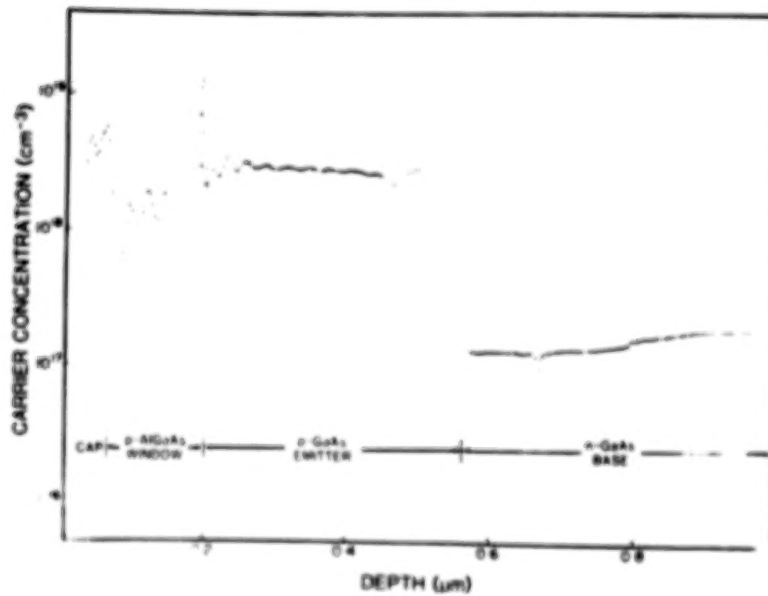


Figure 5. - Profile plot of GaAs/GaAlAs heteroface cell structure.

ORIGINAL PAGE IS
OF POOR QUALITY

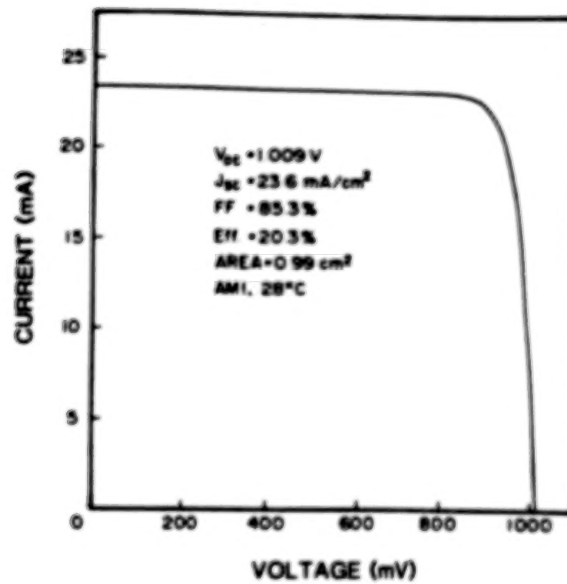


Figure 6. - I-V characteristic of OM-CVD heteroface cell.

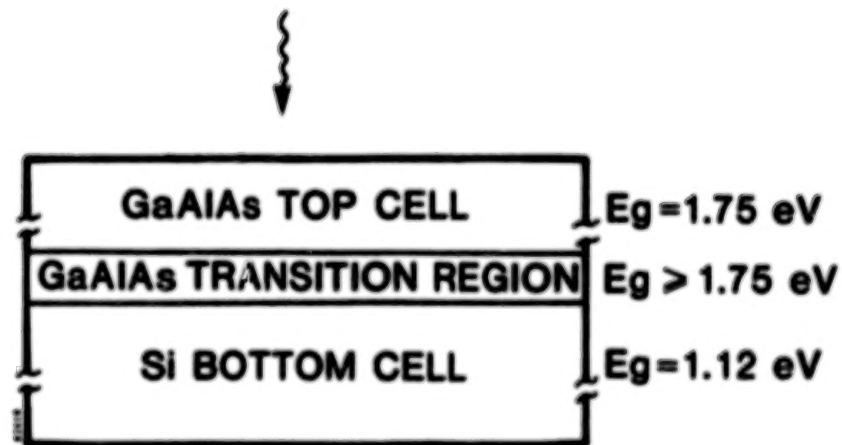


Figure 7. - Two-junction cascade structure.

ORIGINAL PAGE 12
OF POOR QUALITY

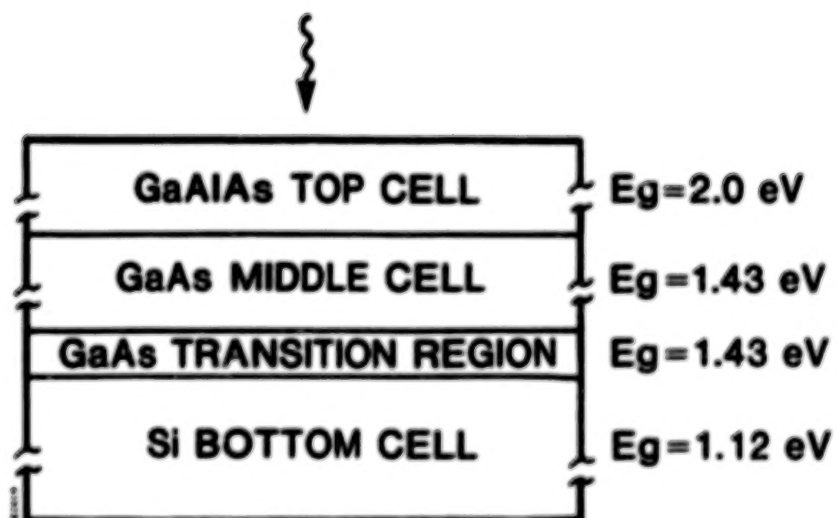


Figure 8. - Three-junction cascade structure.

N84
29328

UNCLAS

N84 29328

DEVELOPMENT OF A 30 PERCENT EFFICIENT 3-JUNCTION
MONOLITHIC CASCADE SOLAR CELL*

C. R. Lewis, W. T. Dietze, and M. J. Ludowise
Varian Associates, Inc.
Palo Alto, California

The goal of this project is the development of a 30% efficient 3-junction monolithic cascade solar cell (100 AMO suns, 80°C), using III-V materials systems. One option for optimum utilization of the solar spectrum (extrapolated from the requirements of the $\text{Al}_y\text{Ga}_{1-x-y}\text{In}_x\text{As}$ materials system) requires bandgaps of 1.15 eV (lower cell), 1.55 eV (middle cell) and 2.05 eV (upper cell). The cells may be mismatched relative to each other if appropriate grading layers are present. This permits the use of a wide range of high luminescence efficiency materials.

$\text{Ga}_{0.75}\text{In}_{0.25}\text{As}$ (1.15 eV) has been established as the material of choice for a high-efficiency lower cell. For the middle cell, $\text{Ga}_{0.28}\text{In}_{0.72}\text{P}$, $\text{Al}_{0.05}\text{Ga}_{0.95}\text{As}$ and $\text{GaAs}_{0.88}\text{P}_{0.12}$ (all 1.55 eV) have been developed; the latter two yield the highest quality material. High-efficiency cells in these materials have been constructed atop $\text{Ga}_{0.75}\text{In}_{0.25}\text{As}$ by a "double mismatch" technique, in which the grading layer ($E_g \leq 1.55$ eV) between the lower and middle cells is transparent with respect to the lower cell.

Also currently under study are three promising candidates for the upper cell junction: $\text{Al}_{0.50}\text{Ga}_{0.50}\text{As}$, $\text{GaAs}_{0.50}\text{P}_{0.50}$, and $\text{Al}_{0.45}\text{Ga}_{0.55}\text{As}_{0.88}\text{P}_{0.12}$ (all 2.05 eV). The final choice of a top cell material will be influenced by the middle cell selection.

To short the interconnecting junctions, two options are being developed. First, the appropriate junction has been shorted via metal deposition during processing. However, more facile processing would be permitted if a tunnel interconnect (or any high-conductance-grown junction) were substituted.

INTRODUCTION

This work describes the development of appropriate materials systems needed for a three-junction monolithic cascade concentrator solar cell. The optimum bandgaps of the individual subcells depend upon whether the subcells are lattice matched or mismatched with respect to each other. We have found that high-efficiency subcells, which are crystallographically mismatched with respect to each other and/or to the GaAs substrate, can be produced in III-V materials systems grown by MOCVD. A key feature is the insertion of appropriate grading layers between the subcells, which leads to the maintenance of high crystallographic, optical and electrical properties of the mismatched materials.

*Different aspects of this work were supported by NASA (Contract NAS3-22232) and by SERI (Contracts XP-9-8081-1 and XE-3-03015-1).

SELECTION OF CELL MATERIALS

The cascade cell may be grown lattice matched. If direct bandgaps are to be maintained throughout, two quaternary materials systems are available: $\text{Al}_y\text{Ga}_{1-x-y}\text{In}_x\text{As}$ and $\text{Al}_x\text{Ga}_{1-x}\text{As}_{1-y}\text{Sb}_y$. The cell bandgaps which will maximize the utilization efficiency of the solar spectrum under these conditions are 1.16 eV, 1.55 eV and 2.07 eV (Ref. 1). A cross-section of such a cascade is illustrated schematically in Fig. 1. Internal windows and conductivity layers are omitted for clarity; but included in the cross-section are the interconnects between the sub-cells; the uppermost window layer (to reduce carrier recombination at the surface) and the top contact layer.

Alternatively, the lattice matching and direct E_g constraints may be removed from the system; this opens up a wider range of III-V semiconductors to consideration. The optimum individual cell bandgaps drop to 1.0 eV, 1.4 eV and 1.95 eV, and the maximum theoretical cascade efficiency (100 AMO suns, 80°C) rises from ~35% to ~38% (Ref. 1).

Initial materials development work was carried out in the lattice-matched $\text{Al}_y\text{Ga}_{1-x-y}\text{In}_x\text{As}$ system, in which only moderate cell efficiencies were obtained. Subsequent research on lattice-mismatched systems has been significantly more productive and is discussed exclusively here. The 1.16/1.55/2.07 eV bandgap goals have been temporarily retained in this work, although replacement by the lower- E_g set is anticipated.

$\text{Ga}_{0.75}\text{In}_{0.25}\text{As}$ (1.15 eV) is the material of choice for the low- E_g cell. Several options have been tested for the middle cell (1.55 eV); the most successful are the ternaries $\text{GaAs}_{0.88}\text{P}_{0.12}$ and $\text{Al}_{0.06}\text{Ga}_{0.94}\text{As}$, although $\text{Ga}_{0.28}\text{In}_{0.72}\text{P}$ and $\text{Ga}_{1-x}\text{In}_x\text{As}_{1-y}\text{P}_y$ have also been studied. Options for the upper cell (2.07 eV) include $\text{Al}_{0.50}\text{Ga}_{0.50}\text{As}$, $\text{Al}_{0.45}\text{Ga}_{0.55}\text{As}_{0.88}\text{P}_{0.12}$, and $\text{GaAs}_{0.50}\text{P}_{0.50}$. The two Al-containing materials are lattice matched to the $\text{Al}_{0.06}\text{Ga}_{0.94}\text{As}$ and $\text{GaAs}_{0.88}\text{P}_{0.12}$ middle cells, respectively.

THE $\text{Ga}_{0.75}\text{In}_{0.25}\text{As}$ LOWER CELL

A cross-section of a typical $\text{Ga}_{0.75}\text{In}_{0.25}\text{As}$ lower cell ($E_g = 1.15$ eV) is illustrated in Fig. 2. Se and Zn are the n- and p-dopants; the structure is grown at 625°C. Between the GaAs buffer layer the cell proper is inserted a $\text{Ga}_{1-x}\text{In}_x\text{As}$ ($0 \leq x \leq 0.25$) grading layer of 6 steps in 2.0 μm . This particular grading yields the best overlying cell material, although a linear ramp followed by a short (10-period) superlattice is competitive (Ref. 2). The remaining cell layers, in order of growth, are the base ($\text{Ga}_{0.75}\text{In}_{0.25}\text{As:Se}$), emitter ($\text{Ga}_{0.75}\text{In}_{0.25}\text{As:Zn}$), window ($\text{Al}_{0.65}\text{Ga}_{0.10}\text{In}_{0.25}\text{As:Zn}$) and contact layer ($\text{Ga}_{0.75}\text{In}_{0.25}\text{As:Zn}^{++}$). Spectral response data for this cell (Fig. 3) are excellent. For spectral response samples (0.9 cm x 0.9 cm), front contacts are made by evaporation of Au/Zn and annealing under H_2 . Four 20-mil-diameter dot contacts are symmetrically placed near the sample edges. Back contacts are made by soldering In/Sn contacts to the substrate. No AR coating is used, and the upper contact layer is removed by a selective chemical etch prior to testing. The sample is tested at 300K by illumination with light passed through a monochromator. One calibrated Si reference cell samples the incident light intensity and another measures the front surface reflectivity of the sample. The current generated in the test sample is measured by a picoammeter and recorded as a function of incident photon energy. The final plot of internal

quantum efficiency is corrected for reflectance. The quantum efficiency curve is then integrated against AM0 and AM2 ideal spectral distributions to yield the projected J_{sc} (AM0) and J_{sc} (AM2).

The peak internal quantum efficiency (Fig. 3) of this cell is 92% at 1.82 eV. The high "red" (near-bandgap) response indicates near-optimum junction depth; the high "blue" response indicates an excellent lattice match between the emitter and upper window, and hence little loss of photogenerated carriers to recombination at that interface. The integrated short-circuit current projected for 1 sun (AM0) is 23.1 mA/cm². Diodes (area = 1.8×10^{-3} cm²) fabricated from this structure show excellent ideality factors of 1.2.

Tests of full cells under AM2.4 suns concentration (Fig. 4) corroborate the high quality of the cell. The techniques of cell fabrication by standard photolithographic and metal liftoff techniques have been previously described (Ref. 2). The peak overall cell efficiency (η), uncorrected for grid obscuration or reflection losses, is 21.5% at 172 suns (700 W/cm²) and remains high at higher concentrations (η = 21.4% at 380 suns). The peak fill factor is 0.82 at 113-172 suns concentration. Throughout the range of concentrations tested (36-987 suns), the V_{oc} values are high, peaking at 0.85V. This V_{oc} value is 73% of the E_g value (1.16 eV), which is excellent.

It may be concluded that the Ga_{0.75}In_{0.25}As cell is competitive with the best currently available cells of comparable E_g . The Ga_{0.75}In_{0.25}As cell operates at higher efficiency with higher V_{oc} under concentration than do comparable Si cells (Ref. 3).

GROWTH OF THE MIDDLE CELL BY "DOUBLE MISMATCH"

GaAs_{0.88}P_{0.12} and Al_{0.06}Ga_{0.94}As (1.55 eV) possesses significantly smaller lattice constants (a) than does Ga_{0.75}In_{0.25}As (a = 5.650 Å for GaAs_{0.88}P_{0.12} and a = 5.626 Å for Al_{0.06}Ga_{0.94}As; mismatch with respect to Ga_{0.75}In_{0.25}As at 300K = 2.20% and 1.78%, respectively). Grading in tension between the lower and middle cell materials is therefore carried out. For the Al_{0.06}Ga_{0.94}As middle cell, a linearly graded layer, 4-μm thick, of Al_yGa_{1-x-y}In_xAs ($0.11 \leq y \leq 0.40$; $0 \leq x \leq 0.25$; $E_g \geq 1.55$ eV) is used. For the GaAs_{0.88}P_{0.12} middle cell, the Al_yGa_{1-x-y}In_xAs grading, as above, is followed by an additional step grading (6 steps in 1.8 μm) of Al_{0.06}Ga_{0.94}As_{1-z}P_z ($0 < z \leq 0.12$; $E_g \geq 1.55$ eV).

The use of these optimized grading layers ensures the retention of good materials characteristics in the overlying semiconductors. Note also that the grading is transparent with respect to the lower cell. Middle cells grown by this "double mismatch" technique show photoluminescence efficiencies, I-V characteristics and internal quantum efficiencies virtually indistinguishable from comparable cells grown directly upon GaAs substrates. The substitution of Mg for Zn in at least the lower portion of the transparent grading insures that no degradation of the lower cell occurs. Because the diffusion coefficient of Mg is approximately 10^{-4} that of Zn under comparable conditions (Refs. 4 and 5), excess p-dopant does not diffuse into the lower cell during the growth of overlying layers. A modest loss (10%) of internal quantum efficiency for the lower cell results if this substitution is not performed.

Spectral response curves for p-on-n and n-on-p $\text{Al}_{0.06}\text{Ga}_{0.94}\text{As}$ cells ($E_g = 1.55$ eV) grown by the double-mismatch method are compared in Fig. 5. For the p-on-n cell, $\eta_{\text{max}} = 80.7\%$, integrated J_{sc} (AM0) = 14.49 mA cm^{-2} , integrated J_{sc} (AM2) = 9.98 mA cm^{-2} . For the corresponding n-on-p cell: $\eta_{\text{max}} = 89.7\%$; integrated J_{sc} (AM0) = 15.91 mA cm^{-2} ; integrated J_{sc} (AM2) = 10.98 mA cm^{-2} . The cell layers for the p-on-n structure are, in order of growth: collector ($\text{Al}_{0.06}\text{Ga}_{0.94}\text{As}$), emitter ($\text{Al}_{0.06}\text{Ga}_{0.94}\text{As}$) conductivity layer ($\text{Al}_{0.06}\text{Ga}_{0.94}\text{As}$), window ($\text{Al}_{0.69}\text{Ga}_{0.06}\text{In}_{0.25}\text{As}$) and contact layer (GaAs). Beneath the cell are the $\text{Ga}_{0.75}\text{In}_{0.25}\text{As}$ layer and its associated grading layer on either side. The n-on-p cell is similar, but the conductivity layer is omitted, due to the requisite thinness of the emitter. The higher internal quantum efficiency of the n-on-p structure likely is related to the use of a thin, highly-doped emitter. The overall responses, however, are excellent for both structures.

Similar behavior is observed for $\text{GaAs}_{0.88}\text{P}_{0.12}$ ($E_g = 1.55$ eV) p-on-n and n-on-p cells grown by double mismatch (Fig. 6). For the p-on-n cell: $\eta_{\text{max}} = 78.3\%$; integrated J_{sc} (AM0) = 12.06 mA cm^{-2} ; integrated J_{sc} (AM2) = 8.34 mA cm^{-2} . For the corresponding n-on-p cell: $\eta_{\text{max}} = 88.4\%$; integrated J_{sc} (AM0) = 15.30 mA cm^{-2} ; integrated J_{sc} (AM2) = 10.33 mA cm^{-2} . Again, the n-on-p cell contains a thin emitter and no conductivity layer.

Small-area ($1.8 \times 10^{-3} \text{ cm}^2$) mesa diodes have been fabricated in the $\text{Al}_{0.06}\text{Ga}_{0.94}\text{As}$ and $\text{GaAs}_{0.88}\text{P}_{0.12}$ structures. It is noteworthy that the p-on-n cells display higher V_{oc} values, lower forward resistances and lower dark reverse-bias leakage than do their n-on-p counterparts. These characteristics may forecast improved performance under high concentration. Typical values of V_{oc} are 1.0V (for p-on-n) and 0.78V (n-on-p).

The surfaces of the cells grown by double mismatch are specular, displaying the crosshatch typical of lattice-mismatched growth. Only very low incidences of surface defects (pyramids, cracks, etc.) are observed, further testimony as to the high quality of the material thus grown.

Preliminary studies on $\text{Ga}_{0.28}\text{In}_{0.72}\text{P}$ (1.55 eV) as an alternative middle cell material reveal inferior luminescence efficiencies relative to $\text{Al}_{0.06}\text{Ga}_{0.94}\text{As}$ and $\text{GaAs}_{0.88}\text{P}_{0.12}$. $\text{Ga}_{0.28}\text{In}_{0.72}\text{P}$ is lattice matched to the lower cell ($\text{Ga}_{0.75}\text{In}_{0.25}\text{As}$) but appears extremely sensitive to even very small numbers of residual material dislocations.

GROWTH OF THE UPPER CELL

The three most promising materials for the upper cell (2.05 eV) are: $\text{Al}_{0.50}\text{Ga}_{0.50}\text{As}$; $\text{Al}_{0.45}\text{Ga}_{0.55}\text{As}_{0.88}\text{P}_{0.12}$; and $\text{GaAs}_{0.50}\text{P}_{0.50}$. The two Al-containing materials are lattice matched to $\text{Al}_{0.06}\text{Ga}_{0.94}\text{As}$ and $\text{GaAs}_{0.88}\text{P}_{0.12}$, respectively -- the two most successful options for the middle cell. Because both compounds are indirect-gap at these compositions (the direct-indirect crossover lying at approximately 1.95 eV), consideration must be given to the reduced absorption coefficients and carrier diffusion lengths which result. These systems undoubtedly would benefit from a reduction in bandgap to 1.95 eV. Moderate efficiency cells in these two materials ($\eta_{\text{max}} \sim 55\%$) have been obtained, and efforts to increase these values are in progress.

$\text{GaAs}_{0.50}\text{P}_{0.50}$ is lattice mismatched with respect to the middle cell; hence an additional grading ($E_g \geq 2.05$ eV) will be necessary between it and the middle cell.

Efforts here will focus upon optimization of the grading layer as to eliminate tension cracking in the upper cell. This material is of particular interest because the direct-indirect crossover lies at higher E_g than in the two Al-containing competitors; hence higher luminescence efficiencies and spectral responses are anticipated. Work on this system, especially at 1.95 eV (direct E_g) is also in progress.

OPTIONS FOR CELL INTERCONNECTS

Currently two methods of interconnecting the cascade subcells are available. The first is the growth of a tunnel junction or leaky junction integral to the monolithic structure; the second, the fabrication of metal interconnections during processing subsequent to growth. Of these options, the grown interconnect requires significantly less processing; the insertion of a few additional layers into the cascade poses no problem in an automated system. It is crucial, however, that the extremely abrupt doping profile and higher carrier concentrations of the tunnel or leaky junction be maintained during the growth of overlying layers. To support a cascade cell operating at 100 suns concentration, interconnect conductances must exceed $10 \text{ A V}^{-1}\text{cm}^{-2}$. Several leaky, high-conductance junctions in GaAs, using Mg and Se as the dopants, have been developed; one isolated junction displays conductances as high as $210 \text{ A V}^{-1}\text{cm}^{-2}$, theoretically sufficient to support a cascade operating at ~1000 suns concentration.

A cross-section of this isolated, high-conductance interconnect is illustrated in Fig. 7. Mg is the p-dopant of choice due to its low diffusion coefficient (Ref. 5). Se is used as the n-dopant because of the relatively high N_D-N_A attainable in GaAs ($\sim 10^{19}\text{cm}^{-3}$), despite its moderately high diffusion coefficient. Similar structures substituting Si or Sn as the n-dopant display significantly lower conductances, due to the lower maximum N_D-N_A . A number of factors tending to increase junction leakiness by maximizing its abruptness have been previously described (see Ref. 6); they include n-on-p growth of the interconnect, low interconnect growth temperatures, and intentional compensation of the p-side of the junction by the n-dopant. These techniques minimize the effects of Se memory and diffusion degradation upon the shorting junction. As seen in Fig. 7, the leaky junction displays high conductances, of $19 \text{ A V}^{-1}\text{cm}^{-1}$, when grown at 730°C and $210 \text{ A V}^{-1}\text{cm}^{-2}$ when grown at 630°C . Note that there is no Se concentration gradient across the junction, eliminating a potential degradation pathway. The total thickness of this prototype interconnect is $2 \mu\text{m}$. In a real cell, this dimension would be limited to $\sim 285 \text{ \AA}$ (125 \AA n-type, 160 \AA p-type) (Ref. 7) in order that $\leq 1\%$ of the light destined for the underlying cells be absorbed, if E_g for the overlying cell $\geq 1.4 \mu\text{m}$. The relatively low E_g of GaAs increases the theoretical tunneling probability across the junction (Ref. 8); the maximum attainable N_D-N_A increases and the donor ionization energy decreases at lower E_g , also enhancing this probability. In this particular interconnect, there may be additional intragap states induced by the high doping and heavy compensation in the p-layer, which are conducive to defect tunneling.

Despite these high dopant concentrations, the material is not damaged. Overlying middle cell material shows photoluminescence, diode I-V characteristics and internal quantum efficiencies very similar to those at middle cell material grown directly on GaAs substrates. This is most clearly seen if no electrical junction is present in the underlying interconnect material (i.e., doped throughout with Mg and Se).

Mg diffusion across the prototype interconnecting junction is relatively insignificant. Deposition of GaAs: (Mg^{++} , Se^{++}) may be continued under overlying cell growth conditions (e.g., 780°C , 1 hour), with negligible decreases of junction conductance resulting. Se diffusion, however, is a more serious problem. When low-doped material sandwiches the interconnect (especially on the p-side and if the interconnect is thin), significant increases in interconnect resistivity result. It appears that Se outdiffusion lowers $\text{N}_D\text{-N}_A$ at the p/n interface of the leaky junction. Efforts to circumvent this effect are in progress.

The alternate strategy, of metal-interconnecting the subcells, has already been successfully demonstrated for a GaAs- $\text{Al}_{0.30}\text{Ga}_{0.70}\text{As}$ prototype 2-junction cascade system (see Ref. 9). The extension to 2 subcells of the lattice-mismatched system appears obvious. Eventual extrapolation of a metal-interconnect technique to a 3-junction cascade may be envisioned, with due respect for the more complex processing.

CONCLUSIONS

The individual subcells of the 3-junction monolithic cascade concentrator cell may be grown lattice mismatched with respect to each other, if appropriate grading layers are inserted between the mismatched layers. Under these conditions, negligible degradation of the properties of either underlying or overlying material results, and high-efficiency subcells are produced by this technique.

REFERENCES

1. H. C. Curtis, "Determination of Optimum Sunlight Concentration Level in Space for III-V Cascade Solar Cells", Space Photovoltaic Research and Technology 1982 Conference Proceedings (NASA Conf. Publication 2256), p. 69.
2. M. J. Ludowise, W. T. Dietze, R. Boettcher, N. Kaminar, Appl. Phys. Lett. 43, 468 (1983).
3. P. G. Borden and R. W. Walsh, Appl. Phys. Lett. 41, 649 (1982).
4. K. A. Arseni, B. I. Boltaks, T. D. Dzhaferov, Phys. Stat. Sol. 35, 1053 (1969).
5. E. C. Wurst, "Final Report on Research and Development of High Temperature Semiconductor Devices", Dept. of the Navy, NO-77532 and NO-85424 (March 1963).
6. C. R. Lewis, W. T. Dietze, M. J. Ludowise, J. Electron. Mat. 12, 507 (1983).
7. D. L. Miller, S. W. Zehr, J. S. Harris, Jr., J. Appl. Phys. 53, 744 (1982).
8. S. M. Sze, Physics of Semiconductor Devices, 2nd Edition (Wiley-Interscience, New York, NY, 1982).
9. P. G. Borden, R. A. LaRue, M. J. Ludowise, "Progress Towards Cascade Cells Made by OM-VPE", Space Photovoltaic Research and Technology 1982 Conference Proceedings (NASA Conf. Publication 2256), p. 57.

ORIGINAL PAGE 13
OF POOR QUALITY

SCHEMATIC 3 - JUNCTION CASCADE
(MONOLITHIC STRUCTURE)
GOALS: 30% EFFICIENCY AT 100 AMO SUNS, 80 °C

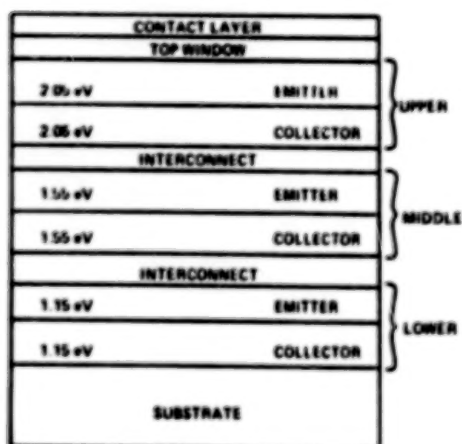


Figure 1. - Schematic cross section of 3-junction monolithic cascade solar cell.

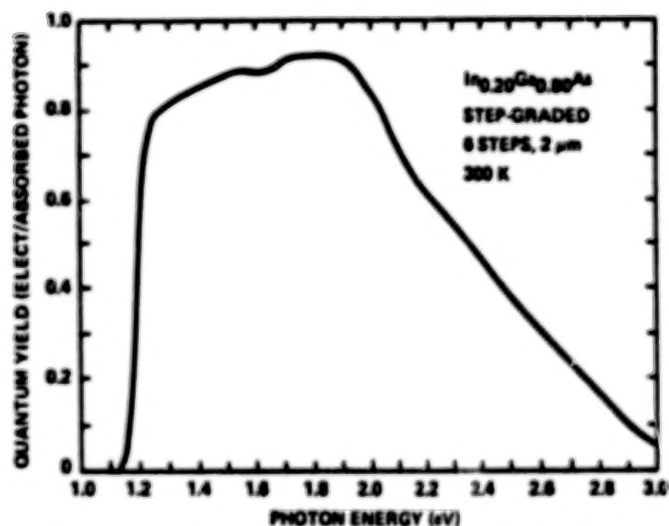


Figure 3. - Spectral response curve of $\text{Ga}_{0.75}\text{In}_{0.25}\text{As}$ lower cell of figure 2.

$\text{Ga}_{0.80}\text{In}_{0.20}\text{As} : \text{Zn}^{++}$	$0.3 \mu\text{m}$	CONTACT
$\text{Al}_{0.65}\text{Ga}_{0.15}\text{In}_{0.20}\text{As} : \text{Zn}$	$0.1 \mu\text{m}$	WINDOW
$\text{Ga}_{0.80}\text{In}_{0.20}\text{As} : \text{Zn}$	$0.8 \mu\text{m}$	EMITTER
$\text{Ga}_{0.80}\text{In}_{0.20}\text{As} : \text{Se}$	$1.0 \mu\text{m}$	COLLECTOR
$\text{Ga}_{1-x}\text{In}_x\text{As} : \text{Se}$	$2.0 \mu\text{m}$	GRADING (8 STEPS)
$\text{GaAs} : \text{Se}$	$0.5 \mu\text{m}$	BUFFER
$\text{GaAs} : \text{Sn}$		SUBSTRATE

PEAK QUANTUM EFFICIENCY = 92% (1.82 eV)
 J_{sc} (AMO) = 23.1 mA/cm^2
DIODE IDEALITY FACTOR = 1.2

Figure 2. - Cross section of typical $\text{Ga}_{0.75}\text{In}_{0.25}\text{As}$ ($E_g = 1.15 \text{ eV}$) lower cell.

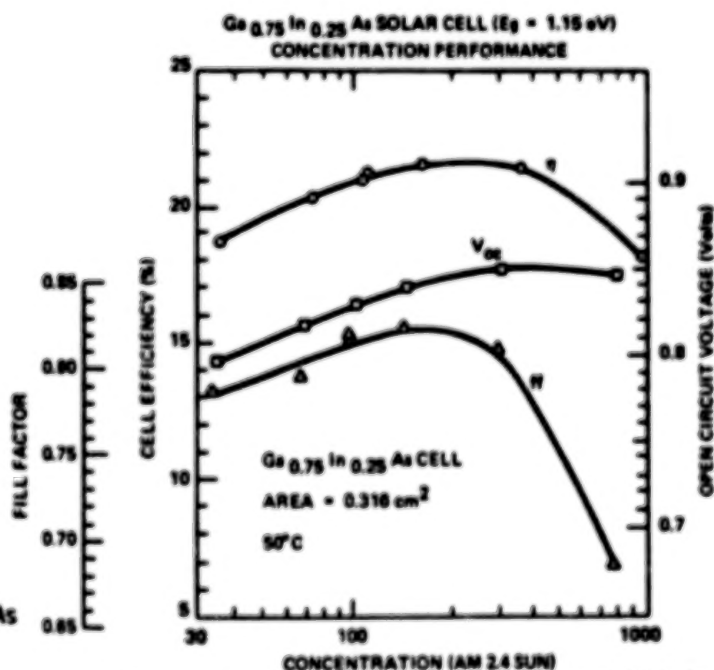


Figure 4. - Overall cell efficiency V_{OC} and fill factor of $\text{Ga}_{0.75}\text{In}_{0.25}\text{As}$ concentrator lower cell as function of incident AM2.4 concentrator.

ORIGINAL PAGE 12
OF POOR QUALITY

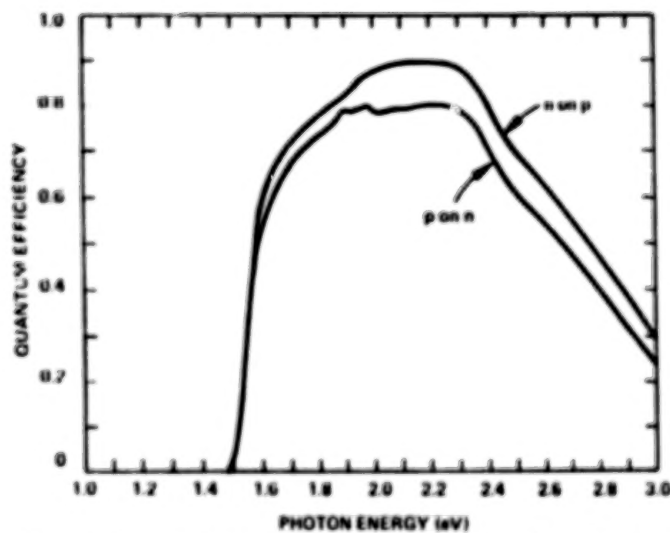


Figure 5. - Spectral response curves for $\text{Al}_{0.06}\text{Ga}_{0.94}\text{As}$ ($E_g = 1.55 \text{ eV}$) middle cells (p-on-n, n-on-p) grown by double mismatch on $\text{Ga}_{0.75}\text{In}_{0.25}\text{As}$.

$\text{GaAs} : \text{Mg}^{++}, \text{Se}^{++}$	1.0 μm	$p = 1.6 \times 10^{19}$ $n = 6.5 \times 10^{18}$
$\text{GaAs} : \text{Se}^{++}$	1.0 μm	$n = 6.5 \times 10^{18}$
$\text{GaAs} : \text{Sn}$		SUBSTRATE
GROWTH TEMP.	630 °C	730 °C
RESISTIVITY (Ω) AT 0.05 V	2.6	29
CONDUCTIVITY ($\text{A/V} \cdot \text{cm}^2$)	210	19.1

Figure 7. - Cross section of isolated, high-conductance GaAs interconnecting junction.

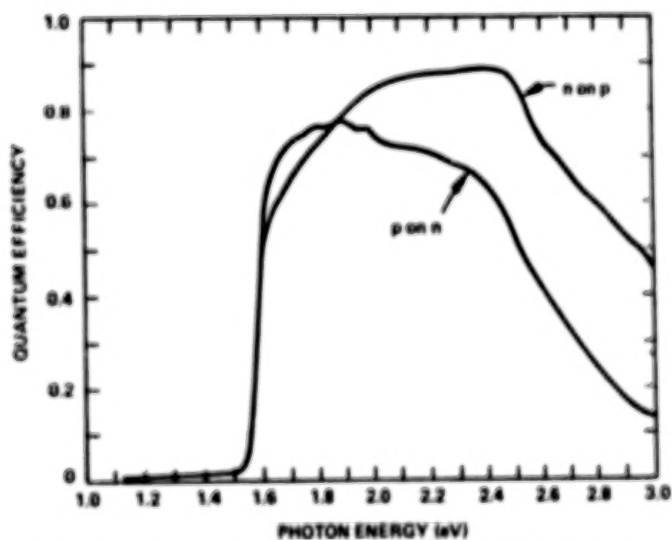


Figure 6. - Spectral response curves for $\text{GaAs}_{0.88}\text{P}_{0.12}$ ($E_g = 1.55 \text{ eV}$) middle cells (p-on-n, n-on-p) grown by double mismatch on $\text{Ga}_{0.75}\text{In}_{0.25}\text{As}$.

N84
29329

UNCLAS

HIGH-EFFICIENCY SOLAR CELLS FABRICATED BY VACUUM MO-CVD

L. M. Fraas, J. A. Cape, L. D. Partain, and P. S. McLeod
Chevron Research Co.
Los Angeles, California

High-efficiency, monolithic, two-color, three-terminal solar cells have been fabricated by a novel growth technique, vacuum metal-organic chemical vapor deposition. The technique uses the expensive metal alkyls efficiently and toxic gases sparingly. The fact that the outer chamber is constructed of nonbreakable stainless steel is an attractive safety feature associated with this deposition system.

INTRODUCTION

Over the last few years at Chevron, we have been developing high-efficiency multicolor solar cells for terrestrial applications. We are using a novel MO-CVD growth technique, vacuum MO-CVD, for growing the sequential epitaxial layers making up our multicolor cells. Since our growth technique uses the metal alkyls efficiently and since the outer reactor is nonbreakable, we feel that our epitaxial growth technology offers some advantages for production scale-up as well as some safety advantages. Our two-color cell design currently consists of a $\text{GaAs}(1-x)\text{P}(x)$ top cell and a $\text{GaAs}(1-y)\text{Sb}(y)$ bottom cell in a three-terminal configuration. We have chosen $\text{GaAs}(1-x)\text{P}(x)$ rather than the Al-containing III-V alloys in order to avoid reactions of Al with trace O and C impurities during layer growth. We have pioneered the development of this phosphide alloy cell (ref. 1). We are developing the antimony alloy cell rather than an In-based cell because the Sb-alkyl source vapor pressures are much higher than the In-alkyl vapor pressures. We feel that this will be an important advantage in cell production. In this paper, we first describe our vacuum Mo-CVD system and then the current status of our two-color, three-terminal solar cell work. Most of the work described herein is applicable to both space and terrestrial solar cells.

VACUUM MO-CVD

Basic Concepts

A schematic drawing of our vacuum MO-CVD deposition system is shown in Fig. 1. A reaction chamber is contained within a stainless steel vacuum chamber. The vacuum chamber can be pumped down to 10^{-8} torr by a turbomolecular pump, and the residual gases in this chamber can be monitored with a quadrupole gas analyzer. The reaction chamber consists of graphite and molybdenum refractory parts. The reactant gases (e.g., triethyl-Ga (TEGa) and arsine) are introduced into the bottom of the reaction chamber as shown. The substrate wafers are set over holes in the top of the reaction chamber and radiatively heated from above. Films are deposited on the bottom side of the wafers where the reactant gases contact the hot substrate surfaces. The arsine source is a 1:1 arsine-hydrogen mixture. The Ga source is pure TEGa introduced into the reaction chamber without a carrier gas. During a film deposition, the primary species in the reaction chamber is arsine at a pressure of approximately 5×10^{-3} torr, or 0.7 Pa. The GaAs films are deposited via the reaction



(1)

It follows that the hydrogen atom required to convert an ethyl radical to ethane is supplied by an arsine molecule.

Vacuum MO-CVD Versus "1 Atmosphere" MO-CVD

Vacuum MO-CVD differs from the conventional "1 atmosphere" MO-CVD in several respects. First, recall that in conventional MO-CVD there is a thin reaction boundary layer adjacent to the substrates. Reactants within this boundary layer can diffuse to the substrate and react, but reactants outside this layer simply pass by the substrate and are lost. This leads to a poor utilization efficiency for the expensive metal alkyl sources. In our system, the low pressure in the reaction chamber leads to long mean free paths, and nearly all of the metal alkyls hit the hot surfaces and react. If the top of the reaction chamber consists of wafer surface, over half of the metal alkyls contribute metal add-atoms to the epitaxial film. Long mean free paths also facilitate uniform depositions over large areas.

A second important difference between our vacuum MO-CVD system and conventional systems lies in the mode of construction. Conventional systems generally use quartz tubes and rf heating, whereas our system uses a chamber constructed of stainless steel and radiation heating. This difference is in part traceable to the difference in rates of heat conduction to the reactor walls. A gas at 1 atmosphere will efficiently transport heat away from the substrates to the reactor walls. So a lot of heat is required (rf heating) and inert reactor walls are required (quartz). The quartz is also required to avoid rf coupling. On the other hand, in our system the stainless steel chamber walls are thermally insulated from the substrates by vacuum. Three hundred and fifty watts of radiation heating is sufficient to maintain the substrates at a growth temperature of 625° C. Obviously, stainless steel does not break as easily as does quartz.

A final important difference between these two systems is that vacuum MO-CVD does not use a carrier gas. This implies a much lower total gas throughput for vacuum MO-CVD (i.e., 10 standard milliliters/min rather than 1 standard liter/min). It also means that the metal-alkyl vapor pressures and flows are monitored directly and that the purity of the metal-alkyls and the background purity of the system can be monitored with a quadrupole residual gas analyzer.

It is sometimes argued that reducing the hydrogen carrier gas pressure can be detrimental because the hydrogen carrier gas can play a role in reducing carbon contamination of the growing films. This argument assumes that the hydrogen atom required to convert an alkyl radical to an alkane molecule is supplied by an H₂ molecule. However, it is our belief that the AsH₃ molecule supplies this hydrogen atom. This follows because the As-H bond strength (65 kcal/mole) is much weaker than the H-H bond strength (104 kcal/mole). In support of our argument, Manasevit has pointed out that he has grown GaAs films using He as a carrier gas. Electrical performance data on our GaAs films grown by vacuum MO-CVD also indicate that the carbon content is less than 1 ppm.

Vacuum MO-CVD Versus MBE

Although some work has been reported on the growth of GaAs films in vacuum using molecular beam sources of trimethyl-Ga and arsine, our vacuum MO-CVD system is not a molecular beam system. An important difference is that our vacuum MO-CVD system contains an internal hot wall reaction chamber. Thus, in vacuum MO-CVD, a given arsine molecule will collide many times with the walls of the hot chamber and can hit the substrates hundreds of times before reacting or escaping through the exit orifice. In an MBE system, a given arsine molecule hits the substrate only once. It is our belief that reaction (1) occurs in two steps. First, a Ga-alkyl hits the surface and easily reacts to eliminate an alkyl radical. Then the alkyl radical is freed from the surface by reaction with arsine. The arsine reaction is the rate-limiting step. Therefore, a higher arsine beam flux is desirable. To be more specific, in the MBE work reported, the TMGa beam flux was $10^{15}/\text{cm}^2 \text{ sec}$ and the AsH₃ beam flux was $10^{16}/\text{cm}^2 \text{ sec}$. The TMGa reacted efficiently with one collision. In vacuum MO-CVD, the arsine flow rate is typically approximately 10 times the TEGa flow rate, but an arsine molecule hits a substrate 500 times before escaping. So, when the TEGa beam flux is $10^{15}/\text{cm}^2 \text{ sec}$, the AsH₃ beam flux is $5 \times 10^{18}/\text{cm}^2 \text{ sec}$. This higher beam flux insures that the alkyl radicals are converted to alkane molecules.

Advantages of Vacuum MO-CVD

The production scale-up advantages are the efficient use of the metal-alkyls and uniform coatings over large areas. The safety advantages are that the stainless steel construction avoids glass breakage and that low arsine throughputs are utilized.

III-V Film Properties

We have characterized III-V films grown by vacuum MO-CVD via room temperature Hall measurements, secondary ion mass spectroscopy (SIMS) profiling, and deep level transient spectroscopy (DLTS). Hall measurements made at room temperature on unintentionally doped GaAs samples show n-type conduction with carrier concentrations of $1 \times 10^{16}/\text{cm}^3$ and mobilities of $5000 \text{ cm}^2/\text{V sec}$. This implies an $N_A + N_D$ of $5 \times 10^{16}/\text{cm}^3$ or a shallow level density of 1 ppm. SIMS profiles of C and O show these impurities at the film-air and film-substrate interfaces. However, these impurities are below the detection limits ($1 \times 10^{18}/\text{cm}^3$) in the film bulk. DLTS measurements on GaAs(1-x)P(x) diodes show an EL2 peak with a density of up to $8 \times 10^{14}/\text{cm}^3$. It is our belief that these level densities can be reduced by source purifications and more systematic growth parameter studies. However, these level densities are adequate for solar cell fabrication.

TWO-COLOR, THREE-TERMINAL SOLAR CELL

Status

Figure 2 shows our two-color cell design. The visible light sensing cell is a p-on-n GaAs(1-x)P(x) cell with an Al(1-z)Ga(z)As(1-x)P(x) passivating window layer. This cell is fabricated on top of an n-on-p GaAs

(1 - y)Sb(y) IR sensing cell. Figure 3 shows the light-generated I-V curves for our best performing monolithic two-color cell to date. As can be seen, the active area efficiencies for the phosphide and antimonide alloy cells were 17.1 percent at 133x and 4.0 percent at 360x, respectively (AM2). TEGa, TMA1, AsH₃, and PH₃ were used to synthesize the top cell and TEGa, AsH₃, and trimethyl-antimony (TMSb) were used to synthesize the bottom cell. H₂Se and diethyl-zinc (DEZn) were used as dopant sources.

Problems

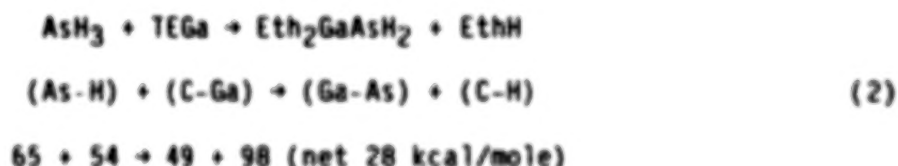
Although the results of Fig. 3 are encouraging, the theoretical AM1 (200x) conversion efficiency is 38 percent. Several problems can be identified. Three problems are highlighted here. First, the phosphide cell fill factor is starting to fall off at over 100x. This is attributable to insufficient doping density in the top p layer. This problem can therefore be solved by higher p-type doping densities. The more difficult problems at present are in the bottom cell. The current in this cell is low for two reasons. First, the GaAs(1 - y)Sb(y) cell band gap is too high because too little antimony has been incorporated, and second, the peak quantum yield is only 50 percent. We have determined that the junction in some of our antimony cells is over 0.5 μ m deep. So, interface recombination in the transition region between the two cells may explain the poor quantum yields in the low-band-gap cell. Since we had fabricated good shallow-junction antimony alloy cells previously (ref. 2), a deep junction could well explain poor quantum yields in the two-color device. In the shallow-junction devices, the junction depth was optimized by etching back from the top side. Ideally, the junction position should be precisely controlled by the dopant flow valves. Unfortunately, there are variable memory effects associated with Zn doping that position the junction somewhat arbitrarily. The solution may well be to use an alternative p-type dopant to precisely locate the antimony alloy cell junction just below the antimony-to-phosphide transition region.

Solution

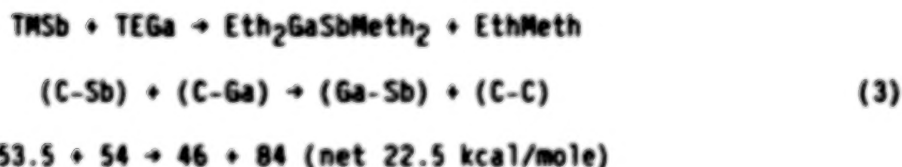
Two materials problems are at the root of the device problems stated above: First, we need an alternative less volatile p-type dopant. A less volatile dopant should allow for both higher doping levels and less memory. Second, we need to incorporate more antimony in our antimony alloy films.

Mg and Be are less volatile p-type dopants. We have begun experiments using (C₅H₅)₂Mg (ref. 3), but these experiments are still in progress and will not be reported herein.

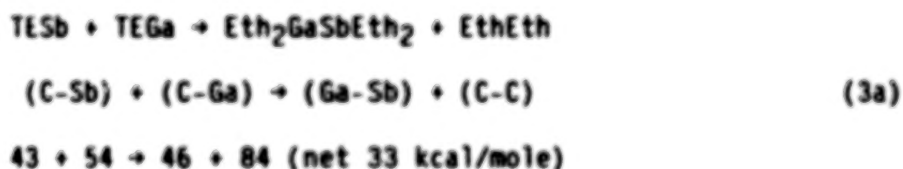
We have recently discovered that more antimony can be incorporated in GaAs(1 - y)Sb(y) films by using triethyl-Sb (TESb) rather than TMSb as the antimony source. We have now grown films with 1.0- and 1.1-eV band gaps. The fact that TESb should be the preferred source can be understood as follows. In growing GaAs(1 - y)Sb(y) using AsH₃ and TMSb, there are two competing reactions:



and



As can be seen from the bond strength calculation, the AsH_3 reaction is favored. This means that in order to incorporate antimony, one has to limit the AsH_3 flow and provide an excess of TMSb. This leads to a lot of hydrocarbon free radicals and possible carbon incorporation. It also leads to touchy control problems because one is trying to grow an As-rich solid phase from an antimony-rich gas phase. When TESb is substituted for TMSb, equation (3) becomes



Because the C-Sb bond strength is now weaker for the ethyl compound than for the methyl compound, the antimony reaction (3a) is now favored over the As reaction (2). This means that one grows films with an excess of AsH_3 in the gas phase and controls the Sb content with the TESb flow. Three advantages result: the Sb alkyl is used efficiently; the carbon content should be low; and composition control is facilitated.

CONCLUSIONS

Vacuum MO-CVD is a novel method of depositing III-V alloy films in sequence for multicolor solar cell fabrication. This technique uses expensive metal-alkyls efficiently and toxic gases sparingly and safely. By using this technique, two-color, three-terminal solar cells have been fabricated with active area efficiencies as high as 21 percent (AM2 under concentration). Triethyl-antimony has been used successfully to grow $\text{GaAs}(1-y)\text{Sb}(y)$ layers.

REFERENCES

1. L. M. Fraas, SPIE Vol. 23 - Semiconductor Growth Technology, 110 (1982)
2. L. M. Fraas et al., 16th IEEE PV Spec. Conf., 655 (1982).
3. C. R. Lewis et al., J. Elec. Materials 12, 507 (1983).
4. The Chem. of Metal-Carbon Bond, F. R. Hartley and S. Patai, eds., p. 69 (1982).

ORIGINAL PAGE
OF POOR QUALITY

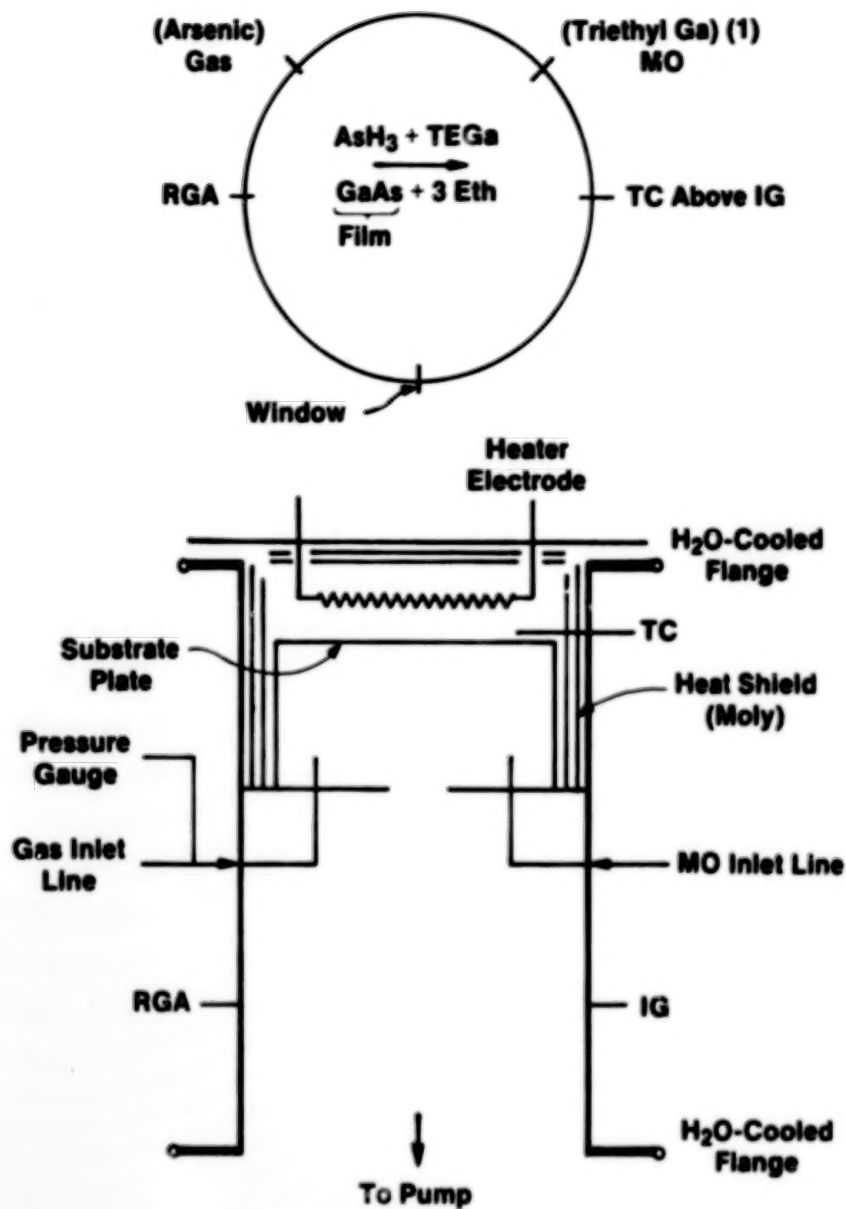
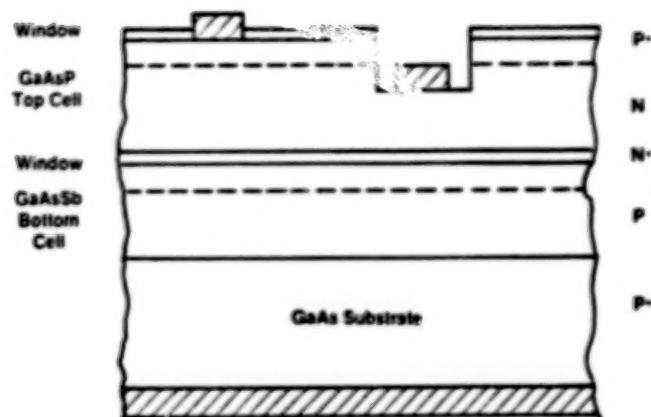


Figure 1. - Schematic cross section of Chevron Research vacuum MO-CVD reactor. Internally heated reaction chamber (at substrate plate) is fabricated from molybdenum and graphite. Outer chamber is stainless steel. (RGA = residual gas analyzer.)

ORIGINAL PAGE 19
OF POOR QUALITY



Advantages

1. No Shorting Junction Required
2. Easy Component Cell Testing
3. Current Matching Not Necessary

Figure 2. - Schematic cross section of two-color solar cell.

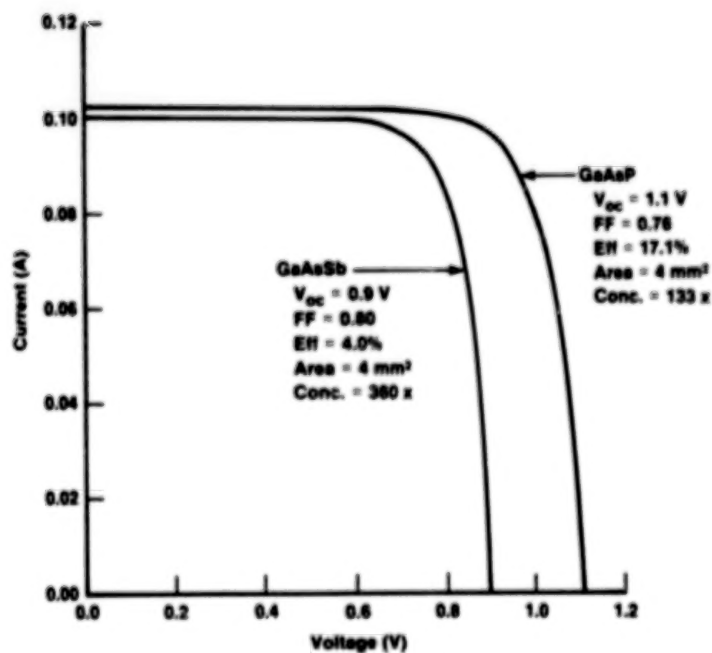


Figure 3. - Light-generated current versus voltage curves for two-junctions in a monolithic two-color device fabricated at Chevron Research. (The performance characteristics are indicated.)

N84
29330

UNCLAS

N84 29330

PLASMON DEVICE DESIGN: CONVERSION FROM SURFACE TO
JUNCTION PLASMONS WITH GRATING-COUPLEDERS

Lynn M. Anderson
National Aeronautics and Space Administration
Lewis Research Center
Cleveland, Ohio

The outlook on harnessing surface plasmons for solar energy conversion has brightened considerably: scaling calculations from Lewis and numerical studies from the University of Arizona's Optical Sciences Center indicate that grating-couplers should provide effective energy transfer between surface plasmons and slower modes localized in the tunnel diodes. Within first-order perturbation theory in grating amplitude, 90 percent efficient energy transfer occurs within micrometers for some realistic structures with experimental materials parameters. (Refined calculations and experiments are in progress.) Scaling laws will be derived. Seventy to 90 percent of the em field energy can be concentrated in the oxide layer of an MDM diode after the energy has been distributed by longer range modes that have less than 0.1 percent overlap with the tunneling region. The mode conversion allows the designer to separate requirements for energy transport and power production by inelastic tunneling.

N84
29331

UNCLAS

N84 29331

INTERACTIONS BETWEEN VOLUME AND SURFACE EM WAVES
IN LAYERED STRUCTURES

S. Ushioda
University of California
Irvine, California

If one wants to use thin films of metals and/or insulators in solar cell applications, one needs to understand the interactions between the incident volume EM wave (VEW) from the sun and the surface EM waves (SEW) of layered solid structures. A simple film on a substrate constitutes a three layered structure which supports several kinds of SEW. One of the SEW, surface plasmon polariton (SPP) in metals, has been suggested as an efficient receiver of solar radiation. Using light scattering spectroscopy, we have investigated the interaction of SPP in silver films on a glass substrate with the incident radiation and with optical phonons of an external medium in contact with the film. From this experiment we could determine the mean free path and the field strength of SPP. The same SPP plays an important role in light emitting tunnel junctions (LETJ) in which an electrical current is converted into VEW. We are studying the efficiency of light emission from LETJ through a prism coupler rather than through surface roughness. In another experiment we are investigating the coupling between phonon surface polaritons (PhSP) and optical guided waves (OGW) in thin films of GaP. Both OGW and PhSP are SEW of the dielectric film structure which can carry energy in the film. We will review these experiments and their relevance to photovoltaic cell applications.

N84
29332

UNCLAS

**PRELIMINARY CONCEPT OF A 100-KILOWATT MINIATURIZED
CASSEGRAINIAN CONCENTRATOR SOLAR ARRAY**

**Robert E. Patterson
TRW Space & Technology Group
Redondo Beach, California**

A miniaturized Cassegrainian concentrator (MCC) solar array system study was performed under contract NAS8-34131 to assess the practicality of assembling the basic MCC element into a total array system capable of producing multi-hundred kilowatts of power for Space Platform/Space Station or other low earth orbit long life-time missions. Preliminary mechanical and electrical subsystems were developed in order to determine first order performance characteristics. Results of the study support the feasibility of a 100-kilowatt MCC array system with beginning-of-life (BOL) performance of 160 W/m^2 and 28 W/kg and which would occupy approximately 8 lineal feet of Shuttle Cargo Bay in the fully stowed configuration. The performance numbers are based on 20 percent efficient (at operating temperature) solar cells and 0.25-millimeter thick electroformed nickel optics. These performance numbers can be improved upon significantly with the development of higher efficiency solar cells and/or lighter weight optics.

Key first-order array system design requirements were defined to provide a focus for the development of a representative array system concept for a "Space Station Type" application. These requirements are summarized in figure 1. Array area and W/kg performance requirements are consistent with previous concentrator array performance predictions. Element alignment requirements are based on predicted element off-pointing performance. The key design driver for this study is minimum cost per kilowatt at the array system level.

Summary results of the 100-kilowatt system study are presented in figure 2 to provide a general view of the overall concept developed. Figure 3 shows the size of the deployed 100-kilowatt array and identifies the location and name for each of the major components. The substrate for this configuration is made of graphite epoxy to minimize thermal distortion and is shown in figure 4. The entire panel is a one piece construction with an integral frame. The deployment concept is illustrated in figure 5 and is the same approach used on Skylab and now being employed on the Gamma Ray Observatory spacecraft. The performance prediction for the 100-kilowatt solar array system concept is summarized in figure 6 and shows a BOL performance of 160 W/m^2 and 28 W/kg . Array area is total gross panel area and, consequently, areal power density is based on total gross panel area.

Performance of the MCC solar array can be significantly improved upon with technology development as shown in figure 7. The use of lighter weight optics results in specific power (W/kg) improvement. Lighter weight optics can be achieved by either reducing baseline optical element thickness (0.25-millimeter thick electroformed nickel) or changing to a low density optical element base material (such as aluminum, copper, or plastic). The use of higher efficiency cells results in specific power and areal power improvements. The MCC approach offers early opportunity for the

application of advanced high efficiency cell types that may be more readily available as small area devices in large quantities from production facilities otherwise limited by market size and capital investment factors. Parallel-processing with surface plasmons ("Plasmon Cell") is a new strategy for efficient solar energy conversion which is being developed by NASA/LeRC and which could be utilized with the MCC. The "Plasmon Cell" offers the potential of 50-percent conversion efficiency.

Technical feasibility of the miniaturized Cassegrainian concentrator (MCC) has been demonstrated at the element level and preliminary system level conceptual studies have been encouraging. However, a number of related technology issues, listed in figure 8, must be successfully addressed to achieve technology readiness status for the HCC solar array.

PARAMETER	REQUIREMENT/DESIGN GOAL
ORBIT	235 NMI, 57° INC
BOL POWER	100 KW
ARRAY AREA	650 m ² MAXIMUM
BOL SPECIFIC POWER	27 W/KG MINIMUM
ELEMENT ALIGNMENT*	(A) ±3 DEGREE MAXIMUM (FROM NORMAL INCIDENCE) (B) 1.5 DEGREE MAXIMUM RSS (ALL ELEMENTS)
ARRAY ASSEMBLY	(A) SELF-DEPLOYABLE (B) ERECTABLE (EVA)
DEPLOYED DYNAMIC CHARACTERISTICS	COMPATIBILITY WITH SPACE PLATFORM DYNAMIC MODEL
STOWED DYNAMIC CHARACTERISTICS	COMPATIBILITY WITH SHUTTLE LAUNCH ENVIRONMENTS
BOL COST	100 TO 150 \$/W

* INCLUDES THERMAL DISTORTION, MANUFACTURING TOLERANCES, DYNAMIC DISTORTION, AND CONTROL SENSING ERROR.

Figure 1. - Key first-order array system design requirements for concentrator solar array.

ORIGINAL PAGE 19
OF POOR QUALITY

- THERMAL, OPTICAL AND ELECTRICAL TEST RESULTS DEMONSTRATE ELEMENT TECHNICAL FEASIBILITY
- DESIGN AND ANALYSIS SUPPORT FEASIBILITY OF 100-KW ARRAY SYSTEM WITH BOL PERFORMANCE OF 100 W/m^2 AND 20 W/kg
- NO "TECHNICAL BREAKTHROUGHS" ARE REQUIRED
 - 20% GaAs CONCENTRATOR CELLS HAVE BEEN PRODUCED
 - LOW COST ELECTROFORMED NI OPTICS ARE USED IN FLASHLIGHTS
 - GRAPHITE-EPOXY TECHNOLOGY IS USED IN SPACE AS WELL AS IN NUMEROUS COMMERCIAL TERRESTRIAL APPLICATIONS
- POTENTIAL OF 80 W/kg WITH TECHNOLOGY DEVELOPMENT

Figure 2. - Summary results of the 100-kW system study.

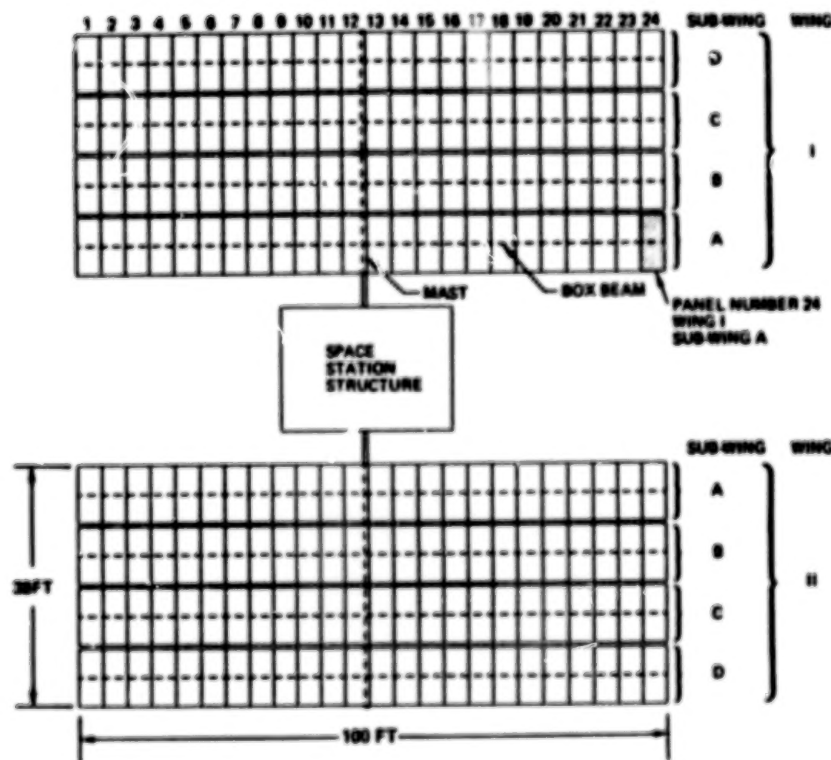


Figure 3. - Deployed 100-kW array.

ORIGINAL PAGE IS
OF POOR QUALITY

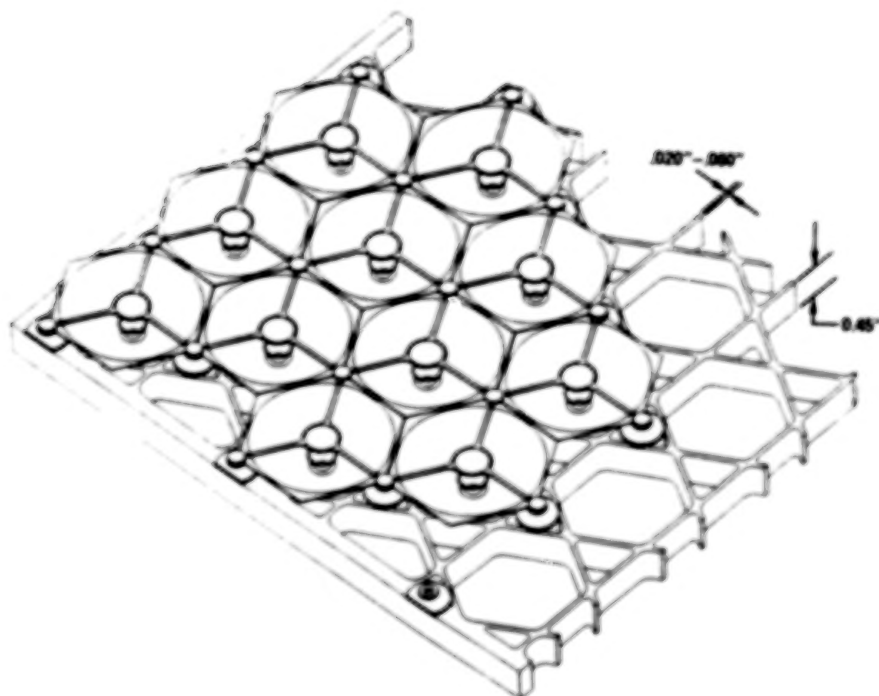


Figure 4. - Panel concept with tri-hex grid element support structure and integral frame.

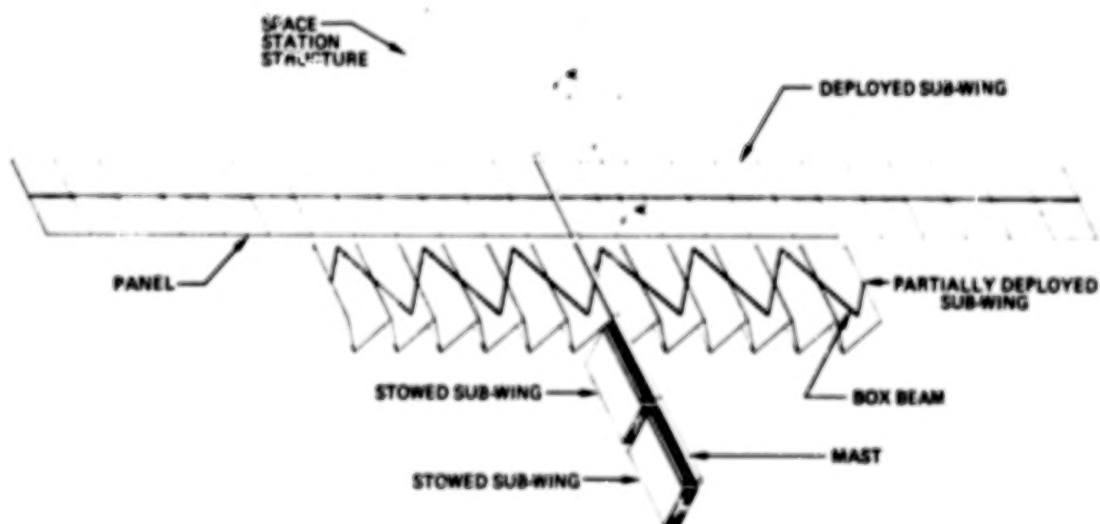


Figure 5. - Folded box beam deployment of concentrator solar array subwing.

ORIGINAL PAGE IS
OF POOR QUALITY

NOMINAL DESIGN FACTORS		NOMINAL PERFORMANCE	
PARAMETER	VALUE	PARAMETER	VALUE
CELL EFFICIENCY	20% AT 85°C	ARRAY POWER	104 kW
OPTICAL EFFICIENCY	0.81	ARRAY AREA	651 m ²
WIRING & DIODE DROP	0.97	ARRAY MASS	3700 kg
CELL MISMATCH	0.98	AREAL POWER	160 W/m ²
OFF-POINTING	0.98	SPECIFIC POWER	28 W/kg

Figure 6. - BOL performance prediction for a 235-nautical mile orbit.

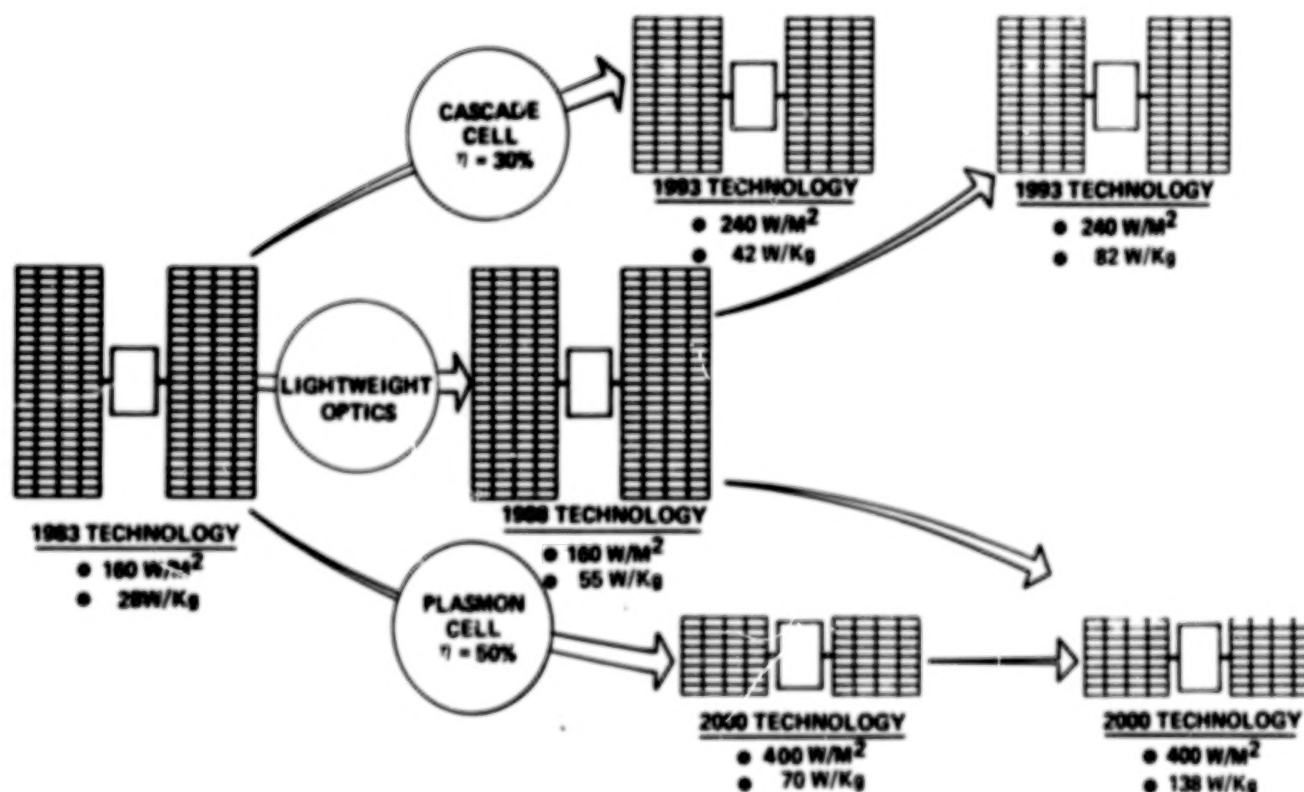


Figure 7. - Cassegrainian concentrator array enabling technology evolution.

- ENVIRONMENTAL STABILITY OF OPTICS
 - NATURAL PARTICLE RADIATION
 - THERMAL CYCLING
 - PLASMA INTERACTION
 - ATOMIC OXYGEN
 - ULTRA-VIOLET EXPOSURE
 - CONTAMINATION
- LIGHTWEIGHT SUBSTRATE/STRUCTURE DEVELOPMENT
 - LOW COST COMPOSITE FABRICATION
 - DIMENSIONAL STABILITY OF EXPOSED STRUCTURES
- LIGHTWEIGHT OPTICAL ELEMENT DEVELOPMENT
 - LOW COST FABRICATION
 - MAGNETIC EFFECTS ASSESSMENT
- CONCENTRATOR CELL DEVELOPMENT
 - EFFICIENCY IMPROVEMENT
 - CONTACT INTEGRITY
- SADA STIFFNESS
- SUB-WING MATING MECHANISM
- CONCENTRATOR ARRAY PERFORMANCE TESTING
 - PANEL ILLUMINATION TEST EQUIPMENT
 - MECHANICAL ALIGNMENT AND DEPLOYMENT SIMULATION FIXTURES

Figure 8. -- Cassegrainian concentrator solar array related technology issues.

N84
29333

UNCLAS

N84 29333

PERFORMANCE MEASUREMENT OF LOW CONCENTRATION RATIO*
SOLAR ARRAY FOR SPACE APPLICATION

Michael W. Mills
Rockwell International Corporation
Los Angeles, California

The measured performance of a silicon and a gallium-arsenide low concentration ratio solar array (LCRSA) element is presented. The element characteristics measured in natural sunlight were off-pointing performance and response to mechanical distortions. Laboratory measurements of individual silicon and gallium-arsenide solar cell assemblies were also made. The characteristics measured in the laboratory involved responses to temperature and intensity variations as well as to the application of reverse-bias potentials. The element design details covered include the materials, the solar cells, and the rationale for selecting these specific characteristics. The measured performance characteristics are contrasted with the predicted values for both laboratory testing and high-altitude natural sunlight testing. Excellent agreement between analytical predictions and measured performance was observed.

INTRODUCTION

The capabilities and overall usefulness of a manned space station will be directly linked to the utility power available for the users. Estimates of space station solar array capacity range from not less than 50 kilowatts to approximately 350 kilowatts. To supply this level of power, an entirely new approach to array design will be needed. Existing solar array designs do not readily scale up to this range, and the cost of such power is prohibitively high.

NASA's Marshall Space Flight Center funded previous concentrator technology studies (references 1 and 2) which promised lower cost of power. This technology was also shown to be consistent with the large area/high power applications and with the practical packaging requirements for Shuttle launch. Rockwell recently completed a preliminary design effort of an LCRSA for NASA MSFC (ref. 3) which satisfies emerging requirements listed below:

Low recurring cost of power (target of \$30/watt)

1984 technology readiness date

Low earth orbit, Shuttle launch

Consistency (interchangeability) with both silicon and gallium-arsenide solar cells

*The work reported in this paper was performed under NASA contract NAS8-34214 in support of the George C. Marshall Space Flight Center. The author wishes to thank the contract monitors W.L. Crabtree and M.R. Carruth.

Watts per kilogram governed by transportation cost

300 to 1000 kW per Shuttle launch

Four-sided concentrator configuration

Geometric concentration ratio (GCR) in the range of 2 to 6

This set of requirements is unique and as a whole quite different from that for a relatively low-power geosynchronous application. The array elements described in this paper are the photovoltaic building blocks of this preliminary array design (see fig. 1).

DESIGN DESCRIPTION

Previous configuration studies by Rockwell have shown the geometric configuration of the concentrator element used in this preliminary design to be simple to deploy and potentially low in cost (refs. 1, 2, and 3). The selection of a geometric concentration ratio of six is based in part on the requirement for "consistency" in the design of an element which can be used with either silicon or gallium-arsenide solar cells. The following description breaks the concentrator element down into three parts: reflectors, solar panel, and substrate/radiator.

The reflector design selected for the preliminary design is a rigid frame supporting a stretched thin film. The frame is molded from a polysulfone material filled with chopped graphite fibers. The film reflectors are bonded to this frame with a low-viscosity, high-temperature epoxy adhesive (EA 956). The reflectors are an aluminized 0.05-mm Kapton film. This material provides a low-cost, high specular-reflectance surface (88 percent specular, 90 percent total reflectance at 0.63 micrometers).

The reflector assembly comprise six reflector surfaces. These are hinged, using strips of aluminized Kapton tape, which allows the reflector assembly to fold for compact storage. The hinges are taped in such a manner that the side panels cannot fold past a nominally flat position and the corner hinges cannot fold past a nominally right-angle position from their collapsed state. In the collapsed condition this assembly is 13 mm thick. The physical size of the element in its collapsed and deployed state is given in figure 2.

The reflectors are attached to two stamped aluminum plates which serve as both a substrate for the solar cells and a radiator. The radiator size was selected so its surface area is twice as large as the continuous substrate material (beneath the solar cells). This results in an overall outside dimension of 350 mm by 350 mm when deployed. The thickness of this material is 0.8 mm. These dimensions were selected as a result of a radiator/solar cell cost trade study.

The radiator/substrate has a 0.03-mm Kapton insulator bonded with a layer (approximately 0.15 mm thick) of epoxy adhesive (EA 956). The low viscosity of this adhesive is needed to achieve a thin and void-free bondline. These criteria were established to maximize the thermal conductance to the substrate/radiator below.

The uninsulated surface of the substrate/radiator is coated with a matte-white high-temperature paint. This thermal control coating is intended to lower the solar alpha/thermal epsilon ratio in order to minimize the operating temperature. Typical values for this type of paint are $\alpha = 0.2$ and $\epsilon = 0.85$, $\alpha/\epsilon = 0.23$.

The solar cells are bonded to the radiator/substrate using silicone adhesives. The silicon panels are assembled by using RTV 577 applied to the back of individual cells and then pressing them on to the substrate and weighting them in place. The GaAs cells are assembled using DC93-500 and a vacuum bonding method. The intent in either case is to provide a relatively thin bondline of known and controlled thickness while ensuring complete, void-free coverage of the back surface.

Applied Solar Energy Corporation (ASEC) fabricated and delivered two mechanically interchangeable silicon solar panels. ASEC also supplied ten individual cells with interconnects attached.

Spectrolab, Incorporated, fabricated one solar panel and supplied ten interconnected gallium-arsenide cells. The solar cells were supplied by Hughes Research Laboratory.

In the test program, cells measuring 20-mm by 20-mm were selected for both cell types to provide comparative performance data. The preliminary design of the silicon half-panel for space application calls for 50-mm x 50-mm cells. The larger cells were selected because they offer a significant recurring cost advantage over the smaller ones in both the cell fabrication and in subsequent array assembly. The gallium-arsenide preliminary design for space application calls for the use of 20-mm by 20-mm solar cells since no lower recurring cost cells are projected to be available by the 1984 technology readiness date.

All solar cells delivered for use in this test program were assembled using a soldering process. The preliminary design for space application calls for a welded interconnection process. The selection of a welded process is based partly upon the relatively high on-orbit temperatures to be experienced. Just as important is the need to survive the extreme number of temperature cycles inherent in the low earth orbit environment. A solar array for space station application will be expected to survive ten or more years with more than 5,000 temperature cycles per year.

There are two different types of interconnects used in the construction of the two kinds of development hardware. The silicon solar panels use a silver mesh interconnect with an out-of-plane stress relief loop. The interconnect material is a perforated and expanded silver foil which is subsequently rolled and annealed. The individual interconnects are cut and formed from this. The GaAs cells are interconnected by using Spectrolab's proprietary Solaflex (a silver-plated Kovar material with out-of-plane stress relief loops).

TEST OBJECTIVES

The individual solar cells were used for laboratory characterizations under concentrated sunlight/elevated temperature conditions, for fabrication of secondary reference standards, and for reverse-bias testing. Laboratory solar simulator tests were also performed on the individual half panels. The laboratory tests were conducted at Rockwell's Seal Beach, California, facility using a Large Area Pulsed Solar Simulator (LAPSS) and the associated data acquisition unit. The laboratory testing served several purposes. The delivered hardware was checked for compliance with the requirements of the subcontract (buy-off). The ability to control the conditions of the laboratory allowed determination of response coefficients to change in intensity and temperature for analytical model development. The measured reverse-bias performance of the hardware was used for design purposes. The absolute response of these devices established a benchmark from which the program's 1985 projections of performance can be referenced. A summary of the laboratory tests performed is given in table I.

While the LAPSS is a high-fidelity reproduction of the space sunlight spectrum and intensity, the differences in apparent source size and divergence of the beam would affect the energy distribution on the solar panel. This prevented its use for testing the assembled concentrator elements. The predicted distributions for the space sunlight conditions are shown in figure 3. The conversion of energy with this unique distribution was a major concern of the design which required demonstration. These considerations demanded the use of natural sunlight for element testing.

The natural sunlight testing of the concentrator elements was performed to verify the performance of a unique physical configuration. Performance was measured as a function of off-angle pointing and various mechanical distortions. If the results of the testing confirmed the predicted terrestrial output, this would tend to validate the analytical methods and modeling used. Such results would also tend to validate the predicted space output since the same analytical methods were used but with a different environmental model. The concentrator element represents a complex structure (relative to most solar panels in use) and a new power production technology. Independent verification of performance was therefore desired. A summary of the natural sunlight tests is given in table II.

TEST DESCRIPTIONS AND RESULTS

The method used to generate illumination levels greater than one sun in the laboratory was to reduce the distance between the flash-lamp and the device under test. The reference standard solar cell was always in the same plane as the device under test. A cross-check was made between displacement and reference standard short circuit current (I_{sc}). The displacement (X_{cal}) between the reference standard and the lamps was initially measured when the output of the standard equaled its calibration value. This intensity and displacement were scaled using an inverse-squared relationship to determine a new displacement (X) at a higher intensity (fig. 4). When the reference standard was relocated from its initial location to the intended displacement, repeated measurements were made of its output. Good agreement between predicted and measured output was achieved (table III).

The one-sun I_{sc} calibration values (I_{cal}) for the reference standards were based upon the measurements performed by the subcontractors (Spectrolab and ASEC). The individual devices were measured against primary balloon-flight reference standards of the same generic cell type (identical spectral response). The following technique is normally used to correct measured data (I) to air mass zero (AMO) conditions (I').

$$I' = \frac{I_{cal}}{I_{sc}} \cdot I$$

This must be modified as follows for use at higher illumination levels, for which no I_{cal} is known:

$$I' = \left(\frac{I_{cal}}{I_{sc}} \right) \cdot \left(\frac{X_{cal}}{x} \right)^2 \cdot I$$

This is based upon the previously established assumption of reference standard I_{sc} linearity with intensity. It proved to be especially important at the elevated intensities to ensure that the front surface of the reference standard was in the same plane and equally distant from the lamp as the device under test. This was ensured through repeated measurements of the test setup geometry and by measurements of reference standard output in its normal position and in that of the device under test. The results of the intensity and temperature tests are given in figures 5 and 6.

Several of the solar cells were subjected to dark, reverse-bias tests. These were performed to assist the evaluation of the need for bypass diodes in the concentrator array design. The cells were tested after the installation of interconnects and were mounted on a water-cooled block at 28°C and 60°C. The characteristics were measured with a curve tracer. Figure 7 shows the typical results of the reverse-bias testings.

As a result of the pretest optical analyses of the concentrator element, it was expected there would be an interaction between the cell arrangement (series/parallel direction) and the direction of tilt in the off-pointing tests. The element was rotated in three directions: about the x-axis, about the y-axis, and about the diagonal. The measured short-circuit current and the calculated power output are shown as a function of pointing angle. Some sensitivity was shown to direction of tilt, but this was not dramatic. The results of the pointing tests are presented in figure 8.

The apparatus used for measuring the pointing angle of the element is shown schematically in figure 9. The location of the projected image of the small hole in an aperture cover on the receiver plane determines the alignment between the element optical axis and the solar direction. To facilitate measurement of pointing angle, a calibrated overlay is placed on the receiver to allow direct reading of angular orientation. During the alignment procedure, the aperture is covered and the element temperature drops. When the cover is removed, the panel is allowed to return to a steady-state temperature before the measurements are made.

The only technique used for calculating effective element output power (P) for the natural sunlight tests is given below, based upon a measured curve fill factor (CFF):

$$P = I_{sc} V_{oc} CFF$$

The curve fill factor was taken from the LAPSS test data for the individual devices when measured at AM0, CR=4, 70°C test conditions. The efficacy of this technique is demonstrated in the data contained in table IV, since the CFF value changes very little with dramatic variations in measurement conditions. During the testing, the panels were allowed to reach thermal equilibrium at or near their maximum power point, and V_{oc} was immediately measured at this temperature, followed by I_{sc} due to its lesser sensitivity to temperature.

The concentrator element was also tested for the sensitivity of its output to externally applied distortions of its geometry as well as to a full deployment. The change in output as a result of the deployment and distortions is shown in figure 10.

CONCLUSIONS

The objectives of the test program to provide experimental verification of LCRSA element performance were successfully met. The analytical prediction of output under conditions of normal and off-normal pointing in the terrestrial environment was substantiated. This agreement in both magnitude and sensitivity tends to validate the analytical models of the LCRSA element. These models can then be used with high confidence in the context of a space environment. The laboratory test program provided sufficient detail concerning solar cell performance to validate the cell models used in the preliminary design.

The project supervisor at Rockwell International was S. J. Nalbandian. Thanks also to Zdenek Backovsky and Edward French, whose support was vital in completing the test program and preparing this paper.

REFERENCES

1. Study of Multi-kW Solar Arrays for Earth Orbit Applications, Final Report. Contract NASA MSFC NAS8-3288. Rockwell International Corporation, SSD80-0064, May 15, 1980.
2. Study of Multi-kW Solar Arrays for Earth Orbit Application, Final Report. Lockheed Missile and Space Company, LMS80 715841, April, 1980.
3. Low Concentration Ratio Solar Array for Low Earth Orbit, Multi-100kW Application, Final Report. Contract NASA MSFC NAS8-34214. Rockwell International Corporation, SSD83-0075, July, 1983.

TABLE I. - LABORATORY TEST PROGRAM SUMMARY

Silicon and Gallium-Arsenide Individual Solar Cell Testing		
Temperature (°C)	Intensity (CR)	Characteristics
28, 50, 70	1	Output
28, 70	4	Output
28, 70	6	Output
28, 60	0	Reverse Bias
Silicon and Gallium-Arsenide Half-Panel Testing		
Temperature (°C)	Intensity (CR)	
Ambient (19-21)	1, 6	

TABLE II. - NATURAL SUNLIGHT TEST PROGRAM SUMMARY

Silicon/Silicon and Silicon/Gallium-Arsenide Concentrator Element Testing	
Normal-pointing	Output I, V
Off-pointing	Output I, V
Deployment	Output I, V
Distortions	Output I, V

TABLE III. - GOOD AGREEMENT BETWEEN MEASURED AND EXPECTED VALUES OF
REFERENCE STANDARD OUTPUTS AT ELEVATED CR LEVELS

CR Level	Silicon Standard	Gallium-Arsenide Standard
1	1.000	1.000
4	0.999	1.006
6	1.006	1.027
	$\left(\frac{1}{CR} \cdot \frac{I_{sc}}{I_{cal}} \right)$	$\left(\frac{1}{CR} \cdot \frac{I_{sc}}{I_{cal}} \right)$

TABLE IV. - MEASURED CURVE FILL FACTOR (CFF) VERSUS INTENSITY
AND TEMPERATURE VARIATIONS FOR SILICON AND GALLIUM-
ARSENIDE SOLAR CELLS

Silicon Solar Cell CFF			
CR	Temperature (°C)		
	28	50	70
1	0.78	0.75	0.74
4	0.80	-	0.76
6	0.80	-	0.75
Gallium-Arsenide Solar Cell CFF			
1	0.79	0.78	0.78
4	0.78	-	0.78
6	0.75	-	0.74

ORIGINAL PAGE IS
OF POOR QUALITY

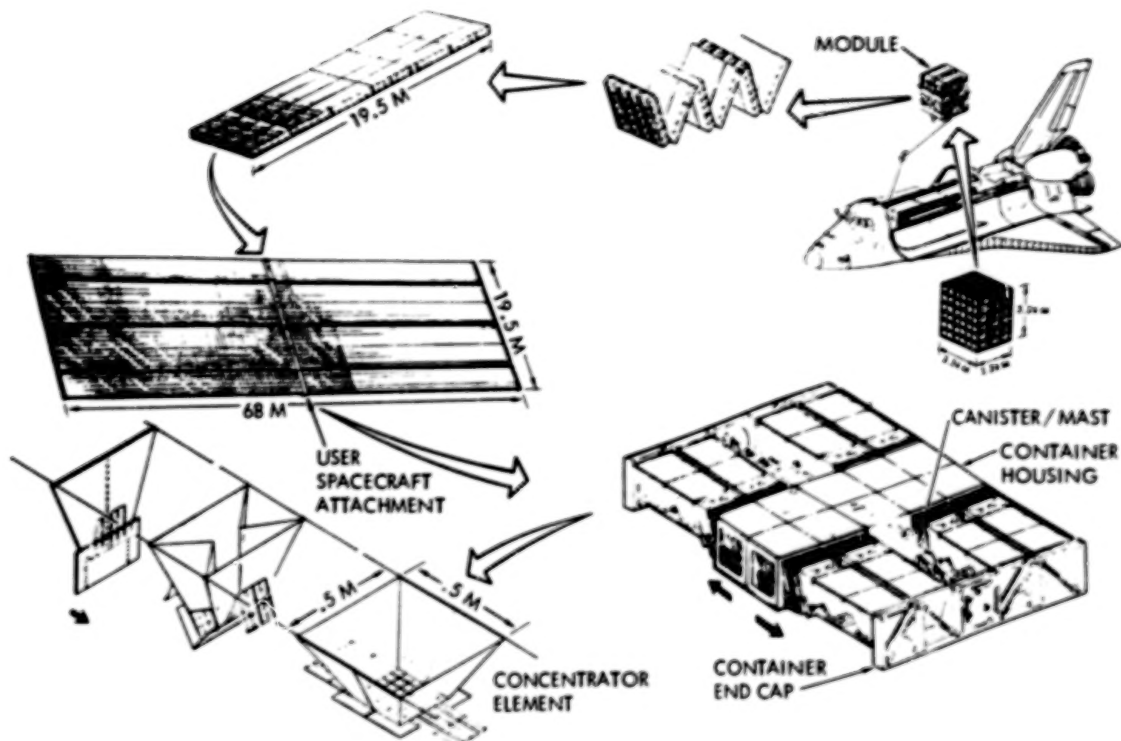
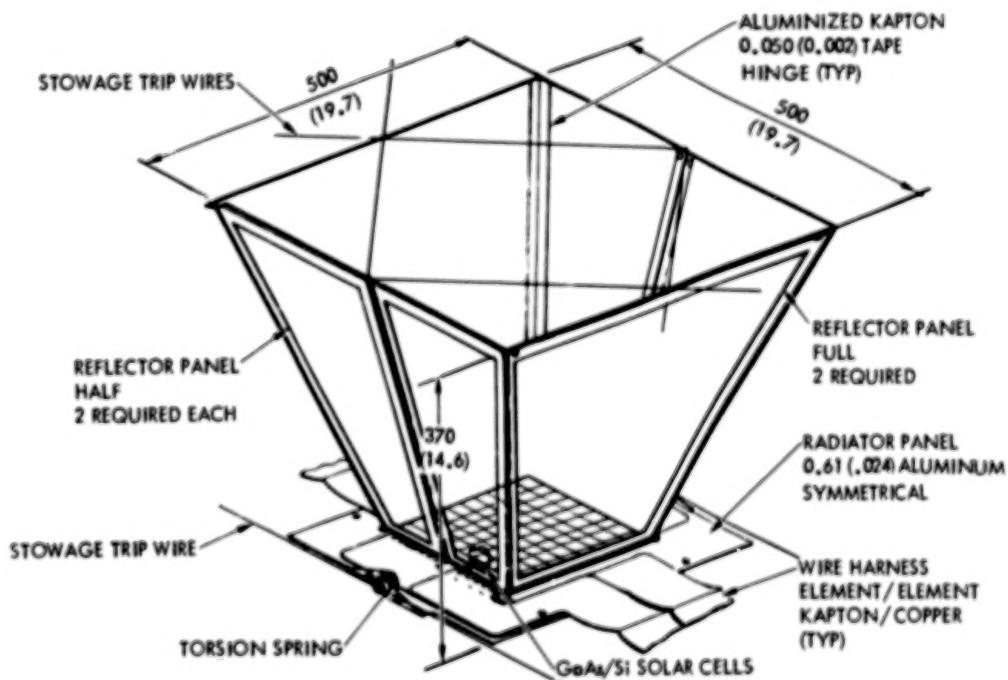


Figure 1. - Concentrator array module nomenclature.



ALL DIMENSIONS ARE IN mm WITH in. IN PARANTHESIS

Figure 2. - Concentrator element details.

ORIGINAL PAGE IS
OF POOR QUALITY

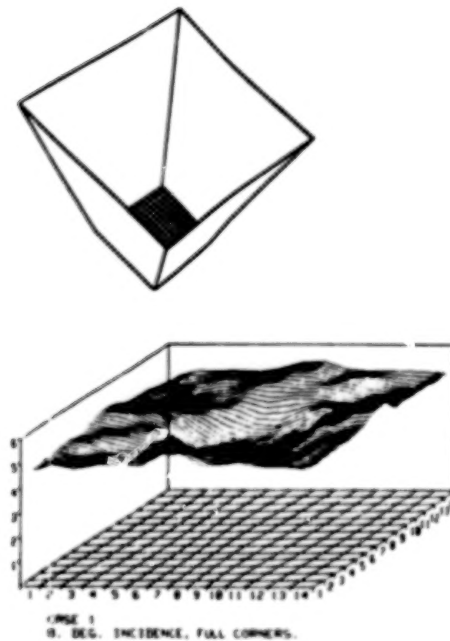


Figure 3. - Optical performance - fully reflecting corners (geometric CR = 6.0; reflectivity = 90 percent).

<div> <div> <div>■</div> <div>REF. STD.</div> </div> <div> <div>●</div> <div>DEVICE UNDER TEST</div> </div> </div> <div> <div>PULSED XENON SOURCE</div> </div>			
1	4	6	CR
7.20 m	3.60 m	2.94 m	SI DEVICES
6.74 m	3.37 m	2.75 m	GaAs DEVICES

Figure 4. - Test matrix and experimental setup (schematic).

ORIGINAL PAGE IS
OF POOR QUALITY

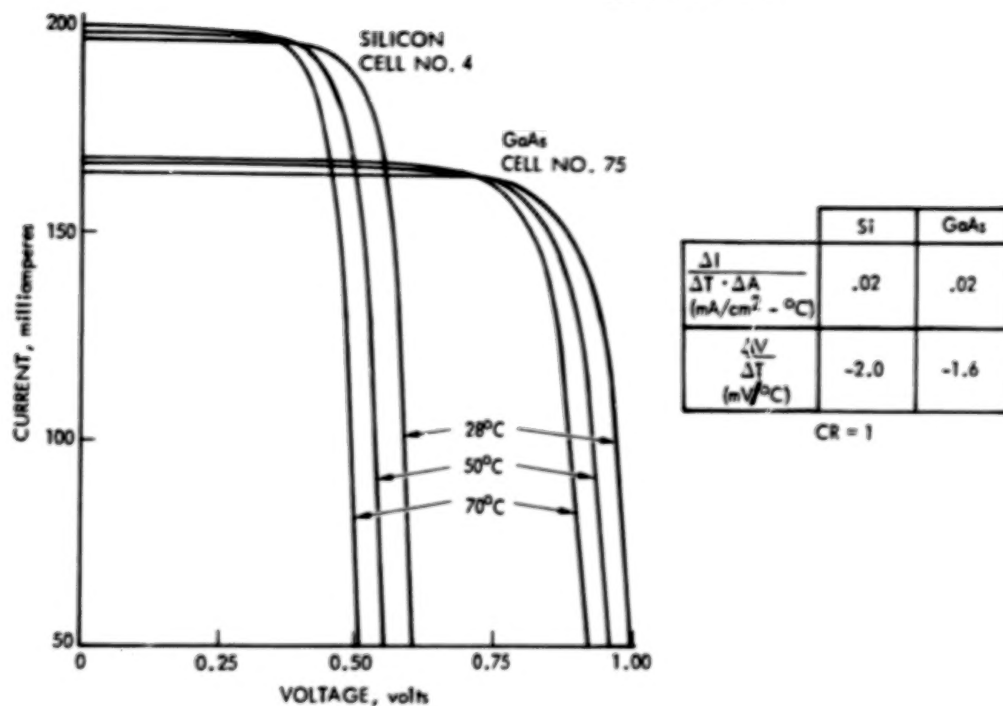


Figure 5. - Measured performance versus temperature for gallium-arsenide and silicon solar cells. Test conditions: CR = 1, AMO corrected.

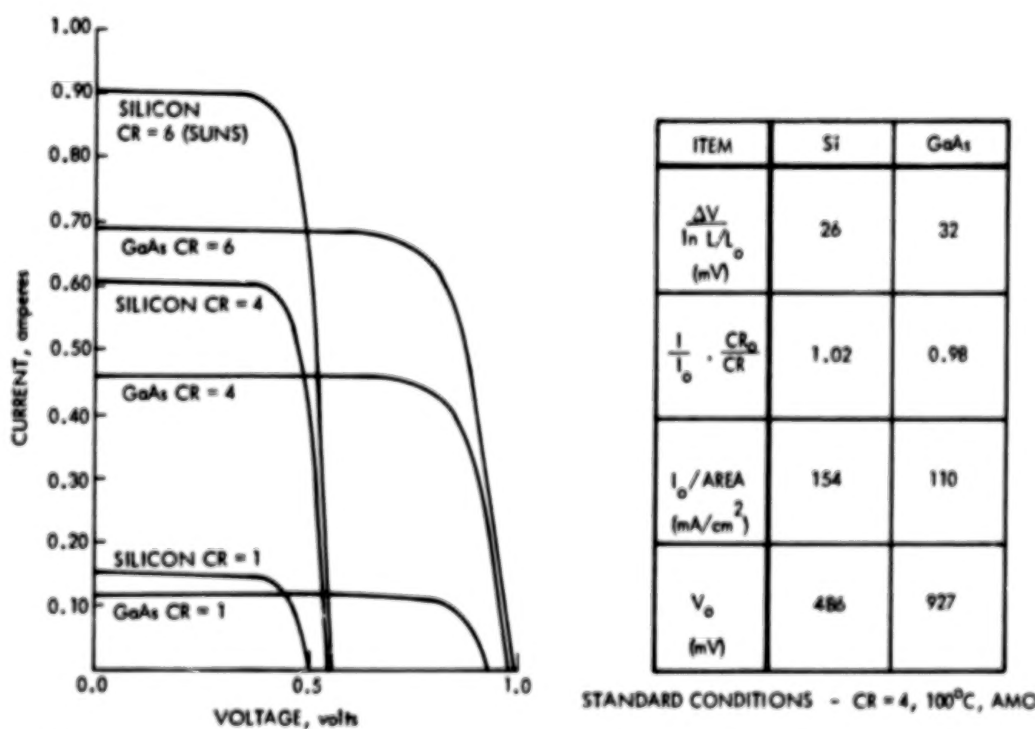


Figure 6. - Measured performance versus flux for gallium-arsenide and silicon solar cells. Test conditions: 70° C AMO corrected (CR = test flux, spectrally corrected).

ORIGINAL PAGE IS
OF POOR QUALITY

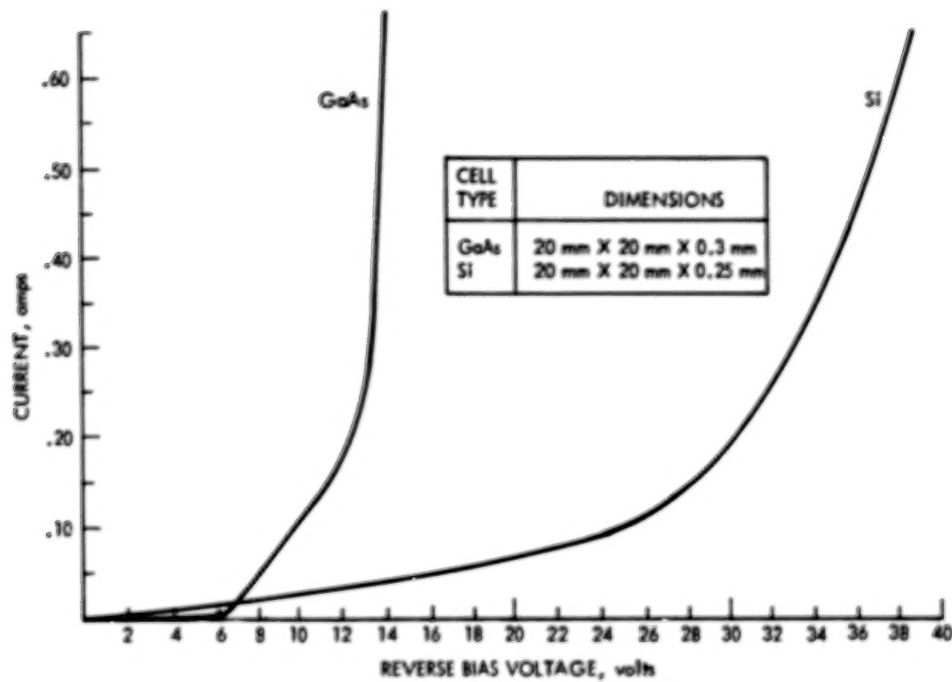


Figure 7. - Solar cell reverse bias characteristics (28° C, not illuminated).

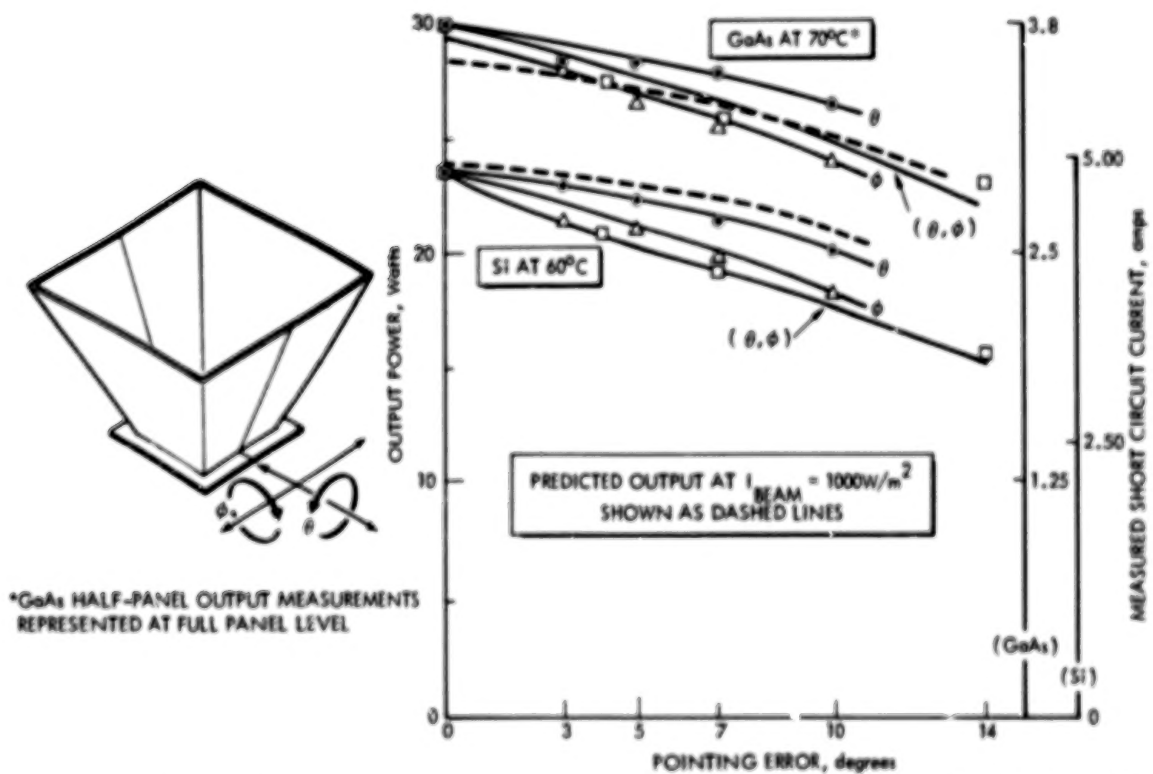


Figure 8. - Silicon full-panel and GaAs half-panel output versus pointing error (Table Mountain Observatory).

ORIGINAL PAGE IS
OF POOR QUALITY

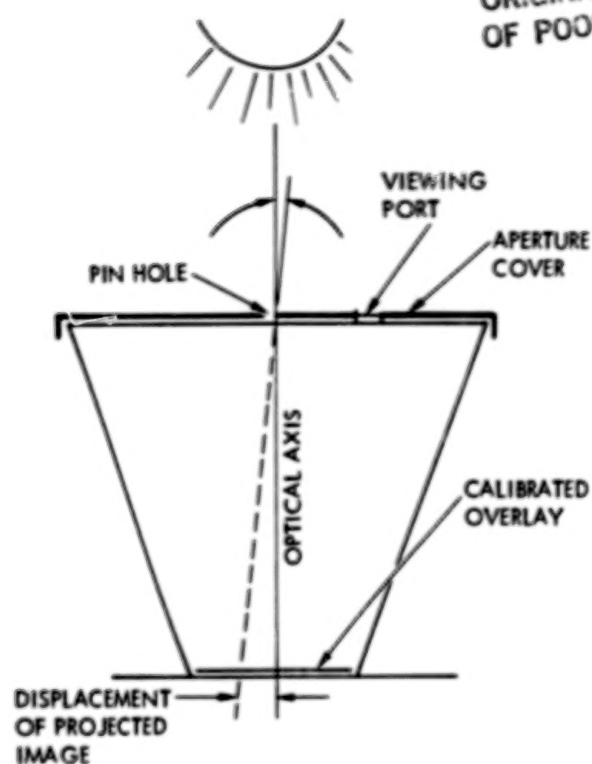


Figure 9. - Element pointing measurement technique.

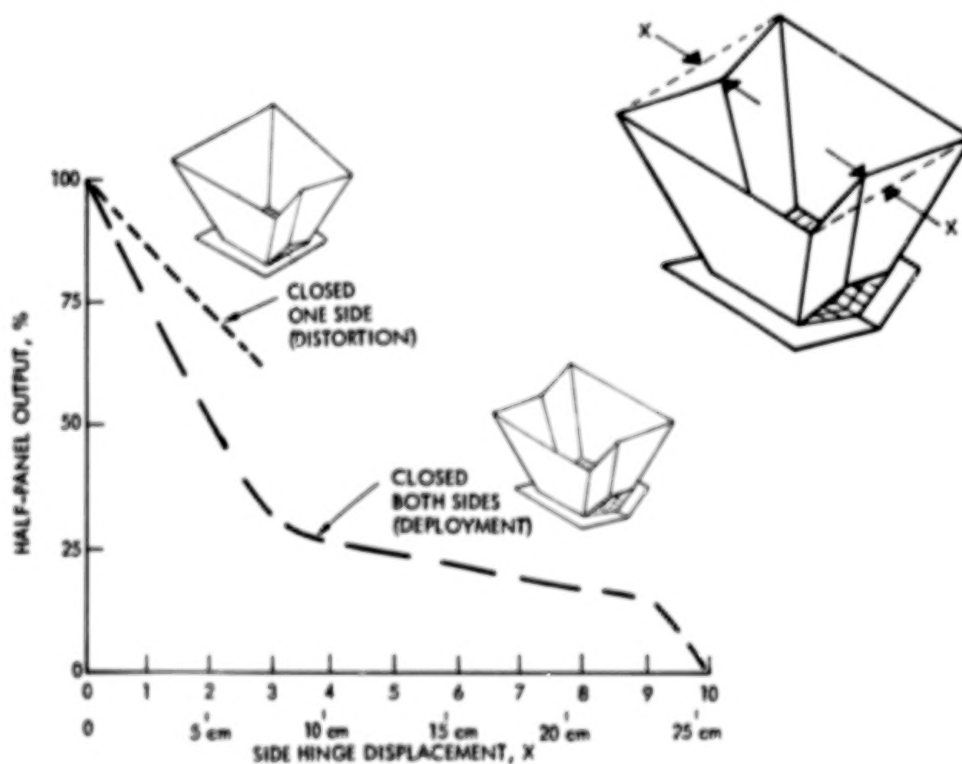


Figure 10. - Silicon half-panel output with hinge distortions.

N84
29334

UNCLAS

LN84 29334

PREFLIGHT STUDY OF SAN MARCO D/L GaAs SOLAR CELL PANELS*

John H. Day, Jr.
Goddard Space Flight Center
Greenbelt, Maryland

This paper describes, in general, the solar array for the San Marco D/L spacecraft and examines, in detail, the performance of 4 GaAs solar cell panels of which 2 will be included in the San Marco D/L flight solar array. In comparison to the typical Si solar cell panel for San Marco D/L, it is shown that each GaAs solar cell panel provides at least 23 percent more specific power at maximum output and 28°C. Also described here, are several measurements that will be made to evaluate the relative performance of Si and GaAs solar cell panels during the San Marco D/L flight.

INTRODUCTION

The San Marco D/L spacecraft, which is scheduled for launch in 1984, has a power system that consists of a solar array, rechargeable nickel-cadmium batteries, power conditioning and control electronics, and the spacecraft loads. The solar array consists of 28 panels connected in parallel. The panels are mounted inside the spacecraft behind transparent (transmissivity = 0.86) mica windows, in lieu of conventional exterior panels so that the spinning spacecraft may be aerodynamically suitable for accurate wind velocity measurements. As illustrated in figure 1, the windows and their respective array panels are positioned around the equator of the spacecraft in 2 loops. Each of 26 panels contains 56 2cm by 1cm Si cells connected in series. In addition, the San Marco D/L solar array consists of 2 GaAs solar cell panels, courtesy of the U.S. Air Force Aero Propulsion Laboratory (APL).

CELL CHARACTERISTICS

The San Marco D/L GaAs solar cells were fabricated by the APL contractor (ref. 1) using their liquid phase epitaxial growth technique (ref. 2) which has consistently produced 16 percent to 18 percent air mass zero (AM0) efficient GaAs solar cells. In addition to the conventional cell layers (substrate, n-doped and p-doped), this GaAs solar cell structure includes an (AlGa)As window layer that reduces carrier recombination near the GaAs surface to achieve high efficiency. Characteristics of the typical San Marco D/L GaAs solar cell are given in Table 1.

*The GaAs solar cell panels were supplied by the U.S. Air Force Aero Propulsion Laboratory.

PANEL STRUCTURE

A total of 5 GaAs solar cell panels (001, 002, 003, 004, and 005) were acquired for San Marco D/L. Panel 003 was used for qualification test performed by the manufacturer. The remaining 4 panels, of which 2 will be flown, were evaluated at the Goddard Space Flight Center (GSFC). Each GaAs solar array panel consists of 28 2cm by 2cm cells connected in series with conventional stress-relief interconnect tabs and adhered to a 170.0mm by 84.3mm micaply insulated aluminum panel, as illustrated in figure 2.

The 4 GaAs solar cell panels were subjected to a microscopic visual inspection for structural defects. No cell on either panel is loose; and only 1 cell on panel 001 is displaced from its ideal position in the array, as evidence of a repair. However, the cell is securely adhered to the panel and adequately shielded by its coverslide. The most persistent visible defects on all 4 panels are scratches on the surface of GaAs cells. One cell on panel 004 and 3 cells on panel 005 are scratched so deep as to suspect a cracked cell. For this reason, panels 001 and 002 were recommended to serve as the 2 GaAs flight panels.

ELECTRICAL PERFORMANCE

Each GaAs solar cell panel was exposed to 1 solar constant AMO irradiation, as simulated by a pulsed Xenon source. The intensity calibration was performed with a 2cm by 2cm silicon solar cell (balloon standard) that was thermally anchored at 28°C. The current-voltage (I-V) data were acquired during the light pulse while external load resistances were switched electronically. The I-V parameters that were reported (ref. 3) for the typical San Marco D/L Si solar panel are listed in Table 2 along with the I-V parameters for each GaAs solar cell panel. Each GaAs solar cell panel provides at least 23 percent more power than the typical Si solar cell panel at maximum output and 28°C.

The outputs of 2 solar cell panels (1 Si and 1 GaAs) will be monitored aboard San Marco D/L. The operating voltage of each panel will be approximately 21.8 volts which includes 20.5 volts for the regulated bus plus a 1.3 volt loss due to wiring and diode resistance. The operating current of each panel will depend on sun angle, panel temperature, and solar cell radiation damage. The sun angle will vary seasonally between +30° and -30° with respect to a normal to the equator of the spinning spacecraft. As a part of housekeeping for the attitude control system, the sun angle will be measured continuously with an accuracy of ±0.25° which allows each I-V measurement to be corrected for solar illumination. The operating temperature of each panel, according to preflight thermal analysis, will vary between -5°C and +45°C. A thermistor is mounted on the rear of each of the 2 test panels to provide an accurate temperature reading so that all I-V data can be extrapolated to a desired reference temperature.

The San Marco D/L radiation environment will cause the electrical performance of the flight solar array to degrade with time. A worst case orbit (period, 100 minutes; inclination, 3 degrees; perigee, 290 kilometers; and apogee, 1400 kilometers) was integrated over the most current space radiation models to estimate the multienergetic charged

particle fluxes that San Marco D/L will experience (ref. 4). Using the standard method for calculating solar cell radiation dosage in space (ref. 5) for an array panel with infinite rear shielding and .03cm thick fused silica front shielding, it is found that each San Marco D/L solar cell panel will receive equivalent 1MeV electron fluences of $3.78\text{E}+13$ electrons/cm² for Isc and $4.59\text{E}+13$ electrons/cm² for Voc & Pmax after 18 months in flight. Degradation factors for the I-V parameters of the San Marco D/L Si and GaAs solar cell types have been previously characterized as a function of 1MeV electron irradiation (ref. 6,7). The I-V parameters for each GaAs solar cell panel and the typical Si solar cell panel after irradiation are given in Table 3. However, it should be noted that the validity of an equivalent electron fluence for GaAs solar cells is under scrutiny (ref. 8). Thus, the accuracy of these results are subject to flight data verification. The actual degradation in the available power from the Si and GaAs test panels during the San Marco D/L flight may be compared to degradation factors which resulted from equivalent fluence calculations.

SUMMARY

Compared with Si solar cells for space applications, GaAs solar cells offer more electrical power per array area, especially at elevated array temperatures, and less degradation in available electrical power due to space radiations. However, the use of GaAs solar cells in space has been limited because of low availability, high cost, and the reliability of Si solar cell arrays. Previous space flight experiences with GaAs solar cells have been as on-board experiments. In contrast, San Marco D/L will utilize GaAs solar cells as an essential element in its power system. Thus, a successful performance by GaAs solar cell panels throughout the San Marco D/L mission would be a significant advancement toward the development of reliable GaAs solar arrays for space applications.

REFERENCES

1. Hughes Aircraft Company, Space Communications Group, "High Efficiency Solar Panel - GaAs Solar Cells," U.S. Air Force Aero Propulsion Laboratory Contract Number F33615-77-C-3150, January 1980.
2. R.C. Knechtli, G.S. Kamath, J. Ewan and R.Y. Loo, "Development of Space-Qualified GaAs Solar Cells," Hughes Research Laboratories, Research Report Number 534, April 1980.
3. Spectrolab, "Preliminary Data Package: San Marco D/L Solar Arrays," July 1980.
4. E.G. Stassinopoulos, "Analysis of the San Marco D/L Orbit Radiation Exposure," NASA-GSFC X-601-79-0, December 1978.
5. H.Y. Tada, J.R. Carter, Jr., B.E. Anspaugh, and R.G. Downing, "Solar Cell Radiation Handbook," 3rd Edition, NASA-JPL Publication 82-69, November 1980.

6. B.E. Anspaugh, D.M. Beckert, R.G. Downing, T.F. Miyahira, and R.S. Weiss, "Electrical Characteristics of Spectrolab BSF, BSR, Textured 290-Micron Solar Cells (K7) as a Function of Intensity Temperature and Irradiation," NASA-JPL Publication 78-15, Volume VIII, September 1979.
7. B.E. Anspaugh, R.G. Downing, T.F. Miyahira, and R.S. Weiss, "Electrical Characteristics of Hughes Liquid Phase Epitaxy Gallium Arsenide Solar Cells as a Function of Intensity, Temperature and Irradiation," NASA-JPL Publication 78-15, Volume XIV, November 1981.
8. J.W. Wilson, J.J. Smith, and G.H. Walker, "On the Validity of Equivalent Electron Fluence for the GaAs Solar Cells," IEEE Photovoltaic Specialists Conference, September 1982.

TABLE 1. - GaAs CELL CHARACTERISTICS (1)

<u>Property</u>	<u>Description</u>
n contact	(Au-Ge-Ni)Ag
substrate layer	GaAs, Te doped
n layer	GaAs, Sn doped
p layer	GaAs, Be doped
window layer	(AlGa)As, Be doped
p contact	(Au-Zn)Ag
AR coating	Ta ₂ O ₅
peak power	24.4mW/cm ²
cell area	2cm x 2cm
cell thickness	.03cm
coverslide thickness	.03cm

TABLE 2. - I-V PARAMETERS AT 28° C BEFORE IRRADIATION

I-V Parameter	Panel				
	GaAs <u>001</u>	GaAs <u>002</u>	GaAs <u>004</u>	GaAs <u>005</u>	Si <u>Typical</u>
Isc (A)	.114	.116	.117	.115	.086
Voc (V)	28.8	28.7	29.1	29.1	32.1
Pmax (W)	2.63	2.64	2.70	2.60	2.11
Imp (A)	.104	.107	.107	.103	.081
Vmp (V)	25.4	24.6	25.3	25.3	26.2
Vop (V)	21.8	21.8	21.8	21.8	21.8
Iop (A)	.109	.112	.111	.109	.085
Pop (W)	2.38	2.43	2.41	2.38	1.86

TABLE 3. - I-V PARAMETERS AT 28° C AFTER IRRADIATION

I-V Parameter	Panel				
	GaAs <u>001</u>	GaAs <u>002</u>	GaAs <u>004</u>	GaAs <u>005</u>	Si <u>Typical</u>
Isc (A)	.111	.113	.113	.112	.083
Voc (V)	28.1	28.0	28.4	28.3	30.3
Pmax (W)	2.53	2.54	2.61	2.51	1.88
Imp (A)	.101	.104	.104	.100	.077
Vmp (V)	25.1	24.4	25.0	25.0	24.5
Vop (V)	21.8	21.8	21.8	21.8	21.8
Iop (A)	.106	.109	.108	.106	.082
Pop (W)	2.32	2.37	2.35	2.32	1.78

ORIGINAL PAGE 13
OF POOR QUALITY

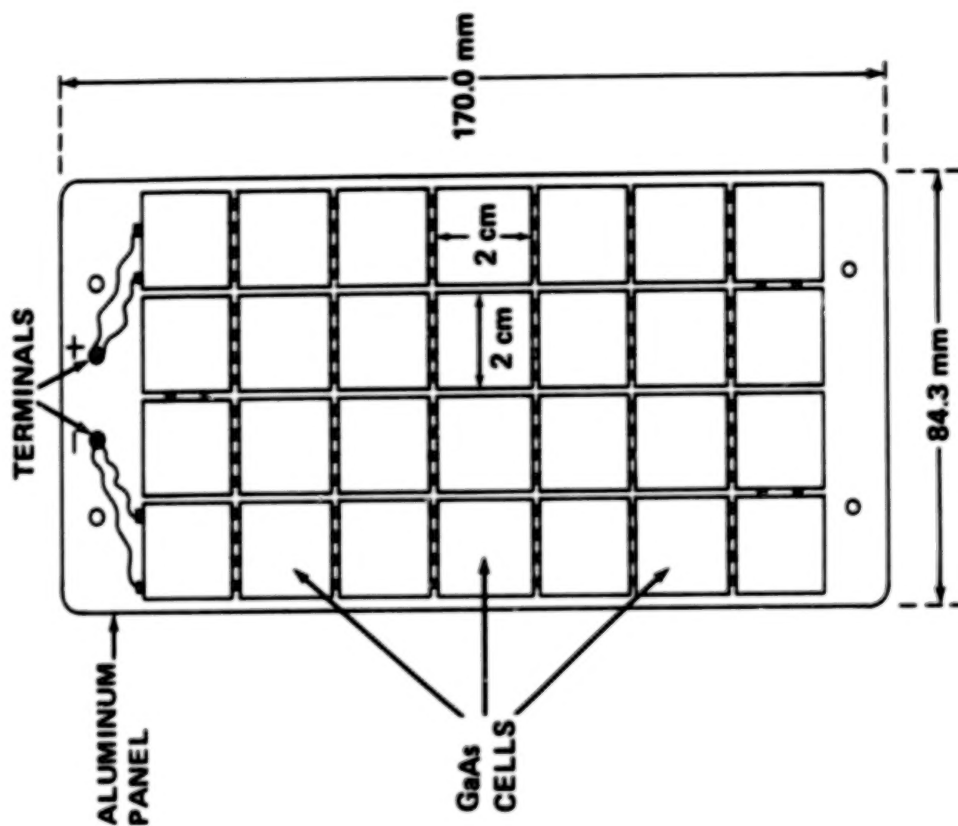


Figure 2. - GaAs solar cell panel configuration.

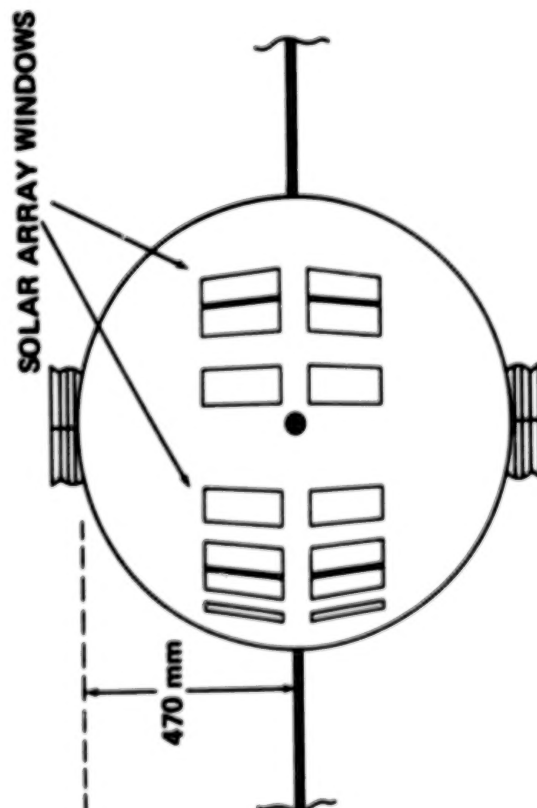


Figure 1. - San Marco D/L solar array configuration.

N84
29335

UNCLAS

N84 29335

PRELIMINARY SPACE STATION SOLAR ARRAY
STRUCTURAL DESIGN STUDY

John T. Dorsey, Harold G. Bush, and Martin M. Mikulas, Jr.
National Aeronautics and Space Administration
Langley Research Center
Hampton, Virginia

A preliminary design study was conducted to identify structurally efficient ways to support the large solar arrays ($3,716 \text{ m}^2$ ($40,000 \text{ ft}^2$)) which are currently being considered for space station. An erectable truss concept is presented for the on orbit construction of winged solar arrays. The means for future growth, maintenance, and repair are integrally designed into this concept. Results from parametric studies, which highlight the physical and structural differences between various configuration options are presented. Consideration is given to both solar blanket and hard panel arrays.

INTRODUCTION

Now that the Space Transportation System (STS) is fully operational, the aerospace community can begin considering projects which require large structures in space. As a result, the possibility of orbiting a permanent U.S. space station by the early 1990's is receiving increasing attention. (See reference 1.) A system consisting of the STS and a permanent space station would permit efficient and continuous operation in the space environment. (See reference 2.)

The space station, like all spacecraft, is subject to a number of factors which drive the structural design and are directly related to cost. Any large spacecraft which is to be placed in orbit by the STS is subject to at least four design drivers. They are; weight, packaging, structural predictability, and technology readiness.

The first two drivers, weight and packaging, are directly related to restrictions imposed by the shuttle. All payloads must fit within the orbiter bay, a cylindrical volume approximately 4.57 m (15 ft) in diameter and 18.3 m (60 ft) long. Also, the payload weight must be kept at or under 29,500 kg (65,000 lb), the shuttle limit to low Earth orbit (LEO).

The total space station weight has a direct influence on transportation costs to LEO. Since the cost of a shuttle flight is fixed, it is desirable to fully load each flight, thus minimizing the cost per pound to orbit. In reference 3, it was shown that shuttle transportation costs dominate the spacecraft hardware costs. Thus, it is imperative that weight minimization and packaging be emphasized in the spacecraft design.

The space station will be a very large structure with high stiffness requirements for attitude control purposes, but low requirements for strength because of the small loads encountered in LEO. Since a large space station cannot be assembled and tested on the ground, the issue of structural predictability becomes important. The thermal, static and dynamic behavior of the complete space station will be required

before it is placed in orbit and, therefore, must be accurately predicted using available computer codes. Test data will be available for some of the space station components and can be used to calibrate corresponding analytical models. There remains the problem, however, of accurately predicting the behavior of the total space station assemblage using a limited amount of test data, and having a high level of confidence in the results. Manufacturing structural components such as struts, joints and connectors precisely and requiring their assembly with little free play will increase the confidence in the accuracy of any analytical structural predictions.

A large amount of on orbit assembly will be required for the space station. The various habitat, service, etc. modules must be either structurally connected together, or connected to a support truss, and then linked with pressure tunnels. The solar arrays and their support structure, support trusses, etc. will have to be either erected or deployed once in orbit.

The decision on whether to use erectable or deployable technology for space station will depend on the readiness of each technology at the time a final design decision is made. Currently, erectable technology has demonstrated structural predictability and is limited only by EVA readiness. Current deployable structures, although limited to masts, booms and small antennas, have flown on actual space missions. Deployable trusses, however, should be ready by the late 1980's and thus available for a space station. Since, depending on the situation, erectable and deployable structures each have certain advantages to offer, it is likely that a space station will incorporate a combination of the two technologies.

INITIAL SPACE STATION CONCEPT

Figure 1 shows an initial space station study configuration. The space station consists of a central collection of logistics, habitat, utility, laboratory and docking modules, and two large solar arrays. The arrays are shown mounted to gimbals on the sides of a utility module. Gimbaling the solar arrays allows them to follow the sun during the orbit while the modules remain Earth pointed at all times. Each array is 76.2 m (250 ft) long and 24.4 m (80 ft) wide with a surface area of 1,858 m² (20,000 ft²). The total power generated by the two solar arrays is 150 kw at the bus bar.

A characteristic of this design is a very low (on the order of .008 to .012 Hz) space station fundamental frequency which is driven by the large flexible solar wings. Increasing the stiffness of the solar array structure, and thus increasing the space station fundamental frequency, is a desirable goal in order to reduce control system complexity and mass. Therefore, space station/solar array concepts were designed which had a fundamental frequency of at least 0.4 Hz.

INITIAL STUDY CONSIDERATIONS

One basic space station design requirement being examined by NASA concerns the power level. The fully mature station must deliver 150 kw of power at the bus bar and thus, would require approximately 3,716 m² (40,000 ft²) of silicon solar cells. Figure 2 summarizes four initial considerations which will also have a direct impact on the final space station design and configuration.

A space station in low Earth orbit will experience drag forces because of the large frontal area of the solar arrays. The total amount of drag experienced by the space station per orbit will be a function of how the solar arrays are oriented with respect to the orbital flight path. One option, shown in figure 2a, is to keep the arrays sun pointing. For a station flown in this mode, there will be times when the arrays are parallel to the flight path, thus exposing a minimum frontal area and in a minimum drag configuration, and times when the arrays are perpendicular to the flight path, giving maximum frontal area and a maximum drag configuration. Another flight mode, keeps the space station in a minimum drag configuration so that the solar arrays are always parallel to the flight path (see figure 2a). The quantity of fuel required to maintain the proper space station altitude will be a function of the drag forces integrated over an entire orbit.

Kyser (see reference 4) has shown that for a given total amount of power generated per orbit, a minimum drag solar array would require 80% more collection area than a sun pointing array. Associated with the increased array area would be an increased initial space station weight which, in turn, would increase initial launch and fabrication costs.

The total power system weight, however, does not include just the array and battery storage weight. It must also include the weight of fuel required to maintain the orbital altitude for a particular drag configuration. Figure 3 shows the total power system weight (array weight + battery weight + fuel weight) as a function of design lifetime for a minimum drag solar array and a sun pointing solar array. The initial system weight is approximately 50 percent greater for the minimum drag array than it is for the sun pointing array. After a year in orbit the fuel saved by the minimum drag array becomes larger than its initial weight gain and the total system weights are equal for the two arrays. The predicted savings in orbital weight of a minimum drag array is 26,000 kg (57,000 lb, or one shuttle flight) over a 20 year lifetime. The drag issue clearly must be addressed because of the large impact it will have on the space station structural design.

The space station stiffness must be considered with respect to the attitude control problem. In general, the stiffer a spacecraft, the less massive and complex the control system equipment (such as control moment gyros) must be. For this study, a fundamental free-free elastic frequency of 0.5 Hz was chosen as a design goal (see figure 2b) for the station and solar array structure.

The solar array technology which will be available for the space station in the early 1990's must also be considered in the design process. In this study, it was assumed that solar array blanket technology would weigh on the order of 1.1 kg/m^2 (0.22 lb/ft^2) and hard panels, or concentrator arrays, would weigh approximately 4.9 kg/m^2 (1 lb/ft^2) (see figure 2c).

The final requirement considered in this design study was the modularity and growth potential of the concept (see figure 2d). Although the final space station configuration will consist of many modules and enough solar arrays to generate 150 kw of power, it may be several years before that level is required. The initial space station may be of modest size with a very minimum power requirement. However, space station growth, from its initial to final configuration, must be carefully planned and integrally designed into the structure from the start.

SPACE STATION SOLAR ARRAY CONFIGURATIONS

The functional requirements discussed in the previous section form the basis from which the concepts described in this study were generated. In general, most attention went into designing the solar array support structure, the arrays themselves, and how the two might be integrated into a system with growth capability. The space station/solar array concepts which will be discussed cover a range of assumptions on drag configurations, type of solar array, and structural assembly technology. Assessing a variety of different concepts provides the preliminary data needed for making decisions concerning the final space station design or configuration.

Erectable Solar Array Support Structure

The initial 150 kw space station study configuration had a low fundamental frequency because of (1) the extreme length of the large solar array wings, and (2) the low stiffness of the coilable longeron truss-beam which deployed and then supported the wings. The fundamental frequency can be increased by making the arrays shorter and wider, and by increasing the stiffness of the support truss. Since the maximum diameter of a coilable longeron beam is limited to less than one meter, this deployable truss-beam concept cannot supply adequate stiffness for a large solar array. The concept also does not provide the solar array growth potential which is required.

The structural approach devised to meet the requirements for stiffness as well as modularity and growth is shown in figure 4. The required stiffness of each solar array wing is obtained by erecting a large structural backbone truss. Solar blankets are deployed off of the truss and, as part of the erection process, are propped at their free end by outriggers. Also, the installation of various systems (such as power and fluid) can be integrated into the erection process. The erector, in addition to providing a maintenance and repair capability, will provide the solar array with the means for modular growth.

Figure 4 also shows details of the solar array and support structure, the transition truss, and module with gimbal. The solar array support structure is a single laced three longeron beam built with .051 m (2 inch) diameter graphite-epoxy tubes. Astronauts, riding a moving erector which runs along the beam interior, would erect the triangular beam. The solar arrays, which are either rolled up or folded solar blankets, are attached to the top longeron of the truss at one end as shown. A deployable mast serves to both deploy the blankets and provide torsional stiffness for the arrays. A pair of outriggers extend from hard points on the bottom longeron of the truss and connect to the free end of the deployable mast to form a stiff tripod. Similarly, another solar blanket is deployed from the top longeron in the opposite direction. One complete section of the solar array (shown in figure 4) thus consists of two bays of the triangular truss beam and two 15.2 m (50 ft) by 10.2 m (33.3 ft) solar blankets with associated support structure. Modularity and growth are inherently designed into this solar array so that bays can be added to the free end of the truss beam and more solar blankets deployed.

The initial space station study configuration gimballed the solar arrays so that they could follow the sun while the modules remained Earth pointed. In the configuration shown in figure 4, the solar arrays are gimballed from the end of a module rather than a side. Now, the full 4.27 m (14 ft) diameter of the module can be used

as a gimbal race. A transition truss connects the three longerons of the solar array truss beam to six points forming a hexagon on the gimbal race. The solar arrays rotate about an axis which passes through the center of the module end. Since the solar blankets make up most of the solar array weight, the center of mass for the array lies on an axis which runs along the top longeron of the triangular truss. In order to minimize rotational inertia about the gimbal axis, it is desired to line up the center of mass of the solar arrays with the gimbal center of rotation. Thus, the transition truss is used to offset the solar arrays as shown in figure 4.

Module Cluster - Gimbale Wing Arrays

Using the erectable approach, the first configuration studied is shown in figure 5. The solar arrays in this case are wings 30.5 m (100 ft) wide and 61.0 m (200 ft) long, as opposed to 24.4 m (80 ft) by 76.2 m (250 ft) on the original configuration. Simply decreasing the length of the solar array serves to increase the fundamental frequency of the space station. In the initial study configuration, the solar arrays were gimbale from the side of a utility module. In the design shown in figure 5, a space station module is turned sideways and the solar arrays are gimbale from the two ends. The gimbal radius can be made as large as the radius of a module 4.27 m (14 ft). A truss serves as the transition structure between the solar arrays and the gimbal bearing race on the end of the module as shown in figure 5.

Module Cluster - Fixed Wing Arrays

The space station shown in figure 6 is a slight variation on the previous configuration, the difference being, that the solar arrays are not gimbale. It is anticipated that only certain elements such as telescopes, star trackers, or antennas need total freedom of pointing. If this is the case, the orientation of the modules should not be important and the arrays would not have to be gimbale, only the few devices which require freedom of pointing would. Removing the gimbals removes the problems associated with rotating large solar arrays and transmitting power through a large rotary joint.

This arrangement consists of a continuous triangular truss with solar arrays and support structure exactly as that described in the previous section. The open section in the middle of the solar arrays measures 4.27 m (14 ft), wide enough for a module to be attached end first to the base of the triangular truss. Note that this concept can be flown as a sun pointer (the configuration shown in figure 6) in which case the modules would point away from the sun. It can also be flown in a minimum drag configuration by adding 80% more area to the solar arrays, in which case, the modules would always be Earth pointing. In both the gimbale and fixed array configurations, the various modules would be connected by tunnels (see figures 5 and 6) which have to serve as both a structural and pressure connection.

Core Platform - Winged Arrays

A third space station/solar array approach (shown in figure 7) consists of a core platform to which three solar arrays are attached. The core platform, a hexagonal tetrahedral truss, can be either deployed or erected. The platform serves as a strong-back to which the various modules can be attached. In this case, the tunnels between modules only have to serve as a pressure connection. Since the

tunnels are not structural connections, adding or removing modules with this concept is simplified. Up to twelve modules and two berthing adaptors can be attached to the 34.1 m (112 ft) platform as shown. Each of the three solar arrays measures 40.5 m (133 ft) long by 30.5 m (100 ft) wide, and are of the same construction as shown in figure 4.

Platform - Solar Panel and Concentrator Arrays

Technical or economic reasons may dictate that some type of hard panels or concentrator panels be used for the space station solar arrays. The increased weight associated with going from solar blankets to hard solar panels (from 1.1 kg/m² to 4.9 kg/m²) requires that a stiffer array support structure be used to give a minimum space station frequency of 0.5 Hz. One concept for achieving the desired minimum frequency is shown in figure 8. Here, the space station arrangement consists of a large planar tetrahedral truss. Although the truss can be deployed, an erectable truss shows more promise in terms of modularity and growth potential. The space station modules are grouped at the center of the truss platform and the remaining truss surface is covered with the hard solar panels. The three platform sizes shown in figure 8 are for a 75 kw platform, a 150 kw platform, and a 150 kw minimum drag platform. For each of these hard panel arrays, the solar cell efficiency is assumed to be equal to that used for the blanket arrays.

DESIGN SUMMARY

Structural characteristics of a 150 kw solar array are summarized for five different space station configurations in Table I. The platform space stations with hard panels are heavier than the configurations with blanket arrays because of the increased weight of the hard panels and because of the greater amount of structure required to support the hard panels. The part count, or number of struts, is also greater because a large area support truss is required.

The fundamental frequency shown for each concept is the first elastic free-free frequency for the total space station. A 91,000 kg (200,000 lb) mass, representing the modules, was assumed at the center of each space station arrangement. All of the concepts have fundamental frequencies which are acceptable although the concept with gimbaled arrays is slightly below the frequency requirement established at the beginning of the study. The structural efficiency of a particular concept is obtained by dividing the solar array plus support structure weight by the power generated (150 kw).

PRELIMINARY STUDY TRENDS

In this study, a number of different space station solar array configurations were presented. A set of design requirements were identified and then different space station/solar array concepts were developed which met the requirements. Analysis of the different configurations identified the following trends:

- For a given solar collection area, truss platform arrays are 3 to 4 times stiffer than winged arrays.

- Winged arrays provide modular growth capability.
- Winged arrays with blanket technology are 1/3 as heavy as arrays using hard panels.
- Winged arrays are compatible with a blanket or panel approach.
- A minimum drag array configuration has the potential to reduce space station life cycle costs and system complexity.

REFERENCES

1. Olstad, Walter B.: Targeting Space Station Technologies. Astronautics and Aeronautics, March 1983, pp. 28-32.
2. Culbertson, Philip E.: Current NASA Space Station Planning. Astronautics and Aeronautics, September 1982, pp. 36-43, 59.
3. Mikulas, Martin M., Jr.; and Bush, Harold G.: Advances in Structural Concepts. NASA CP 2269, 1982, p. 257-283.
4. Kyser, Alber C.: The Effect of Atmospheric Drag on the Design of Solar-Cell Power System for Low Earth Orbit. (College of William and Mary; NASA Contract NAS1-16042.) NASA CR-166020, June 1983.

TABLE I. - PRELIMINARY DESIGN SUMMARY - 150 kW SOLAR ARRAY

	Module Cluster-Gimbaled Wing Arrays ¹	Module Cluster-Fixed Wing Arrays	Core Platform-Winged Arrays ¹	Platform-Panel Arrays ¹	Minimum Drag Platform-Panel Arrays ²
Array and Support Structure Weight, kg (lb)	6,913 (15,240)	6,868 (15,140)	7,453 (16,430)	24,450 (53,900)	44,000 (97,000)
Number of Struts ³	288	270	700	3,900	7,000
Strut Length, m (ft.)	5.09 (16.7)	5.09 (16.7)	5.09 (16.7)/ 4.27 (14.0)	3.66 (12.0)	3.66 (12.0)
Fundamental Freq., ⁴ Hz	.40	.55	.50	1.5	.59
Structural Efficiency, kg/watt, (lb/watt)	.046 (.10)	.046 (.10)	.050 (.11)	0.16 (.36)	

1. Array Area = 3,716m² (40,000 ft²)
Blanket Weight = 1.1 kg/m² (0.22 lb/ft²)
Panel Weight = 4.9 kg/m² (1.0 lb/ft²)

2. Array Area = 6,689 m² (72,000 ft²)

3. Strut Diameter = .051 m (2 in)
Strut Modulus = 28. x 10⁹ Pa
(40. x 10⁶ lb/in²)

4. 91,000 kg (200,000 lb) Mass
assumed at center of station.

ORIGINAL PAGE IS
OF POOR QUALITY

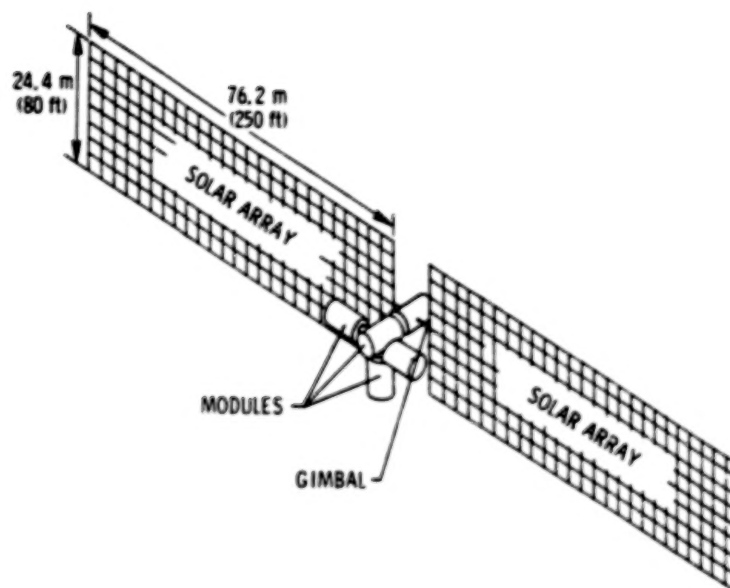


Figure 1. - Initial 150 kW space station configuration.

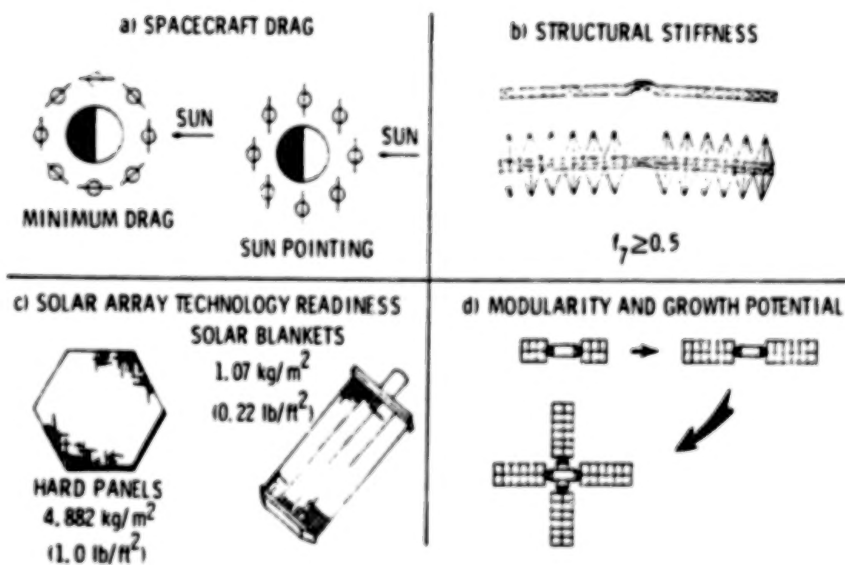


Figure 2. - Initial space station study considerations.

ORIGINAL PAGE IS
OF POOR QUALITY

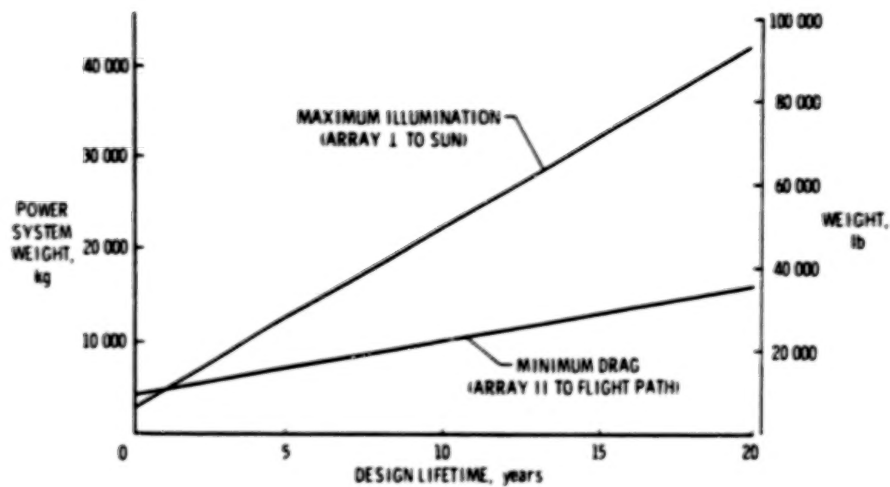


Figure 3. - Comparisons of total orbited weights versus design lifetime for two types of 150-kW solar power systems: sunpointing and minimum drag (ref. 4).

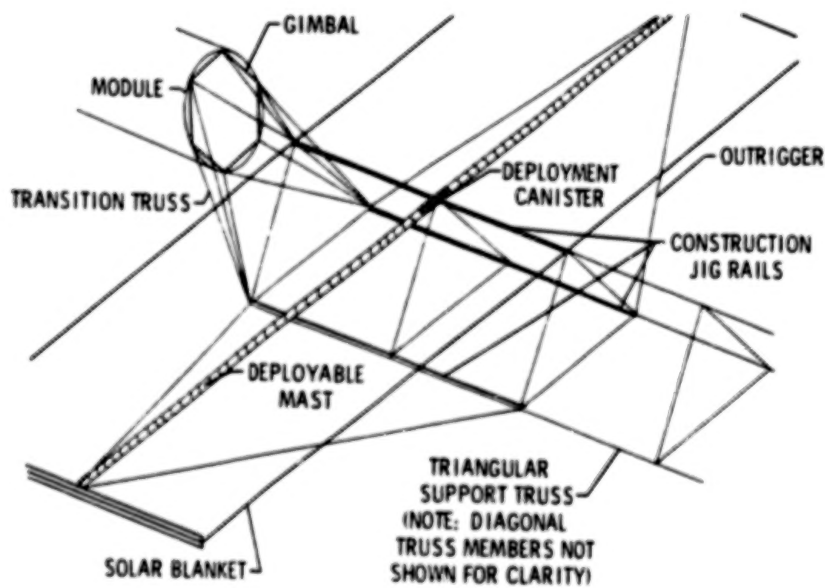


Figure 4. - Details of winged solar arrays.

ORIGINAL PAGE IS
OF POOR QUALITY

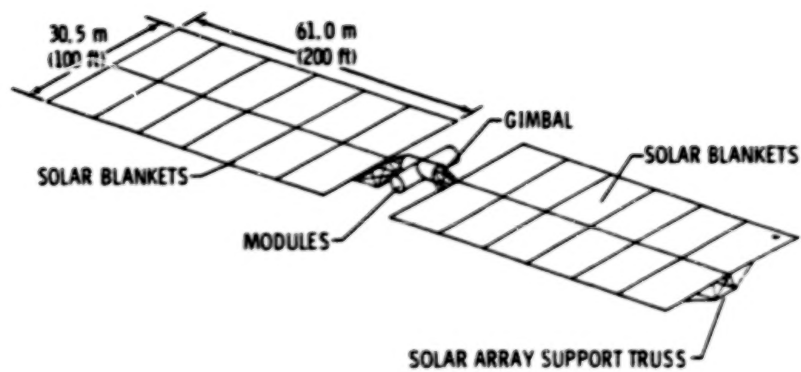


Figure 5. - Module cluster - gimbaled wing arrays.

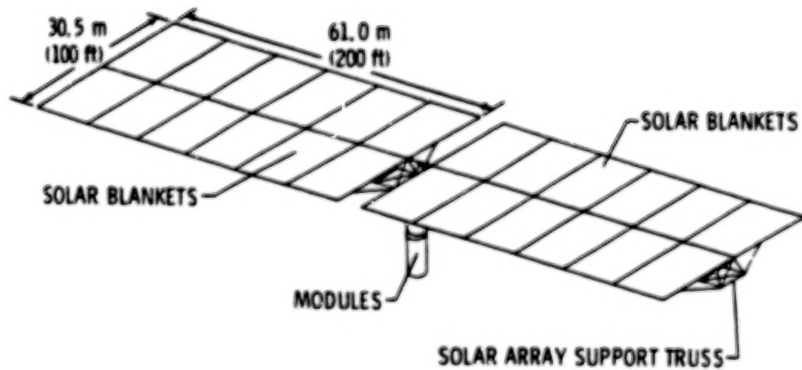


Figure 6. - Module cluster - fixed wing arrays.

ORIGINAL COPY
OF POOR QUALITY

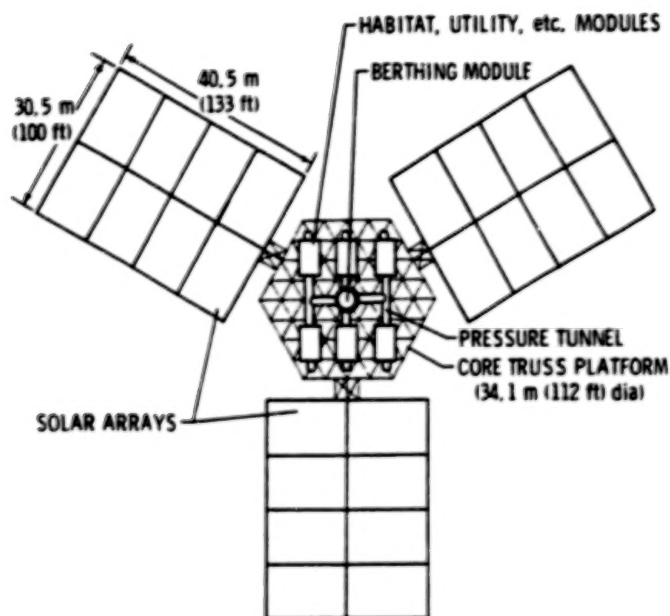


Figure 7. - Core platform - winged arrays.

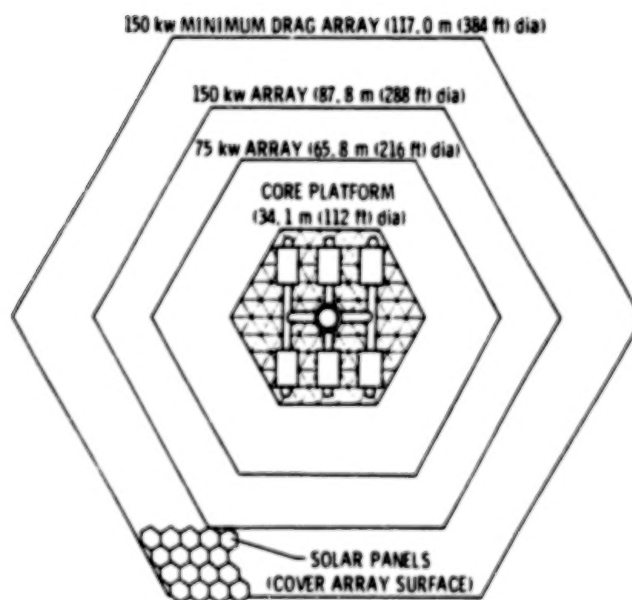


Figure 8. - Platform - panel/concentrator arrays.

N84
29336

UNCLAS

DEVELOPMENT AND SUPPORT STRUCTURES FOR HIGH-POWER SOLAR ARRAYS

Karl Knapp
Astro Research Corporation

Future space missions will require solar arrays of unprecedented size and efficiency. Prior to examining how we might deploy such structures, it is useful to review the large arrays that have been deployed in the past or are planned for the near future. The highest power array deployed to date, at least in the West, was the 6.2-kW Orbital Workshop array of SKYLAB shown in figure 1. The array developed about 6 watts per kilogram. Its twin was damaged during launch as a result of the failure of an aerodynamic fairing. The Space Telescope dual arrays, illustrated in figure 2, will develop a total of 5.4 kW with a specific performance of 24 watts per kilogram. These arrays are unrolled by BI-STEMs (Storable Tubular Extendible Member) using a FRUSA configuration.

The first deliberate attempt to make a step increase in the specific performance of a large array was the SEPS design where a prototype has demonstrated 66 watts per kilogram for a wing-type array of 12.5 kW. The first flight of a similar configuration will be the ESA L-SAT arrays, illustrated in figure 3, with each array developing 1.8 kW and 29 watts per kilogram. Later expansions of the design will increase the wing power to 3.5 kW and 40 to 45 watts per kilogram. This design uses a new version of the Astromast, the Supermast, with additional battens and diagonals at each half bay length, as shown in figure 4, at the root of the deploying column. This configuration produces four times the strength at the same mast diameter, although the bending stiffness remains unchanged.

Astro Research Corporation has been involved for several years in the development of deployable structures for very lightweight solar arrays based on the lightweight blanket technology being developed by Jet Propulsion Laboratory (JPL). The simple curve shown in figure 5 illustrates the importance of providing mass-efficient structures to ensure that the low-mass blankets result in high-performance systems. Our work for JPL was initiated using the three design cases listed in table 1 and the following ground rules:

1. Launch compatible with Shuttle
2. Operation at GEO or from one to three AU
3. Design modularity and adaptability
 - Wing-like configuration
 - Attachment at rotary joint
 - Baseline 126 m² area
4. Minimum constraint on blanket design
 - Separate packaging
 - Blanket nonstructural and uncooperative
 - Small structurally induced temperature variations (less than 5K)

We were able to develop a number of structurally efficient configurations for wing-type arrays by a combination of deepening the planform of the blanket and structure and by partitioning the blanket with battens and frequent attachments to the support structure as shown in figure 6. This technique reduces the tension required to avoid a low natural frequency for the blanket, and the load reduction results in a lighter structure. We investigated the use of three different structures: the Astromast, the Extendible Support Structure (ESS), and a new beam

called the STACBEAM (Stacking Triangular Articulated Compact Beam) and compared their relative performance. One comparison is shown in figure 7 and table 2. The ESS usually resulted in the lowest mass system since this synchronously deployed structure does not require a deployer. However, we have elected to pursue the investigation of the STACBEAM because its sequential deployment is more reliable for very long systems, and its linear deployment facilitates local attachments to the blanket and the development of a low-mass deployer.

The STACBEAM structure has been developed with single-degree-of-freedom hinges which results in well defined kinematics during deployment. A structural model of the STACBEAM, fabricated from graphite/epoxy rods, is shown in figure 8, and an engineering model of the deployer is shown in figure 9. The deployer operates in a reciprocating fashion while maintaining structural support of the deployed beam at all times. The entire deployer is initially stowed in a length that is no longer than the packaged STACBEAM. An improved version of the STACBEAM is currently being manufactured with redesigned hinge hardware and graphite/epoxy tubes replacing the original rods.

These solar array structural improvements can be applied to low Earth applications as well. Tables 3 and 4 illustrate an example of updating a SEPS-type array for a power module. The original design had a natural frequency of less than 0.05 Hz and had to be retracted during reboost of the power module or had to withstand firing of the Shuttle primary RCS thrusters. A STACBEAM version of this design raises the natural frequency to 0.18 Hz and meets the reboost requirement without retraction. For an additional mass penalty, the RCS capability can also be incorporated.

The relative performance of current solar array technology is compared with the potential performance of the JPL designs in table 5. The STACBEAM and a new articulated version of the Astromast with rigid folding diagonals are shown in figure 10. The previously mentioned ESS, which was used to deploy and support the Seasat SAR antenna, is shown in figures 11 and 12. This structure, because of its inherent accuracy potential, may prove to be appropriate for the support of high concentration solar arrays such as those currently described by TRW.

Some of the primary considerations influencing the design of large solar array structures are:

1. High transportation costs lead to requirements for low mass and good packaging
2. Mission requirements determine strength and stiffness
3. Highest costs are associated with engineering activities to establish reliability
4. Man's intelligence and dexterity should be used appropriately in space

The high cost of transportation to orbit requires that large arrays be mass efficient and have good packaging. Mission requirements will continue to determine needs for strength and stiffness, both of which can normally be obtained by the selection of good structural configurations. The highest costs associated with these structures result from the engineering activities necessary to establish reliability. To minimize these costs, we must select structures whose performance is predictable, design reliable deployers, and, whenever possible, make the systems ground testable. In order to create very large arrays for applications such as a space station, we should use man's intelligence and dexterity in space in an appropriate way. Today's paper from NASA Langley Research Center, for example, shows a rational combination of deployable and assembled structures.

ORIGINAL PAGE 19
OF POOR QUALITY

TABLE 1. - DESIGN CASES

<u>ITEM</u>	<u>SEP</u>	<u>DESIGN 1</u>	<u>DESIGN 2</u>	<u>DESIGN 3</u>
BLANKET				
AREA	126 m ²	126 m ²	126 m ²	126 m ²
MASS	113 kg	81 kg	53 kg	30 kg
DENSITY	0.897 kg/m ²	0.645 kg/m ²	0.421 kg/m ²	0.238 kg/m ²
STRUCTURE MASS	76 kg	≤ 54 kg	≤ 35 kg	≤ 21 kg
LENGTH/WIDTH	7.9	---	---	---
NATURAL FREQUENCY	0.05 Hz	---	---	---

TABLE 2. - POINT DESIGNS: ESS DESIGN 2, ASTROMAST, ASTRO STACBEAM

FREQUENCY = 0.20 Hz

<u>DESIGN COMPONENTS</u>	<u>ESS</u>	<u>ASTROMAST</u>	<u>ASTRO STACBEAM</u>
M _{BLANKET} * M _{B1}	53 kg	53 kg	53 kg
M _{CONTAINER} * M _{CONT}	8.1 kg	8.1 kg	8.1 kg
M _{HARNESS}	4.0 kg	4.0 kg	4.0 kg
BLANKET TENSION	26 N	47 N	24 N
STRUT DIAMETER (WALL)	0.68 cm (0.50 mm)	0.35 cm	0.31 cm
BAY LENGTH (DIAMETER)	1.65 m	(0.70 m)	0.45 m
M _{BEAM}	9.0 kg	4.1 kg	10.0 kg
M _{DEPL MECH}	4.5 kg	38.8 kg	8 kg
M _{ACTUATOR}	2.6 kg	4.7 kg	2.4 kg
M _{GUIDE CABLES} * M _{gc}	0.5 kg	0.5 kg	0.5 kg
M _{BATTENS}	0.9 kg	0.7 kg	0.9 kg
M _{STANDOFFS}	0.5 kg	0.5 kg	0.5 kg
SYSTEM MASS	83.1 kg	114.4 kg	87.4 kg

ORIGINAL PAGE IS
OF POOR QUALITY.

TABLE 3. - POWER SYSTEM ORBITAL LOADS

REBOOST

- FOUR THRUSTERS AT 137 N EACH
- MASS (FF-0) = 12,400 kg
- ACCELERATION = 0.058 m/s^2

PRIMARY REACTION CONTROL

- ONE PAIR OF ROLL CONTROL THRUSTERS AT 3880 N EACH
- LOCATED 3.35 m FROM CENTERLINE
- ROLL MOMENT OF INERTIA (SORTIE) = $2.76 \times 10^6 \text{ kg-m}^2$
- ANGULAR ACCELERATION = 0.0094 rad/s^2

BENDING MOMENT

- NOMINAL MASS (- UNIFORMLY DISTRIBUTED) = 400 kg
- LENGTH = 40 m
- DESIGN LOAD FACTOR = 3
- DESIGN MOMENT = 1400 N-m (REBOOST)
= 6000 N-m (PRIMARY RCS)

TABLE 4 - EXAMPLE DESIGNS: 40-m-LONG POWER SYSTEM WING

<u>ITEM</u>	<u>DEPLOYED CAPABILITY</u>	
	<u>REBOOST</u>	<u>PRIMARY RCS</u>
• STACBEAM		
BAY LENGTH	0.6 m	0.8 m
STRUT SIZE	11 mm OD x 1.5 mm WALL	18 mm OD x 3 mm WALL
STRENGTH	1404 N-m	8400 N-m
EI	$2.66 \times 10^6 \text{ N-m}^2$	$15.0 \times 10^6 \text{ N-m}^2$
STOWED LENGTH	1.50 m	1.80 m
MASS (K=2)	77.3 kg	244.1 kg
• BLANKET AND HARNESS		
TENSION (10 INTERVALS)	147 N	588 N
MASS	315.1 kg	315.1 kg
• OTHER MASSES (BUDGETARY)		
BATTEN, STANDOFFS, ETC.	11.3 kg	11.3 kg
CANISTER	80.4 kg	253.8 kg
CONTAINER	<u>48.2 kg</u>	<u>48.2 kg</u>
• TOTAL MASS	532.3 kg	872.5 kg
• CANTILEVER FREQUENCY	0.18 Hz	0.36 Hz

ORIGINAL PAGE IS
OF POOR QUALITY

TABLE 5. - EXAMPLE OF MEDIUM-POWER SOLAR ARRAYS

HARDWARE

SKYLAB (1973 FLIGHT) ORBITAL WORKSHOP, 12.5 kW, 5.9 W/kg

SPACE TELESCOPE, 5.4 kW TOTAL, 24 W/kg, .08 Hz

SEPS (SAFE), 12.5 kW PER WING, 66 W/kg, .05 Hz

L-SAT (OLYMPUS), 1.8 kW PER WING, 29 W/kg, .13 Hz

PROTOTYPE

JPL/ASTRO, 20 kW PER WING, 150 W/kg, .20 Hz (B.O.L. GEO)

ADVANCED

JPL/ASTRO, 22.6 kW PER WING, 265 W/kg, .20 Hz (B.O.L. GEO)

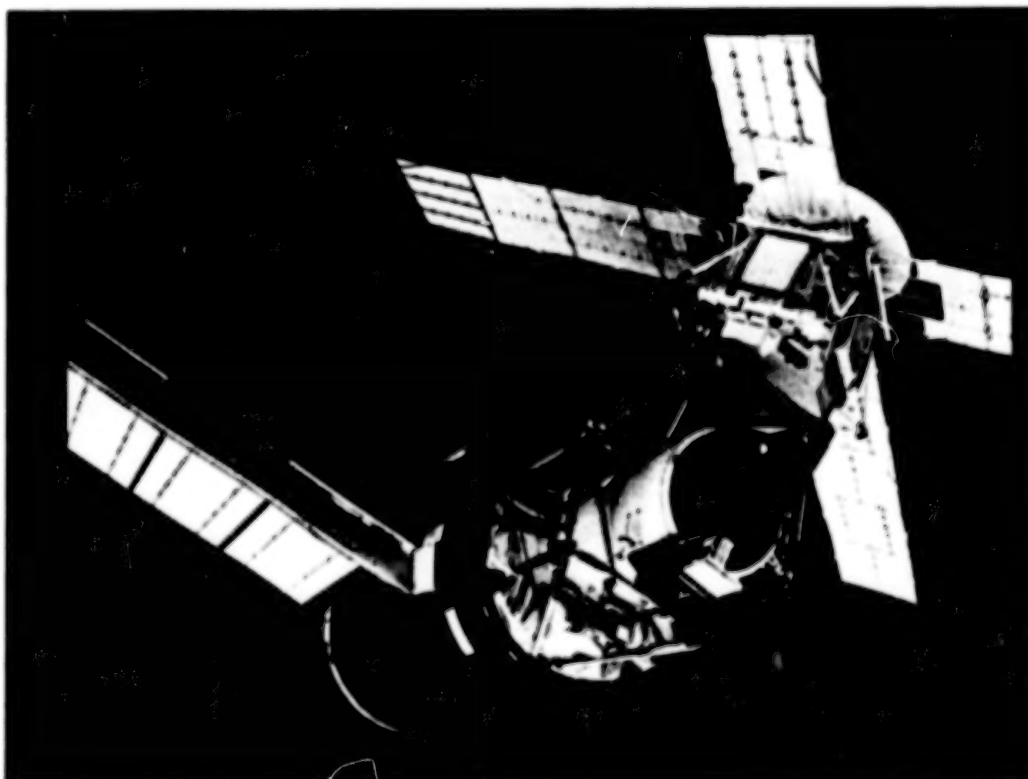


Figure 1. - Skylab.

ORIGINAL PAGE 19
OF POOR QUALITY

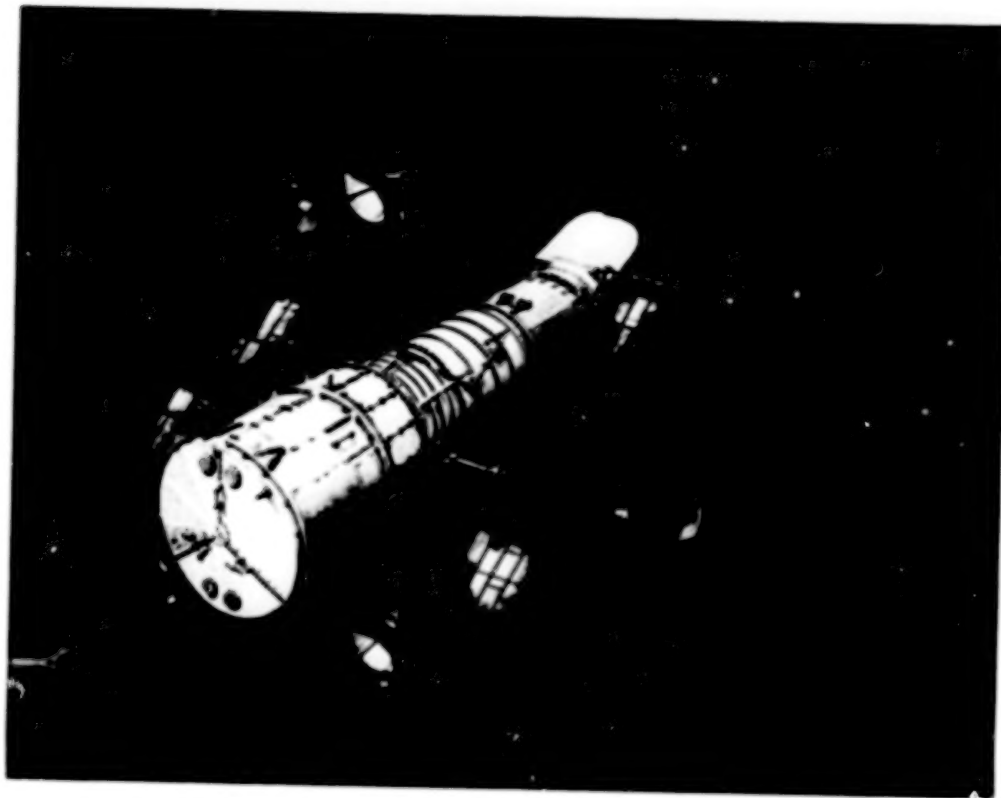


Figure 2. - Space Telescope.

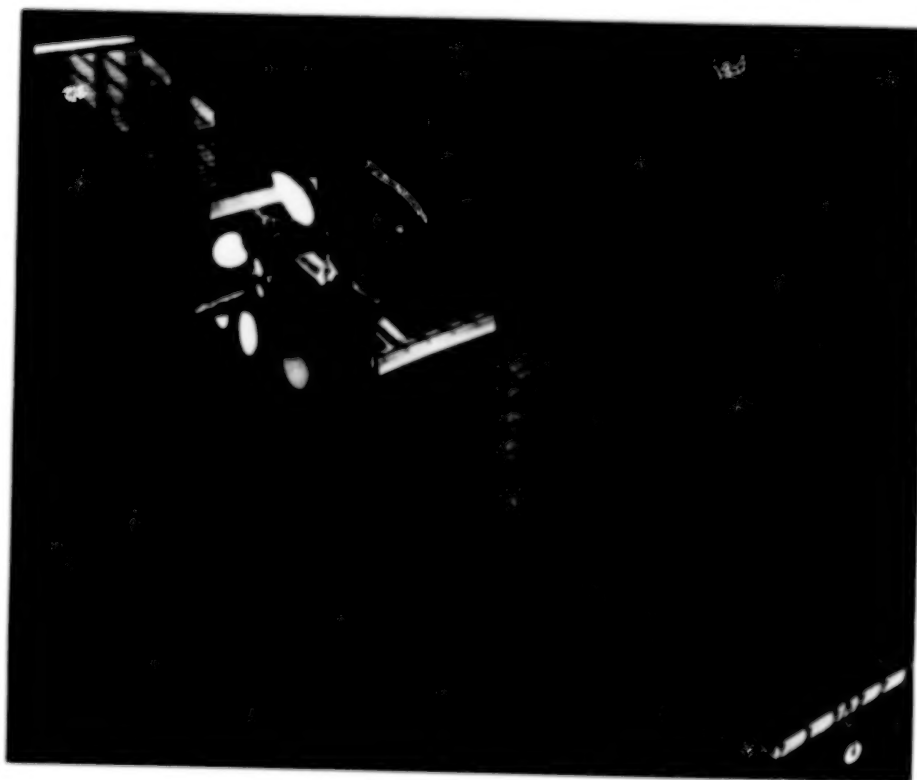


Figure 3. - Olympus (L-SAT).

ORIGINAL PAGE IS
OF POOR QUALITY

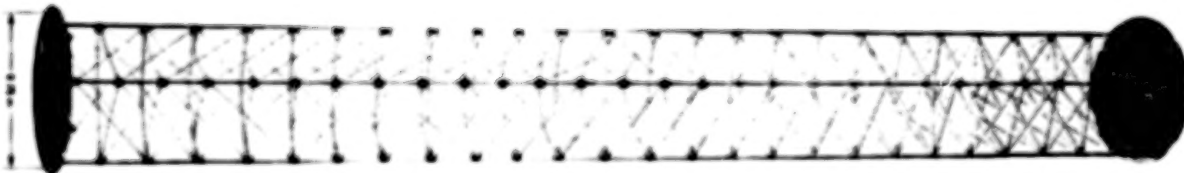


Figure 4. - Large diameter (0.75-m) Supernast model, 20 feet long.

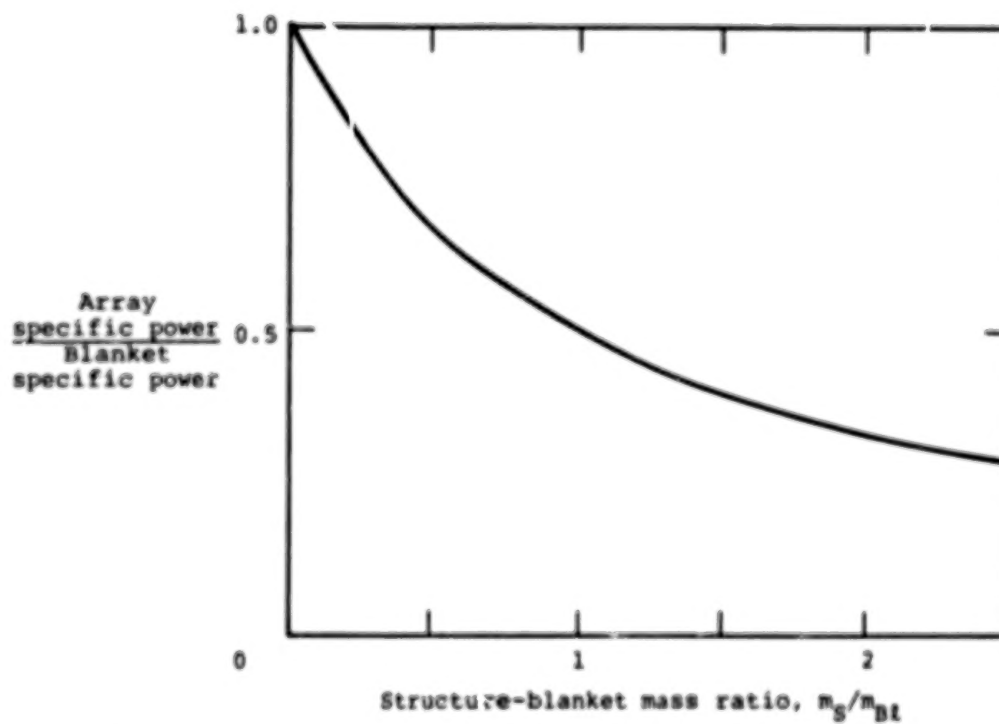


Figure 5. - Effect of structural mass on array specific power.

ORIGINAL PAGE 19
OF POOR QUALITY

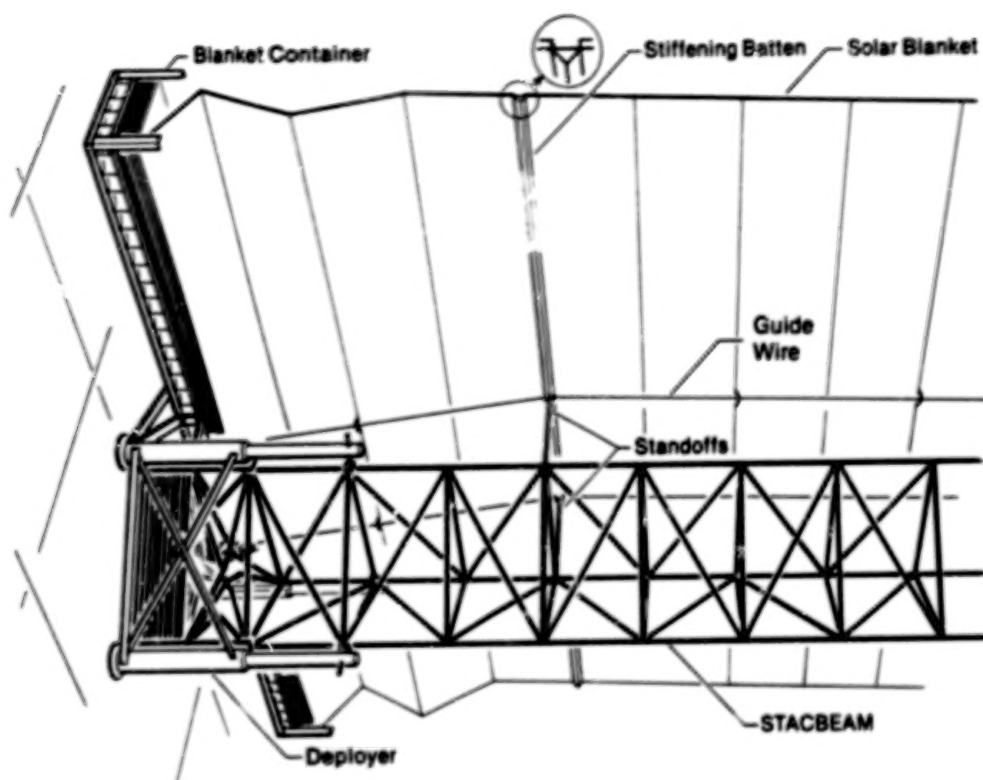


Figure 6. - Solar-array system.

$M_{B1} = 53 \text{ kg}; 0.421 \text{ kg/m}^2$
ASTROMAST (AM)
ASTRO STACBEAM (SB)
EXTENDIBLE SUPPORT STRUCTURE (ESS)

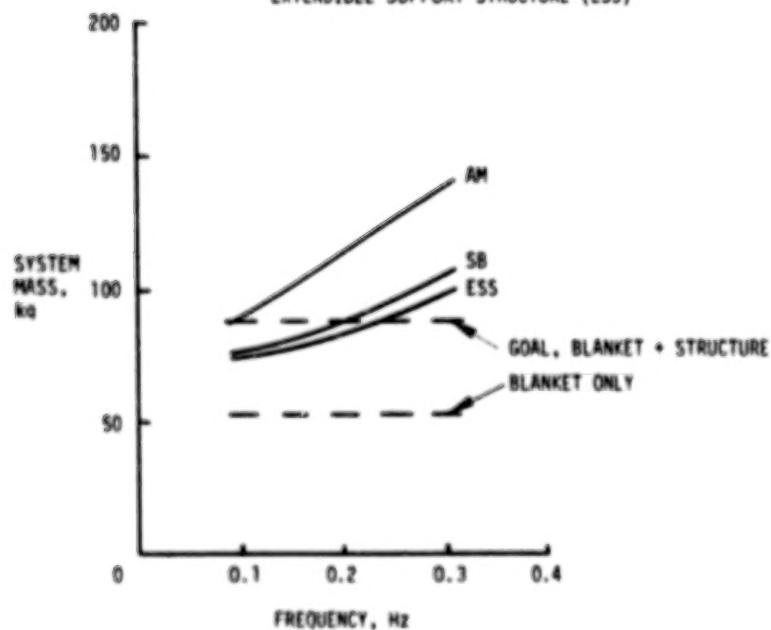


Figure 7. - System mass versus frequency comparisons - Design 2.

ORIGINAL PAGE IS
OF POOR QUALITY

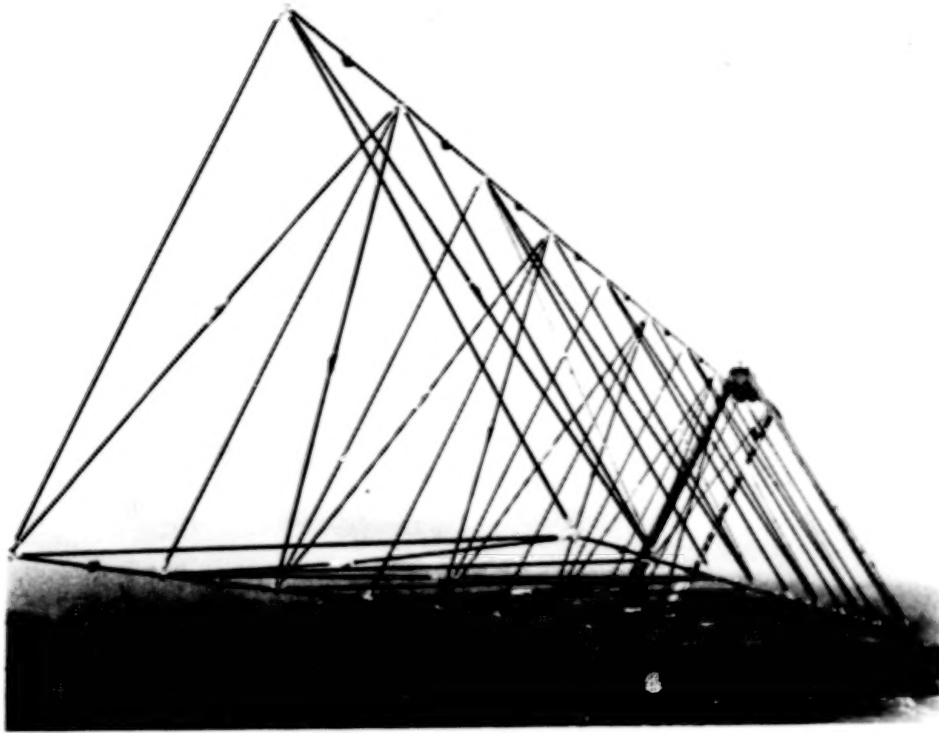


Figure 8. - Deployed STACBEAM.

STACK OF A LONGER BOOM
CAN COMPLETELY FILL THE
VOLUME OF THE PACKAGED
DEPLOYER.

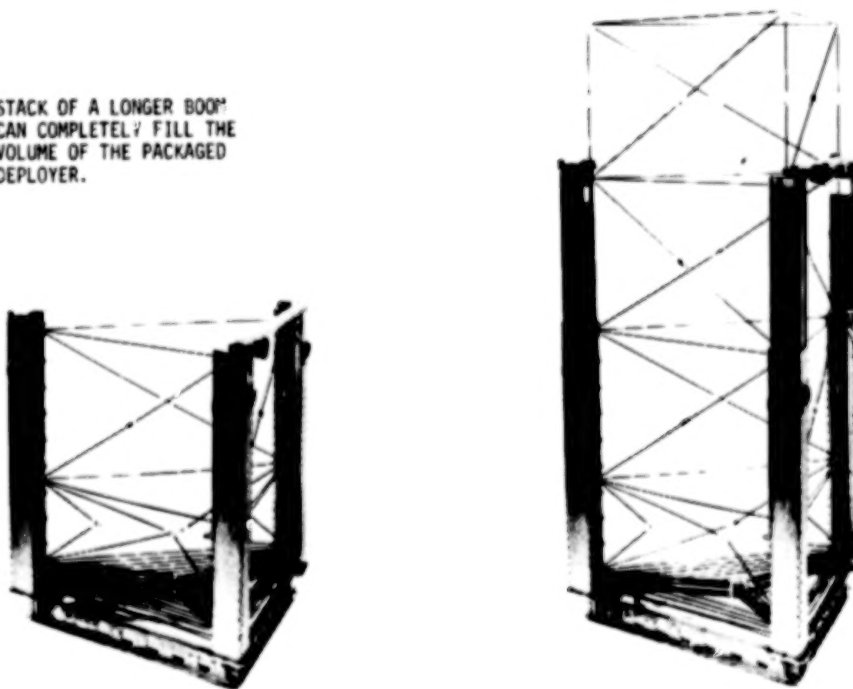
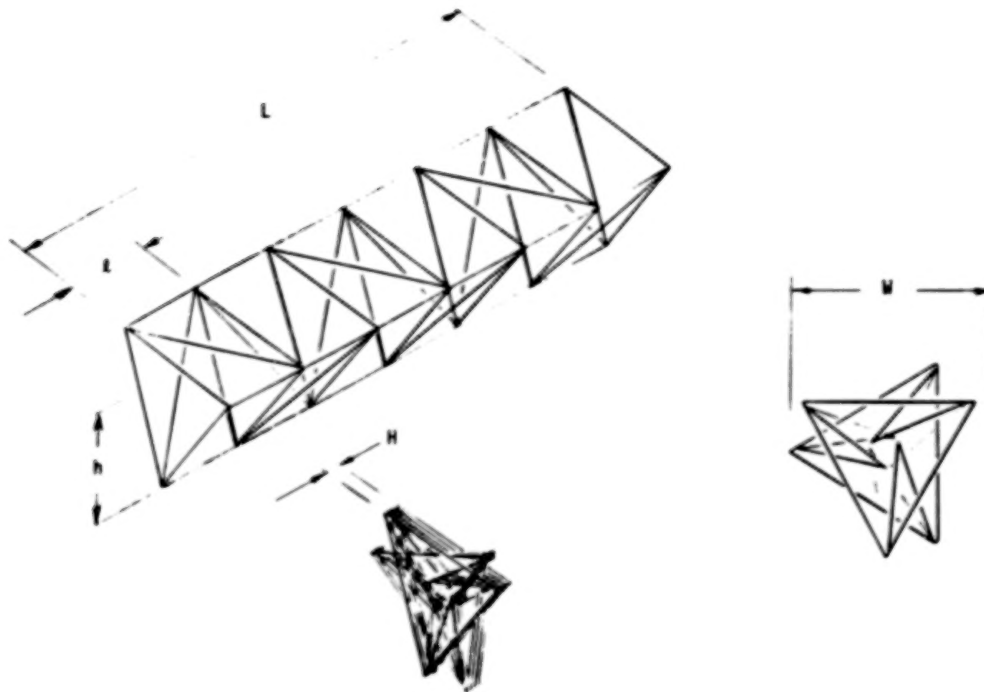
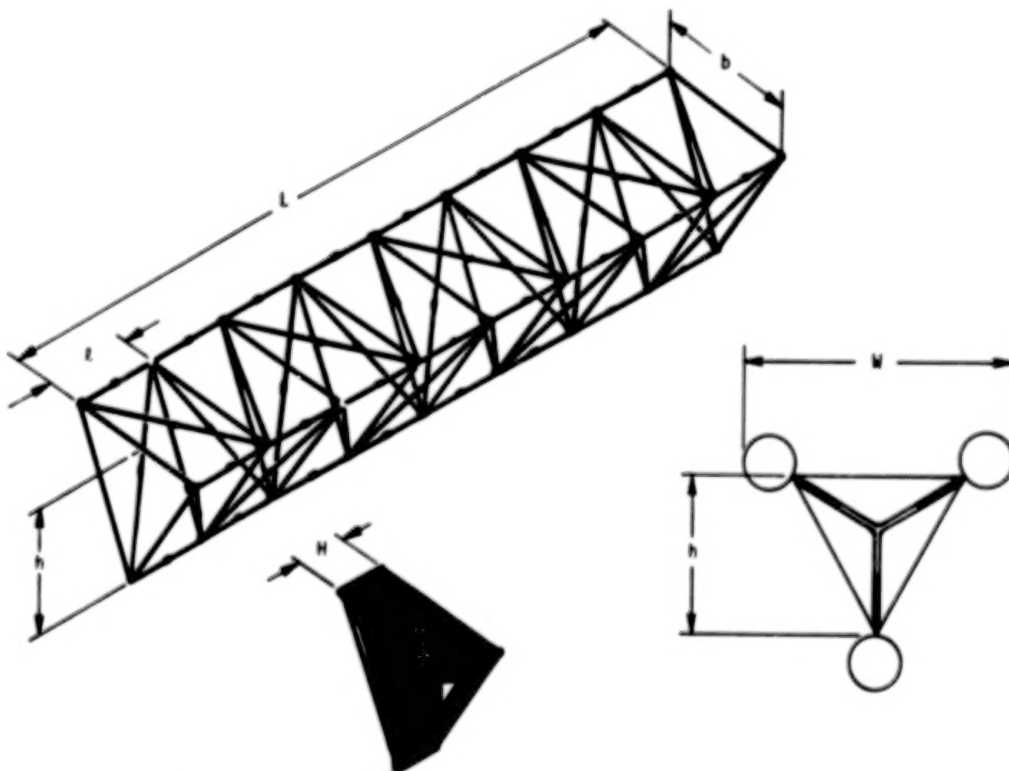


Figure 9. - Deployer for deployable STACBEAM.

ORIGINAL PAGE IS
OF POOR QUALITY



(a) Astronast with rigid folding diagonals.



(b) STACBEAM (Stacking Triangular Articulated Compact Beam).

Figure 10. - Two new articulated booms, all single-degree-of-freedom hinges.

ORIGINAL PAGE IS
OF POOR QUALITY

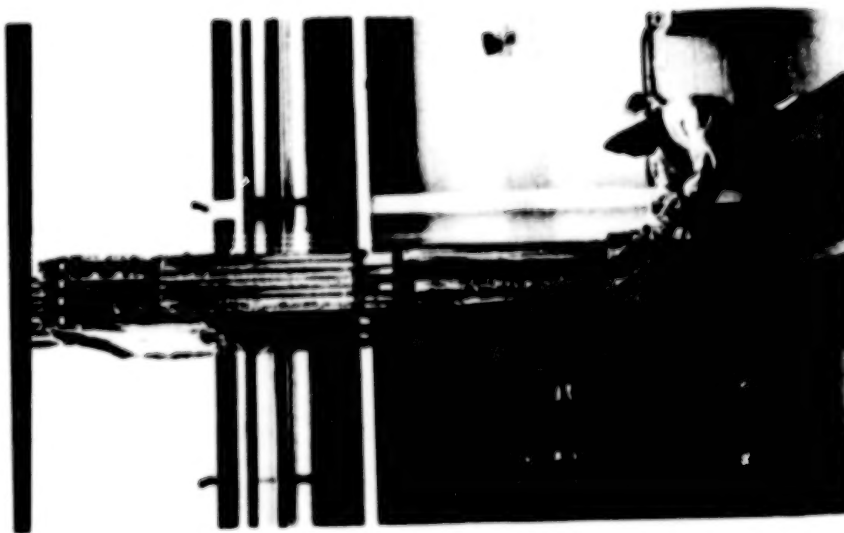


Figure 11. - Extendible support structure (ESS) for Seasat synthetic aperture radar antenna.

ORIGINAL PAGE 13
OF POOR QUALITY

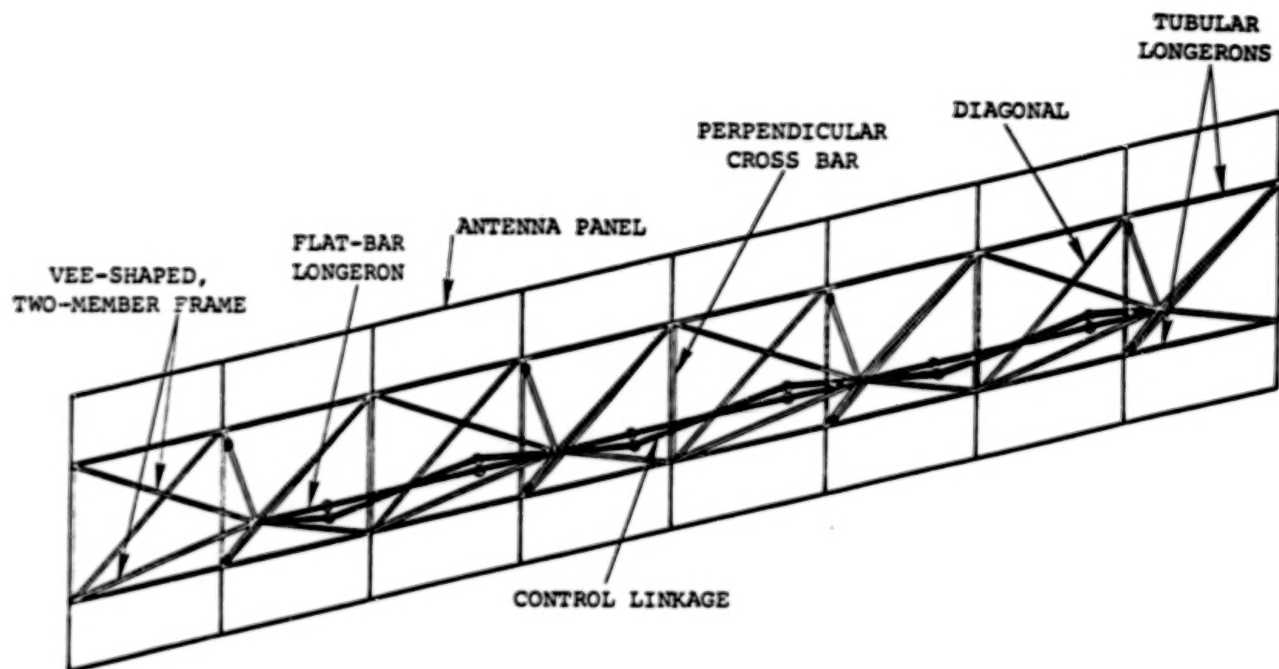


Figure 12. - Deployed extendible support structure.

N84
29337

UNCLAS

N84 29337

PANEL FABRICATION UTILIZING GaAs SOLAR CELLS

N. Mardesich
Spectrolab, Inc.
Sylmar, California

Just within reach lies the availability of GaAs solar cells for space applications. Although the cell cost is at a premium today, fabrication of panels utilizing GaAs cells is essential. This paper describes the recent activities at Spectrolab in the fabrication of GaAs solar panels.

We have recently fabricated a number of panels while introducing improved quality control, soldering laydown and testing procedures. These panels include LIPS II, San Marco Satellite, and a low concentration panel for Rockwell's evaluation. This paper will discuss these panels and their present status.

INTRODUCTION

The success or failure of further space missions may depend upon the availability of GaAs solar panels. The need for small panel programs to develop the necessary understanding and experience is essential for future missions. Spectrolab has recently fabricated a number of GaAs panels under three contracts.

During the panel fabrication, problem areas such as cell contact integrity and soldering techniques have been identified and resolved. Process control and documentation have been established during these programs to ensure reproduction of the product.

The manufacturing problems and techniques for fabricating the LIPS II, San Marco and Rockwell concentrator panels are described in the following sections.

PROCESS CONTROL

The process control implemented on the GaAs solar panels manufactured at Spectrolab were the same as those used for silicon panel fabrication. The receiving inspection consisted of electrical tests and contact integrity tests for cells from Hughes Research Laboratories (HRL). The circuit assembly controls that were implemented consisted of substrate inspection, insulation test, bonded panel inspection, electrical performance and thermal cycling.

PANEL FABRICATION

The process flow for GaAs panel fabrication is shown below:

- o Incoming cell inspection and testing
- o Cell filtering
- o Assembly testing and matching
- o Parallel circuit soldering

- o Sub-circuit testing and matching
- o Series circuit soldering
- o Shunt testing
- o Substrate insulation
- o Circuit bonding
- o Prewire and harness assembly
- o Panel wiring
- o Panel inspection and rework
- o Pre-ATP electrical test
- o Rework
- o ATP electrical test
- o Environmental test
- o Post environmental electrical test and inspection
- o Packing and shipping

TESTING

A number of electrical and mechanical tests were conducted to ensure reliable panel performance. The cell testing included current vs. voltage measurement at AMO and 28°C, using a Spectrolab X-25 simulator setup with GaAs balloon standard 80-130. The contact integrity tests consisted of a tape peel test and a soldered tab pull test.

Panel testing utilized a shunt test to identify shorted cells prior to substrate bonding. Electrical tests (AMO, 28°C) on the LAPSS simulator were calibrated using a silicon second standard 1052. The environmental test involved thermal cycling in accordance with the customer's requirements.

LIPS II

The LIPS II panel consisted of three circuits of 2 cm x 2 cm GaAs cells, which had four cells in parallel and 25 in series mounted on the same substrate. The back side of the panel had two circuits of 2 cm x 6 cm silicon cells and 52 cells in series. Table 1 lists the mission requirement and the basic panel design.

Gallium Arsenide cells received from HRL were electrically tested and evaluated for contact integrity by Spectrolab. The electrical evaluation indicated a slightly lower power than values measured at HRL. The contact integrity evaluation indicated good tape pull test but variable 45° tab pull test. The major difficulty with tape pull test was the fracturing of cells during the test. During

the tab pull test portions of the front P contact had high strength, while sections of the same cell had low strength. A minimum of 100 grams on two tabs for two cells per lot was selected as the pull strength necessary for panel fabrication and panel integrity. Some lots passed these integrity tests while others failed the 45° tab pull test for the front P contact. Filtering and soldering of the parallel subcircuits resulted in good yield with minimum problems associated with shunted cells due to the latter process. The contact integrity of the front P contact proved to be a major problem. Many tabs on both the passed and rejected lots were lifted and required rework. Cells with lifted tabs that would degrade the electrical performance of the panel were replaced and others were conformal coated to prevent external stresses from being applied to the cell's contact.

The electrical I-V trace for the GaAs panel at 30°C and AMO is shown in Figure 1. This actual value is questionable since silicon standard 1052 was used to calibrate the LAPSS. The intensity appears to be 6% lower than later, more reliable test results have indicated. The panel is presently being evaluated in orbit.

SAN MARCO

The experience gained in the manufacturing of the LIPS panel proved invaluable in establishing quality control for the San Marco panel. Since front P contact integrity proved to be the major problem associated with panel fabrication, HRL undertook an effort to improve contact integrity. The results of the effort were very encouraging and produced cells which consistently had pull strengths from 150 to 800 grams. This proved to be sufficient for panel fabrication. High quality panels were produced with the implementation of improved contact, efficient soldering and handling techniques developed during the fabrication of the San Marco panels.

The San Marco panels consisted of five panels with 28 - 2 cm x 2 cm GaAs cells soldered in series. Table 1 lists the mission requirements and the panel design. The electrical I-V characteristics for a typical panel at 28°C and AMO is shown in Figure 2. The panels were also tested at NASA-Goddard (ref. 1) and appeared to be about 6% higher than the value at Spectrolab, Figure 2. This discrepancy is understandable since the LAPSS at both facilities were calibrated with silicon standards.

ROCKWELL CONCENTRATOR PANEL

The most recent GaAs panel fabricated at Spectrolab was a small engineering concentrator panel for Rockwell International, Inc. This panel proved to be the least difficult and fabrication was completed with few problems. The cells were specially designed at HRL to provide maximum power at 5 to 10 sun concentration by forming deeper junctions and thicker window layers. During fabrication only one cell required rework, due to an edge chip.

The Rockwell concentrator panel consisted of two circuits using 2 cm x 2 cm GaAs cells. The first circuit was three cells in parallel and ten in series, and the second was two cells in parallel and ten in series. Table 1 lists the basic panel requirements for the engineering panel. The electrical I-V characteristics of this concentrator panel was measured by two methods. The first method employed a silicon standard for calibrating the LAPSS, Figure 3, as performed for the San Marco panel. The second method used a hand-held GaAs standard for calibration of the LAPSS which was calibrated with a JPL balloon flown standard 80-130, Figure

3. The I-V characteristics of the panel when calibrated with the GaAs standard proved to be approximately 6% higher than the measurement with the silicon standard.

CONCLUSIONS

The process control and fabrication techniques recently developed have allowed Spectrolab to provide reliable high quality GaAs solar panels. The initial LIPS panel had problems associated with contact integrity, soldering and testing. The contact integrity and soldering problems were resolved during the fabrication of the five San Marco panels. The electrical characteristics were not resolved until the Rockwell panel had been manufactured. The electrical I-V characteristics of the LIPS and San Marco panels appear to be approximately 6% lower when tested with a LAPSS system calibrated with a silicon 1052 standard rather than with a GaAs standard.

REFERENCE

1. J. H. Day and N. V. Mejia
Goddard Space Flight Center, "San Marco D/L GaAs Solar Array Panels at Beginning of Life", March 1983.

TABLE 1. - GaAs PANEL MANUFACTURING

GaAs PANEL MANUFACTURING

PROGRAM:	LIPS II	SAN MARCO	ROCKWELL
Orbit	600 nm, 60° inc.	600 nm, Circular	Engineering Evaluation
Thermal	-20°C to +60°C	-40°C to +40°C	-100°C to 150°C
Panel Size (inches)	12.75 x 24 x 0.25	3.24 x 6.69 x 0.050	15.10 x 7.17 x .032
Substrate Type	Aluminum Honeycomb	Aluminum Sheet	Aluminum Sheet
Insulation	Micaply	Micaply	Kapton
Bonding Adhesive	RTV-511	93-500	93-500
Interconnects (soldered)	Ag Plated Kovar	Ag Plated Moly	Ag Plated Kovar
Panel Power (AMO)	24.6 W @ 30°C	2.63 W @ 28°C	4.37 W @ 28°C
Number of Cells/Panel	300 each	28 each	50 each
Number of Panels Manufactured	1 each	5 each & Qual	1 each
Circuit Configuration	4P x 25S x 3 Ckts	28S	2P x 10S + 3P x 10S
Solar Cell Size	2 x 2 cm	2 x 2 cm	2 x 2 cm
Cell Thickness	0.014"	0.014"	0.014"
AR Coating	Ta ₂ O ₅	Ta ₂ O ₅	Ta ₂ O ₅
Coverglass	FS 350 umR	FS 350 umR	FS 350 umR 12 mils
Adhesive	93-500	93-500	93-500
Cell η (on Panel)	15.5% @ 30°C	16.5% @ 28°C	16.45% @ 19°C (a 6X)

ORIGINAL PAGE IS
OF POOR QUALITY

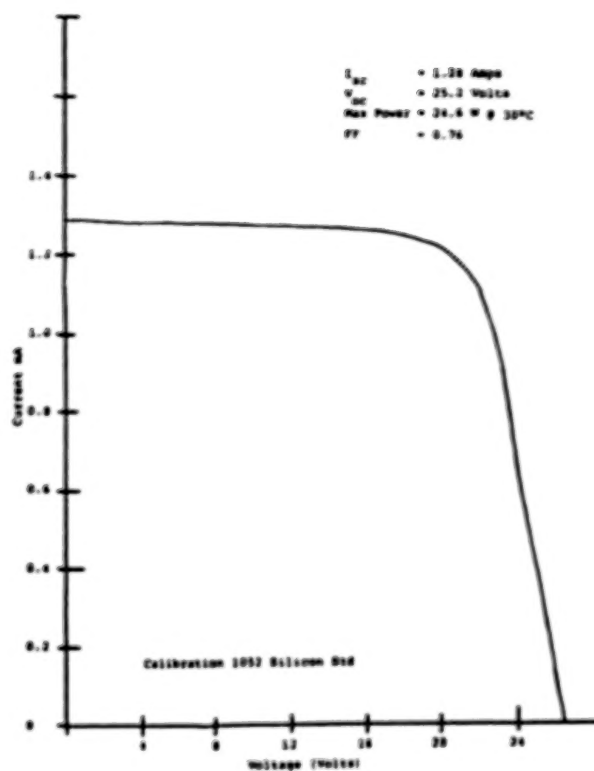


Figure 1. - Current-voltage curve for LIPS II.

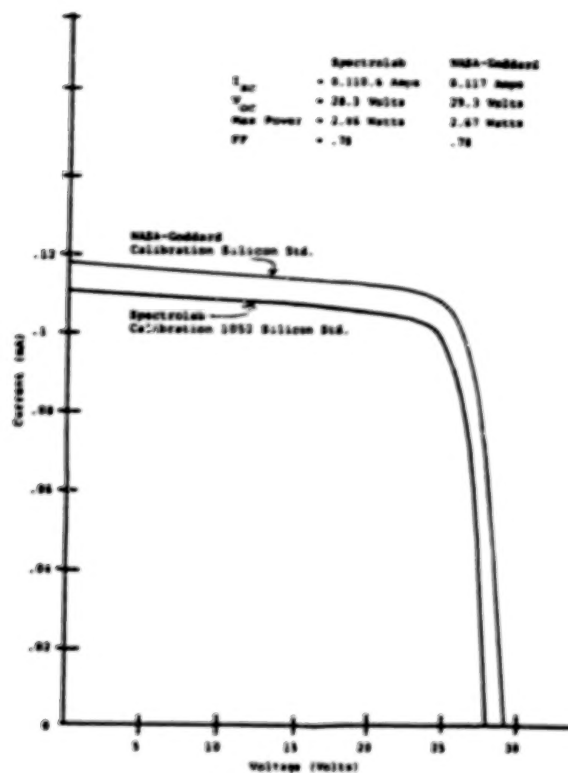


Figure 2. - Current-voltage curves for San Marco.

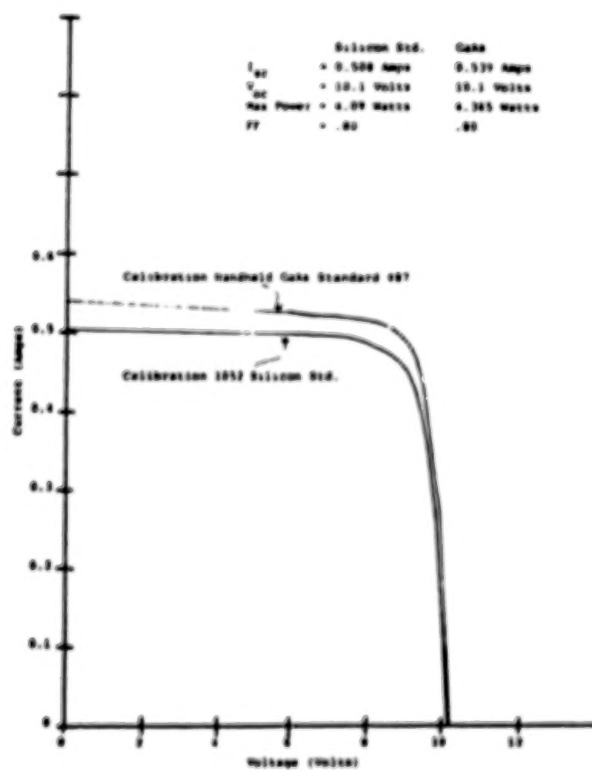


Figure 3. - Current voltage curves for Rockwell concentrator.

N84
29338

UNCLAS

N84 29338

TRANSPARENT ARRAYS - PROGRESS TOWARD
HIGHER EFFICIENCY

G. J. Pack
Lockheed Missiles & Space Company, Inc.
Sunnyvale, California

Principles and design considerations of IR transparent solar arrays are discussed. This work is an outgrowth of studies carried on at LMSC to optimize the performance of flexible solar arrays. As a result, measured solar absorptance as low as $\alpha_s = 0.59$ has been achieved leading to a predicted BC/L power density of $182.7 = \text{W/m}^2$. Advanced array concepts, system level cascaded panels, and transparent rigid panels are proposed and expected benefits discussed.

BACKGROUND

Flexible solar arrays are being developed for NASA and DoD missions through the 1990's. Figure 1 shows a typical example of the general configuration. The key mechanical features of this type of design are a thin, non-rigid membrane to which the solar cells are attached, a containment unit for stowage and protection during launch, and a deployment device to extend and tension the array on orbit. While on orbit, the only loads which the blanket is subject to are tensile and inertial. Because strength considerations are minimal and frequency response is driven by design of the mast, a large variety of materials are available for use within the blanket. In addition, more emphasis can be given to other performance parameters in the choice of those materials.

Operating temperature is one of the variables which affects the array power to a large extent. A flexible array is an inherently simple thermal system with few adjustable parameters. The most important parameter which can be varied to reduce the operating temperature (figure 2) and thereby increase the system efficiency is the solar absorptance. Figure 3 shows a normalized solar spectrum and a typical silicon cell response curve. There are three distinct thermal regions shown. Thermal loading due to radiation shorter than 0.35μ is reflected by a multilayer dielectric stack on the cover. Incident radiation between $0.35\mu \leq \lambda \leq 1.0\mu$ interacts with the silicon to produce power. Radiation longer than 1.0μ penetrates into the cell and interacts with the back surface.

Since approximately 25% of the solar energy is contained within the $1.0\mu \leq \lambda \leq 4.0\mu$ region, absorption in this band should be minimized. Conventional solar cell designs, shown in figure 4, attempt to minimize absorption in this region by depositing an aluminum reflector layer on the back surface. Practical considerations limit the effectiveness of this approach in reducing α_s . Several factors influence the disposition of energy in the IR. Figure 5 shows the effect on reflectance (and absorptance) of a back surface field. In addition, surface roughness, contact sintering and reflector material all contribute to absorption.

* This work has been and is being funded by NASA-MFSC and LMSC Independent Development Project.

These problems can be eliminated and total absorptance substantially reduced by gridding the back contact and taking advantage of the inherent transparency of silicon. This introduces another variable or degree of freedom in the array design process. In order to take advantage of the cell transparency, all the materials in the optical path must also be chosen with low absorptance and high transmittance. Components affected include the cover, adhesives and the substrate. Most of the materials currently used in solar arrays already partially satisfy the requirements for an IR transparent array.

PROGRESS

Progress has been made in developing a transparent array design using flight qualified materials. Figure 6 shows second generation gridded cells from both ASEC and SPL. Maximum measured efficiencies of 13.7% have been obtained with 10 Ω -cm P⁺ cells and 13.4% with 2 Ω -cm cells. The minimum solar absorptance measured to date is $\alpha = 0.60$ on the 2 Ω -cm cells. Reflectance and transmittance measurements shown in figure 7 tend to verify the approach.

Substrate development has also started for an IR transparent array. Preliminary design and development have centered on an interconnect pattern retaining the Kapton blanket as a carrier. The baseline Kapton/polyester blanket material has fair performance as an IR transparent material and was mainly retained due to the considerable experience at LMSC in using it for flexible arrays.

Several alternate approaches utilizing transparency as a design element are also being pursued. Figure 8 shows a completed development module using 0211 microsheet as a load carrying superstrate. This module is the initial venture into a larger class of transparent, rigid panels. Significant cost reductions and performance improvements are expected as a result of this type of approach.

In order to quantify the benefits of the previously discussed designs, cost and performance estimates have been made on proposed systems incorporating them. Figure 9 shows the results of a cost study on a 25 kW array for three different constructions and four cell sizes.

The most important results of this study are the trend toward substantially lower cost with increasing cell size and the significant cost reduction achieved by incorporating transparency into the design. Figure 10 shows some cell designs which could substantiate the model assumptions.

Comparison of transparent planar systems with concentrator designs is also of interest to NASA. Figure 11 shows a comparison of the results of three current large array studies sponsored by NASA-MSFC.

The final approach to be considered is a system level cascaded panel. Significant effort has been expended in recent years on the development of component level cascaded designs. Major technical challenges involved in growing layers with different lattice constants and matched currents have rendered production of a practical device an elusive goal. From a system level view point, a two-terminal component is unnecessary. By producing two different cells and using a two-bus architecture, the advantages of a cascaded system should be available as a near term option. Preliminary analysis of this type of system indicates efficiencies of 24% should be attainable.

CONCLUSIONS

Highly transparent gridded back contact cells have the potential to increase the power output of planar arrays by approximately 15%. Preliminary measurements on prototype components verify that high efficiency, gridded back contact cells can be produced. Progress is being made in integrating these cells into an IR transparent system.

ORIGINAL PAGE IS
OF POOR QUALITY

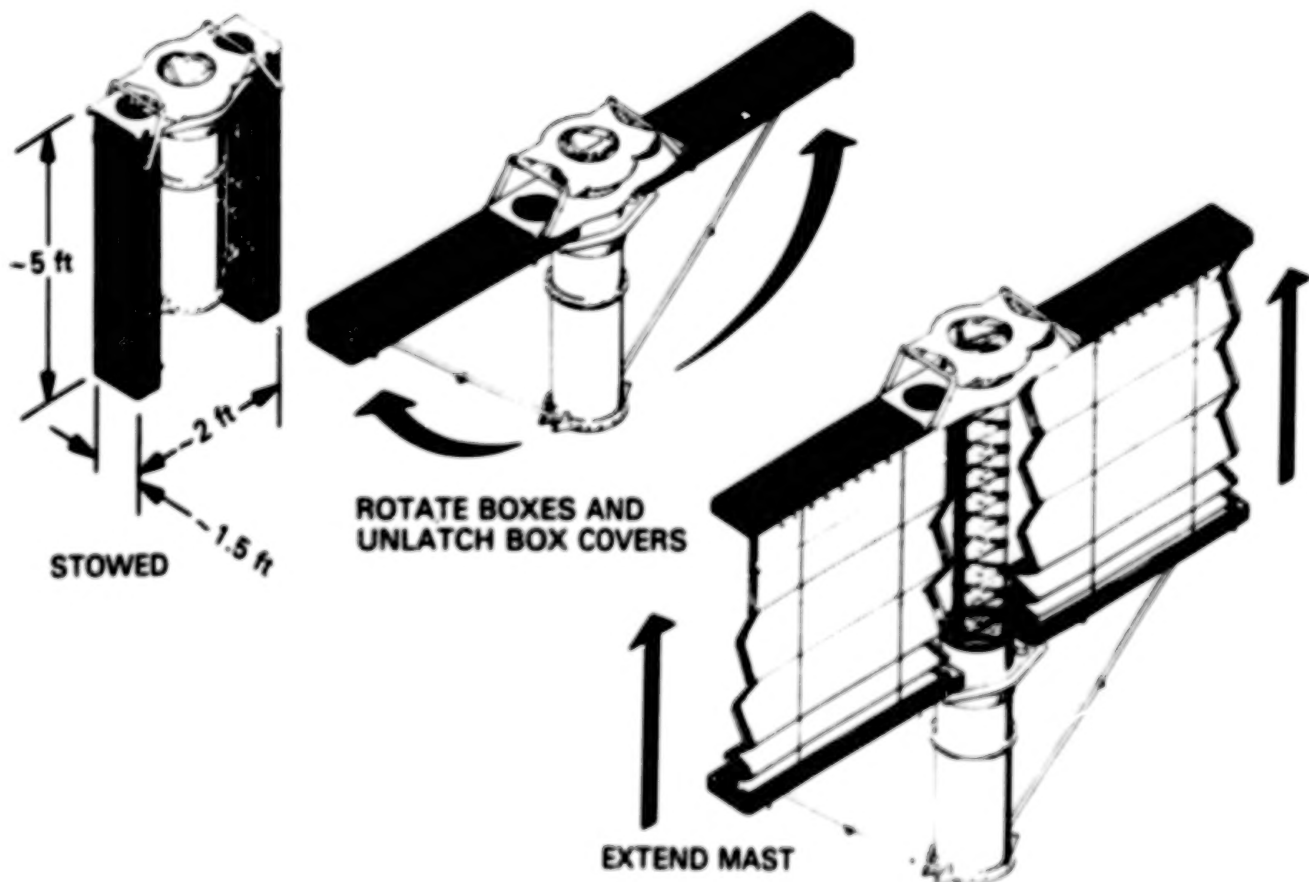


Figure 1. - 2-to-20 kW solar array functional sequence.

ORIGINAL PAGE 12
OF POOR QUALITY

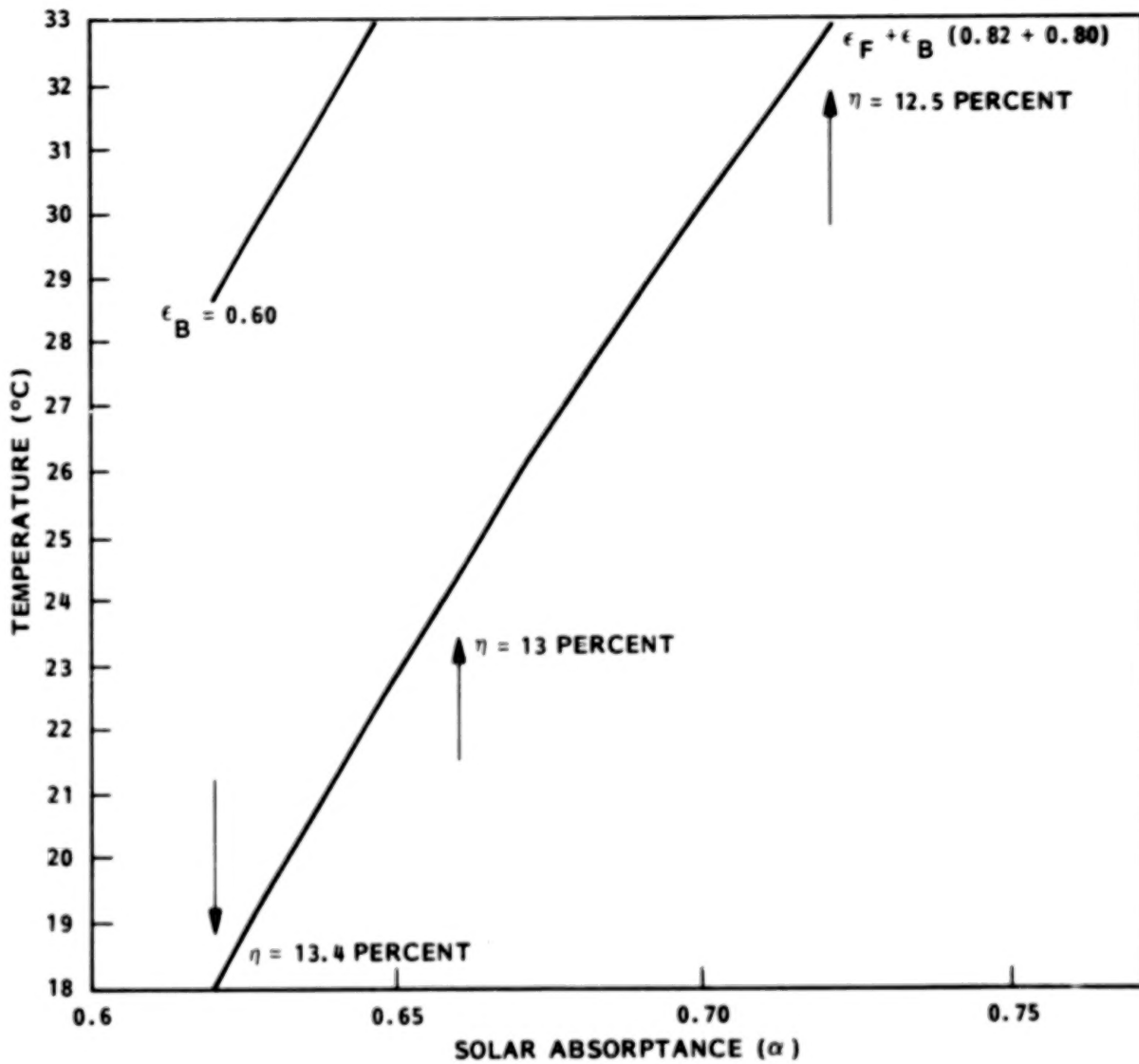


Figure 2. - Predicted thermal performance versus α .

ORIGINAL FACT IT
OF POOR QUALITY

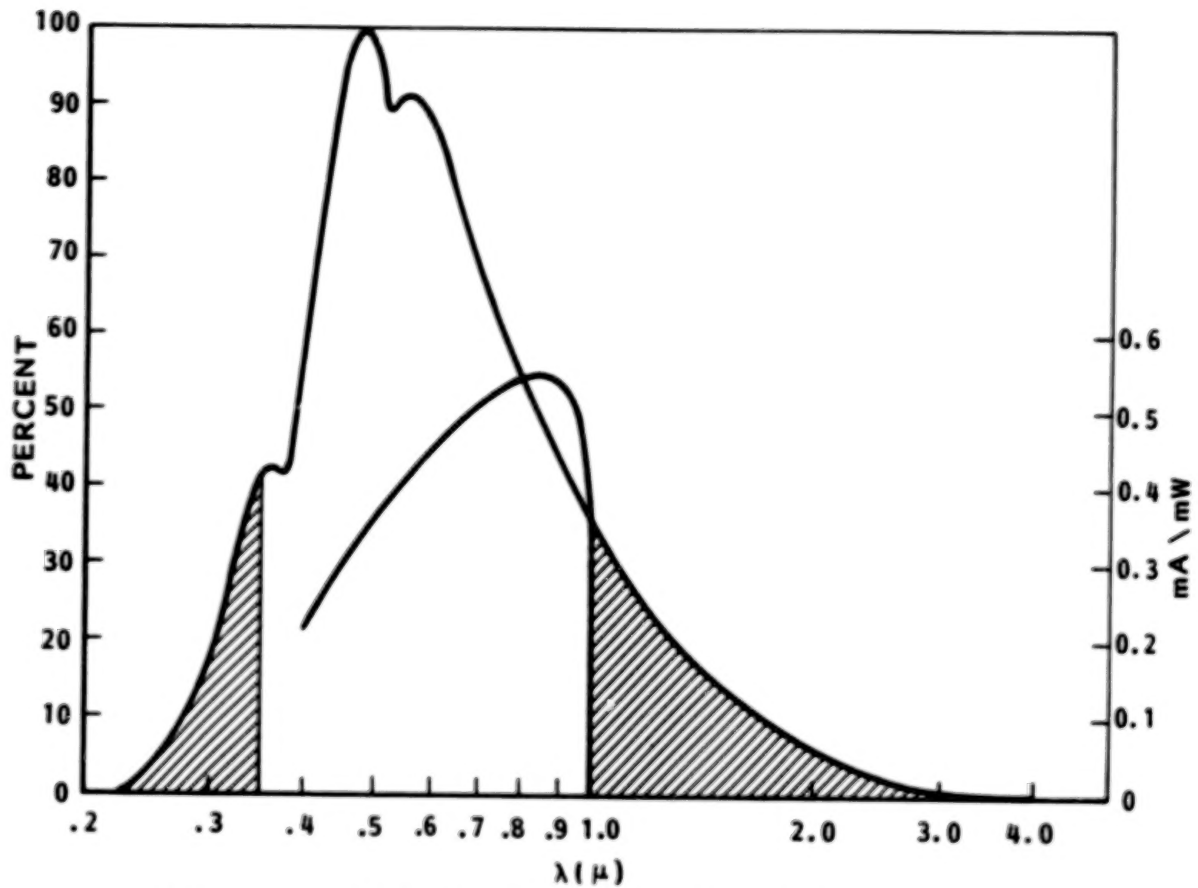


Figure 3. - Normalized solar spectrum and cell spectral response.

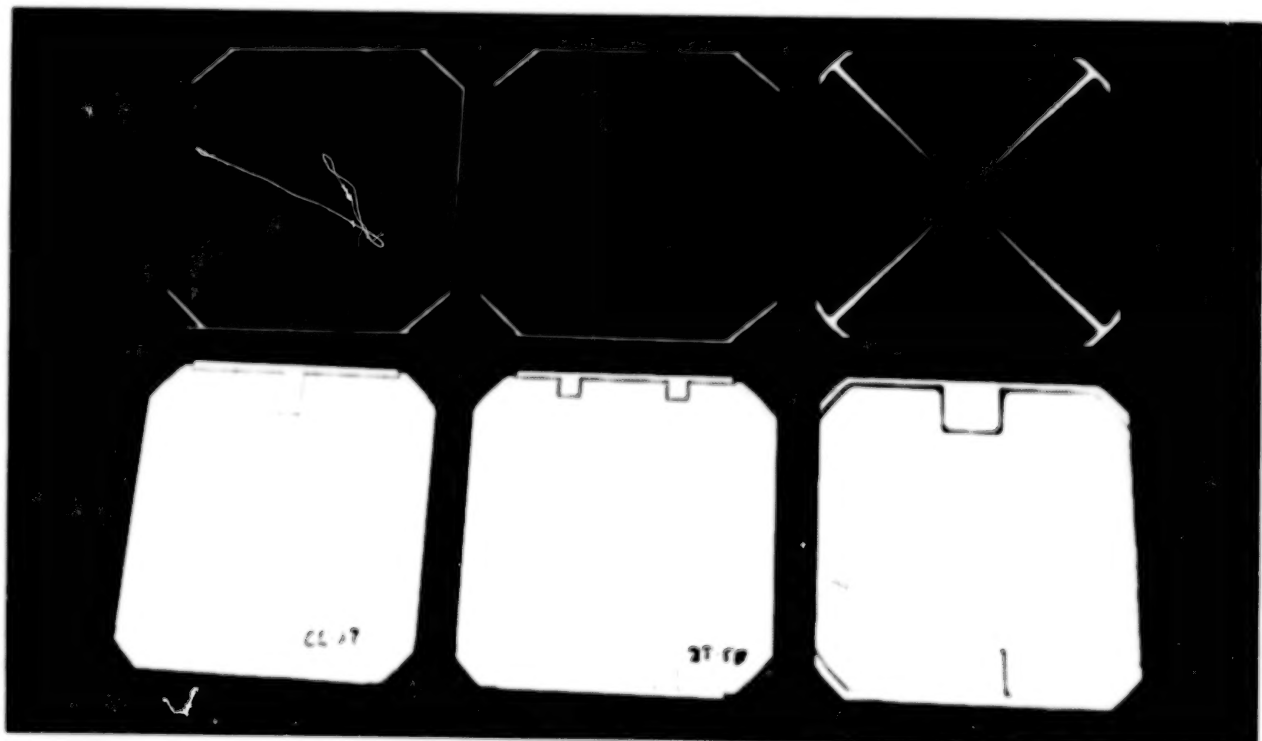
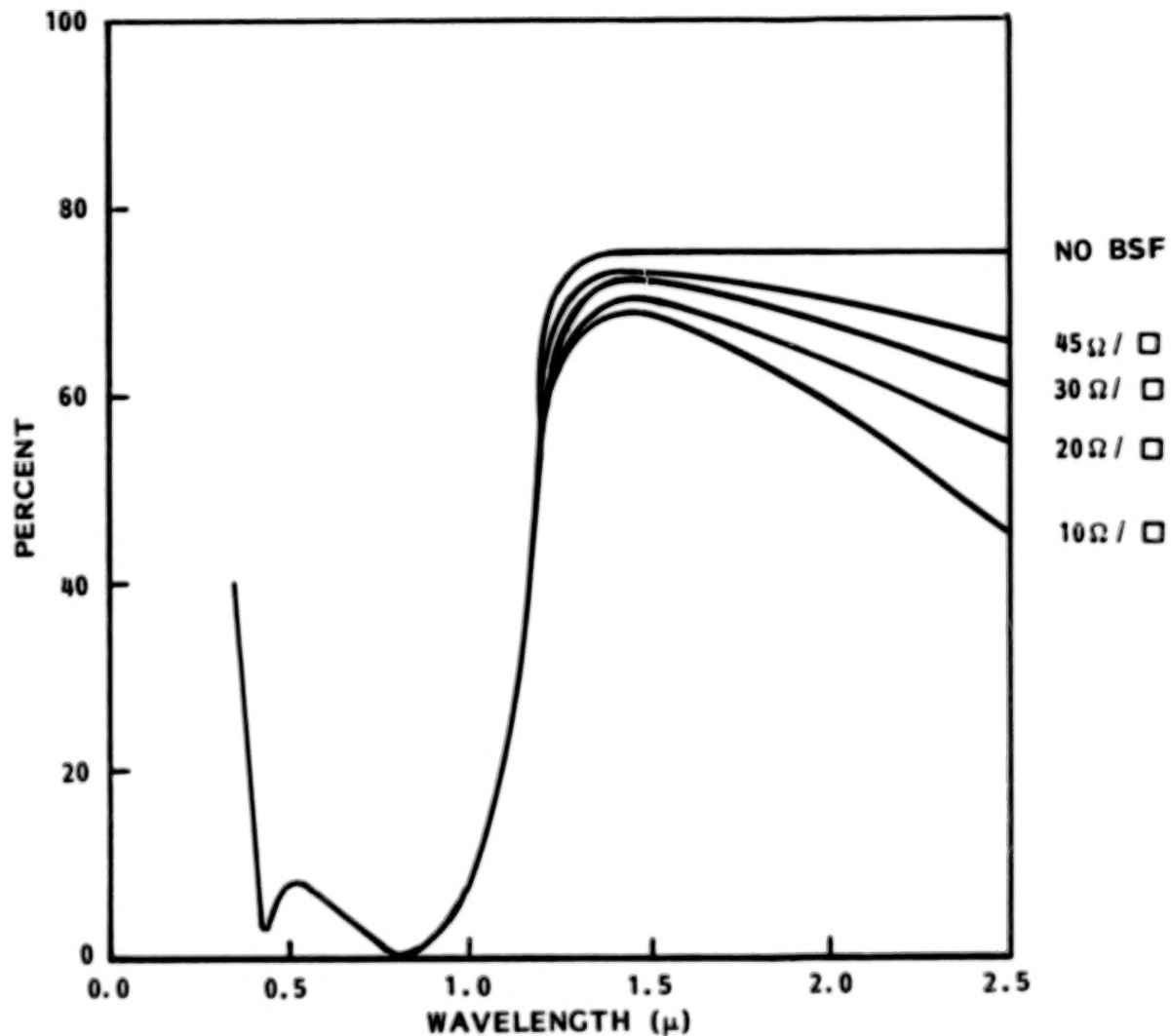


Figure 4. - Large area back surface reflector solar cells.

ORIGINAL PAGE IS
OF POOR QUALITY



* FROM F. HO, P. ISLES, H. CURTIS AND C. BARONA - RECENT
ADVANCES IN THIN SILICON SOLAR CELLS: 16th IEEE
PHOTOVOLTAICS SPEC. CONF.

Figure 5. - Spectral reflectance versus wavelength (varying Boron doping).

ORIGINAL PAGE IS
OF POOR QUALITY

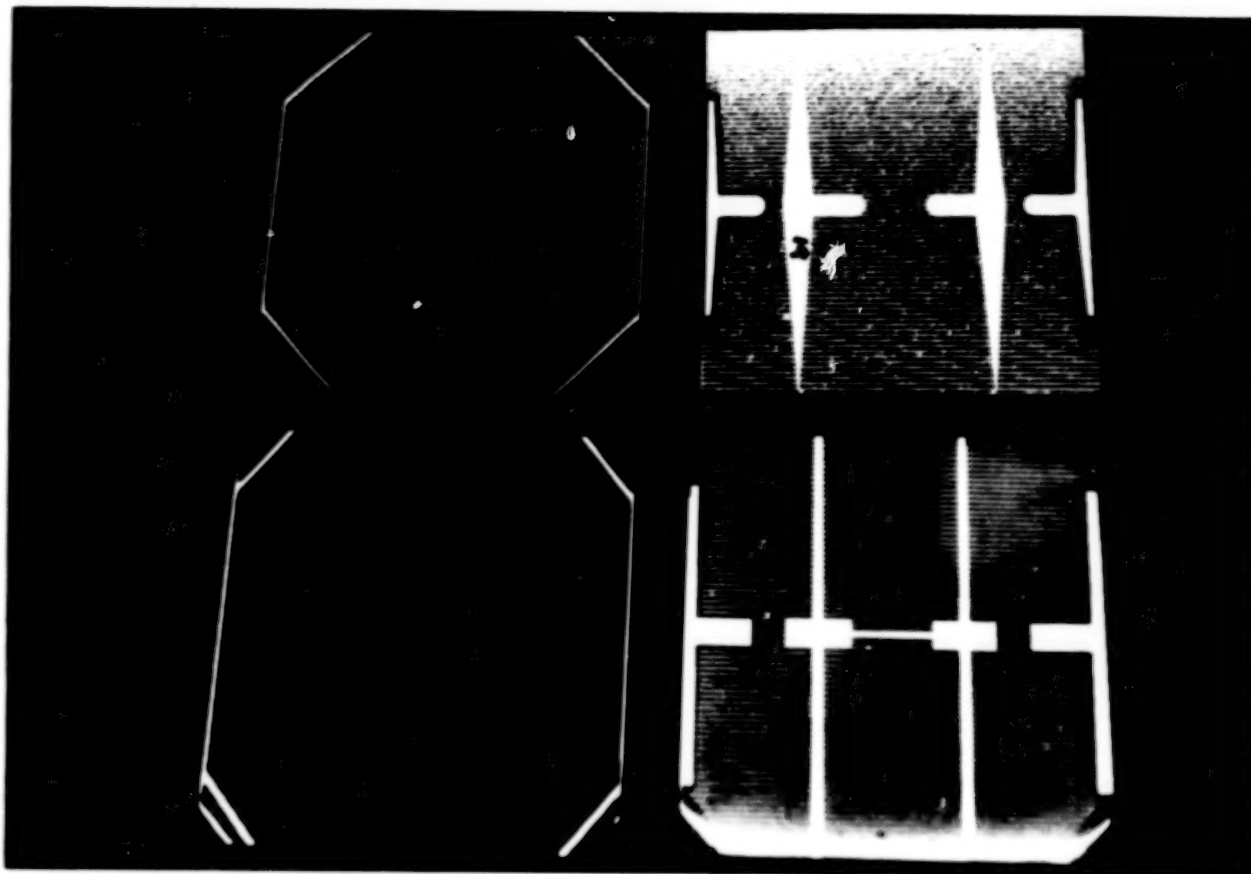


Figure 6. - Gridded back contact solar cells.

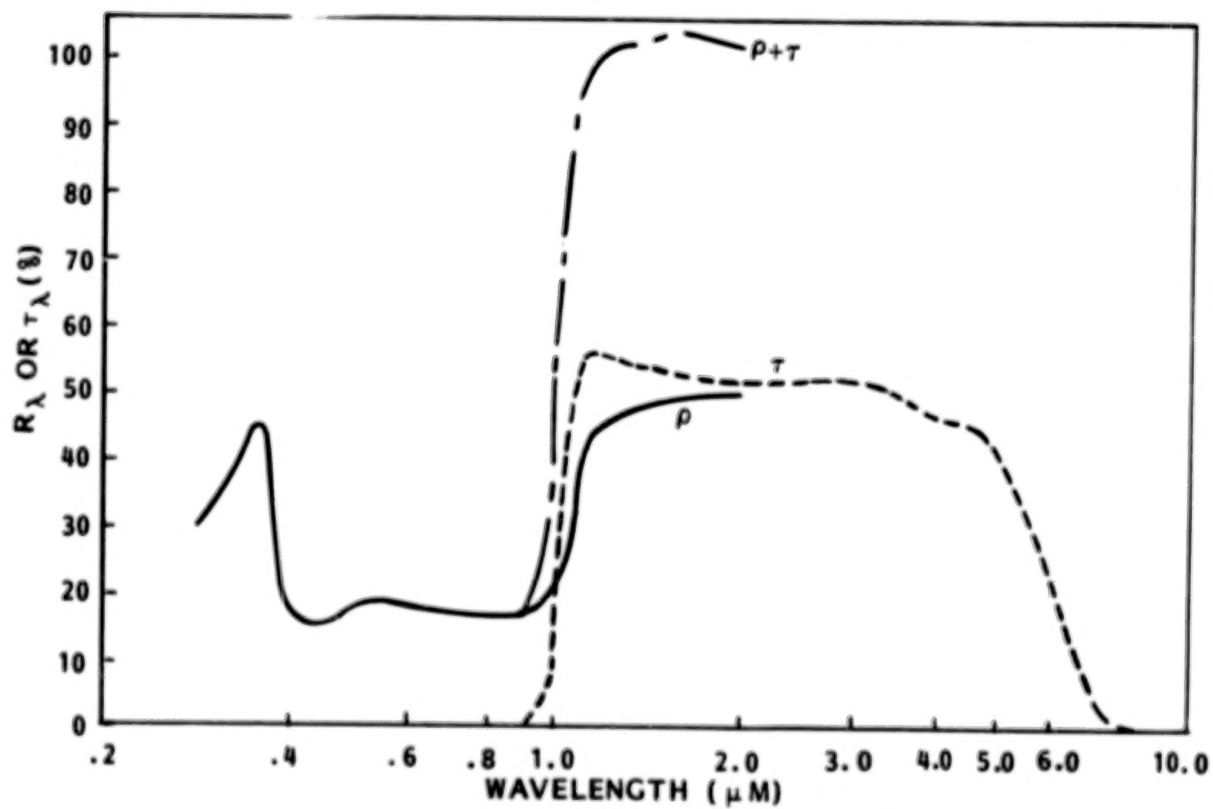


Figure 7. - Spectral reflectance and transmittance data.

ORIGINAL PAGE IS
OF POOR QUALITY

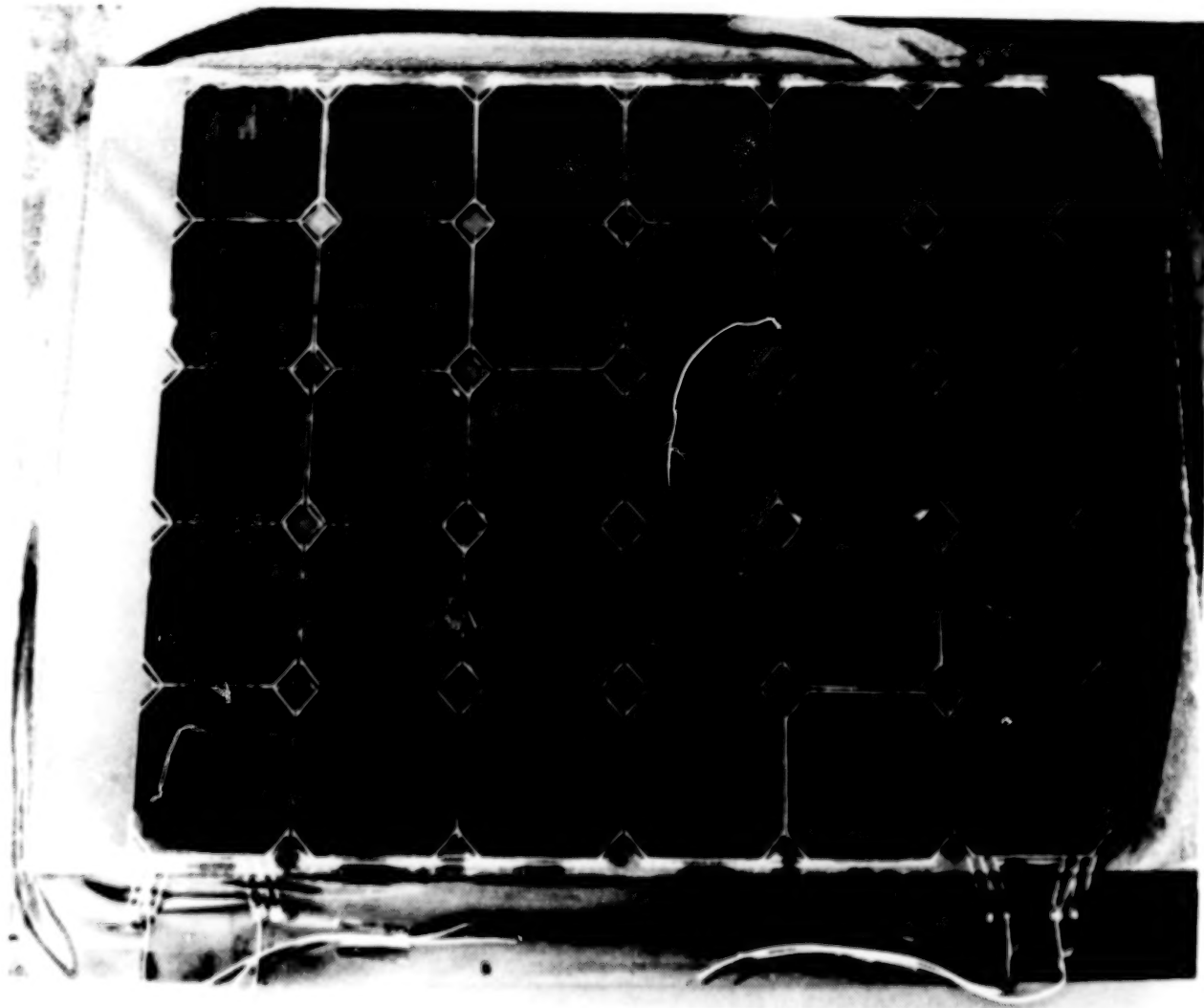


Figure 8. - 30-cell superstrate module.

ORIGINAL PAGE IS
OF POOR QUALITY

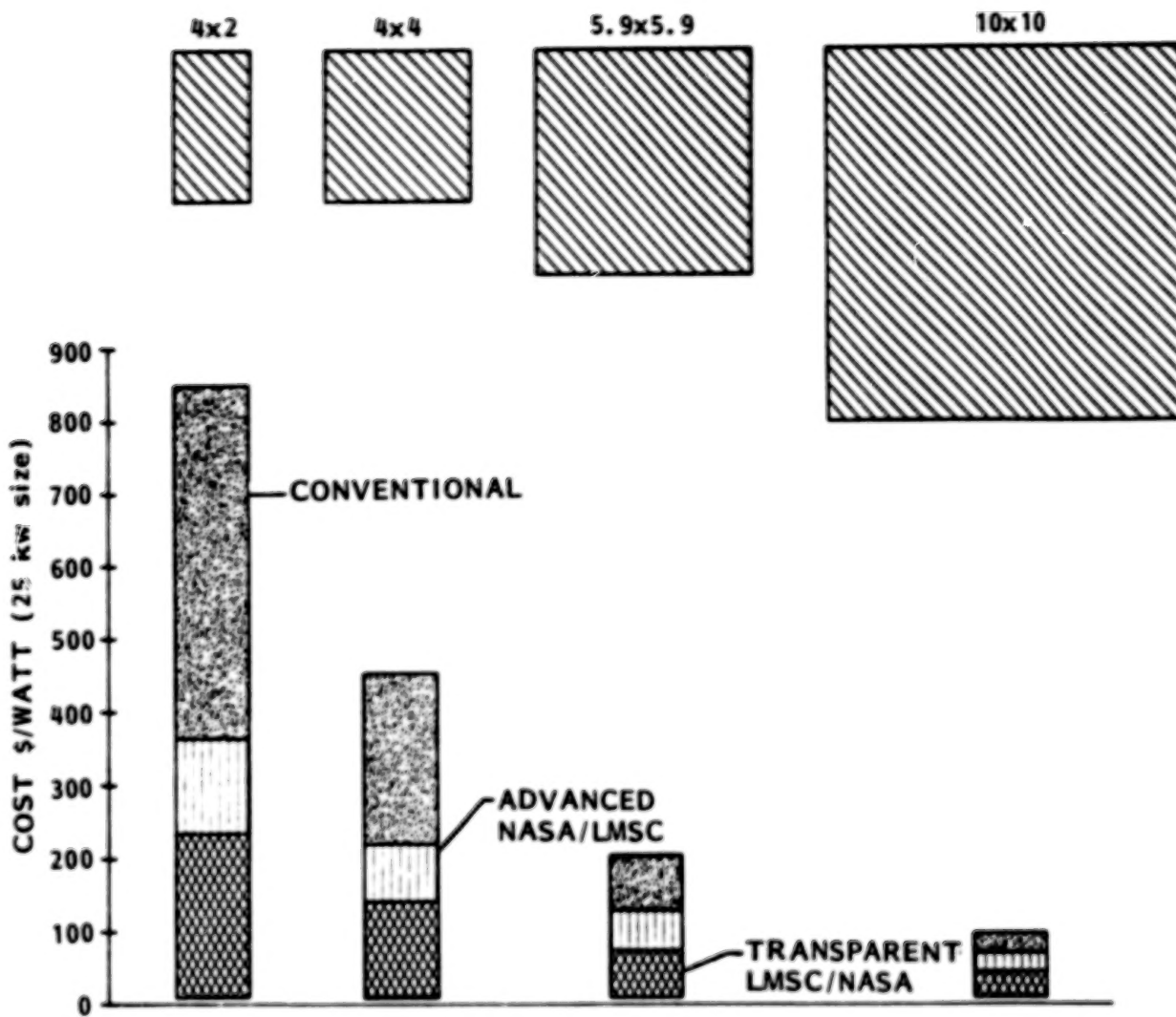


Figure 9. - Array blanket cost trends.

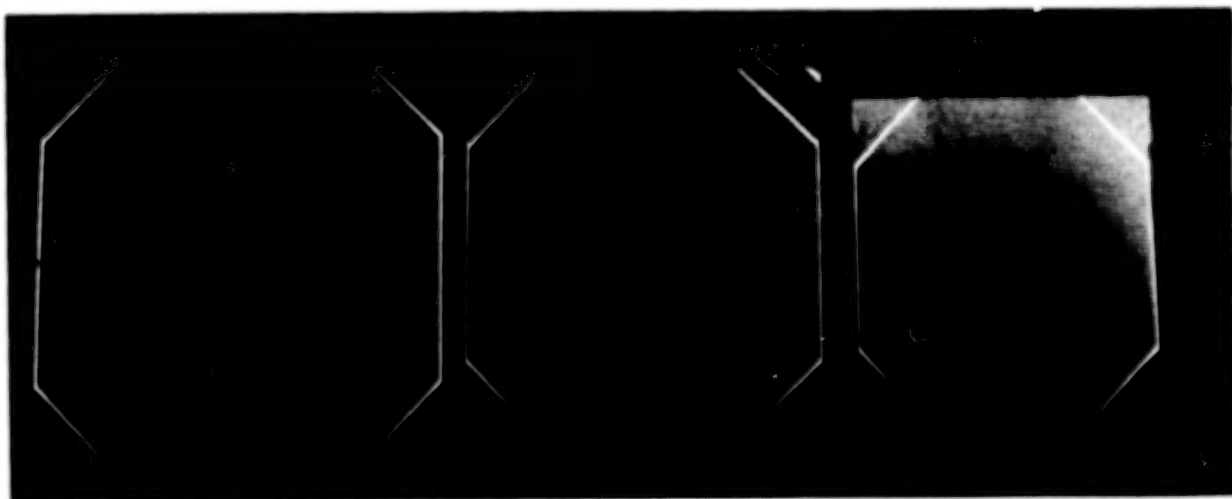


Figure 10. - Development large area cell.

PARAMETER	LMSC PLANAR	ROCKWELL LOW CR	TRW HIGH CR
CELL TYPE	GRIDDED BACK SI	GaAs	GaAs
SOLAR ABSORPTANCE	0.62	0.75	
OPERATING TEMP. (°C)	20	116	85
EFFICIENCY AT T (op)	13.4% (12.8 at 28°C)	15% (18% at 28°C)	20%
OPTICAL EFFICIENCY	1.0	0.77	0.55 (0.81) ^(A)
PACKING FACTOR	0.90	0.825	0.83 ^(C)
WIRING AND DIODE DROPS	0.97	0.99	0.97
CELL MISMATCH	0.98	0.99	0.98
OFF POINTING	1.0	1.0	0.98
BOL ARRAY POWER (W/m ²)	155 (220) ^(D)	133	115 ^(B) 160
SPECIFIC POWER (W/kg)	144	41	20 ^(B) 28
RECURRING COST (\$/W)	100	166	100-150
DESIGN LIFETIME (YRS)	15	10	5
ORBIT	250 nmi 60°	270 nmi 28.5°	235 nmi 57°
CELL DEGRADATION	0.96	?	0.95
EOL ARRAY POWER	149	?	109 152

NOTES: (A) PREDICTED MAXIMUM EFFICIENCY
 (B) CALCULATED BY LMSC FROM LISTED DATA
 (C) PACKING FACTOR AND EDGE EFFECTS
 (D) PROJECTED POWER DENSITY USING GRIDDED BACK GaAs

Figure 11. - Performance comparison.

N84
29339

UNCLAS

N84 29339

THE NASA WELDING ASSESSMENT PROGRAM*

John Scott-Monck
Jet Propulsion Laboratory
California Institute of Technology
Pasadena, California

John Bozek
National Aeronautics and Space Administration
Lewis Research Center
Cleveland, Ohio

This paper discusses the background and status of the NASA welding assessment program. The various approaches taken by those organizations involved in this effort are described along with the test program that has been initiated.

INTRODUCTION

For over a decade the potential cost and performance advantages of welding have been understood but ignored by solar panel manufactures in the U.S. Although NASA, DOD and COMSAT have supported welding development efforts, soldering remains the only U.S. space qualified method for interconnecting solar cells. The primary reason for this situation is that no U.S. satellite prime contractor has found it necessary, due to mission requirements, to abandon the space proven (low risk) soldering process. It now appears that the proposed NASA Space Station program will provide an array requirement, namely ten year operation in a low earth orbital environment, that mandates welding. Anticipating this demand, NASA has initiated a program to assess the status of welding technology in the U.S.

PROGRAM BACKGROUND

The NASA Lewis Research Center was charged with the responsibility to carry out the program. A survey of U.S. industry capability was made. This information was combined with inputs from potential users, such as DOD, to develop a plan to bring welding technology to flight readiness. The plan addressed existing (silicon) and projected (GaAs) solar array components.

* The research described in this paper presents the results of one phase of research carried out by the Jet Propulsion Laboratory, California Institute of Technology, under contract with the National Aeronautics and Space Administration.

A key element of this plan was the determination of the current status of U.S. welding technology. In order to expediently obtain this information it was decided to modify a number of existing NASA-JPL blanket development programs to incorporate this objective. This was done and four of the five major U.S. solar array manufacturers were involved in this effort.

PROGRAM APPROACH

Each participant provided a number of coupons and modules for evaluation and testing. These samples represented each organization's current approach to the requirements given, namely a welded, flexible substrate array capable of operating for ten years in a low earth orbit environment. In addition soldered modules were provided by each organization. The test modules (welded and soldered) were to be evaluated by subjecting them to thermal cycling over the temperature range between -80 and $+80 \pm 5^{\circ}\text{C}$.

Figure 1 describes the modules (welded and soldered) that were fabricated for the thermal cycling tests. It can be seen that there are many areas where there is a significant difference in approach. The choice of welding technique, interconnect material, solar cell and substrate are valid examples of the divergent options available from U.S. panel manufacturers.

Three welded and one soldered module were then subjected to thermal cycling testing at each organization's facility. In one case two organizations (Hughes Aircraft and Spectrolab) shared the test chamber. Two tests are being performed using a dry nitrogen environment, while the other (TRW) is being conducted in thermal vacuum. The initial test was limited to twelve thousand cycles, equivalent to two years in a low earth orbit. Electrical tests and visual inspections are made periodically to determine the status of the modules.

RESULTS AND CONCLUSIONS

At the request of one participant (LMSC), thermal cycling was suspended at five thousand cycles in order to allow a second source of the advanced cell ($5.9 \times 5.9\text{cm}$ wraparound contact) they had selected to be included in this assessment. The other tests have now exceeded nine thousand cycles with no significant electrical or mechanical degradation. If these encouraging results are confirmed at the twelve thousand cycle point, testing will be continued to thirty thousand cycles with electrical and visual inspections performed after each six thousand cycle increment.

The NASA welding assessment program has provided U.S. industry with a unique opportunity to directly compare welding to soldering. This series of tests involving nearly every U.S. manufacturer of solar arrays in a common test program will hopefully resolve the conjecture that a welded joint is inherently

ORIGINAL PAGE 10
OF POOR QUALITY

more resistant to thermal induced failure than one formed by soldering. This program has already demonstrated that there is a wide variation in U.S. opinion on the elements that constitute a reliable welded interconnect system for flexible blanket applications in a low earth orbital environment. Data obtained to date indicates that there is no significant difference between the various approaches taken to welding. Further testing will be needed in order to determine if the wide variety of welding options offer a suitable solution to the requirement that a solar array be capable of operating for ten years in a low earth orbital environment.

LMSC

TRW

HAC

Spectrolab

	LMSC	TRW	HAC	Spectrolab
Substrate	25 μ m Kapton & 13 μ m ployester	125 μ m Kevlar between 25 μ m layers of kapton	100 μ m Kevlar	100 μ m Kevlar
Substrate Adhesive	None	DC 93-500	Epoxy Resin	Epoxy Resin
Cell	5.9 x 5.9 cm wraparound (ASEC & SPECT)	2 x 4 cm BSL/MLAR (ASEC)	2 x 4 cm BSR-MLAR-BSF (SPECT.)	2 x 4 cm BSR-MLAR-BSF (SPECT.)
Cover	150 μ m 0211 (microsheet)	150 μ m fused silica	150 μ m fused silica	150 μ m fused silica
Cover Adhesive	DC 93-500	DC 93-500	DC 93-500	DC 93-500
Inter- connect	36 μ m Copper	25 μ m Invar/10 μ m plated silver	25 μ m Silver	30 μ m Silver plated Invar
Welding	Parallel-gap	Parallel-gap	Ultrasonic	Parallel-gap

N84
29340

UNCLAS

HIGH SPEED, LOW COST, LEO-THERMAL-CYCLING FACILITY

R. E. Hart, Jr., and L. G. Sidorak
National Aeronautics and Space Administration
Lewis Research Center
Cleveland, Ohio

Thermal cycling facilities have been constructed for years with various design criteria. Some were designed to duplicate as closely as possible the conditions a cell or module would encounter while in orbit about the earth. For example, a typical facility to perform this type of cycling was a large vacuum system with liquid nitrogen cooled walls. The cells were heated by an AMO spectrum solar simulator, then a shutter was closed allowing the cells to give up their heat to the cold walls. This system was good at duplicating the orbital conditions but was slow and very costly to operate.

Other systems used a gas atmosphere and heated the cells with radiant heat and cooled the cells by moving them into close proximity to a cold plate. These systems greatly increased the cycle times. Still, other systems moved the heating and cooling atmosphere into and out of the test areas and were able to achieve reasonable cycle rates. However, all these systems are expensive to operate.

This paper describes the design and operation of a low cost, high rate thermal cycling facility designed for LEO conditions.

EXPERIMENTAL

Critical design features of this thermal-cycling facility include the ability to cycle cells or modules over a range of $\pm 80^{\circ}\text{C}$, considered appropriate for a low earth orbit and a nitrogen gas atmosphere for heat transfer and temperature control. This atmosphere also ensures that possible oxygen and water contamination are kept to a minimum.

Because the mass of the solar cell modules or cells themselves greatly affect cycle time, we decided to build a facility to accept cells mounted on thin Kapton or plastic sheets or cells fastened onto wires. The modules on Kapton substrates are spring loaded to allow for some movement during the thermal cycles. Therefore, the ends of the Kapton are clamped to ensure that the tension is spread evenly over the width of the module.

Although early experiments using a dipping facility showed that high rates of temperature change could be obtained when a cell is plunged into liquid nitrogen, the rate of change was felt to be too severe. A better method would be to use a cold chamber filled with nitrogen gas to obtain acceptably high rates of cooling. The cells are moved from this cool environment into a heated chamber. This approach requires heating and cooling of only the cells/modules and their frames. With these changes, we believed high cycle

rates could be obtained experimentally.

Figure 1 is a drawing of the cycling chamber showing both front view and side views. The front view shows the chamber divided into two parts by an insulated shelf. The lower compartment is cooled to -110°C with liquid nitrogen or at least the cold gas injected onto the floor of the compartment. Most of the exhaust gases are expelled just below the insulated shelf, removing the warmest gases from the chamber. Some gas seeps into the upper chamber and flushes out all the air by way of small openings in the top. The upper compartment is heated to $+110^{\circ}\text{C}$ with two 500 watt strip heaters mounted in chimney-like fixtures on either side. Also shown are four frames which slide in guides in half-inch wide openings in the shelf. Each frame independently slides back and forth between the two compartments. A 1-1/2 inch wide flange on each end of the frame seals the compartment on both the up and down strokes. The side view shows how the frames are moved using an air drive and a lever arrangement on each frame. The connecting tube serves two purposes, one to move the frame and second, to furnish a way for the thermocouples and other wiring to exit the chamber. This also helps keep wires from one frame getting caught in another.

Figure 2 is a picture of a module mounted in its frame. The frame has an opening with 9x10 inches of usable modules mounting area. This particular module, mounted on a Kapton substrate, is supported by steel clamps. The upper clamp is wired directly to the frame at the top and the lower clamp is spring loaded to the bottom. The springs pull with a total force of 20 grams per centimeter width, including the weight of the lower clamp.

Figure 3 is a picture of the thermal cycling facility, including two refrigerators and the rack of necessary electronics. The refrigerators are placed underneath a hood which removes all the exhausted nitrogen gas and any other odors escaping from the boxes.

The electronics rack on the right includes a basic language, desk top computer. A computer was chosen for control because of its flexibility of controlling instruments, processing data, performing functions, displaying data and outputting data as a function of time.

The voltmeter measures all thermocouples, module resistances and voltages if required. The scanner sweeps all inputs and performs control functions on command, such as operating heaters, liquid nitrogen valves and all air drives.

The temperature regulator at the top of the rack senses the temperature of the upper compartment. If the system overheats, the regulator shuts down the entire system.

RESULTS

By controlling the lower compartment temperature to -110°C and the upper compartment to $+110^{\circ}\text{C}$ and setting the cycle limits to $\pm 78^{\circ}\text{C}$, cell temperatures of $\pm 80^{\circ}\text{C}$ were achieved on four frames having single cells mounted in the center of each. Each frame completed more than 1000 cycles in a twenty-four hour period or less than 1.4 min./cycle.

ORIGINAL PAGE IS
OF POOR QUALITY

Liquid nitrogen consumption for the same period was less than 150 liters and electrical consumption by the two 500 watt heaters was about 12 kilowatt-hours.

Figure 4 is a bar plot showing the symmetry of a typical thermal cycle with limits of $+100^{\circ}\text{C}$ and -115°C . Even with the additional temperature range, we were able to maintain rates of less than 1.3 minutes per cycle on a bare cell mounted in the center of the frame. The printer prints a permanent record during the test.

This facility has completed tests on four solar cell modules mounted on Kapton. This test had a duration of 20,000 cycles between $+80^{\circ}\text{C}$ and -115°C - a range more severe than was originally required. Even with this greater temperature range, more than 600 cycles/day were obtained.

CONCLUSION

We believe this high speed (greater than 1000 cycles per day), low cost (less than \$12,000 for equipment), economical (150 liters of liquid nitrogen and 12,000 watts of electricity per day), shows this system to be a functional and dependable system for studying failure mechanisms in solar array interconnections.

Its versatility in extending the operational temperature range has also been demonstrated.

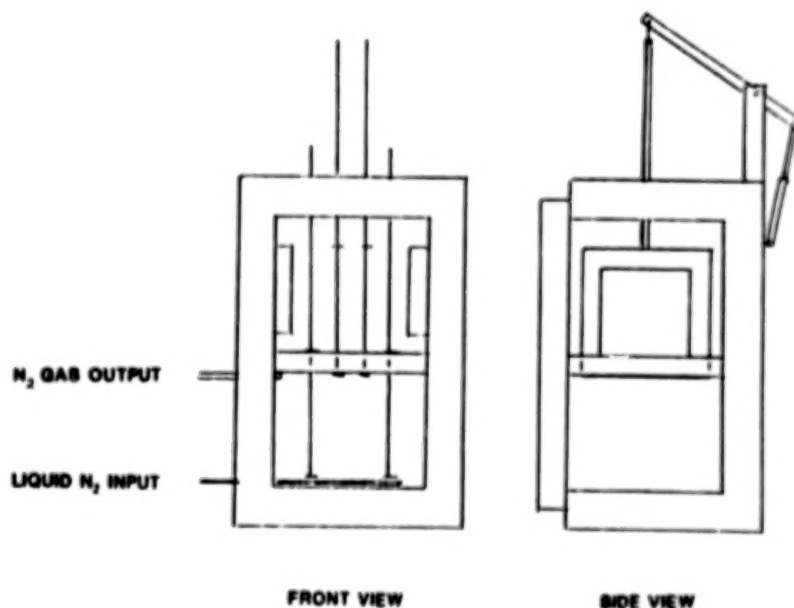
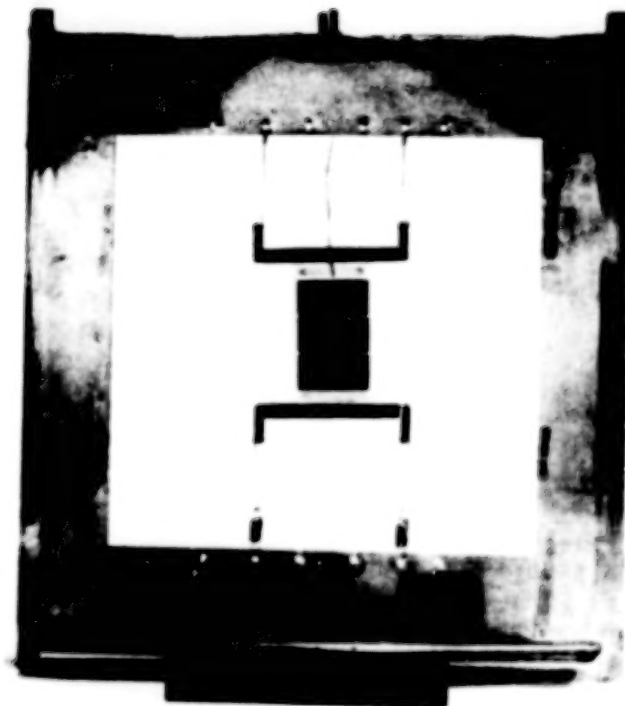


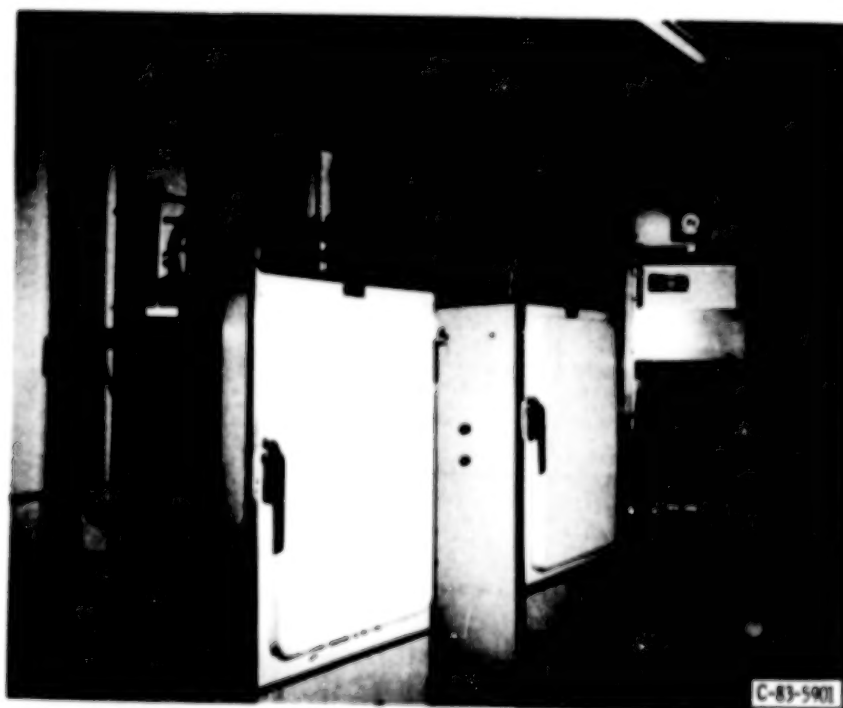
Figure 1. - Thermal cycling chamber.

ORIGINAL PAGE IS
OF POOR QUALITY



C-83-6202

Figure 2. - Module mounted in frame.



C-83-5901

Figure 3. - Thermal cycling facility.

ORIGINAL PAGE IS
OF POOR QUALITY

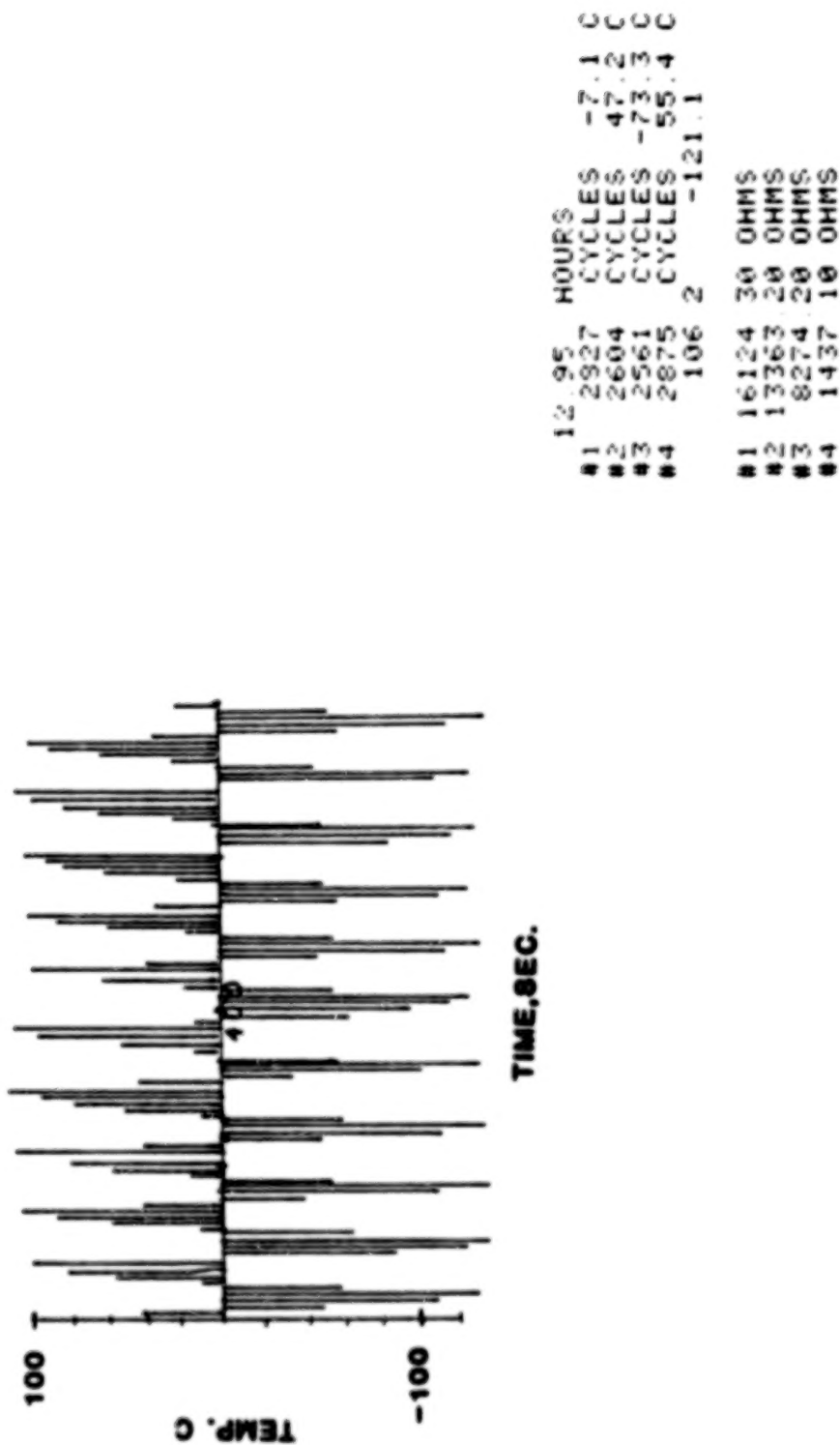


Figure 4. - Typical printout.

N84
29341

UNCLAS

N84 29341

IMPROVED TECHNIQUES OF PARALLEL GAP WELDING AND MONITORING

N. Mardesich and M. S. Gillanders
Spectrolab, Inc.
Sylmar, California

Recent activities in the space solar panel market have shown an increasing interest in welded solar circuits. Spectrolab is presently developing a manufacturing system which monitors and controls the fabrication of parallel gap welding circuits utilizing an infrared detector.

This paper will outline the basic manufacturing and control system and describes the utilization of Acoustic Microscopy as the non-destructive technique for evaluating weld integrity. A number of different cell types, including GaAs, have been evaluated using parallel gap welding. Status of welded panels which have been built and are under evaluation will be reported.

INTRODUCTION

The trend in American industry today is to mass-produce products with the aid of automated equipment. Spectrolab has been developing a parallel gap welding system that can effectively reduce labor time necessary to assemble silicon solar cell circuits. The welded circuits have the added advantage over soldered circuits in that they are capable of withstanding higher temperatures. The goal that Spectrolab has set for itself is to reliably assemble solar cell circuits using a parallel gap welded system that controls the welding temperature while the temperature is monitored and recorded. An additional goal that Spectrolab is interested in achieving is a non-destructive post-weld technique for evaluating weld integrity.

This paper addresses the recent activities at Spectrolab in the fabrication of welded circuit and panel assemblies. Spectrolab has manufactured reliable solar cell circuits utilizing parallel gap welding monitored by a thermal monitoring system. These circuits and panels were manufactured for environmental tests such as thermal cycling. Test results to date have indicated that these panels have undergone environmental tests with very good results. Table 1 is a list of the three panel programs Spectrolab has recently been involved with.

Spectrolab has also been interested in evaluating the welding of GaAs cells for the future space solar panel market. This program has recently been initiated and only limited results are available.

EQUIPMENT

The equipment utilized for parallel gap welding interconnection onto solar cells is basically the same as that used for soldered interconnections. This equipment consists of a printed circuit weld station (Hughes Model HPC-500) which utilizes the MCW-550 constant voltage welding power supply and the VTA-66 parallel gap weld head. The circuits are aligned under the weld head with a Hughes Model HXY 012D XY Table. The position of the cell is maintained with vacuum while the welding is performed.

The weld temperature is monitored with the aid of a Vanzetti Thermal Monitoring System. This system measures the temperature of the weld tip/interconnect area with an IR detector which displays the temperature by LED's. The weld integrity is measured with a Unitek Micropull Tester by pulling the tab at 45 degrees.

PROCESS CONTROL

It is imperative to control the welding operation to ensure product consistency. The welded interconnects cannot be visually inspected for integrity after welding, therefore in-process controls must be implemented. The parallel gap welding equipment has a built-in control that maintains power and controls duration. The variation in weld tip condition will vary the voltage through the interconnection/cell contact area and change weld temperature. By dressing the weld tip periodically the weld conditions can be maintained constant.

An experiment was performed to determine the variation of weld temperature when the weld tips were dressed every four welds. The temperature of the interconnection/weld tip area was monitored with a Vanzetti Thermal Monitor and indicated that the P welds reached a temperature of $740 \pm 25^{\circ}\text{C}$. The variation in temperature was due more to drifting of the monitor's position rather than the welding temperature. The 45 degree pull strength of the monitored cells on a sample basis varied from 740 to 1300 grams with the average being 864 grams. This monitoring procedure is a very good method of ensuring in-process control.

Spectrolab is planning on using the Vanzetti Thermal Monitor system as a weld duration controller. The system will monitor the temperature and allow a constant voltage to be applied to the interconnect/cell contact until a pre-set temperature is reached, at which time the voltage is dropped to zero. The temperature will be recorded by a computer and cells will be selected at random for tab pull test. The temperature controller/monitor, along with destructive tests, will ensure product consistency.

In addition to the destructive contact pull test control, Spectrolab is evaluating the use of non-destructive contact integrity techniques. One of these methods is with the use of a post-weld reflection acoustic microscopy (ref. 1). The microscopic technique utilizes water as a transfer media and obtains acoustic material signature which characterizes the material of interest. An acoustic image of the cell/interconnect interface can be obtained by the selection of the proper node. The acoustic image can be compared with the optical image to determine the area of good weld integrity and verify reliability of the product.

ESTEC PANEL

The European Space Agency, through its European Space Research and Technology Centre (ESTEC) was interested in the state-of-the-art lightweight welded solar panel which could withstand geostationary or low earth orbits. They planned to subject the panels to two accelerated thermal cycling 3000 cycles which ranged from $+130$ to -180°C in five-minute durations for the deep thermal cycles (geostationary) and medium thermal cycles (low) environment, 20,000 cycles which ranged from $+100$ to -100°C in two-minute durations.

This environment appeared challenging and Spectrolab offered to manufacture a 28 cm x 25 cm graphite reinforced Kapton panel. This panel was to consist of 4 parallel by 10 series circuits made from 2 cm x 6 cm, 100 micron BSF/BSR cells

with 50 micron CMS filter glass. The cells were to be parallel gap welded together with 25 micron Invar interconnects with 5 micron silver plating. The circuit was to be bonded with R-2568 adhesive.

The interconnect design is given in Figure 1. Silver plated Invar was selected because of its weldability and its close thermal expansion match to that of silicon. In plane stress relief loops were incorporated in the design to minimize stress on the back P welds. Two welds were made on each pad (six per cell) which minimizes the torsional stress on the weld areas. The parallel gap welding of the cells did not present any major problems. The rework on a circuit level did not present complications and rework was not required on the panel level.

A few problems did occur during the performance of the contract which stemmed from the use of 50 micron CMS filters. The filters had a very long lead time and did not arrive on schedule. Ten percent of the filters arrived fractured and handling was difficult. The yield of cell/interconnect/cover (CIC) assemblies was poor (approximately 75%) due to the fragility of the covers.

The I-V characteristic of the panel is given in Figure 2. The power of the panel was 8.5 watts (AMO, 28°C) with an average cell efficiency of 12.7% on the panel.

HAC/JPL CIRCUITS

NASA-Lewis was interested in evaluating the state-of-the-art techniques in welding and funded a program with JPL and Hughes Aircraft Company (HAC). Under this program Spectrolab would provide cells to HAC for ultrasonic welding. Welded and soldered circuits were also provided for bonding to a Kevlar fabric.

The circuits consisted of 3 parallel by 3 series, 2 cm x 4 cm, 200 micron BSF/BSR cells with 150 micron fused silica covers. The selected interconnects were silver plated Invar, similar to those used for the ESTEC panel except one weld pad was removed. A total of 10 circuits (six welded and four soldered) were provided for evaluation. Two of the six welded panels required rework due to fractured cells. The circuit was readily repaired by fracturing the back P weld and replacing the cell.

A typical I-V characteristic curve for a circuit is given in Figure 3. The power of the circuit was 1.5 watts (AMO 28°C) with an average cell efficiency of 14.5%. These bonded circuits have recently undergone a thermal cycle treatment of +80 to -80°C for 12,000 cycles with no indication of visual or electrical change.

RCA PANEL

RCA was interested in evaluating welded panels for a special program. Spectrolab would provide two 2 parallel by 3 series circuits for preliminary evaluation and a 5 parallel by 10 series panel for testing.

The cells used to manufacture these circuits and panel were 2 cm x 4 cm, 250 micron 2 ohm-cm, BSR components. The silver plated Invar interconnects (the same interconnects used on the HAC/JPL circuits) were used to assemble the circuits. The N+ welds were monitored with a Vanzetti Thermal System and indicated that the interconnect/weld tip interface reached 610°C. The 45 degree pull strength for the N+ contacts was 250 to 750 grams with an average of 450 grams, where the 250 gram sample pulled silicon from the cell. During the P contact

welding the thermal monitor was used to determine the temperature fluctuation of the interconnect/weld tip interface during welding. The monitor indicated a temperature of $740 \pm 25^\circ\text{C}$ for over 150 welds performed. The pull strength of the contacts on a sample basis was 740 to 1300 grams with an average of 864 grams. These welded circuits were then bonded to an aluminum honeycomb substrate without filters.

The electrical I-V characteristic of the 5×10 panel is given in Figure 4. The power of the circuit was 7.53 watts (AM0, 28°C) with an average cell efficiency of 13.6%. The mechanical integrity of the panel was excellent with no sign of peeling or delamination.

GaAs WELDING

Recently, limited effort of welding GaAs solar cells has proven fruitful. With the use of 25 micron silver interconnects we have been able to reliably weld onto the P and N contacts. The 45 degree pull strength of these contacts was 250 grams. An extensive program into the welding and panel fabrication of GaAs solar cells is necessary to provide the industry with reliable information. Spectrolab will be pursuing this effort on a limited basis.

CONCLUSION

The work performed on the recent welding programs have shown that the parallel gap welding performed at Spectrolab is a reliable process. As more monitoring, controls and non-destructive testing is incorporated into the process, the more reliable and cost effective parallel gap welding becomes. The positive results obtained from the panel fabrication techniques and HAC thermal cycling test indicate reliable product integrity. Presently our production personnel are heavily involved in designing and building automated type tooling and fixturing for welding in production.

REFERENCE

1. R. D. Weglein, "Metrology and Imaging in the Acoustic Microscope", Scanned Image Microscopy, Academic Press, New York, p. 127.

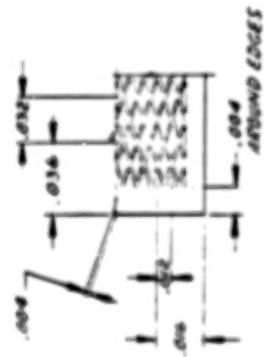
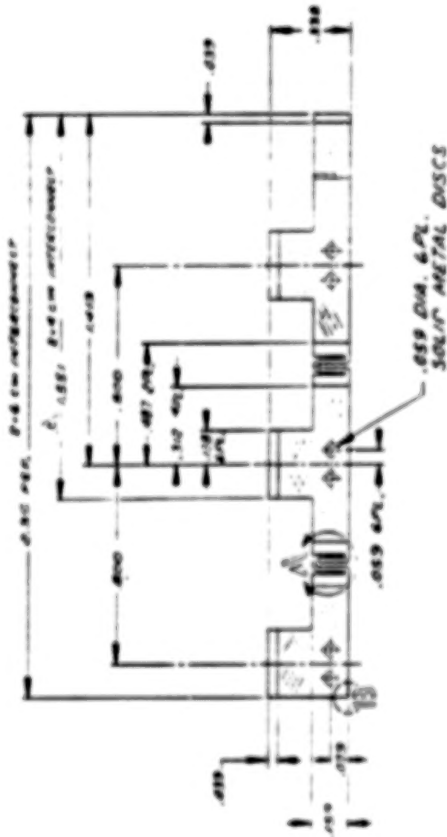
ORIGINAL PAGE IS
OF POOR QUALITY

TABLE 1. - RECENT WELDED-PANEL MANUFACTURING

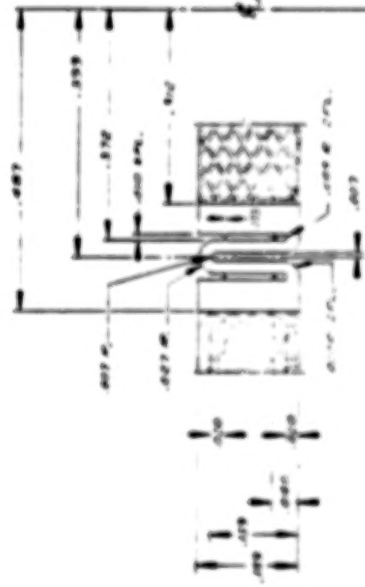
PROGRAM	ESTEC	BAC/JPL	RCA
MISSION	THERMAL CYCLE	THERMAL CYCLE	UNKNOWN TESTS
	+130 to -180°C (3,000) +100 to -100°C (20,000)	+80 to -80°C (12,000)	Unknown Tests
Panel Size (cm)	28 x 25 cm	12.7 x 8.3 cm	23.5 x 21 cm
Substrate Type	Kapton/Graphite	Circuit Only	Aluminum Honeycomb
Insulation	Kapton	-	Kapton
Bonding Adhesive	R-2568	-	R-2568
Interconnects	Silver Plated Invar	Silver Plated Invar	Silver Plated Invar
Panel Power (AMG)	8.5 W @ 28°C	1.5 W @ 28°C	7.53 W, .89 W
Number of Cells/Panel	40 each	9 each	50 ea, 6 ea
Number of Panels Manufactured	1 Each	6 Each	1, Ea, 2 Ea
Circuit Configuration	4P x 10S	3P x 3S	5P x 10S, 2P x 3S
Solar Cell Type	10 μ -cm K6.75	10 μ -cm, K6.75	2 μ -cm, K4.75
Solar Cell Size	2 x 6 cm	2 x 4 cm	2 x 4 cm
Cell Thickness	0.004"	0.008"	0.010"
AR Coating	Dual AR	Dual AR	Dual AR
Coverglass	0.002" GHS	0.006" FS	None
Adhesive	93-500	93-500	-
Cell η (on Panel)	12.7% @ 28°C	14.5% @ 28°C	13.6%, 13.4% @ 28°C

ORIGINAL PAGE 13
OF POOR QUALITY

姓名	性别	年龄	职业	住址	电话
王德胜	男	45	教师	XX路XX号	XXXX
李小红	女	32	护士	XX街XX号	XXXX
张小明	男	28	学生	XX村XX组	XXXX
赵大伟	男	50	工人	XX厂XX车间	XXXX
陈丽娟	女	38	医生	XX医院XX科	XXXX
周国强	男	42	农民	XX乡XX村	XXXX
吴小芳	女	25	职员	XX公司XX部	XXXX
郑大刚	男	35	工程师	XX研究所	XXXX
孙丽娜	女	30	记者	XX报社	XXXX
马志远	男	40	律师	XX律师事务所	XXXX
徐小梅	女	22	会计	XX公司XX部	XXXX
黄大强	男	55	退休	XX小区XX栋	XXXX
宋小红	女	35	作家	XX作协	XXXX
周国强	男	48	商人	XX公司	XXXX
吴小芳	女	28	歌手	XX音乐公司	XXXX
郑大刚	男	32	程序员	XX互联网公司	XXXX
孙丽娜	女	25	设计师	XX设计公司	XXXX
马志远	男	40	科学家	XX研究院	XXXX
徐小梅	女	22	翻译	XX翻译公司	XXXX
黄大强	男	55	教授	XX大学	XXXX
宋小红	女	35	画家	XX画院	XXXX
周国强	男	48	企业家	XX集团	XXXX
吴小芳	女	28	模特	XX经纪公司	XXXX
郑大刚	男	32	产品经理	XX科技公司	XXXX
孙丽娜	女	25	市场专员	XX公司	XXXX
马志远	男	40	销售经理	XX公司	XXXX
徐小梅	女	22	客服专员	XX公司	XXXX
黄大强	男	55	财务总监	XX公司	XXXX
宋小红	女	35	人力资源	XX公司	XXXX
周国强	男	48	行政主管	XX公司	XXXX
吴小芳	女	28	法务专员	XX公司	XXXX
郑大刚	男	32	IT支持	XX公司	XXXX
孙丽娜	女	25	培训专员	XX公司	XXXX
马志远	男	40	质量经理	XX公司	XXXX
徐小梅	女	22	采购专员	XX公司	XXXX
黄大强	男	55	仓储主管	XX公司	XXXX
宋小红	女	35	物流专员	XX公司	XXXX
周国强	男	48	销售助理	XX公司	XXXX
吴小芳	女	28	市场专员	XX公司	XXXX
郑大刚	男	32	产品经理	XX公司	XXXX
孙丽娜	女	25	市场专员	XX公司	XXXX
马志远	男	40	销售经理	XX公司	XXXX
徐小梅	女	22	客服专员	XX公司	XXXX
黄大强	男	55	财务总监	XX公司	XXXX
宋小红	女	35	人力资源	XX公司	XXXX
周国强	男	48	行政主管	XX公司	XXXX
吴小芳	女	28	法务专员	XX公司	XXXX
郑大刚	男	32	IT支持	XX公司	XXXX
孙丽娜	女	25	培训专员	XX公司	XXXX
马志远	男	40	质量经理	XX公司	XXXX
徐小梅	女	22	采购专员	XX公司	XXXX
黄大强	男	55	仓储主管	XX公司	XXXX
宋小红	女	35	物流专员	XX公司	XXXX
周国强	男	48	销售助理	XX公司	XXXX
吴小芳	女	28	市场专员	XX公司	XXXX
郑大刚	男	32	产品经理	XX公司	XXXX
孙丽娜	女	25	市场专员	XX公司	XXXX
马志远	男	40	销售经理	XX公司	XXXX
徐小梅	女	22	客服专员	XX公司	XXXX
黄大强	男	55	财务总监	XX公司	XXXX
宋小红	女	35	人力资源	XX公司	XXXX
周国强	男	48	行政主管	XX公司	XXXX
吴小芳	女	28	法务专员	XX公司	XXXX
郑大刚	男	32	IT支持	XX公司	XXXX
孙丽娜	女	25	培训专员	XX公司	XXXX
马志远	男	40	质量经理	XX公司	XXXX
徐小梅	女	22	采购专员	XX公司	XXXX
黄大强	男	55	仓储主管	XX公司	XXXX
宋小红	女	35	物流专员	XX公司	XXXX
周国强	男	48	销售助理	XX公司	XXXX
吴小芳	女	28	市场专员	XX公司	XXXX
郑大刚	男	32	产品经理	XX公司	XXXX
孙丽娜	女	25	市场专员	XX公司	XXXX
马志远	男	40	销售经理	XX公司	XXXX
徐小梅	女	22	客服专员	XX公司	XXXX
黄大强	男	55	财务总监	XX公司	XXXX
宋小红	女	35	人力资源	XX公司	XXXX
周国强	男	48	行政主管	XX公司	XXXX
吴小芳	女	28	法务专员	XX公司	XXXX
郑大刚	男	32	IT支持	XX公司	XXXX
孙丽娜	女	25	培训专员	XX公司	XXXX
马志远	男	40	质量经理	XX公司	XXXX
徐小梅	女	22	采购专员	XX公司	XXXX
黄大强	男	55	仓储主管	XX公司	XXXX
宋小红	女	35	物流专员	XX公司	XXXX
周国强	男	48	销售助理	XX公司	XXXX
吴小芳	女	28	市场专员	XX公司	XXXX
郑大刚	男	32	产品经理	XX公司	XXXX
孙丽娜	女	25	市场专员	XX公司	XXXX
马志远	男	40	销售经理	XX公司	XXXX
徐小梅	女	22	客服专员	XX公司	XXXX
黄大强	男	55	财务总监	XX公司	XXXX
宋小红	女	35	人力资源	XX公司	XXXX
周国强	男	48	行政主管	XX公司	XXXX
吴小芳	女	28	法务专员	XX公司	XXXX
郑大刚	男	32	IT支持	XX公司	XXXX
孙丽娜	女	25	培训专员	XX公司	XXXX
马志远	男	40	质量经理	XX公司	XXXX
徐小梅	女	22	采购专员	XX公司	XXXX
黄大强	男	55	仓储主管	XX公司	XXXX
宋小红	女	35	物流专员	XX公司	XXXX
周国强	男	48	销售助理	XX公司	XXXX
吴小芳	女	28	市场专员	XX公司	XXXX
郑大刚	男	32	产品经理	XX公司	XXXX
孙丽娜	女	25	市场专员	XX公司	XXXX
马志远	男	40	销售经理	XX公司	XXXX
徐小梅	女	22	客服专员	XX公司	XXXX
黄大强	男	55	财务总监	XX公司	XXXX
宋小红	女	35	人力资源	XX公司	XXXX
周国强	男	48	行政主管	XX公司	XXXX
吴小芳	女	28	法务专员	XX公司	XXXX
郑大刚	男	32	IT支持	XX公司	XXXX
孙丽娜	女	25	培训专员	XX公司	XXXX
马志远	男	40	质量经理	XX公司	XXXX
徐小梅	女	22	采购专员	XX公司	XXXX
黄大强	男	55	仓储主管	XX公司	XXXX
宋小红	女	35	物流专员	XX公司	XXXX
周国强	男	48	销售助理	XX公司	XXXX
吴小芳	女	28	市场专员	XX公司	XXXX
郑大刚	男	32	产品经理	XX公司	XXXX
孙丽娜	女	25	市场专员	XX公司	XXXX
马志远	男	40	销售经理	XX公司	XXXX
徐小梅	女	22	客服专员	XX公司	XXXX
黄大强	男	55	财务总监	XX公司	XXXX
宋小红	女	35	人力资源	XX公司	XXXX
周国强	男	48	行政主管	XX公司	XXXX
吴小芳	女	28	法务专员	XX公司	XXXX
郑大刚	男	32	IT支持	XX公司	XXXX
孙丽娜	女	25	培训专员	XX公司	XXXX
马志远	男	40	质量经理	XX公司	XXXX
徐小梅	女	22	采购专员	XX公司	XXXX
黄大强	男	55	仓储主管	XX公司	XXXX
宋小红	女	35	物流专员	XX公司	XXXX
周国强	男	48	销售助理	XX公司	XXXX
吴小芳	女	28	市场专员	XX公司	XXXX
郑大刚	男	32	产品经理	XX公司	XXXX
孙丽娜	女	25	市场专员	XX公司	XXXX
马志远	男	40	销售经理	XX公司	XXXX
徐小梅	女	22	客服专员	XX公司	XXXX
黄大强	男	55	财务总监	XX公司	XXXX
宋小红	女	35	人力资源	XX公司	XXXX
周国强	男	48	行政主管	XX公司	XXXX
吴小芳	女	28	法务专员	XX公司	XXXX
郑大刚	男	32	IT支持	XX公司	XXXX
孙丽娜	女	25	培训专员	XX公司	XXXX
马志远	男	40	质量经理	XX公司	XXXX
徐小梅	女	22	采购专员	XX公司	XXXX
黄大强	男	55	仓储主管	XX公司	XXXX
宋小红	女	35	物流专员	XX公司	XXXX
周国强	男	48	销售助理	XX公司	XXXX
吴小芳	女	28	市场专员	XX公司	XXXX
郑大刚	男	32	产品经理	XX公司	XXXX
孙丽娜	女	25	市场专员	XX公司	XXXX
马志远	男	40	销售经理	XX公司	XXXX
徐小梅	女	22	客服专员	XX公司	XXXX
黄大强	男	55	财务总监	XX公司	XXXX
宋小红	女	35	人力资源	XX公司	XXXX
周国强	男	48	行政主管	XX公司	XXXX
吴小芳	女	28	法务专员	XX公司	XXXX
郑大刚	男	32	IT支持	XX公司	XXXX
孙丽娜	女	25	培训专员	XX公司	XXXX
马志远	男	40	质量经理	XX公司	XXXX
徐小梅	女	22	采购专员	XX公司	XXXX
黄大强	男	55	仓储主管	XX公司	XXXX
宋小红	女	35	物流专员	XX公司	XXXX
周国强	男	48	销售助理	XX公司	XXXX
吴小芳	女	28	市场专员	XX公司	XXXX
郑大刚	男	32	产品经理	XX公司	XXXX
孙丽娜	女	25	市场专员	XX公司	XXXX
马志远	男	40	销售经理	XX公司	XXXX
徐小梅	女	22	客服专员	XX公司	XXXX
黄大强	男	55	财务总监	XX公司	XXXX
宋小红	女	35	人力资源	XX公司	XXXX
周国强	男	48	行政主管	XX公司	XXXX
吴小芳	女	28	法务专员	XX公司	XXXX
郑大刚	男	32	IT支持	XX公司	XXXX
孙丽娜	女	25	培训专员	XX公司	XXXX
马志远	男	40	质量经理	XX公司	XXXX
徐小梅	女	22	采购专员	XX公司	XXXX
黄大强	男	55	仓储主管	XX公司	XXXX
宋小红	女	35	物流专员	XX公司	XXXX
周国强	男	48	销售助理	XX公司	XXXX
吴小芳	女	28	市场专员	XX公司	XXXX
郑大刚	男	32	产品经理	XX公司	XXXX
孙丽娜	女	25	市场专员	XX公司	XXXX
马志远	男	40	销售经理	XX公司	XXXX
徐小梅	女	22	客服专员	XX公司	XXXX
黄大强	男	55	财务总监	XX公司	XXXX
宋小红	女	35	人力资源	XX公司	XXXX
周国强	男	48	行政主管	XX公司	XXXX
吴小芳	女	28	法务专员	XX公司	XXXX
郑大刚	男	32	IT支持	XX公司	XXXX
孙丽娜	女	25	培训专员	XX公司	XXXX
马志远	男	40	质量经理	XX公司	XXXX
徐小梅	女	22	采购专员	XX公司	XXXX
黄大强	男	55	仓储主管	XX公司	XXXX
宋小红	女	35	物流专员	XX公司	XXXX
周国强	男	48	销售助理	XX公司	XXXX
吴小芳	女	28	市场专员	XX公司	XXXX
郑大刚	男	32	产品经理	XX公司	XXXX
孙丽娜	女	25	市场专员	XX公司	XXXX
马志远	男	40	销售经理	XX公司	XXXX
徐小梅	女	22	客服专员	XX公司	XXXX
黄大强	男	55	财务总监	XX公司	XXXX
宋小红	女	35	人力资源	XX公司	XXXX
周国强	男	48	行政主管	XX公司	XXXX
吴小芳	女	28	法务专员	XX公司	XXXX
郑大刚	男	32	IT支持	XX公司	XXXX
孙丽娜	女	25	培训专员	XX公司	XXXX
马志远	男	40	质量经理	XX公司	XXXX
徐小梅	女	22	采购专员	XX公司	XXXX
黄大强	男	55	仓储主管	XX公司	XXXX
宋小红	女	35	物流专员	XX公司	XXXX
周国强	男	48	销售助理	XX公司	XXXX
吴小芳	女	28	市场专员	XX公司	XXXX
郑大刚	男	32	产品经理	XX公司	XXXX
孙丽娜	女	25	市场专员	XX公司	XXXX
马志远	男	40	销售经理	XX公司	XXXX
徐小梅	女	22	客服专员	XX公司	XXXX
黄大强	男	55	财务总监	XX公司	XXXX
宋小红	女	35	人力资源	XX公司	XXXX
周国强	男	48	行政主管	XX公司	XXXX
吴小芳	女	28	法务专员	XX公司	XXXX
郑大刚	男	32	IT支持	XX公司	XXXX
孙丽娜	女	25	培训专员	XX公司	XXXX
马志远	男	40	质量经理	XX公司	XXXX
徐小梅	女	22	采购专员	XX公司	XXXX
黄大强	男	55	仓储主管	XX公司	XXXX
宋小红	女	35	物流专员	XX公司	XXXX
周国强	男	48	销售助理	XX公司	XXXX
吴小芳	女	28	市场专员	XX公司	XXXX
郑大刚	男	32	产品经理	XX公司	XXXX
孙丽娜	女	25	市场专员	XX公司	XXXX
马志远	男	40	销售经理	XX公司	XXXX
徐小梅	女	22	客服专员	XX公司	XXXX
黄大强	男	55	财务总监	XX公司	XXXX
宋小红	女	35	人力资源	XX公司	XXXX
周国强	男	48	行政主管	XX公司	XXXX
吴小芳	女	28	法务专员	XX公司	XXXX
郑大刚	男	32	IT支持	XX公司	XXXX
孙丽娜	女	25	培训专员	XX公司	XXXX
马志远	男	40	质量经理	XX公司	XXXX
徐小梅	女	22	采购专员	XX公司	XXXX
黄大强	男	55	仓储主管	XX公司	XXXX
宋小红	女	35	物流专员	XX公司	XXXX
周国强	男	48	销售助理	XX公司	XXXX
吴小芳	女	28	市场专员	XX公司	XXXX
郑大刚	男	32	产品经理	XX公司	XXXX
孙丽娜	女	25	市场专员	XX公司	XXXX
马志远	男	40	销售经理	XX公司	XXXX
徐小梅	女	22	客服专员	XX公司	XXXX
黄大强	男	55	财务总监	XX公司	XXXX
宋小红	女	35	人力资源	XX公司	XXXX
周国强	男	48	行政主管	XX公司	XXXX
吴小芳	女	28	法务专员	XX公司	XXXX
郑大刚	男	32	IT支持	XX公司	XXXX
孙丽娜	女	25	培训专员	XX公司	XXXX
马志远	男	40	质量经理	XX公司	XXXX
徐小梅	女	22	采购专员	XX公司	XXXX
黄大强	男	55	仓储主管	XX公司	XXXX
宋小红	女	35	物流专员	XX公司	XXXX
周国强	男	48	销售助理	XX公司	XXXX
吴小芳	女	28	市场专员	XX公司	XXXX
郑大刚	男	32	产品经理	XX公司	XXXX
孙丽娜	女	25	市场专员	XX公司	XXXX
马志远	男	40	销售经理	XX公司	XXXX
徐小梅	女	22	客服专员	XX公司	XXXX
黄大强	男	55	财务总监	XX公司	XXXX
宋小红	女	35	人力资源	XX公司	XXXX
周国强	男	48	行政主管	XX公司	XXXX
吴小芳	女	28	法务专员	XX公司	XXXX
郑大刚	男	32	IT支持	XX公司	XXXX
孙丽娜	女	25	培训专员	XX公司	XXXX
马志远	男	40	质量经理	XX公司	XXXX
徐小梅	女	22	采购专员	XX公司	XXXX
黄大强	男	55	仓储主管	XX公司	XXXX
宋小红	女	35	物流专员	XX公司	XXXX
周国强	男	48	销售助理	XX公司	XXXX

[illegible]

A. DETAIL B
TALLER 10



2020-2021

1. What are the main components of a cell?
A cell is the basic unit of life. It is a small structure that can perform all the functions of life. The main components of a cell are the cell membrane, cytoplasm, nucleus, and organelles.

2. What is the function of the nucleus?
The nucleus is the control center of the cell. It contains the cell's genetic material (DNA) and directs the cell's activities.

3. What are organelles?
Organelles are specialized structures within a cell that perform specific functions. Examples include mitochondria, ribosomes, and the endoplasmic reticulum.

4. What is the function of mitochondria?
Mitochondria are the powerhouses of the cell. They convert the energy from food into a form that the cell can use (ATP).

5. What is the function of the endoplasmic reticulum?
The endoplasmic reticulum is a network of membranes that is involved in the production and transport of proteins and lipids.

6. What is the function of ribosomes?
Ribosomes are small structures that are responsible for protein synthesis.

7. What is the function of the cell membrane?
The cell membrane is the outer boundary of the cell. It controls what enters and leaves the cell.

8. What is the function of the cytoplasm?
The cytoplasm is the fluid-filled space within the cell. It contains the organelles and provides a medium for their activities.

9. What is the function of the Golgi apparatus?
The Golgi apparatus is a series of stacked membranes that are involved in the transport and processing of proteins and lipids.

10. What is the function of the lysosomes?
Lysosomes are small structures that contain enzymes that break down waste materials and cellular debris.

Bill - one year on-going meeting

Figure 1. - Interconnect design.

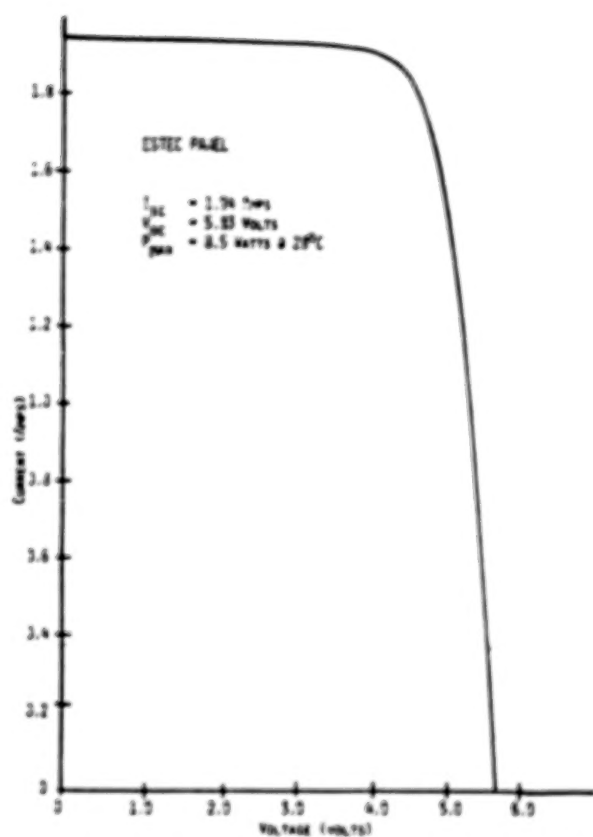


Figure 2. - Current-voltage characteristic of ESTEC panel.

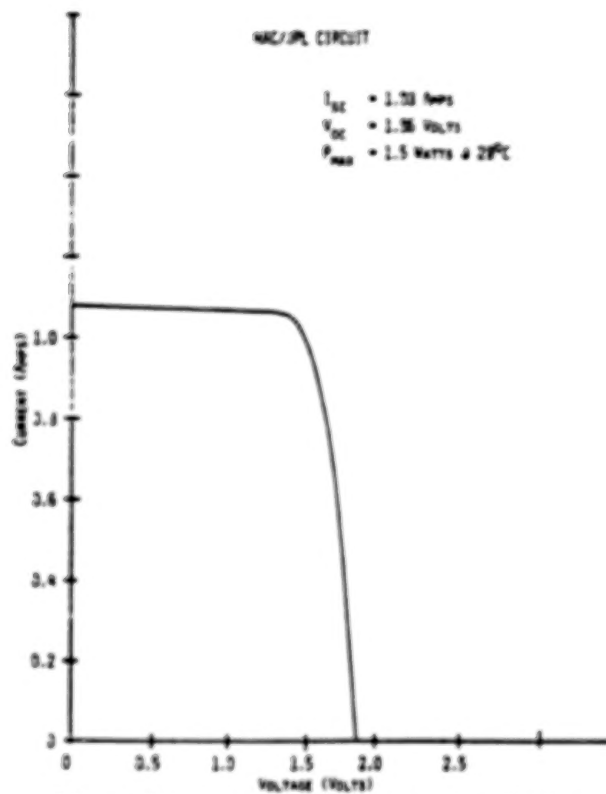


Figure 3. - Current-voltage characteristic of HAC/JPL panel.

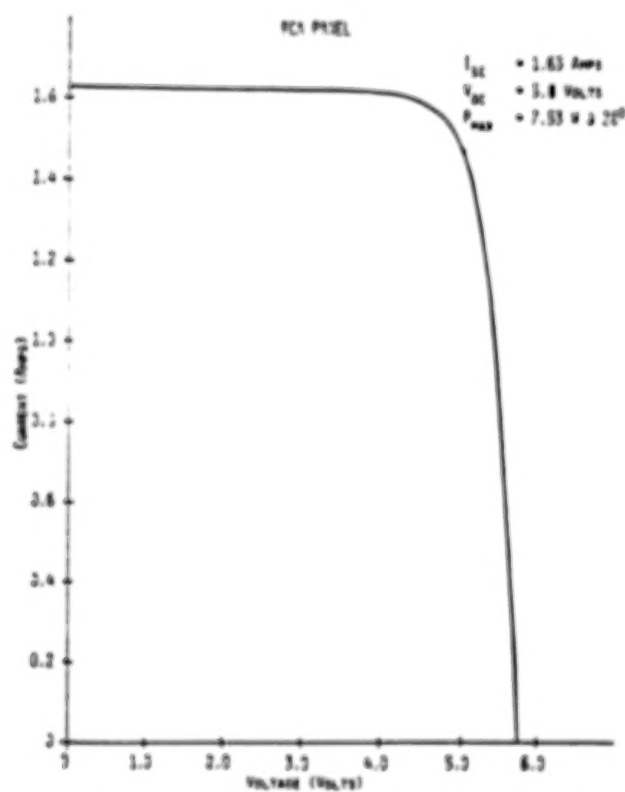


Figure 4. - Current-voltage characteristic of RCA panel.

N84
29342

UNCLAS

ELECTROCHEMICAL STORAGE

Lawrence H. Thaller
National Aeronautics and Space Administration
Lewis Research Center
Cleveland, Ohio

The storage function of an overall power system is usually performed by a battery. In the strictest sense, a battery is an assembly of individual single cells. They are grouped in series/parallel arrangements to provide the required voltage, power, and storage capacity of the mission at hand. Batteries are somewhat notorious for being cantankerous in nature and have been the source of much worry and consternation. Since storage cannot presently be eliminated as an integral part of a complete power system, a number of imaginative solutions, accommodations, and compromises have been suggested, tested, and used over the years in flight spacecraft. In any group associated with the design of spacecraft there is a subgroup responsible for the battery. Sometimes these individuals are electrical engineers by training, sometimes they are chemists, mechanical engineers, etc. Interestingly the solutions that are put forth in response to the cantankerous nature of the battery depend very heavily on the background of the individual trying to solve the problem. The emphasis of this presentation will be on electrochemical solutions to the problem.

The nonelectrochemist might be described as one who does not know what goes on inside the wall of the cell. The electrochemist does indeed know what goes on inside a cell, but for the most part does not know why. Both groups therefore have their work cut out for them. The material to be presented here will first describe the source of the problem, which is in part related to the stochastic properties of cell populations and in part related to the actual electrochemistry and chemistry taking place within the single cell. The complications that can arise in multicell batteries will then be described to set the stage to show how different electrochemistries might alleviate or accentuate these problems. The concept of the electrochemical system will be introduced to show how certain shortcomings of the single cell/battery string concept can be circumvented. In fact some of these electrochemical systems will permit performance characteristics that would simply be impossible using conventional battery design philosophies. The final topic to be addressed will be some projections in terms of energy density and performance characteristics of the concepts you have been hearing about over the years but have yet to see come into practice.

N84
29343

UNCLAS

SOLAR ARRAY - PLASMA INTERACTIONS

Carolyn K. Purvis
National Aeronautics and Space Administration
Lewis Research Center
Cleveland, Ohio

Interactions between space systems and their orbital particle and field environments can have significant impact on the systems' operation and life. Interactions such as radiation damage and aerodynamic drag, for example, must be considered in designing any space system. There are, however, a number of orbital environmental interactions which become important design considerations only for large or high-power systems. Their impact must be assessed to ensure successful design. In particular, interactions between higher voltage solar arrays and the space plasma are of critical concern in designing large orbital photovoltaic power systems.

Most U.S. spacecraft have used low-voltage solar arrays, generating power at about 30 V. The highest voltage array flown by NASA to date was on Skylab, which had a solar array with a normal operating voltage of 70 V that generated 16 kW of power. Large future systems will require increasing power-generating capability. As power levels increase, the penalties for maintaining low solar array voltages become prohibitive and make higher voltage array designs mandatory. It is thus necessary to thoroughly understand high-voltage solar array operation in the space plasma environment.

Solar array systems consist of strings of solar cells with metallic interconnects between them. These interconnects are at voltages depending on their positions in the array circuit and are usually exposed to the space environment. When such systems are placed in orbit, they will interact with the naturally occurring space plasma. Two types of potentially hazardous interactions to a higher voltage solar array in orbit are presently recognized: power loss from parasitic currents through the plasma; and arcing. Both of these interactions are plasma density dependent and present greater hazards at higher densities. The low-temperature ionospheric plasma has a peak density (of 10^6 particles/cm³) at about 300-km altitude. High-voltage system - plasma interactions will therefore be most severe in low Earth orbits.

Interactions between higher voltage solar arrays and orbital plasma environments are being studied as part of the joint NASA/AF Spacecraft-Environment Interactions Investigation. This ground technology program comprises ground testing, modeling of the environment and the phenomena, development and validation of system level models, and materials characterization and development. Outputs include design guidelines and test specifications. Spaceflight data are required to ensure that the phenomena observed in ground testing also occur in orbit, to examine conditions not obtainable in ground facilities, and to validate the models. Two small-scale experiments have been flown, and a series of more comprehensive shuttle-based experiments is proposed, focused specifically on solar array - plasma interactions and their impact on array performance in low Earth orbit.

N84
29344

UNCLAS

N84 29344

SPACE STATION

A. F. Forestieri
Space Station Task Force
NASA Headquarters
Washington, D.C.

The United States Space Station - Is it just over the horizon of the "Final Frontier?" In addition to the major question of "Is there a Space Station in NASA's future" there are many other questions frequently asked. For example: Why is a Space Station needed? What will it cost? What can it do? and When will it be ready? The Space Station Task Force was established by NASA Administrator James Beggs in May of 1982 in order to answer these questions and to provide focus and direction for Space Station planning activities. In addition, the Task Force is to provide Congress and the Administration with sufficient information to allow them to make an informed decision on whether the United States should proceed with a Space Station as the next major national initiative in space.

This paper will discuss the questions listed above and will present current thinking on selected issues, planning guidelines, unique considerations and organization.

INTRODUCTION

The next logical step in space for America is to develop a Space Station that would provide a permanent presence in orbit around the Earth. With such a facility, space would become a medium for manned operations - enhancing our security, advancing our technology, and adding to our scientific knowledge.

NASA believes that such a Space Station could be built and placed in orbit by 1990. Such a facility, together with the Space Shuttle, would dramatically improve our capabilities to operate in space for both civil and military purposes. With the Space Shuttle, America has an unrivaled tool for the practical use of space. Conceived originally with a Space Station in mind, Columbia and her sister ships could routinely deliver payload after payload to the Station. New crews, needed supplies, and new instruments could all be shuttled to and from the Station as required. No longer limited by stay time in orbit, or by one-time payload limitations, the astronauts could operate in space efficiently and extensively.

In all probability, were such a program to be approved, NASA would start out with a small, modest facility permanently orbiting the Earth. In time, units would be added on increasing the utility and versatility of the Space Station. Such an approach holds down costs while allowing the initial step to be useful in its own right. A commitment to a permanently orbiting Space Station needs to be made soon if we are to have a facility in orbit by the end of this decade. And such a Space Station must be built if we are to maintain the position of leadership in space so convincingly demonstrated - in the past by Apollo - and now, most recently, by the flights of Columbia. This position no longer goes unchallenged. Space has become competitive. The Europeans have developed a workable, efficient launch vehicle called Ariane and are building satellites that match ours in complexity and sophistication. The Soviets have demonstrated their intent to continue an aggressive space program. The Japanese too are demonstrating a rapidly growing interest in space with programs in both launch vehicles and satellites. The Space Shuttle still gives us the edge. No one has anything quite like it. But alone, the Shuttle will not enable the United States to realize the full potential of space. Only a Space Station, permanently orbiting the Earth, can do that. It is, as Jim Beggs the NASA Administrator says, the next logical step.

SPACE STATION PLANNING

The United States strategy for manned space flight (Figure 1) began in the early 1960's with the pioneer missions Mercury and Gemini. Exploration of space continued with Apollo, and the demonstration of space operations feasibility was shown with Skylab. Routine access of space began with the advent of the Shuttle in the 1980's. Permanent utilization of space, or a Space Station, will begin in the 1990's and go on beyond the year 2000. The Space Station Task Force was established by NASA Administrator James Beggs in May of 1982 to provide focus and direction for Space Station planning activities (Figure 2). The Task Force will also define possible Space Station initiatives, including mission requirements, architectural options and trade studies, and also develop management and acquisition plans. In order to make these activities an Agency-wide effort, the Task Force is staffed by senior level individuals from NASA Field Centers and Headquarters. Figure 3 shows the current NASA organizational elements of the Space Station Task Force in more detail. The Task Force reports to the Associate Deputy Administrator. The Task Force, the Office of Space Tracking and Data Systems, the Office of Space Science and Application, the Office of Aeronautics and Space Technology, and the Office of Space Flight are all members of the Space Station Steering Committee chaired by the Associate Deputy Administrator. Prior to the creation of the Task Force, NASA formed a Space Station Technology Steering Committee to access technologies relevant to a Space Station in the 1990 time frame. This Space Station Technology Steering Committee supports the Office of Aeronautics and Space Technology and is an advisor to the Space Station Task Force. An Advanced Programs Office likewise supports the Office of Space Flight.

Figure 4 lists statements from the White House and the President on July 4, 1982. The major points are 1) to continue to explore the requirements, operational concepts, and technology associated with permanent space facilities and 2) establish a more permanent presence in space. Three key points in the NASA Space Station definition are to be noted. As listed in Figure 5, they are 1) NASA has under way a modest planning effort to define a possible Space Station, 2) adequate Space Station definition is essential if Congress and the Administration are to be able to make an informed decision on whether the United States should proceed with a Station as the next major national initiative in space, and 3) the planning should be consistent with and support the President's National Space Policy. Figure 6 indicates the Space Station planning approach to the definition task. The Task Force now has NASA Centers onboard. The Technology Steering Committee is at work and preliminary systems definition concept development has begun. Later the concept will be defined, mission requirements will be well understood, and the management plan will be in place. This will all take place so that systems are well understood, technology is reliable, and cost and schedule estimates are real. This will lead to an informed decision on the nature of the development program.

Figure 7 lists several reasons why there should be a Space Station. Primary reasons are to stimulate the development of advanced technologies, develop fully the commercial potential of space, and provide a versatile efficient system for space science and applications. Because of the potential size of the Space Station program, there are a number of issues proposed in Figure 8 as potential lower cost alternatives to the Space Station. None of the issues have as yet proved to be effective. A number of unique technical and programmatic considerations are listed in Figure 9. For example, on the technical side there is regular on-orbit maintenance and repair, development, test, and upgrading of new systems components in operational situations, extensive EVA, and common hardware and spares development. The programmatic side includes extensive and continued user involvement, proper mix of man and machine, and maximum NASA in-house participation. On this last point, Agency-wide participation, the breadth of the program includes substantive involvement by all NASA installations. The program is more than an extension of previous manned spaceflight programs. Its success is critically dependent upon involvement of the science and applications communities as well as technologies generated by the research centers. Thus, all NASA installations have been involved through representation on the Space Station Task Force and Task Force working groups. While the program does appear to have potential for substantive involvement across the Agency, this prospect poses an unprecedented management challenge.

The Space Station is a multi-purpose facility. Several functions of the Space Station are listed in Figure 10. Thus far, 25 to 35 major functions are being considered.

As a laboratory the Space Station would:

- provide for extended observations of the land and oceans for civil-economic, scientific, or national security purposes where man's presence for data integration, instrument selection and adjustment or overall system maintenance is important.
- significantly reduce the cost and time required by private interests to carry out the precursor research necessary to reach sound business decisions to invest in commercial space processing.
- support national security missions where man's presence contributes to mission effectiveness or where research will lead to the definition of new missions.

As an operations base the Space Station would:

- provide for fueling and launch of orbitally based propulsive stages, significantly increasing our capability to place satellites in geosynchronous orbit as well as to maneuver in low earth orbit.
- serve as a construction base for assembly and/or erection of large systems such as antennas, energy collectors, imaging systems, or other civil or military structures too large for launch directly from earth.
- provide a base for maintenance and servicing of free-flying unmanned satellites.

The initial architecture concept for the Space Station system is schematically shown in Figure 11. The manned base is made up of several modules. The Habitat module primarily provides for those crew functions that can be classified as off duty in nature, private crew quarters, gallery, war room, health maintenance or exercise facility, etc. The Docking Hub or Multiple Berthing Adapter is fundamentally a coupling device which provides the means for Space Station modules to be interconnected. The Utility Module provides the Space Station electrical power, communication, data processing, attitude control, and orbit reboost.

This module also has a thermal control/radiator system to reject heat from the utility module equipment and possible equipment in other Station modules. Growth elements include Experiments Modules, Logistics Module, and Orbital Transfer Vehicle support. A number of unmanned platforms are also associated with the Space Station architecture.

The top level management and engineering related planning guidelines are shown in Figure 12. In particular, as stated earlier, NASA-wide participation is one of the management-related functions. Others include initial operating capability in 1991 and cost of the initial capability between 7½ and 9 billion dollars. Engineering-related guidelines include continuously habitable, Shuttle dependent, and evolutionary.

Advanced technologies are needed if the Space Station goals are to be met. As a result, a Space Station Advanced Development Program has been planned. This program will provide needed advanced technology to support an evolutionary Space Station and provide the test bed capabilities needed in key technology areas such as power, life support, and data management. Other objectives and the approach to the advanced development activities are shown in Figure 13. The major technology issues are listed in Figure 14. The ultimate aim is to achieve low life cycle cost with technology optimized designs. Again, evolution is a prime factor, as are autonomy and technology transparency. Some of the technology challenges are listed in Figure 15. This audience is primarily interested in high capacity electrical power generation, especially concentrated gallium arsenide arrays, regenerative fuel cells and nuclear systems. Because of the large solar arrays required for the Space Station, less distributed power systems, such as nuclear, are being closely analyzed.

Figure 16 shows how several different discipline subsystems are closely integrated. For example, in a photovoltaic array, a number of subsystems such as thermal, attitude control, structures, and on-board propulsion are closely dependent on the power subsystem. Finally, a first cut at the capabilities of a Space Station is shown in Figure 17. The initial power system is 60 kilowatts to the customer with an additional 15 kilowatts for housekeeping functions. The total 75 kilowatts on the bus would require in excess of a 200 kilowatt array.

In summary, the Space Station program holds potential for focusing the National civilian space program and preserving U.S. preeminence. It also poses a unique management challenge to the Agency. The potential for Agency-wide and international involvement is high.

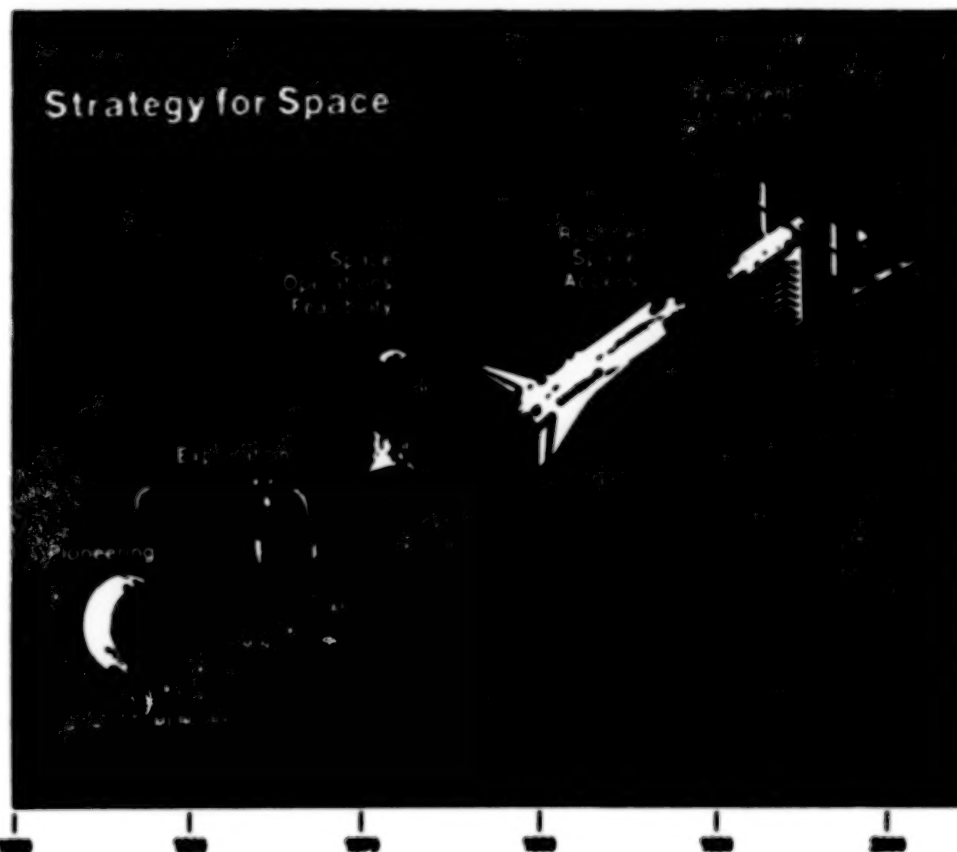


Figure 1. - U.S. strategy for manned spaceflight.

- Established in May, 1982 by the NASA Administrator
- NASA-wide activity: Centers and Headquarters
- Reports to NASA Associate Deputy Administrator

-
- Provide focus and direction for the agency's space station planning activities
 - Define possible space station initiative
 - mission requirements
 - architectural options
 - trade studies
 - "advanced development"
 - concept development ("systems engineering")
 - Develop management/acquisition plans

Figure 2. - NASA Space Station task force.

ORIGINAL PAGE IS
OF POOR QUALITY



Figure 3. - Current NASA elements of Space Station task force.

"UNITED STATES GOVERNMENT PROGRAMS SHALL CONTINUE A BALANCED STRATEGY OF RESEARCH, DEVELOPMENT OPERATIONS, AND EXPLORATION FOR SCIENCE, APPLICATIONS AND TECHNOLOGY. THE KEY OBJECTIVES OF THESE PROGRAMS ARE TO(3) CONTINUE TO EXPLORE THE REQUIREMENTS, OPERATIONAL CONCEPTS, AND TECHNOLOGY ASSOCIATED WITH PERMANENT SPACE FACILITIES."

**WHITE HOUSE FACT SHEET
NATIONAL SPACE POLICY
JULY 4, 1982**

"BEGINNING WITH THE NEXT FLIGHT, THE COLUMBIA AND HER SISTER SHIPS WILL BE FULLY OPERATIONAL AND READY TO PROVIDE ECONOMICAL AND ROUTINE ACCESS TO SPACE FOR SCIENTIFIC EXPLORATION, COMMERCIAL VENTURES AND FOR TASKS RELATED TO THE NATIONAL SECURITY. SIMULTANEOUSLY, WE MUST LOOK AGGRESSIVELY TO THE FUTURE BY DEMONSTRATING THE POTENTIAL OF THE SHUTTLE AND ESTABLISHING A MORE PERMANENT PRESENCE IN SPACE."

**PRESIDENT RONALD REAGAN
DRYDEN FLIGHT RESEARCH FACILITY
JULY 4, 1982**

Figure 4. - Statements on permanent space facility.

ORIGINAL PAGE 17
OF POOR QUALITY

- NASA has underway a modest planning effort to define a possible space station.
- Adequate space station definition is essential if Congress and the Administration are to be able to make an informed decision on whether the United States should proceed with a station as the next major national initiative in space.
- Our planning is consistent with and supports the President's National Space Policy in which a key objective is "to continue to explore the requirements, operational concepts, and technology associated with permanent space facilities."

Figure 5. - NASA definition of Space Station: three key points.

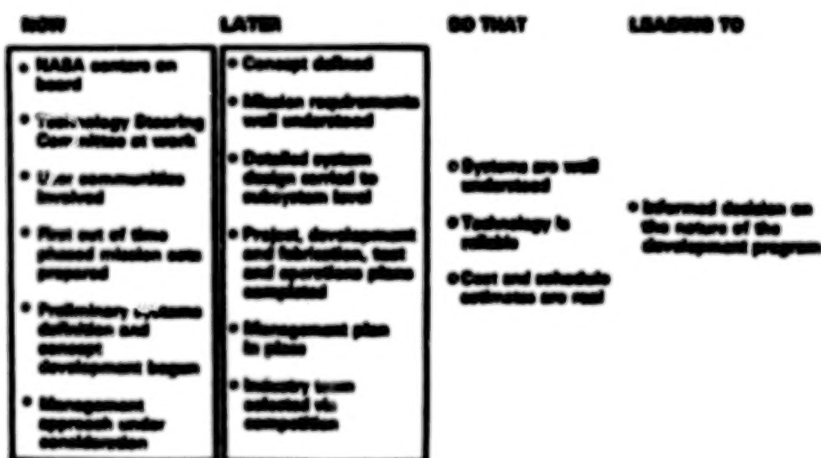


Figure 6. - Space Station planning: approach to definition.

ORIGINAL PAGE IS
OF POOR QUALITY

- ENSURE CIVIL LEADERSHIP IN SPACE DURING THE 1970's. SUCH LEADERSHIP IS DEFINED AS PREEMINENCE IN SPACE SCIENCE AND APPLICATIONS, IN SPACE TECHNOLOGY, AND IN MANNED SPACE FLIGHT
- STIMULATE DEVELOPMENT OF ADVANCED TECHNOLOGIES
- DEVELOP FULLY THE COMMERCIAL POTENTIAL OF SPACE
- PROVIDE A VERSATILE, EFFICIENT SYSTEM FOR SPACE SCIENCE AND APPLICATIONS
- COUPLE MATURING INTERNATIONAL SPACE PROGRAMS TO U.S. SPACE SYSTEMS, AND PROVIDE A VEHICLE FOR INTERNATIONAL COOPERATION IN SPACE
- FUNCTION MORE EFFICIENTLY IN SPACE, BUILDING UPON PREVIOUS NATIONAL INVESTMENTS
- INCREASE PRESTIGE ABROAD AND PRIDE AT HOME
- ENHANCE NATIONAL SECURITY
- STIMULATE INTEREST IN SCIENTIFIC AND TECHNICAL EDUCATION
- PROVIDE CONTINUITY AND FOCUS TO THE NATION'S CIVILIAN SPACE PROGRAM

Figure 7. - Reasons for Space Station.

ISSUE	COMMENT
• Extended orbiter.....	Costly to refurbish and operate orbiter. Inefficient, less capable
• Unmanned station.....	Won't assure leadership, less capable
• Unreliable cost and schedule estimates.....	Extensive, up-front definition will provide reliable estimates
• Crowd out science funds.....	Space science prospered with Apollo. Shuttle funds would not have been appropriated for science. Science, like station, must win OMB and Congressional approval on own merits
• Not needed for space science.....	Not essential for current space science program, but would be an effective system for the future, enabling some science now not possible
• Not needed for defense.....	Station would serve civil requirements. Likely that DOD would conduct R and D aboard a NASA station
• Soviet Salyut station employs second-rate technology and represents no threat.....	Soviet space program is growing quantitatively and qualitatively. Salyut and its successors are threat to U.S. leadership in space

Figure 8. - Lower cost alternatives to Space Station.

UNIVERSITY OF
OF POOR QUALITY

TECHNICAL

- On-orbit assembly
- Regular on-orbit maintenance and repair
- Evolutionary elements, modules and components
- Development, test and upgrading of new systems/ components in operational situation
- Distributed ECL/COMB systems
- Extensive EVA
- Common hardware/spare development
- Few weight and shape constraints
- Operational autonomy

PROGRAMMATIC

- Continuous, evolutionary program
- Extensive and continuous user involvement
- Proper mix of man and machine
- Maximum NASA in-house participation
- New procurement strategies/techniques due to time-related complexity of program
- Discrete elements/systems enables management to be shared
- Continuous use of NASA's capabilities
- Lower cost per utilization hour from longer life on orbit
- Lower cost due to common hardware and spares
- Cost of initial capability less than Shuttle and Apollo

Figure 9. - Space Station unique considerations.

- **On-orbit laboratory**
 - Science and applications
 - Technology and advanced development
- **Permanent observatory(s)**
- **Transportation node**
- **Servicing facility**
 - Free flyers
 - Platforms
- **Communications and data processing node**
- **Manufacturing facility**
- **Assembly facility**
- **Storage depot**

A space station is a multi-purpose facility

Figure 10. - Functions of Space Station.

ORIGINAL PAGE IS
OF POOR QUALITY

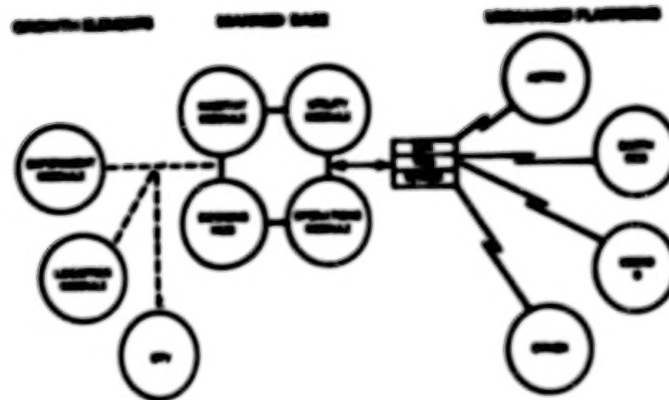


Figure 11. - A Space Station architecture: cluster concepts.

MANAGEMENT RELATED

- Three year extensive definition (5-10% of program cost)
- NASA-wide participation
- Development funding in FY 1987
- IOC in 1991
- Cost of initial capability: 7.5-8B
- Extensive user community involvement
 - Science and applications
 - Industry
 - DoD
 - Commercial
- Possible international participation

ENGINEERING RELATED

- Continuously habitable
- Shuttle dependent
- Manned and unmanned elements
- Evolutionary
- Maintainable/restorable
- Operationally autonomous
- User friendly
- Technology transparent

Figure 12. - Space Station planning guidelines.

ORIGINAL PAGE IS
OF POOR QUALITY

OBJECTIVES

- develop "test bed" capabilities along major subsystem disciplines to evaluate technology and estimate risk
- provide the "transfer function" for new technology into the space station development program
- provide technology options to program manager
- establish a qualified subcontractor cadre for system implementation

APPROACH

- manage advanced development program at NASA centers
 - implement "test bed" capabilities
 - select technologies for breadboard/prototype fabrication and demonstration
 - coordinate advanced development activities with technology
 - establish test efforts and procedures
- coordinate closely with OAST technology program
 - provide developer focus to early technology activities
 - ensure compatibility in program content and schedule

Figure 13. - Space Station planning: advanced development activities.

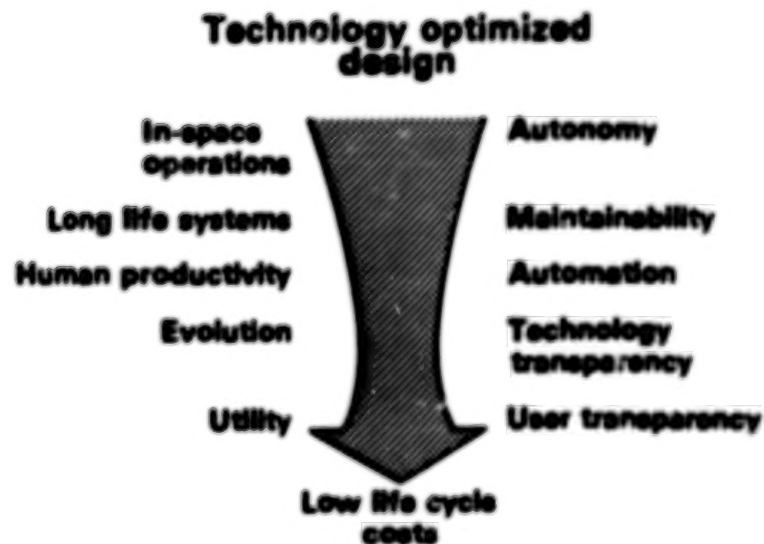


Figure 14. - Space Station planning: major technology issues.

ORIGINAL PAGE IS
OF POOR QUALITY

Advanced end to end information systems	data management systems that are "user friendly" and can grow
High capacity electrical power generation	all power available will be utilized NASA total photovoltaics flown ~100 kw
Cryogenic fluid management	fluid transfer and storage in space required to service Orbit Transfer Vehicles
Thermal management	long life coatings and advanced heat pipe radiators to maximize reliability
Crew systems and life support	closed loop life support systems to minimize resupply requirements
Human capabilities	telepresence and robotics for satellite servicing

Figure 15. - Space Station planning: technology challenges.

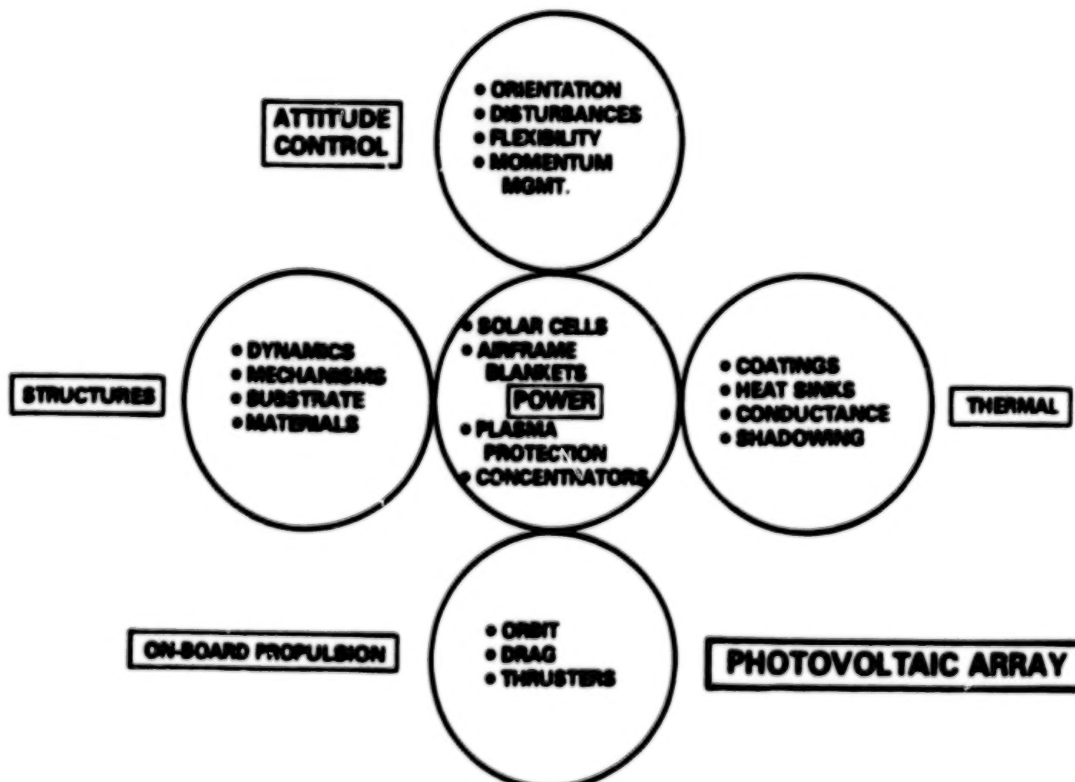


Figure 16. - Integration of disciplines.

ORIGINAL PAGE 18
OF POOR QUALITY

	INITIAL	FUTURE
BASE AT 28.5'		
Crew	6 - 8	12 - 18
Power	80 KW	180KW
Attached payloads	Some	More
R&D pressurized modules	2 - 3 (120M ³)	4 - 6 (300M ³)
Satellite servicing capability	Initial (close by)	Mature
Smart front-end TMS	Available	Available
Data system	300 MBPS	300 MBPS
PLATFORMS		
28.5'/15KW	One	Several
Polar/15KW	One	One
SPACE-BASED OTV	No	Yes
MANNED POLAR STATION	No	?

Figure 17. - Space Station: first cut at capabilities.

N84
29345

UNCLAS

HIGH-EFFICIENCY CONVENTIONAL CELLS WORKSHOP

John C. C. Fan
Massachusetts Institute of Technology
Lexington, Massachusetts

The High-Efficiency Conventional Cells Workshop considered primarily Si and GaAs cells. The majority of participants were interested in the GaAs cells. The discussion was lively.

In Si cells, the beginning-of-life (BOL) efficiency, which is currently between 15 and 16% AMO is not a major problem, and does not require much additional research effort. There are, however, still research efforts needed to improve the end-of-life (EOL) efficiency for Si cells.

In GaAs cells, the research and technology development direction must stress the basic potential advantages of GaAs over Si -- higher conversion efficiency, higher absorption coefficients and thus thinner layers, and more radiation resistant.

With these goals in mind, GaAs BOL efficiency should be brought up to about 20% at AMO. Currently, 19% cells at AMO have been obtained. Using various advanced concepts such as multibandgap windows, or instead of GaAs, $\text{Ga}_{1-x}\text{Al}_x\text{As}$ or $\text{GaAs}_{1-x}\text{P}_x$ cells with $x \approx 0.05$ ($E_g = 1.50$ eV), it is believed that this 20% objective is achievable in the near future.

The efforts in studying the EOL efficiency of GaAs cells should be continued. Results presented in this conference have shown that proton damages in GaAs do not appear to be severe.

The concentrator cell technology is already more advanced than the concentrator optical element and array technology. There are no major technological obstacles that can be foreseen at this time.

There were extensive discussions on the process technology in GaAs cells. Liquid-phase epitaxy (LPE), used by Hughes Research Laboratories, has been adopted by two Japanese companies which each produce about 10,000 2 cm x 2 cm GaAs cells per month. Therefore, mass production of GaAs cells by LPE does not appear to be a problem. Chemical-vapor deposition (CVD), however, is still believed to be more flexible, and should be more adaptable for advanced cell structures. There are no obvious problems that should limit the process yield by either technology.

The workshop participants stressed that for either GaAs cells or advanced Si cells such as 2-mil Si cell to be used in space vehicles, the users must be educated. There appears to be a lack of pioneer spirit in the United States, and it is likely such cells will be first widely used in Japan.

With regard to technology transfer, it is believed that market demands will automatically generate technology transfer, and the workshop participants did not feel it is a problem.

In summary, the major recommendations are:

Si cells

- BOL efficiency is not a major problem
- EOL efficiency needs more research

GaAs Cells

- Bring BOL efficiency up to 20% at AMO
- More proton-damage tests
- Concentrator cell technology is more advanced than concentrator optical element and array technology
- LPE technology is here NOW, and Japan is using it to mass-produce GaAs Cells
- CVD technology is more flexible
- No obvious problems in limiting process yields

General

- Community must be educated to accept GaAs cells and 2-mil Si cells
- Technology transfer would occur when market demands are generated

N84
29346

UNCLAS

RADIATION DAMAGE WORKSHOP

Paul M. Stella
Jet Propulsion Laboratory
California Institute of Technology
Pasadena, California

Although a number of topics were considered at this workshop, the possibility of near term availability of GaAs type cells in quantity, served to provide a focus. In particular, concern was voiced that the lack of sufficient data regarding the radiation behavior of such cells would compromise any ready acceptance. In fact, potential mission use for GaAs was presently felt to be limited to those requiring high temperature survivability, those where array area was critically limited, and possibly missions that would experience electron dominated environments. Clearly the non radiation aspects have been accepted with greater confidence. In order to remedy this situation it will be necessary to have the damage equivalences and behavior under various types of radiations and energies well defined. In support of this, but not as critical to device acceptance, will be the characterization of the damage defect mechanisms in order to fully understand the role of materials and processing on cell behavior and reproducibility.

Although silicon is a much more mature device material, concern was expressed regarding the available radiation data base. Due to the changes that have occurred in silicon cells and evaluation capabilities since the 1960's, it was felt to be important to establish more accurate silicon damage equivalents. Although results are not yet available, it was pointed out that such a program was underway at JPL with NASA and AFWAL funding for silicon and GaAs devices respectively.

Additionally, it was pointed out that it was not always possible to compare results from different researchers, since the test matrices rarely contained any common "reference" cells. The workshop group suggested that this be addressed in future studies by establishing a "standard" silicon cell which could be used as a benchmark. This was then extended to the concept of a large quantity cell purchase possibly by NASA and/or DOD of a common production cell type that could then be made available for various radiation experiments.

Some discussion centered on a question regarding the possibility of further improvements in GaAs and silicon cell radiation behavior. For GaAs the "answers" reflect the lack of knowledge regarding what the baseline behavior is. Suggestions such as N/P vs P/N configurations, shallower junctions, and annealing were mentioned, as in previous meetings, but no new quantitative justifications were offered.

For silicon the situation was understoodly quite different, since it has been in use for over 2 decades. The recent reductions in silicon research funding contributed to the lack of any suggestions for breakthroughs although a number of improvements were suggested. Without any specific indication of payoff these areas included:

- A. Low Carbon, Low Oxygen Silicon Material: Indications of radiation damage defect reduction have been observed although the material is presently unavailable in any reasonable volume.

- B. Lithium Counterdoping: This method has shown the potential for removing damage in irradiated P-type material, although initial efficiencies are not comparable to current state of the art. The possibility of refining the lithium doping method to maintain high initial efficiencies and combining it with radiation tolerant structures such as thin BSF cells or vertical junction cells could provide a substantial improvement in EOL efficiencies. Introduction of the lithium into the cells in unconventional patterns such as grid or checkerboard designs or through use of the VMJ cell base for lithium storage may be of interest.
- C. Improvement of junction quality: Laser annealing of junctions, either those formed from ion implantation or diffusion, may not only improve initial cell performance but might also reduce the radiation degradation rate.
- D. Annealing of silicon was not received with enthusiasm. The barriers to high temperature insitu annealing that presently exist make this primarily a lab diagnostic tool.

Materials other than GaAs and silicon were generally considered too immature for very reasonable radiation evaluations. The lack of concern over the possible catastrophic radiation degradation in cascade cells was felt to be a potentially serious problem. It was suggested that some characterization of these devices be made on available samples to prevent extensive development of a space "useless" device.

Materials such as amorphous silicon and CuInSe_2 based devices should be monitored. Although present efficiencies are low, some limited testing has revealed very low electron degradation rates, which could provide superior cell output at very high fluences when compared to silicon or GaAs cells. If such degradation rates can be achieved with higher initial efficiencies (10-12%), these devices would be superior to silicon and GaAs based cells at EOL on a number of missions. The minimum effort required for an ongoing assessment would readily be justified based on the potential return.

ADVANCED DEVICES WORKSHOP

M. Ludowise
Varian Associates, Inc.
Palo Alto, California

The Advanced Devices Workshop considered five primary questions:

1. Is satisfactory progress being made toward the 30 percent AMO goal?
2. What are the critical barriers and approaches to solving them?
3. What are appropriate cost goals for cascade cells?
4. What fundamental materials research do we need to support 30 percent cascade cell development?
5. What are the approaches other than monolithic stacks for achieving 30 percent or greater efficiency at AMO?

A summary of the general consensus of the group will be given, keyed to the above questions.

1. Satisfactory progress is being made toward a 30 percent cell considering the complexity of the materials and device design problems involved. Some discussion centered on whether or not a 30 percent three-junction cell is an appropriate goal, rather than say a 28 percent two-junction device. Although on the surface the goal of a three-junction cell seems much loftier than a two-junction cell, the three-junction work relies on two-junction demonstrations as milestones. This means that the two-junction approach is in fact ongoing as a part of current three-junction work.
2. Several hurdles to overcome were identified, but the participants considered none of them as critical steps in the path to a 30 percent cell. The problems identified fall more in the category of either being necessary to ensure reliable cells with good EOL performance or as being desirable improvements to ease manufacturability.
 - a. The cracking of III-V epilayers (GaAs and others) on Si (and possibly Ge) should be carefully studied. Specifically, low-temperature growth of the films should be examined, with an aim of preventing the initial cracking during growth. Also, thermal cycling of epilayers, preferably as fabricated cells, should be done to determine whether new cracks develop and if they degrade the cells.
 - b. Contacts and interconnects are an ongoing concern. For manufacturability, a planar buried interconnect is desirable. This category includes tunnel junctions, Ge interconnects, and so-called "defect" interconnects in which highly dislocated material is used to ruin the reverse junction. MIC^2 or three-terminal-type contacts are nonplanar alternatives, but with process and yield

tradeoffs. All of these approaches are currently under investigation.

- c. It was suggested that thermal cycling effects on the degradation of mismatched III-V cells on GaAs substrates also should be investigated. This can be done by using existing GaInAs/GaAs cells.
 - d. Finally, radiation damage effects on lattice-mismatched cells are of some concern, in terms of further propagation mismatch defects. Radiation effects on series-connected cascade cells is a serious concern in that if one subcell decays differently than the other, the cell suffers additional current-mismatch losses. Alternative approaches such as four-terminal, three-junction structures, including mechanically stacked and monolithic structures, may need to be considered. Some participants felt the radiation damage issue may be the most serious issue for cascade cell design. Others felt that, for LEO concentrator applications, thick cover glasses could provide sufficient shielding with little weight penalty.
3. The workshop had difficulty determining what the cost goals should be and decided that this will ultimately be mission and market driven.
 4. Quite a bit of discussion centered on source-alkyl purity for the MO-CVD process. The cooperation of manufacturers of these materials will be necessary, but that too will be market driven. In only one specific instance, that of AlGaInAs, was source purity cited as having been a fatal problem. The workshop consensus was that the materials work should always be coupled to a device goal. In that way, the relevant materials work will be incorporated as appropriate into the programs.
 5. The workshop concluded that cascade semiconductors, from a historical perspective, still seem to be the best approach to 30 percent efficiency at this time. The participants felt that the community should try to be aware of developments in other fields that may be important but that, in a meeting of PV specialists, it is difficult to break out of thinking in terms of semiconductors.

SOLAR ARRAY TECHNOLOGY WORKSHOP

H. S. Rauschenbach
TRW Space & Technology Group
Redondo Beach, California

- Requirements Analysis
 - There are many users with diverging needs
 - High specific performance arrays are enabling for some missions, but not for all
 - Higher W/m^2 , W/kg : allow more payload
 - Low $\$/W$ may be enabling for some missions (large arrays)
- Near-Term Needs: Space Station Array
 - Area (drag), cost, storage volume, and weight
 - Orientation (minimum drag or Sun orientation)
 - Robustness (docking and crew loads, maintenance, growth)
- Near- to Far-Term Needs: Department of Defense Missions
 - Low-altitude orbits, survivable
 - High-radiation orbits, 5-50 kW, weight critical
 - Synchronous, 5-15 kW, medium radiation, weight critical
- Continuing Needs: Commercial and Government
 - Rigid panels providing transfer orbit power
 - W/m^2 and W/kg improvements from program to program

TECHNOLOGY REQUIREMENTS FOR CONCENTRATOR ARRAYS:

- Establish Long-Term Environmental Stability of Reflector Surfaces
 - Protons, UV, micrometeorites, oxygen, vehicle emissions
- Develop More Efficient, Large Support Structures
 - Deployable/erectable masts, booms, platforms
- Develop Required Associated Mechanisms/Hardware/Cables
 - Hinges, latches, cable service loops
 - Connectors, electrical/mechanical, self-mating
 - SADA/power transfer assemblies (stiffness)
- Develop Electro-Optical Measurement Techniques
 - Collimation angle, source image, light level standard

- Resolve Long-Term Reliability Issues
 - Elevated operating temperature, GaAs annealing temperature
 - Cell contacts, other array components, and materials (adhesives)
 - Thermal cycling temperature limits
- Develop Manufacturing Technology and Develop Cost Models
- Optimize and Characterize Advanced Solar Cells (GaAs)
 - Optimized for concentrator spectrum and intensity pattern
 - Define minimal shielding thickness

SPECIFIC POWER GOALS FOR THE 1990's:

- W/kg Goals are Inadequate by Themselves. Must Be Related to
 - Array area (power level) and configuration
 - Deployed natural frequency (stiffness, flatness)
 - Environmental requirements (radiation, lifetime)
 - Survivability requirements (man-made environment)
 - Mission constraints (restowage, docking loads, view obstruction)
- W/m^2 Is More Important for Some Missions than W/kg
 - Space station (drag)
 - Department of Defense missions (special requirements)
- Propose "300" Plan:
 - 300 W/m^2 (BOL)
 - 300 W/kg (BOL)
 - 300 V (V_{mp})

CRITICAL TECHNOLOGY ADVANCES REQUIRED FOR "300" PLAN:

- Advanced Solar Cells for Planar Arrays
 - 2-mil, 8x8 cm, GaAs-based cell on Si substrate
 - Mechanical cascade cell (3 or 4 terminal), followed later by electrical cascade cell
 - Plasmon converters
 - Other new photovoltaic converters
- Advanced Blankets
 - Mechanical cascade blankets
 - Metallic blankets (instead of Kapton)
- Advanced Power Processing
 - 300-V array voltage
 - On-array processing (lower power subsystem weight)

- Undersound Space Charging Engineering
 - Continue problem definition (small and large arrays)
 - Investigate active potential control to prevent arcing
 - Develop power drain (plasma leaking) suppression techniques

TECHNOLOGICAL APPROACHES FOR >200 kW:

- 300-Plan Leads to reduced W/m^2
 - More manageable array area, stiffness, etc.
- Fallout from Implementation of 300-Plan Will in Part, Define Approach for Larger (>200 kW) Arrays
- Innovative New Approaches (Inventions) Should be Strongly Encouraged and Funded

END

DATE

FILMED

OCT 15 1984